Theoretical and Observational Aspects of Wave Propagation in the Solar Corona

Ineke De Moortel

Thesis submitted for the degree of Doctor of Philosophy
of the University of St Andrews

October 31, 2000

Abstract

Phase mixing was introduced by Heyvaerts and Priest (1983) as a mechanism for heating plasma in open magnetic field regions. Here we include a stratified density and a diverging background magnetic field. We present numerical and WKB solutions to describe the effect of stratification and divergence on phase mixing of Alfvén waves. It is shown that the decrease in density lengthens the oscillation wavelengths and thereby reduces the generation of transverse gradients. Furthermore we found that in a stratified atmosphere, ohmic heating is spread out over a greater height range whereas viscous heating is not strongly influenced by the stratification. However, the divergence of the field lines shortens the wavelengths and thus enhances the generation of gradients.Therefore, the convection of wave energy into heating the plasma occurs at lower heights than in a uniform model. The combined effect of a stratified density and a radially diverging background magnetic field on phase mixing of Alfvén waves depends strongly on the particular geometry of the configuration. Depending on the value of the pressure scale height, phase mixing can either be more or less efficient than in the uniform case.

The usefulness of wavelet analysis is demonstrated by considering analytical expressions for phase mixed Alfvén waves in different physical circumstances. The wavelet analysis is briefly introduced and the time and scale resolution of the wavelet transform are then discussed in more detail. As an illustration of the power of wavelet analysis, phase mixed Alfvén waves are investigated. From a comparison between a truly finite harmonic wave and an Alfvén wave, dissipated by phase mixing, it is demonstrated that, using the wavelet transform, it is possible to distinguish between these two 'finite' signals. The value of the dissipation coefficient can be extracted from the wavelet transform. In a wavelet transform of phase mixed Alfvén waves in a gravitationally stratified atmosphere, the lengthening of the wavelengths is clearly evident, providing an independent estimate of the pressure scale height. In a radially diverging atmosphere, the shortening of the wavelengths is also apparant in the wavelet transform, showing how the Alfvén speed varies along the loop and thus providing information on the coronal density and magnetic field.

High cadence TRACE data (JOP 83) in the 171 Å bandpass are used to report on several examples of outward propagating oscillations in the footpoints of large diffuse coronal loop structures close to active regions. The disturbances travel outward with a propagation speed between 80 and 150 km s^{-1}. The variations in intensity are of the order of 2%-5%, compared to the background brightness and these get weaker as the disturbance propagates along the structure. From a wavelet analysis at different positions along the structures, periods in the 200–400 seconds range are found. It is suggested that these oscillations are slow magneto-acoustic waves propagating along the loop, carrying an estimated energy flux of 4×10^2 ergs cm^{-2} s^{-1}.

Declaration

1. I, Ineke De Moortel, hereby certify that this thesis, which is approximately 35,000 words in length, has been written by me, that it is a record of work carried out by me and that it has not been submitted in any previous application for a higher degree

   date ....31./10./2000..... signature of candidate

2. I was admitted as a research student in October 1997 and as a candidate for the degree of PhD in October 1998; the higher study for which this is a record was carried out in the University of St Andrews between 1997 and 2000.

   date ...31./10./2000..... signature of candidate

3. I hereby certify that the candidate has fulfilled the conditions of the Resolution and Regulations appropriate to the degree of PhD in the University of St Andrews and that the candidate is qualified to submit the thesis in application for that degree.

   date .....31/10/2000..... signature of supervisor

4. In submitting this thesis to the University of St Andrews I understand that I am giving permission for it to be made available for use in accordance with the regulations of the University Library for the time being in force, subject to any copyright vested in the work not being affected thereby. I also understand that the title and abstract will be published and that a copy of the work may be made and supplied to any bona fide library or research worker.

   date ...31./10./2000..... signature of candidate

Acknowledgements

Although I risk sounding very cheesy and sentimental, there are (quite) a few people without whom I would have never needed to bother with this acknowledgement. Therefore, I'd like to thank ...

My supervisor, Alan Hood, for his enthusiastic guidance and patience with my many, many questions. For giving me the freedom to follow my own course of research and reading draft after draft of everything I've written in the past three years.

The EU TMR Programme for financial support.

Keith and Tricia, for keeping my computer more or less sane. Daniel, for all his help with various IDL problems and teaching me to 'just write a wee code'.

My current and previous office mates and colleagues in the Solar Theory Group at St Andrews, for far too many and far too long coffee breaks. Jack, for Belgian waffles and blue M&M's.

Tracey and Charlie, for being the most fantastic flatmates and friends one could wish for. Mei-Li, for endless chats about absolutely meaningless things. All my other flatmates, just for putting up with me.

Pia and Clare, your love and enthusiasm for the mountains inspired me!

Allan, Jane & Ian and Robert for believing in me and refusing to let me give up everything.

Anneke, Dagmar, Elke and Joris for lots and lots of long (and short) emails, glasses of wine, ice-creams and visits.

Everyone at Breakaway and St Andrews Mountaineering Club, for many 'quality-mountain-days' and 'whisky-nights'.

Debby and everyone at circuit-classes, for keeping me sane.

Maria, Alessandro and their parents for hosting me everytime Firenze and Tuscany were an escape from my PhD.

My parents and Tom & Koen, for encouraging me to come to St Andrews and start this PhD in the first place. For getting me where I am today ...

Contents

Chapter 1

Introduction

If we knew what it was we were doing, it would not be called research, would it?
Albert Einstein

1.1 General introduction to the Sun

The Sun, our nearest star, has been studied for thousands of years. Being 'only' 1.5×10^8 km (1 *Astronomical Unit*) away, it provides us with a unique opportunity to study a star in close detail. The Sun is a fairly typical star of spectral type G2 and it is the only star that can be seen from the Earth as more than a mere point of light. Therefore, studying the Sun's complex properties forms the basis for our understanding of similar stars which cannot be observed in such detail. The Sun is 4.6×10^9 years old and its mass of 1.99×10^{30} kg of plasma, is held together by gravitational forces. The Sun is composed of 90% Hydrogen and 10% Helium, mostly in a ionised state because of the extremely high temperatures. The remaining about 0.1% consists of heavier elements such as Carbon (C), Nitrogen (N) and Oxygen (O).

We will give a short overview of the Sun's different regions, starting with a description of the solar interior. In the discussion of the three different layers of the solar atmosphere, we will only mention some basic properties of the *photosphere* and *chromosphere* and concentrate mainly on the *corona*, since most of the work in this thesis concerns coronal phenomena. Comprehensive reviews of both theory and observations can be found in Priest (1982), Phillips (1992), Golub and Pasachoff (1997) and Tayler (1997).

1.1.1 The solar interior

The interior of the Sun cannot directly be observed and most of our knowledge is obtained indirectly, through helioseismology, the study of the global solar oscillations. The interior can be divided into three regions; the core, the radiative zone and the convective zone. The *solar core* extends over a region of 0.3 $R_\odot$ (1 $R_\odot$ = 6.96×10^5 km) and generates 99% of the Sun's energy. Standard models give a central temperature of 1.6×10^7 K and a central density of 1.6×10^5 kg/m^3. These values are high enough for the core to be an enormous nuclear reactor, where hydrogen is fused to form helium. The region surrounding the central core, extending from 0.3 $R_\odot$ till 0.7 $R_\odot$, is the *radiative zone*. Here, the energy that is continuously generated in the core, is transferred outwards by radiative diffusion. Temperature and density decrease rapidly as we move away from the Sun's central core. Throughout the radiative zone, the temperature and density decrease until at 0.7 $R_\odot$, the temperature reaches a value of 2×10^6 K, whereas the density has dropped to 200 kg/m^3. This is the start of the *convective zone*. Across this zone, the temperature decreases from 2×10^6 K to 6400 K and it is this steep temperature gradient that generates the convective motions, as the gas can no longer remain in static equilibrium. The density also decreases dramatically in this layer, to 4×10^{-4} kg/m^3. It is believed that the lower boundary of the convective zone, often referred to as the *tachocline*, is the site where the Sun's magnetic field is generated.

1.1.2 The photosphere

The lowest layer of the solar atmosphere is an extremely thin layer, 500 km thick, called the photosphere. This is the Sun's visible surface and it is here that the bulk of the solar radiation is emitted. Throughout the photosphere, temperature and density decrease with increasing height until the temperature falls to a minimum value of 4300 K at the top of this layer. At the temperature minimum, the density has decreased to 8×10^{-5} kg/m^3. In a high resolution photograph of the photosphere a granulation pattern of bright cells with dark boundaries can be seen. These granules have typical diameters of 700 to 1500 km and represent the top of the convective cells. The granules are in continuous motion, with typical lifetimes of about 8 minutes. In the centre of each granule, hot material rises up and moves horizontally outward towards the cell boundaries at 1–3 km/s. Supergranular cells have diameters ranging from 10 000 km to 30 000 km and have a lifetime of 1 to 2 days. Material rises at the centre at 0.1 km/s, moves horizontally outwards at 0.3 to 0.4 km/s and downwards at the cell boundaries at 0.1 to 0.2 km/s. In the boundaries of supergranule cells, magnetic flux is concentrated with extremely high field strengths of 1000 to 2000 Gauss (1 Gauss = 10^{-4} Tesla). The largest magnetic field strengths in the photosphere are found in *sunspots* (2000–4000 G). Sunspots consist of an inner part, called the *umbra* and a surrounding outer region,

the *penumbra*. Typically, sunspots appear in pairs, with the leading spot having the largest field strength of one polarity, and the following spot having a slightly weaker strength of the opposite polarity. The leading spots in one hemisphere have the opposite polarity to the leading spots in the other hemisphere and with every 11-year cycle, the polarities reverse.

1.1.3 The chromosphere and transition region

Above the photosphere is a narrow layer, about 2500 km thick, called the chromosphere. After reaching its minimum value of 4300 K at the top of the photosphere, the temperature rises throughout the chromosphere, reaching about 5×10^4 K. The most dramatic increase in temperature takes place in the *transition region* between the chromosphere and the corona, with a very rapid transition from 5×10^4 K to 10^5 or 10^6 K. The density drops from several times 10^{-5} kg/m^3 to about 10^{-10} kg/m^3. At the limb, plasma jets (*spicules*) ejected from the boundaries of supergranular cells are observed. Spicules are only a few hundred kilometers in diameter and reach velocities of 20 to 30 km/s and altitudes of about 10 000 km. They last approximately 15 minutes before fading away.

1.1.4 The corona

The final part of the solar atmosphere, above the chromosphere, is the extremely hot and tenuous corona. Dominated by the magnetic field, the corona is highly non-uniform and appears in white light as streamers, plumes and other structures extending out from the chromosphere. The temperature of the corona reaches values of several million degrees Kelvin with a density that has dropped to several times 10^{-12} kg/m^3. These high temperatures imply that hydrogen is fully ionised, giving rise to radiation in a wide range of wavelengths (e.g. X-rays, EUV and radio emission). The corona predominantly radiates in the shorter wavelengths, which are absorbed by the Earth's atmosphere. Therefore, for a very long time, our only knowledge about the corona came from white light observations during eclipses. However, during the last decades, our view of the solar atmosphere has been transformed by EUV and X-ray observations from space, by satellites such as Skylab, SMM, and, more recently, SOHO and TRACE. A composite image of the corona, taken by the EIT and LASCO instruments onboard SOHO is shown in Figure 1.1. The sequence of images clearly shows the complex and inhomogeneous structure of the solar corona and the change in activity in the Sun's atmosphere during the solar cycle. At solar minimum, the corona appears as long, symmetrical streamers, almost aligned with the equator, whereas, at solar maximum, many streamers and other structures are present. In soft X-rays, two distinctly different types of regions can be seen in the solar corona; relatively dark regions, where the magnetic field is open are called *coronal holes* whereas regions in which the magnetic field is mainly closed show a multitude of bright *coronal*

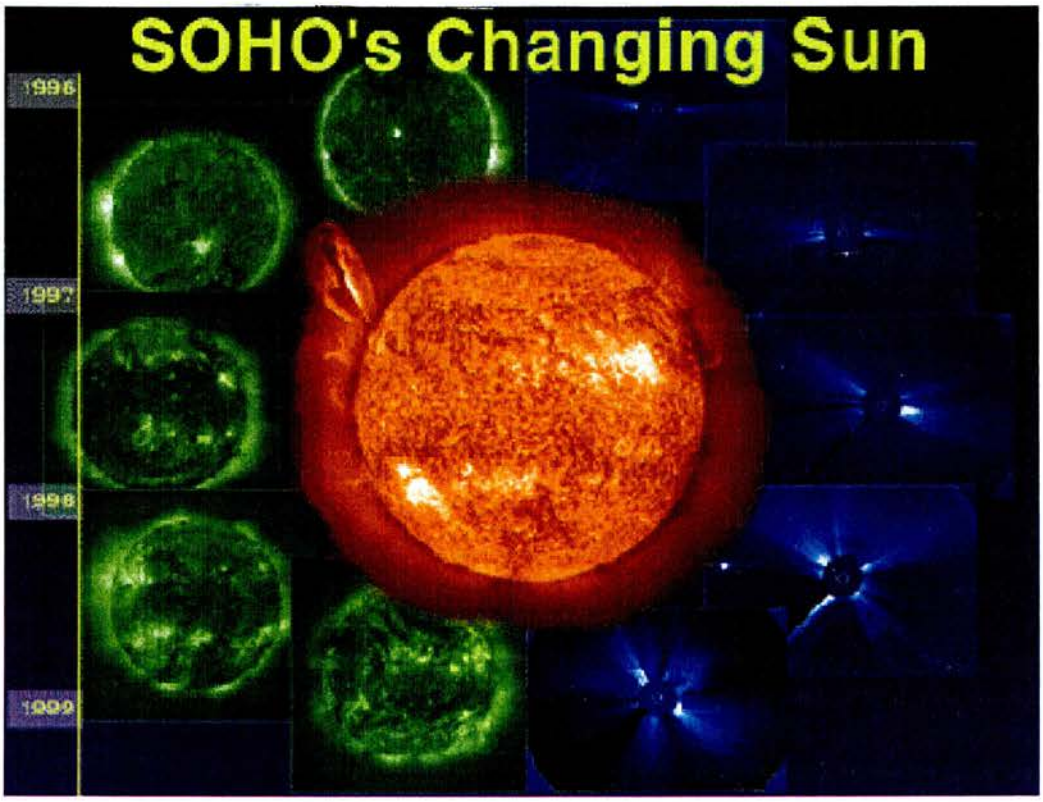

Figure 1.1: A composite of SOHO/EIT and SOHO/LASCO images of the Sun's changing atmosphere (taken from http://sohowww.nascom.nasa.gov). The central image was taken by EIT in the 304 Å passband and shows the solar atmosphere at about 5×10^4 K. The surrounding images on the left hand side, taken by EIT in the 195 Å passband, show the solar atmosphere at about 2×10^6 K. Starting at the top, the sequence shows the evolution of the solar corona from solar minimum to solar maximum. The images on the right hand show the corresponing views of the outer corona, taken by the LASCO C2 coronagraph.

loops. Small *X-ray bright points* are also observed in the solar corona, scattered over the whole of the disk.

Coronal holes

Coronal holes are extended regions from which plasma flows outward as the high-speed *solar wind* ($v \sim 700$ km/s at 1 AU). Most of the fast solar wind originates from the two polar coronal holes, but smaller coronal holes, at lower latitudes, also exist. From measurements of the solar wind, Woo & Habbal (1999) demonstrated that signatures of coronal hole boundaries, active regions and bright points are present at distances between 20–30 $R_\odot$. Using UVCS (SOHO) observations, Giordano et

al. (2000) suggested that the fast solar wind is preferentially accelareted in interplume lanes and in the darker background regions of a polar coronal hole. The density in coronal holes is significantly lower (a factor of approximately 3) than in the surrounding corona. Coronal holes lie above extended, i.e. wider than 3–4 $\times 10^5$ km (Priest, 1982) unipolar regions. Coronal holes have a temperature of the order of 1–1.5 $\times 10^6$ K and a magnetic field strength of 1–10 G. Typical dimensions are 700–900 Mm for the polar holes and 300–600 Mm for low-latitude coronal holes. They have an extended lifetime, lasting several solar rotations, which makes them among the longest-lived features in the solar atmosphere. The polar coronal holes are the most persistent, disappearing only during solar maximum, and reappearing with opposite magnetic polarity soon afterward. A study of the solar cycle dependence of the polar coronal holes has been made by Das et al. (1993). SOHO/SUMER observations of a polar coronal hole during solar minimum (Nov–Dec 1996) are discussed by Doyle et al. (1999) whereas SOHO/UVCS observations are presented by Cranmer et al. (1999) and Esser et al. (1999). EUV and radio observations of an equatorial coronal hole are presented by Chiuderi Drago et al. (1999). Measurements of the electron temperature gradient in a solar coronal hole have been done by David et al. (1998). These authors find temperatures of about 8×10^5 K close to the limb, increasing to a maximum value of less than 10^6 K and then decreasing to 4×10^5 K at $1.3 R_\odot$.

Within coronal holes, faint rays of enhanced density, called *coronal plumes* are observed. They are especially noticeable in the polar holes during solar minimum. The density inside a plume is on average 3–5 times higher than in the surrounding coronal hole (Del Zanna et al., 1997). Plumes are typically about 20–30 Mm wide and are thought to outline the local magnetic field. Comprehensive discussion of observations of coronal plumes can be found in DeForest et al. (1997) and Young et al. (1999).

Active regions and Coronal loops

Active regions appear as bright *plages* of emission in a belt within ± 30 degrees from the equator. Most active regions are associated with bipolar regions with the flux ordered into two regions of opposite polarity; the preceding flux concentrated in a single sunspot and the following flux more diffuse. However, many small, short-lived active regions exist without being associated with a sunspot, while old active regions which did have a sunspot can persist for some time after their spots have disappeared. The temperature and density of the coronal plasma above an active region are enhanced by a factor of 2 and 10 respectively. Also, the temperature of an active region seems to vary with its age with young, bright regions having temperatures of the order of 5×10^6 K. More evolved regions appear fainter and more diffuse, with temperatures about 3×10^6 K.

At high temperatures, the active region corona consists of a multitude of different coronal loops, with

their footpoints anchored lower down in the photosphere or chromosphere. Temperatures in active region loops lie in the range of 1–6 $\times 10^6$ K, with a typical value of 2×10^6 K. Large, relatively faint loops as well as smaller, brighter loops are present. These smaller loops are associated with sunspot groups and are located in active regions. They are short-lived, with typical lifetimes of only a few hours and about 10–100 Mm long. The loops have temperatures about 2.5×10^6 K. Larger loops, or arches, connect distant regions of opposite polarity. They may extend over substantial distances, of the order of several 100 Mm, sometimes even stretching across the equator. They have a typical temperature of 2–3 $\times 10^6$ K. While a single loop has a lifetime of the order of several days, a whole loop system, connecting separate active regions, may last for several rotations. For a comprehensive review of the structure and physical characteristics of loops, see e.g. Bray et al. (1991) or Smith (1997).

X-ray bright points

X-ray bright points are small, almost pointlike features, with, as the name suggests, a relatively bright X-ray emission. Appearing all over the the solar disc, well away from active regions, and with a typical lifetime substantially less than one day ($\sim$ 8 hrs), they are clearly not associated with active regions. Bright point dimensions are of the order of 22 Mm, with a smaller bright core (4–7 Mm). About 40 bright points may be visible on the solar disc at any given time and approximately 1500 of them appear per day. They are associated with small bipolar magnetic regions, known as *ephermal regions*. A more detailed overview of bright points, can be found in Parnell et al. (1994).

1.2 The MHD Equations

The *Magnetohydrodynamic* (or MHD) equations are a system of equations that is used to describe the behaviour of a plasma (ionised gas) when a (strong) magnetic field is present, or how a magnetic field interacts with a plasma. They are a combination of Maxwell's equations, which describe the electromagnetic behaviour of the plasma, and the fluid equations.

1.2.1 Electromagnetic Equations

Maxwell's equations are

Ampère's law

$$\nabla \times \mathbf{B} = \mu \mathbf{j} + \frac{1}{c^2} \frac{\partial \mathbf{E}}{\partial t}, \tag{1.1}$$

where $\frac{1}{c^2} \frac{\partial \mathbf{E}}{\partial t}$ is the displacement current;

The solenoidal condition

$$\nabla.\mathbf{B} = 0\,, \tag{1.2}$$

stating that there are no magnetic monopoles, i.e. there are no magnetic sources or sinks;

Faraday's law of induction

$$\nabla \times \mathbf{E} = -\frac{\partial \mathbf{B}}{\partial t}\,, \tag{1.3}$$

relating the electric and magnetic fields;

Gauss' law for electricity

$$\nabla.\mathbf{E} = \frac{1}{\varepsilon}Q^*\,, \tag{1.4}$$

implying charge conservation.

In these equations, the variable t denotes time, $\mathbf{B}$ the magnetic field, $\mathbf{E}$ the electric field and $\mathbf{j}$ the current density. The total charge density is $Q^* = q_i n_i + q_e n_e$, where n_i and n_e are the number of ions and electrons respectively, and q_i and q_e are the charges on the respective particles. ε and μ are the permitivity and magnetic permeability in a vacuum, and finally, $c = (\mu\varepsilon)^{-1/2} \backsimeq 3 \times 10^8$ m/s is the speed of light in a vacuum. For most phenomena, the typical plasma velocities satisfy $v^2 \ll c^2$, and, thus, the displacement current is usually neglected in Eqn. (1.1). This MHD approximation simplifies Ampère's law to

$$\nabla \times \mathbf{B} = \mu\mathbf{j}\,. \tag{1.5}$$

For most plasmas, the condition for charge neutrality, $n_i - n_e \ll n$, where n is the total number density is satisfied and thus we can neglect the charge density in Eqn. (1.4).

The link between the electromagnetic and fluid equations is given by Ohm's law,

$$\mathbf{j} = \sigma(\mathbf{E} + \mathbf{v} \times \mathbf{B})\,, \tag{1.6}$$

where $\mathbf{v}$ is the plasma velocity and σ is the electrical conductivity. In solar MHD, the electric field $\mathbf{E}$ is usually eliminated from the equations. Using Ampère's law (Eqn. (1.1)) and Ohm's law (Eqn. (1.6)), the induction equation (Eqn. (1.3)) can be written as

$$\frac{\partial \mathbf{B}}{\partial t} = \nabla \times (\mathbf{v} \times \mathbf{B}) - \nabla \times (\eta \nabla \times \mathbf{B})\,,$$

where $\eta = \frac{1}{\mu\sigma}$ is the magnetic diffusivity. Assuming η is constant and using the solenoidal condition $\nabla.\mathbf{B} = 0$, we find

$$\frac{\partial \mathbf{B}}{\partial t} = \nabla \times (\mathbf{v} \times \mathbf{B}) + \eta \nabla^2 \mathbf{B}\,, \tag{1.7}$$

which is the form of the induction equation that is generally used in solar MHD.

1.2.2 Fluid Equations

Next we introduce the fluid equations. By using these equations, we assume the plasma behaves as a single fluid and that the motions of individual particles can be ignored.

The first equation is the mass continuity equation

$$\frac{\partial \rho}{\partial t} + \nabla.(\rho \mathbf{v}) = 0\,, \tag{1.8}$$

which states that matter is neither created or destroyed.

The next fluid equation is the equation of motion

$$\rho \frac{D\mathbf{v}}{Dt} = -\nabla p + \mathbf{F}\,, \tag{1.9}$$

which is basically Newton's second law 'mass x acceleration = force'. The convective time derivative is give by

$$\frac{D}{Dt} = \frac{\partial}{\partial t} + \mathbf{v}.\nabla\,, \tag{1.10}$$

and describes the time derivative as a quantity moves with the plasma.

The energy equation can be written as

$$\frac{\rho^\gamma}{\gamma - 1}\frac{D}{Dt}\left(\frac{p}{\rho^\gamma}\right) = -L\,, \tag{1.11}$$

where L is the total energy loss function and $\gamma = \frac{C_p}{C_v}$ is the ratio of specific heats, normally taken as $5/3$.

Finally, to close the system of equations, the last equation is the ideal gas law

$$p = \frac{\mathcal{R}}{\tilde{\mu}}\rho T\,, \tag{1.12}$$

where T is the plasma temperature, $\mathcal{R}$ is the gas constant and $\tilde{\mu}$ is the mean atomic weight.

The external force in the equation of motion (Eqn. (1.9)) consists of several terms and the importance of each of these terms depends on the particular situation one wants to model. The most frequently used terms are the Lorentz Force,

$$\mathbf{j} \times \mathbf{B}\,, \tag{1.13}$$

the gravitational force,

$$\rho \mathbf{g}\,, \tag{1.14}$$

and a viscous force,

$$\rho \nu \nabla^2 \mathbf{v}\,. \tag{1.15}$$

The actual form of the viscous term is complicated (Braginskii, 1965). Here we have used the incompressible form and ν is the coefficient of kinematic viscosity. The equation of motion thus becomes

$$\rho\frac{D\mathbf{v}}{Dt} = -\nabla p + \mathbf{j}\times\mathbf{B} + \rho\mathbf{g} + \rho\nu\nabla^2\mathbf{v}\,. \tag{1.16}$$

Note here that it is the Lorentz Force $\mathbf{j}\times\mathbf{B}$ that couples the fluid equations to the electromagnetic equations.

The energy equation (Eqn. (1.11)) can be written in many different forms. In the solar corona, the energy loss function L has three main components; thermal conduction, optically thin plasma radiation and coronal heating. L can thus be written as

$$L = -\nabla.(\kappa\nabla T) + \rho^2 Q(T) - H\,, \tag{1.17}$$

where κ is the anisotropic thermal conductivity tensor and Q is the optically thin radiative loss function. Optically thin radiation is a valid assumption above a temperature of about 10^4 K. The coronal heating term H again consists of several terms, e.g.

$$H = H_0 + \frac{j^2}{\sigma} + \rho_0\nu\omega^2\,. \tag{1.18}$$

Here H_0 depends on the coronal magnetic field, e.g. magnetic reconnection. The ohmic heating term, $\frac{j^2}{\sigma}$, and the viscous heating term, $\rho_0\nu\omega^2$, where the vorticity $\omega = \nabla\times\mathbf{v}$, are generally small but become important in regions where lengthscales are sufficiently small. Overall, the energy equation is complicated but in many solar situations, the medium can be assumed to be isentropic or adiabatic, i.e. $L = 0$. The adiabatic energy equation can be written as

$$\frac{\rho^\gamma}{\gamma-1}\frac{D}{Dt}\left(\frac{p}{\rho^\gamma}\right) = \frac{\partial p}{\partial t} + \mathbf{v}.\nabla p + \gamma p\nabla.\mathbf{v} = 0\,. \tag{1.19}$$

1.2.3 Summary of the MHD Equations used in this thesis

$$\frac{\partial\rho}{\partial t} + \nabla.(\rho\mathbf{v}) = 0\,, \tag{1.20}$$

$$\rho\frac{\partial\mathbf{v}}{\partial t} + \rho(\mathbf{v}.\nabla)\mathbf{v} = -\nabla p + \mathbf{j}\times\mathbf{B} + \rho\mathbf{g} + \rho\nu\nabla^2\mathbf{v}\,, \tag{1.21}$$

$$\frac{\partial p}{\partial t} + \mathbf{v}.\nabla p = -\gamma p\nabla.\mathbf{v}\,, \tag{1.22}$$

$$p = 2\rho\mathcal{R}T\,, \tag{1.23}$$

$$\mathbf{j} = \frac{1}{\mu}\nabla \times \mathbf{B}\,, \tag{1.24}$$

$$\nabla.\mathbf{B} = 0\,, \tag{1.25}$$

$$\frac{\partial \mathbf{B}}{\partial t} = \nabla \times (\mathbf{v} \times \mathbf{B}) + \eta \nabla^2 \mathbf{B}\,. \tag{1.26}$$

1.3 MHD waves

1.3.1 Alfvén and magnetoacoustic waves in a uniform plasma

The theory of MHD waves is a very important topic, as observations indicate that various kinds of (quasi)-periodic oscillations occur on the Sun. In this section we briefly introduce the three basic MHD waves. We want to examine the types of disturbances that can arise in a uniform medium, with a uniform magnetic field in the vertical, or z direction. The equilibrium is thus given by

$$\begin{aligned} \mathbf{B}_0 &= B_0\hat{\mathbf{z}}\,, \\ \mathbf{v}_0 &= 0\,, \\ p_0 &= \text{constant} \qquad \text{and} \qquad \rho_0 = \text{constant}\,, \end{aligned}$$

where B_0 is constant. Note here that the equilibrium quantities (denoted by subscript '0') are independent of time. We now consider small perturbations (denoted by subscript '1') to the equilibrium. We set

$$\begin{aligned} \mathbf{B} &= \mathbf{B}_0 + \mathbf{B}_1\,, \\ \mathbf{v} &= 0 + \mathbf{v}_1\,, \\ p &= p_0 + p_1\,, \\ \rho &= \rho_0 + \rho_1\,. \end{aligned}$$

Next we linearise the MHD equations, by substituting these quantities into the equations and ignoring the products of small terms, i.e. of perturbed quantities. The linearised MHD equations take the form

$$\frac{\partial \rho_1}{\partial t} + \rho_0 \nabla.\mathbf{v}_1 = 0\,, \tag{1.27}$$

$$\rho_0 \frac{\partial \mathbf{v}_1}{\partial t} = -\nabla p_1 + (\mathbf{B}_0.\nabla)\frac{\mathbf{B}_1}{\mu} - \nabla\left(\frac{\mathbf{B}_0.\mathbf{B}_1}{\mu}\right)\,, \tag{1.28}$$

$$\frac{\partial p_1}{\partial t} = -c_s^2 \rho_0 (\nabla . \mathbf{v}_1) \,, \tag{1.29}$$

$$\nabla . \mathbf{B}_1 = 0 \,, \tag{1.30}$$

$$\frac{\partial \mathbf{B}_1}{\partial t} = -B_0 (\nabla . \mathbf{v}_1) \hat{\mathbf{z}} + B_0 \frac{\partial \mathbf{v}_1}{\partial z} \,, \tag{1.31}$$

where $c_s^2 = \frac{\gamma p_0}{\rho_0}$ is the sound speed.

The solutions to this set of linearised, ideal MHD equations will tell us about the nature of the perturbations. We now define the perturbed magnetic and total pressure as

$$p_{1M} = \frac{1}{\mu} \mathbf{B}_0 . \mathbf{B}_1 \,, \tag{1.32}$$

$$p_{1T} = p_1 + p_{1M} \,, \tag{1.33}$$

and the perturbed velocities perpendicular and parallel to the ambient field as

$$\mathbf{v}_\perp = (v_{1x}, v_{1y}, 0) \,, \tag{1.34}$$

$$\mathbf{v}_\parallel = (0, 0, v_{1z}) \,. \tag{1.35}$$

Using the linearised induction equation (Eqn. (1.31)), we can write

$$\frac{\partial p_{1M}}{\partial t} = -\frac{1}{\mu} B_0^2 (\nabla . \mathbf{v}_\perp) \,, \tag{1.36}$$

and together with Eqn. (1.29), we find

$$\frac{\partial p_{1T}}{\partial t} = \rho_0 v_A^2 \frac{\partial v_{1z}}{\partial z} - \rho_0 (c_s^2 + v_A^2)(\nabla . \mathbf{v_1}) \,, \tag{1.37}$$

where the Alfvén speed $v_A^2 = \frac{\mathbf{B}_0^2}{\mu \rho_0}$.

After some algebra, differentiating the linearised equation of motion (Eqn. (1.28)) with respect to time yields,

$$\rho_0 \frac{\partial^2 \mathbf{v}_1}{\partial t^2} = \nabla \left(-\frac{\partial p_{1T}}{\partial t} \right) + \rho_0 v_A^2 \left[\frac{\partial^2 \mathbf{v}_1}{\partial z^2} - \frac{\partial}{\partial z} (\nabla . \mathbf{v}_1) \hat{\mathbf{z}} \right] \,, \tag{1.38}$$

or in terms of the velocity components,

$$\rho_0 \left(\frac{\partial^2}{\partial t^2} - v_A^2 \frac{\partial^2}{\partial z^2} \right) \mathbf{v}_\perp = -\nabla_\perp \left(\frac{\partial p_{1T}}{\partial t} \right) \,, \tag{1.39}$$

and

$$\left(\frac{\partial^2}{\partial t^2} - c_s^2 \frac{\partial^2}{\partial z^2} \right) v_{1z} = c_s^2 \frac{\partial}{\partial z} (\nabla . \mathbf{v}_\perp) \,. \tag{1.40}$$

We now look for plane wave solutions of the form

$$v_{1x} = V_{1x} e^{i(\Omega t - \mathbf{k}.\mathbf{r})} \,, \tag{1.41}$$

where V_{1x} is constant amplitude, Ω is the frequency, $\mathbf{k} = (k_x, k_y, k)$ is the wavevector and $\mathbf{r} = (x, y, z)$ is the position vector. This implies,

$$\frac{\partial}{\partial x} \to -ik_x \quad , \quad \frac{\partial}{\partial y} \to -ik_y \quad , \quad \frac{\partial}{\partial z} \to -ik \quad \text{and} \quad \frac{\partial}{\partial t} \to i\Omega \,,$$
$$\frac{\partial^2}{\partial x^2} \to -k_x^2 \quad , \quad \frac{\partial^2}{\partial y^2} \to -k_y^2 \quad , \quad \frac{\partial^2}{\partial z^2} \to -k^2 \quad \text{and} \quad \frac{\partial^2}{\partial t^2} \to -\Omega^2 \,.$$

Before we discuss solutions of Eqn. (1.38), we have a closer look at the different pressure and tension forces. Using Eqns. (1.29), (1.40) and the Fourier representation, we find

$$P_1 = \rho_0 \frac{\Omega}{k} V_{1z} \,, \tag{1.42}$$

which tells us that the pressure perturbations are related to the velocity perturbations along the equilibrium magnetic field. Similarly, the magnetic pressure perturbation (Eqn. (1.36)) is given by

$$P_{1M} = \frac{v_A^2}{c_s^2} \left(\frac{\Omega^2 - c_s^2 k^2}{\Omega^2} \right) P_1 \,, \tag{1.43}$$

and the total pressure perturbation (Eqn. (1.37)) is then found to be

$$P_{1T} = \frac{P_1}{c_s^2 \Omega^2} (v_A^2 + c_s^2)(\Omega^2 - c_T^2 k^2) \,, \tag{1.44}$$

where the tube speed is defined as $c_T^2 = \frac{v_A^2 c_s^2}{v_A^2 + c_s^2}$. Finally we look at the magnetic tension force,

$$\mathbf{f} = (\mathbf{B}_0 . \nabla) \frac{\mathbf{B}_1}{\mu} \,. \tag{1.45}$$

Differentiating with respect to time and using Eqn. (1.31) and the same Fourier analysis, $f_{1x} = F_{1x} e^{i(\Omega t - \mathbf{k}.\mathbf{r})}$, we find

$$F_{1x} = -\frac{\rho_0 v_A^2}{i\Omega} k^2 V_{1x} \,, \tag{1.46}$$

$$F_{1y} = -\frac{\rho_0 v_A^2}{i\Omega} k^2 V_{1y} \,, \tag{1.47}$$

and

$$F_{1z} = -ikP_{1M} \,. \tag{1.48}$$

Across the field, the perturbed tension is related to the perturbed velocity components, whereas along the field, the perturbed tension is related to the perturbed magnetic pressure.

We now return to the system of equations (1.37), (1.39) and (1.40). One trivial solution to these equations is the incompressible solution $\nabla . \mathbf{v} = 0$, $v_{1z} = 0$ and $P_{1T} = 0$. The equations (1.37), (1.39) and (1.40) are then reduced to

$$\left(\frac{\partial^2}{\partial t^2} - v_A^2 \frac{\partial^2}{\partial z^2} \right) \mathbf{v}_\perp = 0 \,. \tag{1.49}$$

Again using the Fourier representation, we find the dispersion relation for *Alfvén waves*

$$\Omega^2 = k^2 v_A^2 \qquad \text{or} \qquad \Omega^2 = K^2 \cos^2\theta v_A^2 \,, \tag{1.50}$$

where θ is the angle between the equilibrium magnetic field $\mathbf{B}_0$ and the wavevector $\mathbf{k}$ and $K^2 = k_x^2 + k_y^2 + k^2$. Because the perturbed total pressure $P_{1T} = 0$, it follows from Eqn. (1.44) that the perturbed plasma pressure $P_1 = 0$, and thus, from Eqn. (1.43) that the perturbed magnetic pressure $P_{1M} = 0$. This implies that the perturbed density $\rho_1 = 0$ and, from Eqn. (1.48), that the magnetic tension along the field $F_{1z} = 0$. The Alfvén wave is an incompressible motion, transverse to the magnetic field and driven by tension forces. It is anisotropic, unable to propagate across the field.

In the compressible case, the system of equations (1.37), (1.39) and (1.40), can be combined into one single equation

$$\Omega^4 - \Omega^2(c_s^2 + v_A^2)K^2 + v_A^2 c_s^2 k^2 K^2 = 0\,, \tag{1.51}$$

or

$$\frac{2\Omega^2}{K^2} = (c_s^2 + v_A^2) \pm \left[(c_s^2 + v_A^2)^2 - 4c_s^2 v_A^2 \cos^2\theta\right]^{1/2}\,. \tag{1.52}$$

These two solutions are called the *fast* and *slow magnetoacoustic waves* respectively. From Eqn. (1.43), we find

$$\frac{P_{1M}}{P_1} = \frac{v_A^2}{c_s^2}\left(\frac{\Omega^2 - c_s^2 k^2}{\Omega^2}\right)\,. \tag{1.53}$$

Thus, for the slow wave, the magnetic and pressure perturbations are out of phase, as $\Omega^2 < c_s^2 k^2$. From Eqn. (1.52) we see that the slow mode cannot propagate across the field.

For the fast wave, $\Omega^2 > c_s^2 k^2$ and hence the magnetic and plasma pressures are in phase. The tension forces (1.46), (1.47) and (1.48) fall to zero for $\theta = \frac{\pi}{2}$, i.e. $m = 0$, but $\frac{P_{1M}}{P_1}$, and hence $\frac{P_{1T}}{P_1}$, has a maximum at $\theta = \frac{\pi}{2}$. The fast wave is isentropic but has its maximum speed perpendicular to the field, when it is driven by plasma and magnetic pressure perturbations acting in phase.

A discussion of the different wave modes, under different physical circumstances would fill more than one PhD thesis. Therefore, we refer the reader to the substantial literature on this topic (e.g. Roberts 1981a, 1981b; Rae & Roberts, 1982; Roberts, 1985). The theoretical work in this thesis will mainly concentrate on phase mixing of Alfvén waves in a non-uniform plasma and will take resistivity and viscosity into account.

1.3.2 Alfvén waves in a uniform, resistive plasma

To obtain a better understanding of the wave problems we will be studying in a non-uniform plasma, we first look at the behaviour of Alfvén waves in a uniform, resistive plasma. We assume an isothermal, low-β plasma with a homogeneous background density ρ_0. Assuming a time dependence of the form $\exp(i\Omega t)$ for both the perturbed magnetic field and the velocity, the linearised induction equation and equation of motion become

$$i\Omega b = B_0 \frac{\partial v}{\partial z} + \eta \nabla^2 b \tag{1.54}$$

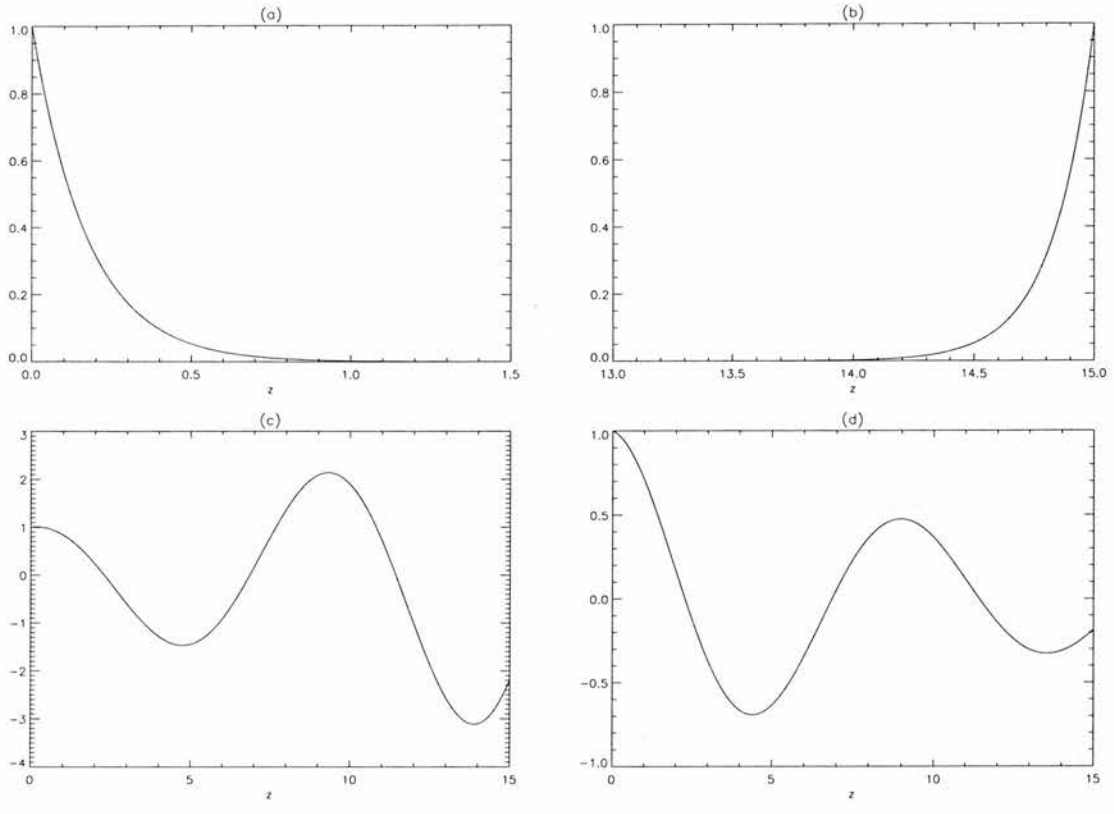

Figure 1.2: The different components (a) v_1, (b) v_2, (c) v_3 and (d) v_4.

and

$$i\rho_0\Omega v = \frac{B_0}{\mu}\frac{\partial b}{\partial z} + \rho_0\nu\nabla^2 v, . \tag{1.55}$$

If we now assume $v \sim e^{-ikz}$ and $b \sim e^{-ikz}$, these equations can be combined into a single quadratic equation for k^2,

$$\eta\nu k^4 + k^2(v_A^2 + i\Omega(\eta+\nu)) - \Omega^2 = 0, \tag{1.56}$$

where the Alfvén speed $v_A^2 = \frac{B_0^2}{\mu\rho_0}$ and the magnetic diffusivity η and the viscosity ν are assumed to be constant. The solutions to Eqn. (1.56) are then given by

$$k_+^2 = \frac{-(v_A^2 + i\Omega(\eta+\nu)) + \sqrt{(v_A^2 + i\Omega(\eta+\nu))^2 + 4\Omega^2\eta\nu}}{2\eta\nu} \tag{1.57}$$

and

$$k_-^2 = \frac{-(v_A^2 + i\Omega(\eta+\nu)) - \sqrt{(v_A^2 + i\Omega(\eta+\nu))^2 + 4\Omega^2\eta\nu}}{2\eta\nu}. \tag{1.58}$$

If we now set

$$k_1 = \sqrt{(k_+^2)}, \quad k_2 = -\sqrt{(k_+^2)}, \quad k_3 = -\sqrt{(k_-^2)} \quad \text{and} \quad k_4 = \sqrt{(k_-^2)}, \tag{1.59}$$

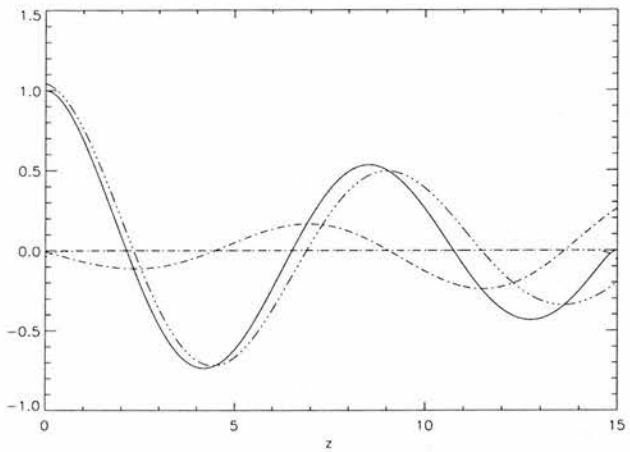

Figure 1.3: The perturbed velocity v (solid line) and the different contributions Av_1 (dotted line), Bv_2 (dashed line), Cv_3 (dot-dashed line) and Dv_4 (dot-dot-dashed line)

the full solution for the perturbed velocity is given by,

$$v = Ae^{-ik_1 z} + Be^{-ik_2(z-L)} + Ce^{-ik_3 z} + De^{-ik_4 z}, \tag{1.60}$$

where the constants A, B, C and D are determined from the boundary conditions and L represents the upper boundary. Assuming $\Omega\nu \ll v_A^2$ and $\Omega\eta \ll v_A^2$, approximate analytical solutions are given by

$$\begin{cases} k_1 = i\dfrac{v_A}{\sqrt{\eta\nu}}, \\ k_2 = -i\dfrac{v_A}{\sqrt{\eta\nu}}, \\ k_3 = -\dfrac{\Omega}{v_A} + \dfrac{i\Omega^2(\eta+\nu)}{2v_A^3}, \\ k_4 = \dfrac{\Omega}{v_A} - \dfrac{i\Omega^2(\eta+\nu)}{2v_A^3}. \end{cases} \tag{1.61}$$

In Figure 1.2 we present the different components $v_1 = e^{-ik_1 z}$, $v_2 = e^{-ik_2(z-L)}$, $v_3 = e^{-ik_3 z}$ and $v_4 = e^{-ik_4 z}$. To obtain these results, we set $\eta = \nu = 2.5 \times 10^{-1}$, $L = 15.0$ and $v_A^2 = 2.0$. We see that v_1 and v_2 represent the lower and upper boundary layer respectively and that v_3 and v_4 represent a growing and decaying spatial oscillation.

In Figure 1.3 the full solution for the perturbed velocity v is shown, as well as the different contributions to this solution Av_1, Bv_2, Cv_3 and Dv_4. To determine the constants A, B, C and D boundary conditions were chosen as follows,

$$\begin{cases} v(z=0) = 1.0, \\ \dfrac{\partial v}{\partial z}(z=0) = 0.0, \\ v(z=L) = 0.0, \\ \dfrac{\partial v}{\partial z}(z=L) = 0.0\,. \end{cases} \tag{1.62}$$

It is clear from Figure 1.3 that the contribution due to the boundary layers v_1 and v_2 is negligible and that the full solution for v mainly consists of the oscillations v_3 and v_4. This results justifies neglecting the product $\eta\nu$ in later work. Indeed, when $\eta\nu \approx 0$, we see that Eqn. (1.56) reduces to

$$k^2(v_A^2 + i\Omega(\eta + \nu)) - \Omega^2 = 0, \tag{1.63}$$

and that the only remaining solutions are k_3 and k_4 which give the growing and decaying oscillations v_3 and v_4. From Figure 1.3 we saw that the contribution of the boundary layers resulting from the solutions k_1 and k_2 was negligible anyway, which means that the solution for the perturbed velocity will not change noticeably when we neglect the product $\eta\nu$.

1.4 The coronal heating problem

1.4.1 A general overview of coronal heating theories

From the above discussion of the different layers of the Sun, we have seen that the temperature decreases radially outward. A sketch of the temperature and density profiles from the convection zone to the corona is shown in Figure 1.4. Starting with a value of about 1.56×10^7 K in the hot core, the temperature declines to roughly 6500 K at the Sun's visible surface, falling further to a minimum value of about 4300 K at the top of the photosphere. Above this, counter to one's intuition, the temperature starts to rise again, at first slowly throughout the chromosphere but then dramatically in the transition region, until it reaches values of several million degrees Kelvin in the corona. Thereafter, the temperature decreases slowly in the outer corona to a value of about 10^5 K at 1 AU. This *coronal heating problem* has proved to be a major challenge for solar physicists since the 1940's and remains yet to be fully answered. The literature on this topic is vast and we will here only very briefly introduce the main suggested heating mechanisms. Comprehensive reviews can be found in Priest (1982), Narain and Ulmschneider (1990, 1996), Browning (1991), Zirker (1993), Golub and Pasachoff (1997) and references therein. As noted by Zirker (1993) all of the above reviews are primarily theoretical. Observations are often used in support of a suggested mechanism but up till now, observations have not been sufficiently detailed to provide direct evidence of any coronal heating mechanism.

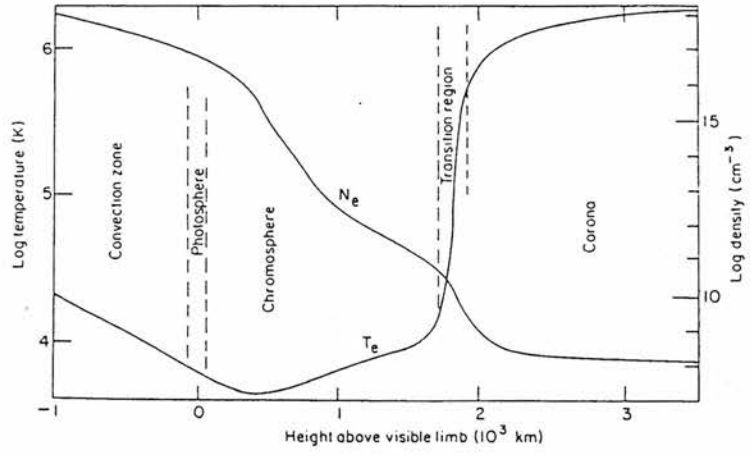

Figure 1.4: The variation of the electron temperature (T_e) and density (N_e) from the convection zone to the corona.

The energy losses in the corona, through a combination of radiation, conduction to cooler layers and the solar wind, have been estimated by Withbroe & Noyes (1977), Priest (1982) and Browning (1991) to be

Quiet region	300 W m^{-2}
Active region	$0.5 - 1 \times 10^4$ W m^{-2}
Coronal hole	800 W m^{-2}

where 1 W m^{-2} = 10^3 erg cm^{-2} s^{-1}. If the Sun's entire corona was made up of quiet region, the total energy loss would be about 2×10^{12} W (Phillips, 1992). Thus, some kind of heating mechanism is required to supply these amounts of energy. As the energy flux carried by acoustic waves is too small and due to the strong correlation between temperature inhomogeneities and magnetic structures (Vaiana & Rosner, 1978; Golub et al., 1980), there is a general consensus that the corona is heated by a mechanism that is magnetic in nature. It is also widely accepted that one of the primary energy sources for coronal heating is the kinetic energy of the photospheric footpoint motions, driven by the convection zone just below the Sun's surface. The coronal field is anchored in the photosphere and thus the footpoints of the magnetic field lines are continuously shuffled round. Coronal heating mechanisms are often divided into two classes (e.g. Ionson, 1984; Browning, 1991), according to the timescale of the footpoint motions (τ_v) in comparison with the Alfvén transit time across the structure (τ_A).

If footpoint motions are slow in relation to the Alfvén transit time, i.e. $\tau_v \gg \tau_A$, the coronal field lines are slowly twisted and braided. Currents are generated which can be dissipated, thus

converting magnetic energy into heat. Additionaly, the close proximity of fieldlines of opposite polarity will lead to *magnetic reconnection*, involving a topological change of the magnetic field and a subsequent release of energy. A more detailed description of the process of magnetic reconnection can be found in Parnell (2000), Priest and Forbes (2000) and references therein. Such heating mechanisms are referred to as *Direct Current* (DC) mechanisms. Alternatively, if footpoint motions are fast, i.e. $\tau_v \ll \tau_A$, both Alfvén and magnetoacoustic waves are launched into the corona. These MHD waves can transport energy from the photosphere to coronal levels and, through dissipation, provide heating. Wave heating mechanisms are reffered to as *Alternating Current* (AC) mechanisms. As the Alfvénic timescale can be both longer or shorter than the photospheric velocity timescale (Browning, 1991), neither of the classes of coronal heating mechanisms can be rejected. In general, DC mechanisms are more often used in shorter active-region loops whereas AC theories usually work better for long quiet-region loops.

In the open field regions of coronal holes, wave heating mechanisms remain the most attractive possibility and the possibility of heating by MHD waves has been investigated intensively. However, a heating theory based on waves faces several problems. Firstly, waves must be generated in the photospheric layers of the Sun. Secondly, the waves have to transport a sufficient energy flux as only a fraction of the wave energy is actually transmitted to the corona. Finally, they have to dissipate efficiently in order to deposit the right amount of energy at the right place. A prime candidate for transferring energy up to chromospheric and coronal levels is a flux of Alfvén waves. Ruzmaikin & Berger (1998) suggested a source for high-frequency waves associated with the emergence of twisted magnetic loops on the solar surface and reconnection with the open field. An extended study of the propagation of Alfvén waves in the solar atmosphere can be found in e.g. Hollweg (1978, 1981, 1982) or Similon & Zargham (1992).

In this thesis, we will mainly concentrate on the final aspect, the damping of the waves. Since it was first realised that Alfvén waves are not easily damped, various effects of the propagation of MHD waves have been investigated.

1.4.2 Phase mixing and Resonant Absorption

An important property of MHD waves in an inhomogeneous plasma is that individual surfaces can oscillate with their own Alfvén frequency. This implies that a global wave motion can be in resonance with local oscillations on a specific magnetic surface. The resonance condition is that the frequency of the global motion is equal to the local Alfvén frequency of the magnetic surface. In this way, energy is transferred from the large scale motion to the small scale oscillations, i.e. to a lengthscale where dissipation can become effective. This process of resonant absorption was first suggested by

Ionson (1978) as a mechanism for heating coronal loops. The mechanism relies on the existence of a continuous spectrum of Alfvén waves and perturbations which are singular at these surfaces where the local Alfvén frequency matches the frequency of the driver. The effect of the underlying chromospheric and photospheric layers on the continuous spectrum of Alfvén waves have been the subject of a lot of discussions. (e.g. Halberstadt & Goedbloed, 1993; Beliën et al., 1997). Since the original work by Ionson (1978), a lot of studies, both numerically and analytically have been done on resonant absorption (e.g. Davila, 1987; Goedbloed & Halberstadt, 1994; Halberstadt & Goedbloed, 1995a, 1995b; Tirry et al., 1997; Berghmans & Tirry, 1997; Tirry & Berghmans, 1997; Poedts & Boynton, 1996; Poedts & Goedbloed, 1997).

Heyvaerts & Priest (1983) proposed a simple but promising idea for the behaviour of Alfvén waves when the local Alfvén speed varies with position. They suggested damping of Alfvén waves due to phase mixing could be a possible source of coronal heating. A more mathematical description of the process will be given in Chapter 2. Basically, phase mixing and resonant absorption are two aspects of the same physical phenomenon, namely that Alfvén waves can exist on individual flux surfaces. Examples of the close interplay between the related phenomena of phase mixing and resonant absorption can be found in e.g. Ruderman et al. (1997a, 1997b). However, the theoretical work in this thesis will not consider resonant absorption and concentrate on damping of Alfvén waves due to phase mixing.

The propagation and damping of shear Alfvén waves in an inhomogeneous medium has been studied in more detail (Ireland, 1996; Cally, 1991; Abdelatif, 1987; Browning & Priest, 1984; Nocera et al., 1984) by relaxing the Heyvaerts and Priest limits of weak damping and strong phase mixing. Sakurai et al. (1995) solve the phase mixing equations for standing Alfvén waves, using a WKB method, combined with a small perturbation method with respect to the diffusivity. More recently, Hood et al. (1997a, 1997b) have found analytical, self-similar solutions describing phase mixing of Alfvén waves in both open (coronal holes) and closed (coronal loops) magnetic configurations. Possible observational evidence of coronal heating by phase mixing is discussed by Ireland (1996). Numerical simulations of phase mixing in coronal holes have been performed by Poedts et al. (1997) who found that in coronal holes, the phase mixing of Alfvén waves is speeded up by the flaring out of the magnetic field lines. Ofman & Davila (1995) found that in an inhomogeneous coronal hole with an enhanced dissipation parameter ($S = 10^3 - 10^4$), the Alfvén waves dissipate within several solar radii and can provide significant energy for the heating and acceleration of the high-speed solar wind. Nakariakov et al. (1997) considered the non linear generation of fast magnetosonic waves by Alfvén wave phase mixing and showed that transversal gradients in the Alfvén wave, produced by phase mixing, lead to the generation of propagating fast waves which are subject to strong damping. This phenomenon may be considered as indirect heating of the coronal plasma by phase mixing.

However, recently obtained numerical results by Botha et al. (2000) indicate that only a very small fraction of the Alfvén wave energy is radiated away as fast waves, leading to the conclusion that the classical model of phase mixing is valid, despite ignoring non-linear wave coupling. The propagation of magnetohydrodynamic waves in a cold plasma with an inhomogeneous steady flow directed along a straight magnetic field was studied by Nakariakov et al. (1998). They found that in regions with transversal gradients in the steady flow, phase mixing of Alfvén waves takes place similarly to classical phase mixing in a static medium with an inhomogeneity in the Alfvén speed.

Ruderman et al. (1998) considered phase mixing of Alfvén waves in planar two-dimensional open magnetic configurations, using a WKB method. However, the validity of the WKB technique requires a particular relationship between the magnetic Reynolds number, the wavelength of the basic Alfvén wave and the coronal pressure scale height. Ruderman et al. (1999) extended this analysis, again using a WKB approximation, to phase mixing on Alfvén waves in two-dimensional axisymmetric magnetic configurations, with a stationary flow along the magnetic field lines. These authors also compare their analytical solution with a numerical simulation of the full set of nonlinear resistive MHD equations and find that the results are in good agreement.

Obviously, phase mixing and resonant absorption are not the only mechansims that have been proposed to improve the damping of Alfvén waves. A critical discussion of the heating of solar coronal holes as a result of the dissipation of waves is give by Parker (1991a, 1991b). Moore et al. (1991, 1992) suggested that coronal holes are heated by Alfvén waves that are reflected back down within coronal holes and propose the process of 'intermittent magnetic levitation' that is driven by the reflection. Musielak et al. (1992) demonstrated that the Alfvén wave equations can be transformed into the form of the Klein-Gordon equation. The local critical frequency for reflection appears as a coefficient and reflection becomes strong as the wave frequency gets smaller than this critical value. Lou & Rosner (1994) studied the propagation of Alfvén waves in stratified (stellar) atmospheres in the context of the acceleration of stellar winds, without taking into account the inhomogeneity of the plasma in the horizontal direction. The acceleration is thought to be due to the reflection of the Alfvén waves from the vertical inhomogeneity in the Alfvén speed, caused by the stratification of the stellar atmosphere. Petkaki et al. (1998) studied the propagation of Alfvén waves in a three-dimensional geometry, using a WKB approximation and found a damping length that scales proportionally to the logarithm of the viscosity and/or resistivity.

Finally, we remark that most work on Alfvén wave heating has been done in a linear framework, assuming perturbations with relatively small amplitudes. Non linear effects on the dissipation of Alfvén waves have been discussed by Boynton & Torkelsson (1995), and Torkelsson & Boynton (1998) for spherical Alfvén waves, who found that non linear Alfvén waves can steepen to form current sheets which enhance the dissipation rate of the Alfvén waves by several orders of magnitude. This

result was confirmed by Nakariakov et al. (2000) who describe the dynamics of non linear, spherical, linearly polarised small amplitude Alfvén waves in the stratified and dissipative plasma of coronal holes by the spherical scalar Cohen-Kulsrud-Burgers equation. From the analysis of this equation it was found that linearly polarised Alfvén waves of weak amplitude and relatively long periods are subject to non linear steepening and efficient non linear dissipation. Narain & Sharma (1998) found that in the non linear regime the viscous damping of Alfvén waves becomes a viable mechanism of solar coronal plasma heating when strong spreading of the magnetic field is taken into account.

1.5 Oscillations in the corona

On theoretical grounds, it is widely accepted that MHD waves occur in the Sun's atmosphere. But whereas a number of periodic oscillations from inside the Sun (5-minute oscillation!) are known in extreme detail, there is still very little consensus on the direct observation of oscillatory phenomena in the solar atmosphere. Such observations would have important consequences for many different aspects of solar physics, such as the acceleration of the solar wind, the heating mechanism of the corona and, with observations becoming progressively more detailed, coronal seismology. Over the past few decades, observational evidence for oscillations in the solar atmosphere has increased greatly, in a wide range of wavelengths. However, with the improvement of spatial and temporal resolutions, more and more structure is seen in the corona. Wikstøl et al. (1997) suggest an alternative approach, by looking for signatures of wave propagation that survive spatial and temporal averaging. Such an approach could not only by applied to the solar corona, but also to (unresolved) stellar sources. Here we only give a very brief overview of some observations of oscillation in the corona. Extended reviews of observations of various periodic and quasi-periodic oscillations in the solar atmosphere can be found in e.g. Aschwanden (1987), Tsubaki (1988), Roberts (1991), Smith (1997), Aschwanden et al. (1999) and Roberts (2000).

1.5.1 Observations of oscillations in the corona

Although the observations of oscillations in the solar corona is clearly an important problem, it is also essential to study the layers below the corona (photosphere, chromosphere and transition region), where the source of the energy is thought to be situated. In a series of four papers, White and Athay (White & Athay 1979a, 1979b; Athay & White 1979a, 1979b) report on the presence of oscillations in the chromosphere and transition region. They find that oscillations at frequencies near 3-10 mHz are common features in the middle chromosphere and have the characteristics of propagating sound waves. By applying a wavelet analysis to Quiet Sun observations, Bocchialini

& Baudin (1994) illustrated the temporal behaviour of chromospheric network and intra-network regions. From analysing center-to-limb line width measurements, Erdélyi et al. (1998) demonstrated that the data clearly show a center-to-limb variation in the upper chromosphere and transition region, with only marginal differences in the coronal lines. Brynildsen et al. (1999a, 1999b) study the 3-minute oscillations above sunspots and suggest that these oscillations are caused by upward propagating linear or non linear acoustic waves. From a wavelet analysis of active region oscillations, Ireland et al. (1999a) found evidence for several wave packets at a number of scales in the He I and O V lines.

Tsubaki (1977) suggested from a line profile analysis of the Fe XIV λ5303 coronal line (see Appendix B for an overview of emission lines and corresponding temperatures) that a significant fraction of the photospheric 5-minute oscillation penetrates into the corona. From coronal observations, Egan & Schneeberger (1979) found observational evidence of 6-minute, low amplitude Doppler width oscillations above active regions. Koutchmy et al. (1983) found Doppler velocity oscillations in the same coronal line with periods of 300 s, 80 s and 43 s which they consider good candidates for being resonant Alfvén waves. The energy flux contained within these oscillations was found to be too low to explain radiative and conductive losses. Ulrich (1996) reported on observations of MHD oscillations in the solar atmosphere and showed that the phase relation between the magnetic field and velocity variations are consistent with outgoing Alfvén waves. During the total solar eclipse of 24 October 1995, Singh et al. (1997) conducted a search for short-period oscillations in the solar corona. They found sinusoidal variations in the intensity which they interpreted to be compressional magneto-acoustic waves. Assuming these oscillations to be fast waves, their calculations indicate the availability of enough flux to heat active regions. McKenzie & Mullan (1997) suggested that the X-ray coronal loops they found to be modulated periodically are oscillating in their global mode, which would favour resonant absorption as a heating mechanism. Harra-Murnion et al. (1999) studied the non-thermal velocity (V_{nt}) in solar active region loops and found that we can no longer assume that the transition region emission in active regions is a transitional layer between the surface and the hot coronal loops. From this they conclude that there is no wave travelling through an active region loop which is stratified in temperature. Sheeley et al. (1997) have identified moving coronal features in LASCO (SOHO) images as tracers of the slow solar wind.

1.5.2 SOHO

The *SOlar and Heliospheric Observatory* (SOHO) satellite was launched on 2 December 1995. The spacecraft orbits around the Lagrangian L_1 point, an equilibrium position where the centrifugal and gravitational forces of the Sun and the Earth are balanced, about 1.5×10^6 km sunward from the Earth. This position allows SOHO to monitor the Sun continuously, without being eclipsed by the

	SOHO helioseismology investigations
GOLF	Global Oscillations at Low Frequencies
VIRGO	Variability of solar Irradiance and Gravity Oscillations
MDI	Michelson Doppler Imager
	SOHO solar atmosphere remote sensing investigations
SUMER	Solar Ultraviolet Measurements of Emitted Radiation
CDS	Coronal Dynamics Spectrometer
EIT	Extreme-ultraviolet Imaging Telescope
UVCS	Ultraviolet Coronagraph Spectrometer for SOHO
LASCO	Large Angle Spectroscopic Coronagraph
SWAN	Solar Wind Anisotropies
	SOHO solar wind in-situ investigations
CELIAS	Charge, ELement and Isotope Analysis System
COSTEP	COmprehensive Supra Thermal and Energetic Particle analyser
ERNE	Energetic and Relativistic Nucle & Electron Experiment

Table 1.1: An overview of the SOHO payload, taken from Golub and Pasachoff (1997)

Earth. Originally designed to observe the Sun during solar minimum, with a lifetime of 2 years, SOHO is still operational at the time of writing, coming close to solar maximum. With a payload of 12 instruments, the SOHO satellite contains one of the largest instrument arrays ever to study the Sun from space (see Table 1.1). A detailed description of each instrument is far beyond the scope of this introduction, and furthermore, most of the data discussed in this thesis was taken by the TRACE satellite (see below). We will only give a brief outline of the instruments onboard SOHO. A detailed description of the SOHO mission and the various instruments can be found in 'The SOHO mission' (Solar Physics 1995, volume 162 - Nos. 1–2). An impressive overview of the first results from SOHO is given in 'The first results from SOHO' (Solar Physics 1997, volume 170 - No. 1 and volume 175 - No. 2).

Three of the instruments primarily concentrate on helioseismology studies. The MDI instrument probes the Sun's interior by measuring oscillations of the solar surface. VIRGO measures intensity changes on the solar surface and its main objective, together with GOLF, is the detection of solar g-modes; oscillations where gravity is the restoring force. The on-disk corona/chromosphere experiments, measuring the UV and EUV emission from the Sun's atmosphere are CDS, EIT and SUMER. The EIT instrument has four different passbands; 171 Å (Fe IX/Fe X) at T$\approx 10^6$ K; 195 Å (Fe XII) at T$\approx 2 \times 10^6$ K; 284 Å (Fe XV) at T$\approx 2.5 \times 10^6$ K and 304 Å (He II) at T$\approx 5 \times 10^4$ K.

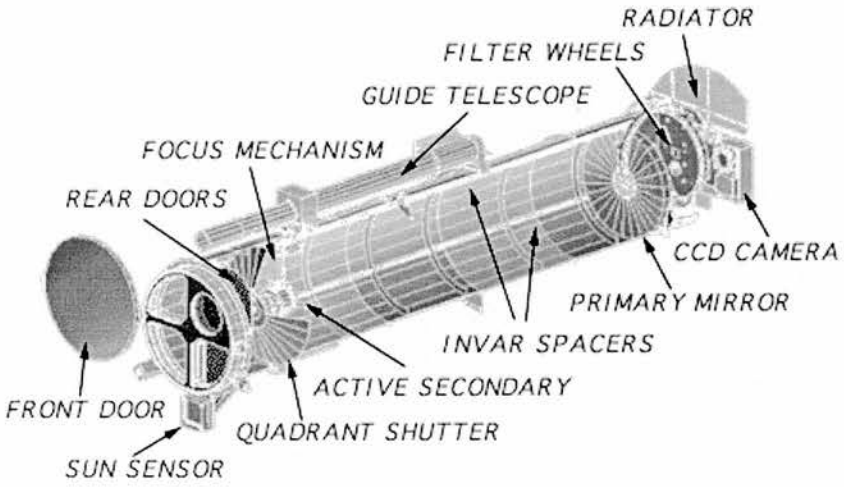

Figure 1.5: A schematic diagram of the TRACE telescope (Handy et al. 1999).

Comparisons of observations taken in each of these wavelengths has revealed the temperature differences in the corona in far more detail than previously possible. SOHO also carries three instruments for off-disk measurements, LASCO, SWAN and UVCS, and three instruments for in-situ solar wind measurements, CELIAS, COSTEP and ERNE.

1.5.3 TRACE

The *Transition Region And Coronal Explorer* (TRACE) - described in a paper by Handy et al. (1999) - offers an opportunity to image the photosphere, transition region and corona with an unprecedented spatial and temporal resolution. The single-instrument spacecraft was launched 2nd April 1998, and is in a polar orbit of 600 × 650 km at an inclination of 97.8 degrees. This allows for continuous observations for 9 months each year, while in the remaining 3 months, the view from part of the orbit is occulted by the Earth. The orbit is such that the instrument routinely passes through the South Atlantic Anomaly and the auroral radiation belts or high-latitude zones (HLZ's) of heavy radiation. Flight software was developed to allow pausing of the observations during passage through these regions. The onboard automatic exposure control (AEC) protects the CCD from excessive damage by intense solar events and can adjust the next exposure duration up or down. The TRACE telescope (Figure 1.5) has a field of view of 8.5 × 8.5 arc min, equivalent to roughly one-tenth of the solar disk. Due to several sources of pointing drift, TRACE absolute pointing coordinates are uncertain by a few arc seconds. The instrument is divided into quadrants, each of them sensitive to a different wavelength: 171 Å (FE IX/X, ~ 1 MK), 195 Å (FE XII, ~ 1.5 MK) and 284 Å (FE XIV, ~ 2 MK) for the three EUV quadrants and an UV passband centered on Lα and three wavelengths around 1550 Å (see Table 1.2).

Central wavelength (Å)	Bandwidth (Å)	Ion	Temperature (K)	Location
5000	broad	White Light	4.0–6.4 $\times 10^3$	photosphere
1700	200	Continuum	4.0–10 $\times 10^3$	chromosphere
1600	275	C I, Fe II, UV cont.	4.0–10 $\times 10^3$	chromosphere
1550	30	C IV	6.0–25 $\times 10^4$	transition region
1216	84	H I Ly α	1.0–3.0 $\times 10^4$	chromosphere
284	10.7	Fe XV	1.25–4.0 $\times 10^6$	corona
195	6.5	Fe XII	5.0–20 $\times 10^5$	corona
		(+ Fe XXIV)	1.1–2.6 $\times 10^7$	flares
171	6.4	Fe IX/X	1.6–20 $\times 10^5$	corona

Table 1.2: An overview of the TRACE spectral information, taken from Golub and Pasachoff (1997) and Handy et al. (1999).

In this thesis we will concentrate on data taken in the 171 Å bandpass. Note here that the 171 channel is actually centered slightly above 173 Å but is called 171 to be consistent with the terminology of EIT on SOHO. In the EUV 171 Å and 195 Å passbands, the temperature for a given emission meassure varies no more than a factor of two. TRACE observes the Sun with a spatial resolution of 1.0 arc sec and an exposure cadence of typically 20–60 seconds. TRACE has the possibility to follow the evolution and dynamics of plasmas at temperatures ranging from 6000 K to 10 MK, spanning a range of the solar atmosphere from the photosphere through the chromosphere and transition region, into the corona. An overview of the initial impressions gained from images taken with TRACE is given by Schrijver et al. (1999). TRACE has revealed a multitude of new properties of the Sun's outer atmosphere. The observations of the corona show very thin loops that are dynamic and evolve continuously. Even regions that traditionally have been referred to as quiescent, seem to exhibit a high degree of spatial and temporal variability. TRACE observations have also revealed a solar corona in which neighbouring regions sometimes appear largely decoupled, while distant regions can be closely linked. There is evidence that heating occurs primarly in the first 10 to 20 Mm from the foop footpoints and that inner parts of coronal active regions have higher average temperatures than the outer parts. At the footpoints of the hottest loops, TRACE observations show a pattern of low-lying, highly structured emission, which has been given the name 'moss'. Surrounding the inner part of active regions, relatively cool 1 MK loops are often seen, surviving for hours to days. Fans of long 1 MK loops are also seen in unipolar environments of the quiet Sun, where they form the bases of long loops. Overall, TRACE observations give us a first glimpse of an extremely dynamic corona, full of flows, wave-like phenomena and rapidly evolving loops.

1.6 Outline of this thesis

In this introductory chapter, we have given a brief outline of the overall properties of the Sun's atmosphere. We introduced the MHD equations and some basic aspects of MHD waves, which will form the theoretical basis for the rest of this thesis. We have discussed the problem of heating the solar corona, paying particular attention to the dissipation of Alfvén waves through phase mixing. An overview of observations of oscillations in the solar atmosphere has been presented, together with a short description of the SOHO and TRACE missions.

In Chapter 2 and 3, we study phase mixing of Alfvén waves in an open and stratified atmosphere. Phase mixing was introduced by Heyvaerts & Priest (1983) as a mechanism for heating plasma in open magnetic field regions. However, heating needs to occur at about 1–2 $R_{\odot}$, where a Cartesian geometry is not appropriate anymore. Additionally, the distances involved are too large to neglect gravity, i.e. the pressure scale height cannot be taken to be infinite. Firstly, in Chapter 2, the standard Heyvaerts & Priest (1983) model is modified to include gravitational stratification of the density. Both analytical WKB solutions and numerical results are presented. In Chapter 3, the basic equilibrium is set up in spherical coordinates to study the combined effect of a radially diverging background magnetic field and a gravitationally stratified density on phase mixing of Alfvén waves.

In Chapter 4, a basic description of the wavelet analysis technique is given. The time and scale resolution are then discussed in more detail and the power of wavelet analysis is illustrated using the WKB solution for phase mixed Alfvén waves, presented in Chapter 3. A comparison is made between the wavelet transform of a truly finite harmonic wave and an Alfvén wave, dissipated by phase mixing. Wavelet analysis is used to retrieve the lengthening of the wavelengths of Alfvén waves travelling in a gravitationally stratified atmosphere and the shortening of the wavelengths when Alfvén waves propagate in a radially diverging atmosphere.

In Chapter 5, we analyse propagating disturbances found in TRACE 171 Å observations of footpoints of large coronal loops. Estimates of the propagation speeds are made, using a running-difference image of the intensities along the loops. A wavelet analysis is used to determine the periods that are present in the various signals and it is suggested that these oscillations are propagating slow magneto-acoustic waves. Density and temperature profiles along the loops are briefly discussed.

Chapter 6 contains our conclusions and suggestion for future work.

Chapter 2

Phase mixing of Alfvén waves in a stratified and open atmosphere.

Science may be described as the art of systematic oversimplification.
Karl Popper

2.1 Introduction

In this chapter we study the effect of both vertical and horizontal density stratifications on phase mixing of Alfvén waves in an open magnetic atmosphere. We restrict ourself to a study of travelling waves, generated by photospheric motions and disturbances and propagating outwards from the Sun without total reflection. The inhomogeneity of the atmosphere in the vertical direction has important consequences for the efficiency of phase mixing.

The basic equilibrium that we are considering in order to explain the effect of gravity on phase mixing consists of a uniform vertical magnetic field with an inhomogeneous density that generates an inhomogeneous Alfvén speed. If we assume that the background Alfvén speed (only) has gradients in the x-direction (Figure 2.1), then Alfvén waves on neighbouring field lines, driven with the same frequency, will have different wavelengths. This will cause them to become out of phase as they propagate up in height and, therefore, large gradients will build up. In this way, short length scales are created which means dissipation eventually becomes important and allows the energy in the wave to dissipate and heat the plasma.

The effect of the (horizontal) Alfvén speed inhomogeneity is easily demonstrated by considering the

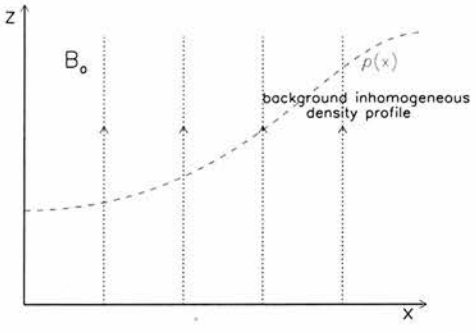

Figure 2.1: Model of phase mixing where the x-direction is the direction of the horizontal inhomogeneity and the z-direction indicates the height.

ideal MHD Alfvén wave equation:

$$\frac{\partial^2 v}{\partial t^2} = v_A^2(x)\frac{\partial^2 v}{\partial z^2}\,.$$

For a wave of a given frequency Ω, the solution is given by

$$v \sim \exp(i(\Omega t - k(x)z)),$$

where $k(x) = \Omega/v_A(x)$. Hence, horizontal gradients are given by:

$$\frac{\partial v}{\partial x} \sim vz\frac{dk}{dx}. \tag{2.1}$$

Thus, we see that the inclusion of a non-uniform background Alfvén velocity causes gradients in the direction of the inhomogeneity to build up with height. These gradients are also dependent on the gradient of the wavenumber. This tells us that large horizontal gradients in the wavefront will build up at lower heights when the plasma is more inhomogeneous and $\frac{dk}{dx}$ is large.

We now adopt a simple model of phase mixing for which the equilibrium is given by

$$\mathbf{B}_0 = B_0\hat{\mathbf{z}},\ \ \rho_0 = \rho_0(x),$$

where $\mathbf{B}_0$ is the background magnetic field and ρ_0 the density profile.
We then consider perturbations $v_y(x,z,t)$ and $b_y(x,z,t)$ in the velocity and the magnetic field so that phase mixing of Alfvén waves is produced.
In this case, the linearised MHD equations are the following:

$$\rho_0\frac{\partial v}{\partial t} = \frac{B_0}{\mu}\frac{\partial b}{\partial z} + \rho_0\nu\nabla^2 v\,,$$

and

$$\frac{\partial b}{\partial t} = B_0\frac{\partial v}{\partial z} + \eta\nabla^2 b\,,$$

where η is the magnetic diffusivity and ν is the kinematic viscosity.

For η and ν small, i.e. neglecting products of η and ν, these equations can be combined to give

$$\frac{\partial^2 v}{\partial t^2} = v_A^2(x)\frac{\partial^2 v}{\partial z^2} + (\eta+\nu)\left(\frac{\partial^2}{\partial x^2} + \frac{\partial^2}{\partial z^2}\right)\frac{\partial v}{\partial t}\,, \tag{2.2}$$

where $v_A(x) = \dfrac{B_0}{\sqrt{\mu\rho_0(x)}}$ is the Alfvén speed.
Because the gradients in the x-direction are much bigger than in the z-direction, the last term on the right hand side in Eqn. (2.2) is not important for phase mixing and will therefore be neglected from now on.

Heyvaerts & Priest (1983) assume in their analysis a solution to the above equation of the form

$$v \sim v(x,z)\exp\left(i(\Omega t - k(x)z)\right)\,.$$

By imposing the condition of weak damping,

$$\frac{1}{k}\frac{\partial}{\partial z} \ll 1\,, \tag{2.3}$$

and strong phase mixing,

$$\frac{z}{k}\frac{\partial k}{\partial x} \gg 1\,, \tag{2.4}$$

they obtain the following solution

$$\vec{v}(x,z) = \vec{v}(x,0)\exp\left(-\frac{1}{6}\left(\frac{k(x)z}{R_{Tot}^{1/3}}\right)^3\right)\,, \tag{2.5}$$

where $R_{Tot} = \dfrac{\Omega}{\eta+\nu}\left(\dfrac{d}{dx}\log k(x)\right)^{-2}$.

The main feature to note here is the $\exp(-z^3)$ damping with height. However, because of the assumption of strong phase mixing, this solution is only valid for large z.

2.2 Stratified atmosphere, zero dissipation

2.2.1 Equilibrium and linearised MHD equations

The question is to see how this picture is modified when gravitational stratification is considered.

Assuming a low-β-plasma and an isothermal atmosphere, i.e. T_0 uniform, the equilibrium is expanded in powers of β. Following Del Zanna et al. (1997), the leading order solution is a vertical, uniform field, $\mathbf{B}_0 = B_0\hat{\mathbf{z}}$.

In this case the magnetohydrostatic force balance equations reduce to

$$\nabla p = \frac{1}{\mu}(\nabla \times \mathbf{B}) \times \mathbf{B} - \rho g \hat{e}_z \,,$$

or, with $z = z_0 \bar{z}$, the pressure scale height $H = \frac{\mathcal{R}T}{\tilde{\mu} g}$ and $\beta = \frac{2\mu p_0}{B_0}$,

$$\frac{\beta}{2}\nabla p = \frac{1}{\mu}(\nabla \times \mathbf{B}) \times \mathbf{B} - \frac{\beta}{2}\frac{z_0}{H} p \hat{e}_z \,.$$

If we now assume $\mathbf{B} = \mathbf{B}_0 + \frac{\beta}{2}\mathbf{B}_0'$ and $p = p_0 + \frac{\beta}{2}p_0'$ we have

$$\nabla \times \mathbf{B}_0 = 0 \qquad \text{and} \qquad \nabla . \mathbf{B}_0 = 0$$

and, therefore,

$$\mathbf{B}_0 = B_0 \hat{e}_z \,.$$

We also find

$$\nabla p_0 = \frac{1}{\mu}\nabla \times \mathbf{B}_0' \times \mathbf{B}_0 - \frac{p_0 z_0}{H}\hat{e}_z \,.$$

The only non-zero component is the vertical component so we find

$$\frac{\partial p_0}{\partial \bar{z}} = -\frac{p_0 z_0}{H} \,.$$

and, therefore,

$$p_0 = p_0(x) e^{-\frac{z_0}{H}\bar{z}} \,,$$

and

$$\rho_0 = \rho_0(x) e^{-\frac{z_0}{H}\bar{z}} \,.$$

The horizontal force balance determines the finite β correction to the magnetic field (Del Zanna et al., 1997). Indeed, if we set $\mathbf{B}_0' = \nabla \times A(x,z)\hat{\mathbf{y}}$, we see that the horizontal component of the force balance equation reduces to

$$\frac{\partial p_0}{\partial \bar{x}} = -\nabla^2 A \frac{B_0}{\mu}\hat{\mathbf{x}} \,,$$

from which the magnetic flux function A, and hence the finite β correction to the magnetic field can be determined. This differs from Ruderman et al. (1998) who expand the equilibrium in powers of the horizontal lengthscales to the vertical scale height, $\frac{x_0}{H}$. To obtain our equilibrium from theirs requires $\beta = O\left(\frac{x_0}{H}\right)$.

Assuming a time dependence of the form $\exp(i\Omega t)$ for both the perturbed magnetic field $\mathbf{B_1} = b(x,z)e^{i\Omega t}\hat{\mathbf{y}}$ and the velocity $\mathbf{v} = v(x,z)e^{i\Omega t}\hat{\mathbf{y}}$, we find that

$$\mathbf{j_1} = \left(-\frac{\partial b}{\partial z}, 0, \frac{\partial b}{\partial x}\right)$$

and that

$$\mathbf{j_1} \times \mathbf{B_0} = \left(0, B_0 \frac{\partial b}{\partial z}, 0\right) \,.$$

The (adiabatic) energy and mass continuity equations reduce to

$$i\Omega p_1 = -\mathbf{v}.\nabla p_0 - \gamma p_0 \nabla.\mathbf{v} = 0\,,$$

and

$$i\Omega \rho_1 = -\nabla.(\rho_0 \mathbf{v}) = -\frac{\partial}{\partial y}(\rho_0 v) = 0\,.$$

The x-component of the magnetohydrodynamic equation of motion is then reduced to

$$i\Omega \rho_0 v_x = -\frac{\partial p_1}{\partial x} + \rho_0 \nu \nabla^2 v_x\,.$$

The y-component reduces to

$$i\Omega \rho_0 v = \frac{B_0}{\mu}\frac{\partial b}{\partial z} + \rho_0 \nu \nabla^2 v\,,$$

and the z-component to

$$i\Omega \rho_0 v_z = -\frac{\partial p_1}{\partial z} - \rho_1 g + \rho_0 \nu \nabla^2 v_z\,.$$

Both the x-component and the z-component are identically zero and therefore automatically satisfied. So in this case, the linearised MHD equations we are left with are the y-components of both the equation of motion and the induction equation:

$$i\Omega \rho_0 v = \frac{B_0}{\mu}\frac{\partial b}{\partial z} + \rho_0 \nu \nabla^2 v\,,$$

and

$$i\Omega b = B_0 \frac{\partial v}{\partial z} + \eta \nabla^2 b\,,$$

where, from Priest (1982) and taking the Coulomb logarithm as 20, the magnetic diffusivity $\eta = 10^{-9} T^{3/2} m^2 s^{-1}$ and the dynamic viscosity $\rho_0 \nu = 10^{-17} T^{5/2} kg m^{-1} s^{-1}$ only depend on temperature and in the isothermal atmosphere are assumed constant. These equations can be combined to give either

$$b + \frac{\partial}{\partial z}\left(\frac{v_A^2(x,z)}{\Omega^2}\frac{\partial b}{\partial z}\right) + i\Lambda^2 \nabla^2 b = 0\,, \tag{2.6}$$

or

$$\frac{\Omega^2}{v_A^2(x,z)} v + \frac{\partial^2 v}{\partial z^2} + i\Lambda^2 \nabla^2 v = 0\,, \tag{2.7}$$

where $v_A^2 = B_0^2 e^{z/H}/\mu\rho_0(x)$ and Λ^2 determines the importance of the damping terms. For simplicity, we consider either the ohmic heating, and solve Eqn. (2.6) with $\Lambda^2 = \eta/\Omega$, or the viscous heating, and solve Eqn. (2.7) with $\Lambda^2 = \rho_0 \nu \mu \Omega / B_0^2$. Including both η and ν at the same time means that, for example, Eqn. (2.7) has an additional higher order term $-\left(\eta \rho_0 \nu \mu / B_0^2\right) \nabla^4 v$. This term adds computational complexity and is usually neglected under the assumption that both η and $\rho_0 \nu$ are small. However, a multiple scales analysis shows that it is important over a height that is proportional to $(\rho_0 \nu \eta)^{-1/5}$. If we assume $\rho_0 \nu \approx \eta$, we obtain $(\eta)^{-2/5}$. The usual phase mixing length is proportional to $\eta^{-1/3}$ and while asymptotically it is true that we can neglect the extra

term, this is not so clear for the values used in the numerical code. We stress here that we will be considering the *dynamic* viscosity $\rho_0\nu$ to be constant, rather than the kinematic viscosity ν.

It is convenient to use dimensionless variables for the numerical solution to Eqns. (2.6) and (2.7). Thus, we select the equilibrium density profile as

$$\rho_0 = \rho_{00}\frac{e^{-z/H}}{1+\delta\cos(m\pi x/L)}. \tag{2.8}$$

Now we set $x = x_0\overline{x}$, $z = z_0\overline{z}$ and

$$v_A^2 = v_{A0}^2\overline{v}_A^2 = v_{A0}^2\left(1+\delta\cos\left(\frac{m\pi\overline{x}x_0}{L}\right)\right)e^{\overline{z}/\overline{H}},$$

with $v_{A0}^2 = B_0^2/2\mu\rho_{00}$. Thus, neglecting the last term on the left hand side, Eqn. (2.6) becomes

$$b + \frac{v_{A0}^2}{\Omega^2 z_0^2}\frac{\partial}{\partial\overline{z}}\left(\overline{v}_A^2\frac{\partial b}{\partial\overline{z}}\right) + i\frac{\eta}{\Omega x_0^2}\frac{\partial^2 b}{\partial\overline{x}^2} = 0\,. \tag{2.9}$$

So set $x_0 = L$, where L is the typical width of the coronal hole, and m is the number of density inhomogeneities inside the hole. This could be, for example, the number of coronal plumes. Unless otherwise stated, we consider $m = 1$ from now onwards. Then set $z_0 = v_{A0}/\Omega$ so that the vertical lengths are related to the wavelength, $2\pi z_0$, of the ideal Alfvén wave. $\overline{H}$ is the ratio of the pressure scale height to z_0 and $\overline{\Lambda}^2 = \eta/\Omega x_0^2$. A similar procedure is used for Eqn. (2.7). From now on we drop the barred variables and emphasise that we are working in terms of dimensionless variables.

The boundary conditions are chosen as

$$v = 0, \qquad x = 0 \text{ and } x = 1, \tag{2.10}$$

$$v = \sin\pi x, \qquad z = 0, \tag{2.11}$$

on the photospheric base and an outward propagating wave on the upper boundary. To obtain this upper boundary condition we assume that the density remains constant with height and dissipation is negligible outside the computational box so that $v_A^2 = k(x)e^{d/H}$. Then Eqn. (2.7), in dimensionless form, becomes

$$\frac{\partial^2 v}{\partial z^2} + k^2(x)e^{-d/H}v = 0\,.$$

The solution corresponding to an outward propagating wave is

$$v \sim \exp(-ik(x)e^{-d/2H}z)\,.$$

Matching v and $\frac{\partial v}{\partial z}$ onto the solution inside the computational box gives

$$\frac{\partial v}{\partial z} = -ik(x)e^{-z/2H}v, \qquad z = d, \tag{2.12}$$

where $k(x) = (1+\delta\cos(m\pi x))^{-1/2}$. When dissipation is included and the height of the numerical box, i.e. d, is taken sufficiently large, the waves are damped and the actual choice of the upper boundary condition is unimportant.

2.2.2 No dissipation

If we neglect dissipation, i.e. $\Lambda^2 = 0$, the solution for the magnetic field perturbations is

$$b = e^{-z/2H} \left\{ C_1(x) J_1(\phi) + C_2(x) Y_1(\phi) \right\}, \tag{2.13}$$

and the velocity is

$$v = D_1(x) J_0(\phi) + D_2(x) Y_0(\phi), \tag{2.14}$$

where $\phi = 2Hk(x)\exp(-z/2H)$ and J and Y are Bessel functions of order either 0 or 1. The amplitude of the perturbed magnetic field decreases with height, whereas the velocity increases with height. The ideal MHD solution can be used to investigate the behaviour of the current, j, and the vorticity, ω. This allows one to see the regions where phase mixing causes the transverse gradients to build up and so obtain the regions where dissipation will become important.

The 'constants' $C_1(x), C_2(x), D_1(x)$ and $D_2(x)$ are chosen to satisfy the boundary conditions and are given by:

$$\begin{cases} C_1(x) = \dfrac{2H}{\phi_0} \dfrac{\sin(\pi x)}{(1 + \delta \cos\left(\frac{m\pi x}{L}\right)} \dfrac{1}{N} (Y_0(\phi_{max}) - iY_1(\phi_{max})) \\ C_2(x) = \dfrac{2H}{\phi_0} \dfrac{\sin(\pi x)}{(1 + \delta \cos\left(\frac{m\pi x}{L}\right)} \dfrac{1}{N} (J_0(\phi_{max}) - iJ_1(\phi_{max})) \,, \end{cases}$$

with $N = (J_0(\phi_0)Y_0(\phi_{max}) - J_0(\phi_{max})Y_0(\phi_0)) - i\,(J_0(\phi_0)Y_1(\phi_{max}) - Y_0(\phi_0)J_1(\phi_{max}))$
and:

$$\begin{cases} D_1(x) = \sin(\pi x) \dfrac{1}{-iN} (Y_1(\phi_{max}) - iY_0(\phi_{max})) \\ D_2(x) = -\sin(\pi x) \dfrac{1}{-iN} (J_1(\phi_{max}) - iJ_0(\phi_{max})) \,. \end{cases}$$

The denominator of the coefficients $C_1(x)$,$C_2(x)$, $D_1(x)$ and $D_2(x)$ is complex and will therefore only be zero when the real and the imaginary part are zero at the same moment. Let us assume that they are both zero:

$$\begin{cases} -J_0(\phi_{max})Y_0(\phi_0) + J_0(\phi_0)Y_0(\phi_{max}) = 0 & \text{(i)} \\ -Y_0(\phi_0)J_1(\phi_{max}) + J_0(\phi_0)Y_1(\phi_{max}) = 0 \,, & \text{(ii)} \end{cases}$$

and that $Y_0(\phi_{max}) \neq 0$. We can then rewrite (ii) as

$$-Y_0(\phi_0)Y_0(\phi_{max})J_1(\phi_{max}) + J_0(\phi_0)Y_0(\phi_{max})Y_1(\phi_{max}) = 0 \,,$$

and by using (i) we get

$$Y_0(\phi_0) \left[-Y_0(\phi_{max})J_1(\phi_{max}) + J_0(\phi_{max})Y_1(\phi_{max}) \right] = 0 \,.$$

If we now take into account the fact that

$$\left[Y_0(\phi_{max})J_1(\phi_{max}) - J_0(\phi_{max})Y_1(\phi_{max}) \right] = \frac{2}{\pi\phi_{max}} \,,$$

we find that

$$-Y_0(\phi_0)\frac{2}{\pi\phi_{max}} = 0\,,$$

which implies that $Y_0(\phi_0) = 0$ as $\dfrac{2}{\pi\phi_{max}} \neq 0$. From Eqn. (i) we then see that

$$J_0(\phi_0)Y_0(\phi_{max}) = 0\,,$$

and because we assumed that $Y_0(\phi_{max}) \neq 0$, this implies that $J_0(\phi_0) = 0$. But because of the interlacing of the zeros of the Bessel functions and their derivatives (if $j_{\nu,s}$ is the s'th order zero of J_ν, then $\nu \leq j'_{\nu,1} < y_{\nu,1} < y'_{\nu,1} < j_{\nu,1} < j'_{\nu,2} < \ldots$) (Abramowitz & Stegun, 1965), this is in contradiction with $Y_0(\phi_0) = 0$.

We now assume that $Y_0(\phi_{max}) = 0$. From Eqn. (i) we then get that

$$J_0(\phi_{max})Y_0(\phi_0) = 0\,,$$

which implies that $Y_0(\phi_0) = 0$. Using this in Eqn. (ii) then leads to

$$J_0(\phi_0)Y_1(\phi_{max}) = 0\,.$$

As $Y_0(\phi_0) = 0$, $J_0(\phi_0)$ cannot equal zero and therefore $Y_1(\phi_{max}) = -Y'_0(\phi_{max}) = 0$, which is in contradiction with the assumption that $Y_0(\phi_{max}) = 0$, again because of the interlacing of the zeros of the Bessel functions.

Hence, the denominator of the coefficients $C_1(x)$, $C_2(x)$, $D_1(x)$ and $D_2(x)$ will not be zero.

No stratification

In the non-stratified case, the background density is given by $\rho_0 = \rho_0(x)$ and the Alfvén velocity can be expressed as $v_A^2(x) = f^{-2}(x)$.

The basic equation

$$b + \frac{v_A^2(x,z)}{\Omega^2}\frac{\partial^2 b}{\partial z^2} = 0$$

then has the following solution:

$$b = K_1(x)\sin\left(-\frac{\Omega}{v_A}z\right) + K_2(x)\cos\left(-\frac{\Omega}{v_A}z\right)\,. \tag{2.15}$$

From the same boundary condition as above we get:

$$K_1(x) = -\frac{v_A(x)}{\Omega}g_1(x)\,,$$

and

$$K_2(x) = \frac{v_A(x)}{\Omega}g_1(x)\frac{-\cos\left(-\frac{\Omega}{v_A(x)}z_{max}\right) + i\sin\left(-\frac{\Omega}{v_A(x)}z_{max}\right)}{\sin\left(-\frac{\Omega}{v_A(x)}z_{max}\right) + i\cos\left(-\frac{\Omega}{v_A(x)}z_{max}\right)}\,.$$

If we now consider the stratified case again, with the density given by $\rho_0 = \rho_0(x)e^{-z/H}$, and let the scale height H tend to infinity, solution (2.13) should reduce to solution (2.15).

First of all, we have a closer look at the argument of the Bessel functions:

$$\begin{aligned}\phi &= 2Hf\Omega e^{-z/H} \\ &= 2Hf\Omega(1 - \frac{z}{2H} + ...) \\ &= 2Hf\Omega - f\Omega z + ...\end{aligned}$$

From this expansion we see that when the parameter H tends to infinity, the argument ϕ of the Bessel functions increases. This means we can replace the Bessel functions by their approximations for large arguments.

$$\begin{cases} J_1(\phi) \cong \sqrt{\dfrac{2}{\pi\phi}} \cos\left(\phi - \dfrac{3\pi}{4}\right) \\ Y_1(\phi) \cong \sqrt{\dfrac{2}{\pi\phi}} \sin\left(\phi - \dfrac{3\pi}{4}\right), \end{cases}$$

and by using these approximations, one can show that the solution for the stratified case,

$$b = e^{-z/2H}[C_1(x)J_1(\phi) + C_2(x)Y_1(\phi)],$$

indeed converges to

$$b = K_1(x)\sin\left(-\frac{\Omega}{v_A}z\right) + K_2(x)\cos\left(-\frac{\Omega}{v_A}z\right),$$

the solution for the non-stratified case. The same can be done for the solutions for the perturbed velocity.

We will illustrate the effect of stratification through the model Alfvén speed profile $v_A^2 = (1 + \delta\cos(m\pi x))e^{z/H}$, where δ regulates the magnitude of the equilibrium density variations.

The ideal MHD solution may be approximated by a simple WKB solution of the form

$$v = \sin\pi x e^{z/4H} \exp\left(-i2Hk(x)(1 - e^{-z/2H})\right), \tag{2.16}$$

corresponding to an outward propagating wave. Since we have analytic solutions in the case of no dissipation, the value of the upper boundary $z = d$, can be taken arbitrarily large and the outward propagating wave is easily identified. Solution (2.16) agrees with boundary condition (2.12) in the limit of large H. This approximate solution shows clearly that stratification increases both the wavelength and the amplitude and this is shown in Figures 2.2 and 2.3 As the Alfvén speed $v_A \sim e^{z/2H}$, the wavelength $\lambda \sim e^{z/2H}$ as well. Hence, the wavelength will indeed get longer as the scale height H gets smaller. At first sight it appears that the heating of coronal holes by the phase mixing of Alfvén waves will be less efficient than in a unstratified medium since it will take longer for waves on neighbouring field lines to get out of phase and hence, to create the necessary short length scales for dissipation to become important! We note here that changing the value of the

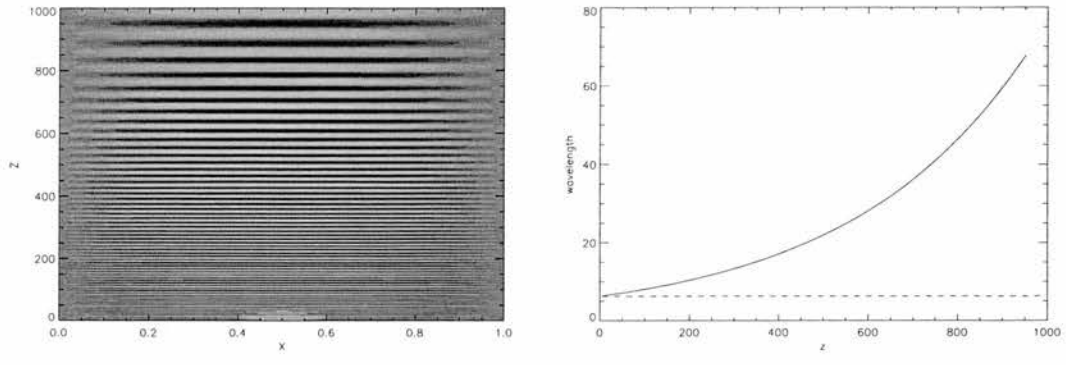

Figure 2.2: (left) A contour plot of the perturbed magnetic field in an stratified plasma, $H = 200$ with $\delta = 0.0$. (right) The behaviour of the wavelength with height (at $x = 0.5$) with $\delta = 0.0$. The solid line is the solution for a stratified plasma, i.e. $H = 200$, the dashed line corresponds to an unstratified plasma, i.e. $H = \infty$.

background density in the unstratified atmosphere will obviously affect the comparison. We have chosen the density in the unstratified atmosphere to equal the density at the base of the stratified atmosphere. In addition, from Figure 2.3, we see that the amplitude of the perturbed magnetic field decreases with height in a stratified atmosphere. However, the amplitude of the perturbed velocity on the other hand increases with height. This suggests that in a stratified atmosphere, viscous heating is the dominant heating mechanism. In a stratified atmosphere, where the density falls off with height, the amplitude of the velocity v will increase with height as $v \sim \rho_0^{-1/4}$ (see Figure 2.3). However, because the Poynting flux, which is proportional to $v.b$, is approximately constant with height, this implies that the amplitude of the magnetic field b will decrease with height as $\rho_0^{1/4}$ (Wright & Garman, 1998; Torkelsson & Boynton, 1998).

Although we are considering the zero dissipation case for the moment, so that we can not strictly talk about ohmic or viscous heating, it is still important to know where the heating would take place. To obtain an estimate of this, we consider the squares of the current density, i.e. j^2, and the vorticity, i.e. ω^2, as these will indicate where the heating would occur if dissipation was included. Figure 2.4 shows that j^2 initially increases with height but soon reaches a maximum and then the exponential decay of b takes over. So ohmic heating is only important if η is sufficiently large. On the other hand, ω^2 continues to increase with height suggesting, yet again, that viscous heating will be more important than ohmic heating.

From Figure 2.5 we see that, when there is no phase mixing, i.e. $\delta = 0$, both the current density j^2 and the vorticity ω^2 remain constant in an unstratified atmosphere, as gradients are not building up. However, when we include stratification, the current density and the vorticity show a very different

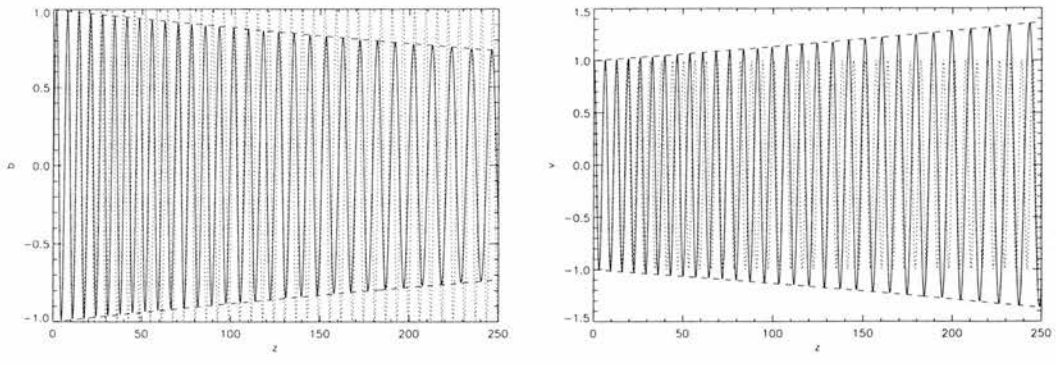

Figure 2.3: A cross-section of the magnetic field (left) and the velocity (right) in a stratified plasma for $H = 200$ at $x = 0.5$. The dotted line is the corresponding solution for an unstratified plasma, $H = \infty$. The dashed lines represent the WKB amplitude envelope $\sim \rho_0^{1/4}$ (left) and $\sim \rho_0^{-1/4}$ (right) at $x = 0.5$.

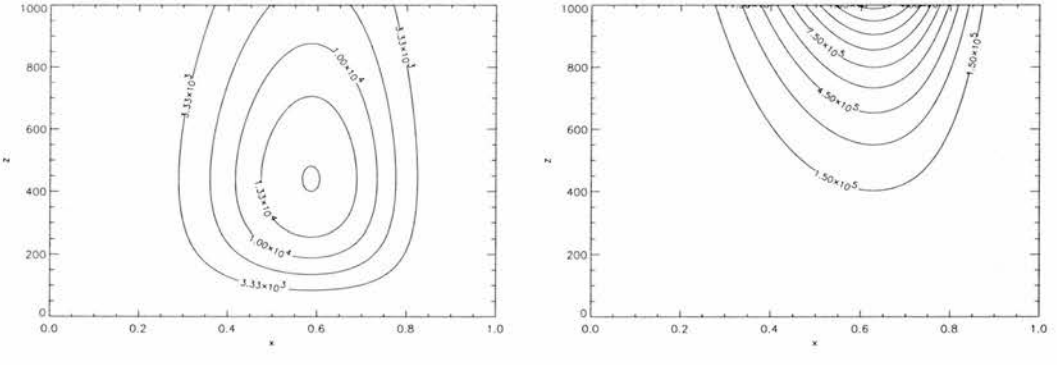

Figure 2.4: A contour plot of j^2 (left) and ω^2 (right) in a stratified plasma, $H = 200$ with $\delta = 0.5$.

behaviour. Due to the exponential decay of the magnetic field, the current density drops off when we include stratification. On the other hand, we see that the vorticity builds up in a stratified atmosphere when $x \neq 0.5$ due to the increasing x-gradients of the velocity. However, when $x = 0.5$ and $\delta = 0$, the vorticity decreases with height, as $\frac{\partial v}{\partial x} = 0$ and the only contribution to the vorticity will come from the z-derivatives of the velocity which do not build up. When we include phase mixing, i.e. $\delta \neq 0$, we see that the current density and the vorticity build up strongly as gradients in the horizontal direction of both the magnetic field and the velocity are now increasing due to phase mixing. In the stratified case, however, j^2 decays away after an initial increase, due to the decrease of the magnetic field caused by stratification. Unlike the current density, the vorticity is enhanced when stratification is included and continues to increase with height due to the increase in the velocity amplitude.

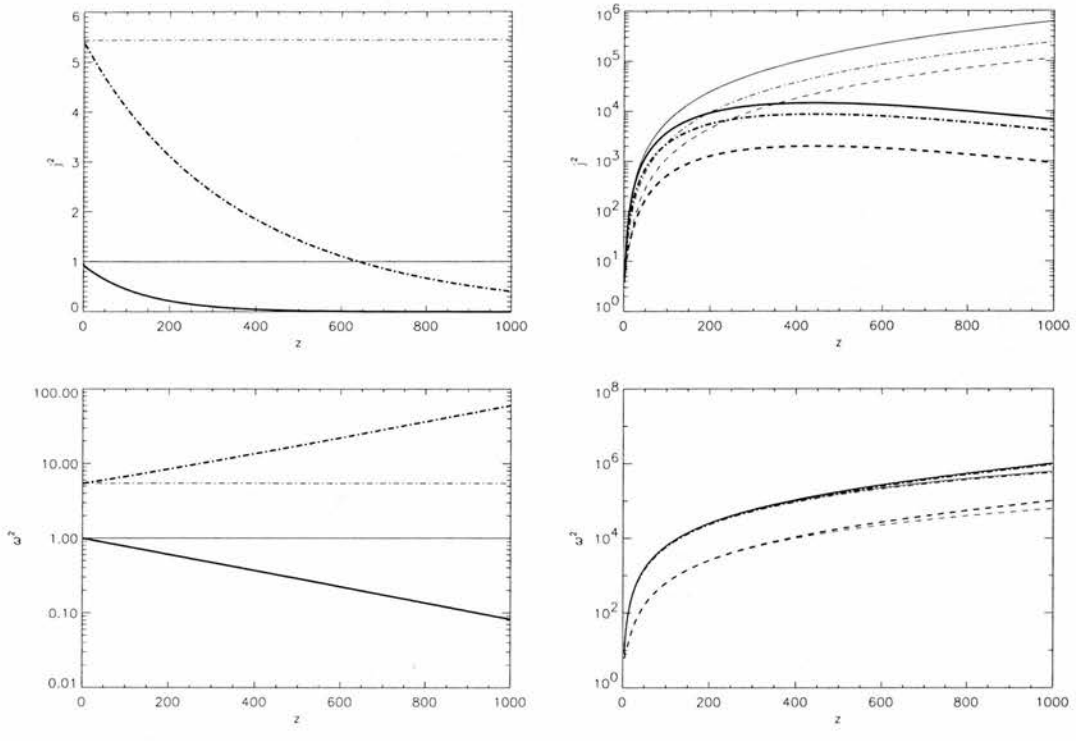

Figure 2.5: A cross-section of the j^2 (top) and ω^2 (bottom) in a stratified plasma for $H = 200$ with $\delta = 0$ (left) and $\delta = 0.5$ (right). The thin lines represent the solution in an unstratified plasma ,i.e. $H = \infty$. Cross-sections at $x = 0.5$ (solid line), $x = 0.25$ (dashed line) and $x = 0.75$ (dot-dashed line)

From Table 2.1, we note that $\int_0^{z_{max}} j^2 dz$ decreases when the plasma becomes more stratified but increases when the phase mixing strength δ increases, i.e. when the plasma is more inhomogeneous. From Table 2.2, $\int_0^{z_{max}} \omega^2 dz$ behaves in a similar manner to the current density when $\delta = 0$. But when horizontal variations are included, $\int_0^{z_{max}} \omega^2 dz$ increases when the stratification is enhanced.

When there is no damping and no phase mixing, both $\int_0^{z_{max}} j^2 dz$ and $\int_0^{z_{max}} \omega^2 dz$ seem to behave as a negative exponential (Figure 2.6). We can try to understand this behaviour from the following analysis. If we have a look at the solution for the magnetic field (Eqn. (2.13)), we notice that for $\delta = 0$, the only x-dependence will come from $g_1(x)$ in the coefficients $C_1(x)$ and $C_2(x)$. When we assume that $g_1(x) = \sin(\pi x)$, the x-derivative of the magnetic field will have a $\cos(\pi x)$ dependence which means it will be zero when we consider the cross-section at $x = 0.5$. This implies that the only contribution to j^2 for this cross-section will come from the z-derivative of the magnetic field. From the expression for the z-derivative of the magnetic field,

$$\frac{\partial b}{\partial z} = -\frac{e^{-z/2H}}{2H}\phi[C_1(x)J_0(\phi) + C_2(x)Y_0(\phi)]\,,$$

$\Lambda^2 = 0.0$	$\delta = 0.0$	$\delta = 0.1$	$\delta = 0.5$
$z_{max} = 1000$			
H = 10^6	999.3	6.32×10^6	8.53×10^6
H = 10^3	517.9	3.45×10^6	6.83×10^6
H = 200	134.7	4.05×10^5	3.64×10^6

Table 2.1: $\int_0^{z_{max}} j^2 dz$, at $x = 0.5$ for different values of the scale height H and the phase mixing strength δ.

$\Lambda^2 = 0.0$	$\delta = 0.0$	$\delta = 0.1$	$\delta = 0.5$
$z_{max} = 1000$			
H = 10^6	999.8	6.32×10^6	8.53×10^6
H = 10^3	786.9	6.78×10^6	1.13×10^7
H = 200	371.2	1.09×10^7	5.46×10^7

Table 2.2: $\int_0^{z_{max}} \omega^2 dz$, at $x = 0.5$ for different values of the scale height H and the phase mixing strength δ.

we can then calculate $|j|^2$:

$$\begin{aligned} |j|^2 &= \int_0^{z_{max}} \left|\frac{\partial b}{\partial z}\right|^2 dz \\ &= \int_0^{z_{max}} \frac{e^{-z/H}}{4H^2}\phi^2 \left|C_1(x)J_0(\phi) + C_2(x)Y_0(\phi)\right|^2 dz \\ &= \int_0^{z_{max}} e^{-3z/2H} dz \qquad\qquad (|C_1(x)J_0(\phi) + C_2(x)Y_0(\phi)|^2 = e^{z/2H}) \\ &= \frac{2H}{3}\left(1 - e^{-3z_{max}/2H}\right). \end{aligned}$$

If $H \gg z_{max}$,

$$\begin{aligned} |j|^2 &= \frac{2H}{3}\left(1 - e^{-3z_{max}/2H}\right) \\ &\approx \frac{2H}{3}\left(1 - \left(1 - \frac{3z_{max}}{2H} + \ldots\right)\right) \\ &\approx z_{max}. \end{aligned}$$

From Figure 2.6, we see that this result (dashed line) agrees quite well with the numerical results we obtained before and that $\int_0^{z_{max}} j^2 dz$ indeed tends to the constant value $z_{max} = 1000$, when the scale height H tends to infinity. Similarly we find that

$$|\omega|^2 = 2H\left(1 - e^{-z_{max}/2H}\right)$$

which also converges to z_{max} when $H \gg z_{max}$ (dashed line).

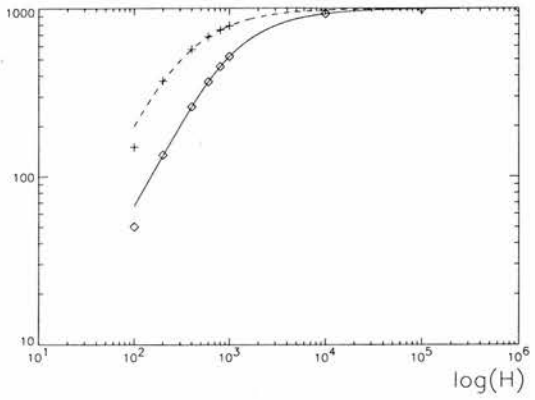

Figure 2.6: $\int_0^{z_{max}} j^2 dz$ (diamonds) and $\int_0^{z_{max}} \omega^2 dz$ (crosses) at x=0.5 in the absence of damping and phase mixing.

2.2.3 Energy

Combining the equation of motion and the induction equation gives the energy equation

$$\frac{\partial}{\partial t}\left(\frac{1}{2}\rho_0 v^2 + \frac{b^2}{2\mu}\right) = \frac{B_0}{\mu}\left(v\frac{\partial b}{\partial z} + b\frac{\partial v}{\partial z}\right) + \rho_0 \nu v \nabla^2 v + \frac{\eta}{\mu} b \nabla^2 b\,.$$

We can rewrite this as

$$\frac{\partial}{\partial t}\left(\frac{1}{2}\rho_0 v^2 + \frac{b^2}{2\mu}\right) = \frac{B_0}{\mu}\frac{\partial}{\partial z}(v.b) + \rho_0 \nu \nabla.(v\nabla v) - \rho_0 \nu (\nabla v)^2 + \frac{\eta}{\mu}\nabla.(b\nabla b) - \frac{\eta}{\mu}(\nabla b)^2\,.$$

Integrating over the volume of the plasma then gives

$$\frac{\partial}{\partial t}\left(\int \frac{1}{2}\rho_0 v^2 + \frac{b^2}{2\mu} dx dz\right) = \frac{B_0}{\mu}\int \frac{\partial}{\partial z}(v.b) dx dz + \rho_0 \nu \int \nabla.(v\nabla v) dx dz + \frac{\eta}{\mu}\int \nabla.(b\nabla b) dx dz - \rho_0 \nu \int \omega^2 dx dz - \frac{1}{\sigma}\int j^2 dx dz\,,$$

as $(\nabla v)^2 = \omega^2$, $(\nabla b)^2 = \mu^2 j^2$ and $\eta\mu = \sigma^{-1}$.

So,

$$\begin{aligned}
\frac{\partial}{\partial t}\int E dx dz &= \frac{B_0}{\mu}\int (v.b)_{z=\infty} dx - \frac{B_0}{\mu}\int (v.b)_{z=0} dx \\
&+ \rho_0 \nu \int \left(v\frac{\partial v}{\partial z}\right)_{z=\infty} dx - \rho_0 \nu \int \left(v\frac{\partial v}{\partial z}\right)_{z=0} dx \\
&+ \rho_0 \nu \int \left(v\frac{\partial v}{\partial x}\right)_{x=L} dz - \rho_0 \nu \int \left(v\frac{\partial v}{\partial x}\right)_{x=0} dz \\
&+ \frac{\eta}{\mu}\int \left(b\frac{\partial b}{\partial z}\right)_{z=\infty} dx - \frac{\eta}{\mu}\int \left(b\frac{\partial b}{\partial z}\right)_{z=0} dx \\
&+ \frac{\eta}{\mu}\int \left(b\frac{\partial b}{\partial x}\right)_{x=L} dx - \frac{\eta}{\mu}\int \left(b\frac{\partial b}{\partial x}\right)_{x=0} dx \\
&- \rho_0 \nu \int \omega^2 dx dz - \int \frac{j^2}{\sigma} dx dz\,,
\end{aligned}$$

where $E = \frac{1}{2}\rho_0(x,z)v^2 + \frac{1}{2\mu}b^2$ is the total energy. Applying the boundary conditions (2.10), (2.11) and (2.12) and neglecting $\nu\dfrac{\partial^2 v}{\partial z^2}$ and $\eta\dfrac{\partial^2 b}{\partial z^2}$, gives

$$\frac{\partial}{\partial t}\int E dx dz = \frac{B_0}{\mu}\int (v.b)_{z=\infty} dx - \frac{B_0}{\mu}\int (v.b)_{z=0} dx \\ -\rho_0\nu\int \omega^2 dx dz - \int \frac{j^2}{\sigma} dx dz\,. \tag{2.17}$$

Averaging over a period in time, it is clear that the difference between the energy flowing through the base and out through the upper boundary is dissipated as either viscous heating or ohmic heating. With dissipation, all the wave energy is dissipated before the upper boundary and so that all the energy propagating through the photospheric boundary goes into the ohmic and viscous heating terms. The ideal solution can be used to obtain how the time averaged Poynting flux through the photospheric boundary varies with the (dimensionless) scaleheight. The total energy is also used as a check on the numerical solutions to the phase mixing equations.

2.3 Stratified atmosphere, non-zero dissipation

In this section, $\Lambda^2 \neq 0$ and numerical results to Eqns. (2.6) and (2.7) are presented. The numerical code used to obtain these results was developed at the University of St Andrews by T.D. Arber. The numerical code uses a V pass multi-grid iteration technique to solve the coupled complex equations. Smoothing is performed by the Gauss-Seidel line relaxation method on all grids except the coarsest. On this grid the solution can be obtained immediately from simple tridiagonal matrix inversion as long as the number of points in the z direction is larger than that in the x direction on the finest grid. The boundary conditions at $z = 0$ and $z = d$ are taken to be Eqns. (2.11) and (2.12) on the finest grid but zero gradient on all sub grids. Iteration is stopped when the ratio of the l_1 *norm* of the residual to the l_1-*norm* of the function is less than 10^{-8}. With this procedure it is found that the code always converges within 5 iterations of the full V cycle. All the results in this section are obtained by using 65 points in the x direction and 1025 points in the z direction as the multi-grid technique requires an approximately square grid to aid convergence.

As in the case of zero dissipation, we can conclude from Figure 2.7 that stratification increases the wavelengths so that we can expect phase mixing to be less efficient when the plasma is stratified. On the other hand, the amplitude of the velocity increases with height and this will enhance the viscous heating of the plasma. From Figure 2.8 it is clear that the effects of stratification in the plasma are far less important when phase mixing is stronger. Indeed, when the plasma is highly inhomogeneous, the horizontal gradients will build up very quickly implying that dissipation is important at much lower heights. Therefore, the waves will have significantly decayed before the effect of stratification

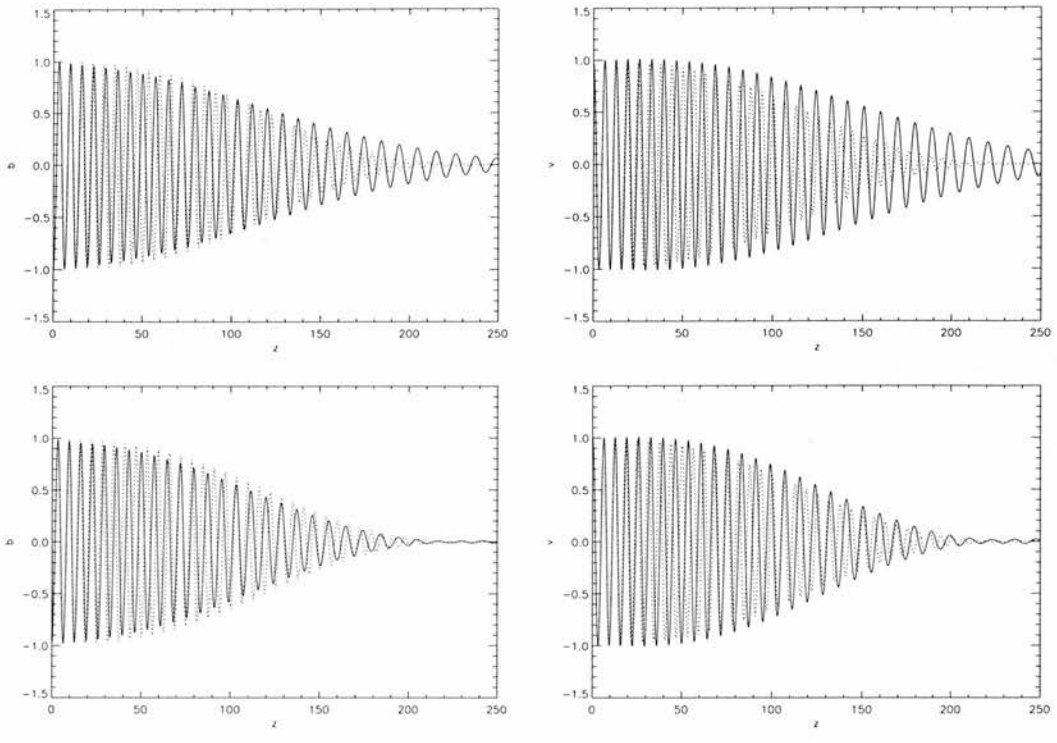

Figure 2.7: A cross-section of the perturbed magnetic field (left) and the perturbed velocity (right) in a stratified atmosphere ($H = 200$) at $x = 0.5$ for the ohmic (top) and viscous (bottom) dissipation $\Lambda^2 = 10^{-4}$ and the phase mixing strength $\delta = 0.1$. The dotted line is the corresponding solution for an unstratified plasma, i.e. $H = \infty$.

can come into play. For example, when $\delta = 0.5$ and $\Lambda^2 = 10^{-3}$, the solution for $H = \infty$ and $H = 200$ are very similar. Due to the strong damping caused by phase mixing, the wave amplitudes have decayed completely before the effect of gravity can be noticed. Therefore, we will concentrate on the weak phase mixing case to examine the effects of stratification. If we look closely at Figure 2.7, we see a slight initial increase in the velocity in the stratified plasma. This is the remnant of the velocity amplitude increase noted in the no dissipation case. We also see that both the perturbed magnetic field and the velocity decay faster in a stratified atmosphere when we consider viscous dissipation instead of ohmic dissipation. This behaviour is confirmed by Figures 2.9 and 2.10 for different values of x.

To see the effect of gravity and dissipation it is useful to examine some approximate solutions. When we consider resistivity, the WKB solutions including dissipation are

$$v = \sin \pi x e^{-ik(x)Z} \exp\left(\frac{z}{4H} - \frac{1}{6}\Lambda^2 k'(x)^2 k(x) Z^3\right), \tag{2.18}$$

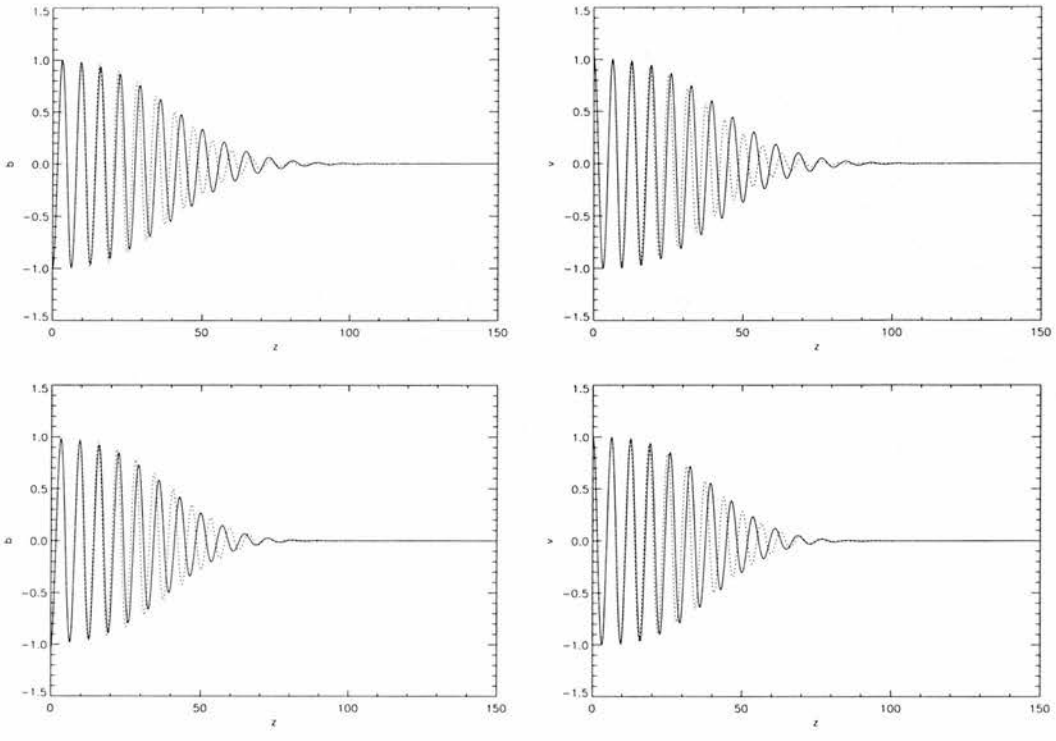

Figure 2.8: A cross-section of the perturbed magnetic field (left) and the perturbed velocity (right) in a stratified atmosphere ($H = 200$) at $x = 0.5$ for the ohmic (top) and viscous (bottom) dissipation $\Lambda^2 = 10^{-4}$ and the phase mixing strength $\delta = 0.5$. The dotted line is the corresponding solution for an unstratified plasma, i.e. $H = \infty$.

and,

$$b = \frac{-\sin \pi x}{\left(\frac{i}{4H} e^{z/2H} + k(x)\right)} e^{-ik(x)Z} \exp\left(\frac{-z}{4H} - \frac{1}{6}\Lambda^2 k'(x)^2 k(x) Z^3\right), \tag{2.19}$$

where $Z = 2H(1 - \exp(-z/2H))$ and $\Lambda^2 = \eta/\Omega x_0^2$ for ohmic dissipation.

When we consider viscosity, the WKB solutions become

$$v = \sin \pi x \, e^{-ik(x)Z} \exp\left(\frac{z}{4H} - \frac{\Lambda^2}{2}\frac{k'(x)^2}{k(x)}(2H)^3\left(\frac{z}{H} - 2\sinh\left(\frac{z}{2H}\right)\right)\right), \tag{2.20}$$

and,

$$b = \frac{-\sin \pi x}{\left(\frac{i}{4H} e^{z/2H} + k(x)\right)} e^{-ik(x)Z} \exp\left(\frac{-z}{4H} - \frac{\Lambda^2}{2}\frac{k'(x)^2}{k(x)}(2H)^3 \left(\frac{z}{H} - 2\sinh\left(\frac{z}{2H}\right)\right)\right), \tag{2.21}$$

where $\Lambda^2 = \rho_0 \nu \mu \Omega z_0^2 / x_0^2 B_0^2$ for viscous dissipation. To obtain these WKB solutions, we neglected the last term on the left-hand side of Eqn. (2.6). This term is not important for phase mixing as we expect the gradients in the x-direction to be much larger than the gradients in the z-direction.

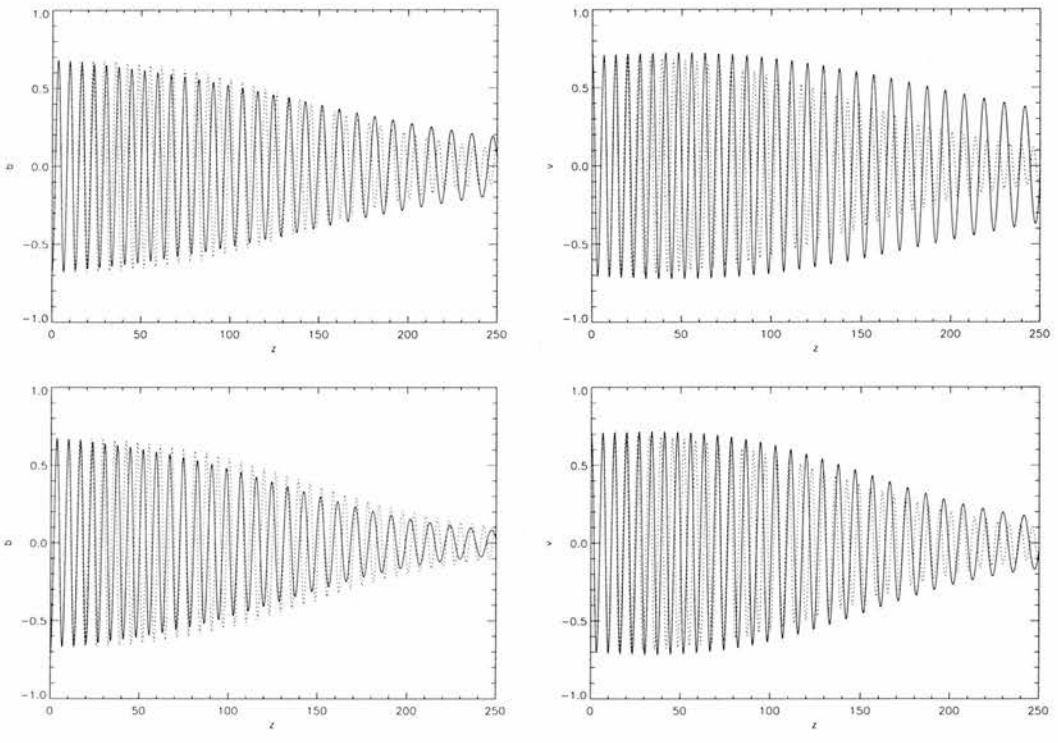

Figure 2.9: A cross-section of the perturbed magnetic field (left) and the perturbed velocity (right) in a stratified atmosphere ($H = 200$) at $x = 0.25$ for the ohmic (top) and viscous (bottom) dissipation $\Lambda^2 = 10^{-4}$ and the phase mixing strength $\delta = 0.1$. The dotted line is the corresponding solution for an unstratified plasma, i.e. $H = \infty$.

However, the numerical code used to obtain the results in this paper solves the full Eqn. (2.9), without neglecting any terms. Note that the solutions for the perturbed magnetic field and the perturbed velocity are different depending on whether we include resistivity or viscosity in the system. When we consider viscous dissipation, the waves will be damped faster and therefore heat will be deposited into the system at lower heights. Furthermore we see that the perturbed magnetic field will decay faster than the velocity in both cases. These differences are confirmed by the results shown in Figure 2.7. We can also remark that solutions (2.18) and (2.20) converge to the Heyvaerts and Priest solution $v \sim e^{-ik(x)z} \exp\left(-\frac{\Lambda^2}{6} k'(x)^2 k(x) z^3\right)$ when H tends to infinity, i.e. when we consider an unstratified atmosphere. Finally, note that the WKB solutions only satisfy the upper boundary condition (2.12) to leading order. Nonetheless, the WKB and numerical solutions give very good agreement for $\frac{d}{H}$ of order unity.

The contour plots of j^2 (Figure 2.11) indicates already that the ohmic heating is spread out over a wider area when the scale height is smaller, i.e. when stratification is larger. But by comparing Figure 2.11 and 2.12, we also see that in the stratified case, the maxima of the vorticity become

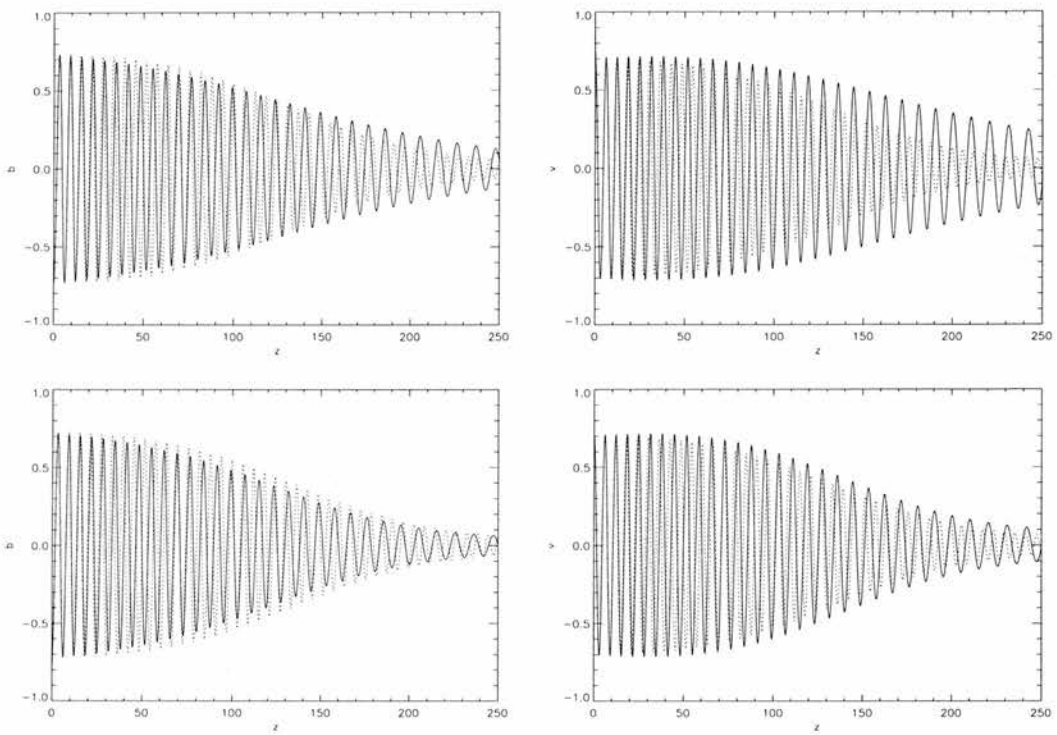

Figure 2.10: A cross-section of the perturbed magnetic field (left) and the perturbed velocity (right) in a stratified atmosphere ($H = 200$) at $x = 0.75$ for the ohmic (top) and viscous (bottom) dissipation $\Lambda^2 = 10^{-4}$ and the phase mixing strength $\delta = 0.1$. The dotted line is the corresponding solution for an unstratified plasma, i.e. $H = \infty$.

larger than the current density. Unlike the current density, the vorticity is not spread out wider than in the unstratified atmosphere. Note that the WKB solution suggests that the velocity amplitude will eventually increase at sufficiently large heights. However, the exact analytical solutions, for no dissipation, presented in the previous section show that the growth should asymptotically be linear with height from the behaviour of the Y_0 Bessel function. So the WKB solution is only valid for heights that satisfy the approximate condition $z < 2H \log 2H$. This is satisfied for all of our numerical solutions of the full set of equations. A similar effect can be found in the Ruderman et al. (1998) solution for a uniform magnetic field and an exponentially decreasing density.

From the cross sections (Figure 2.13) we see that the maximum of the current density is not only broader but also less high when the plasma is stratified. Because wavelengths are increased by a stratified plasma, the wave amplitudes are decaying slower with height than in an unstratified atmosphere. And thus, for a similar height, less energy will have been transferred into heat through ohmic dissipation in the stratified case than in the unstratified case. We see, however, that this does not happen with the vorticity. The vorticity is only spread out very slightly due to the lengthening

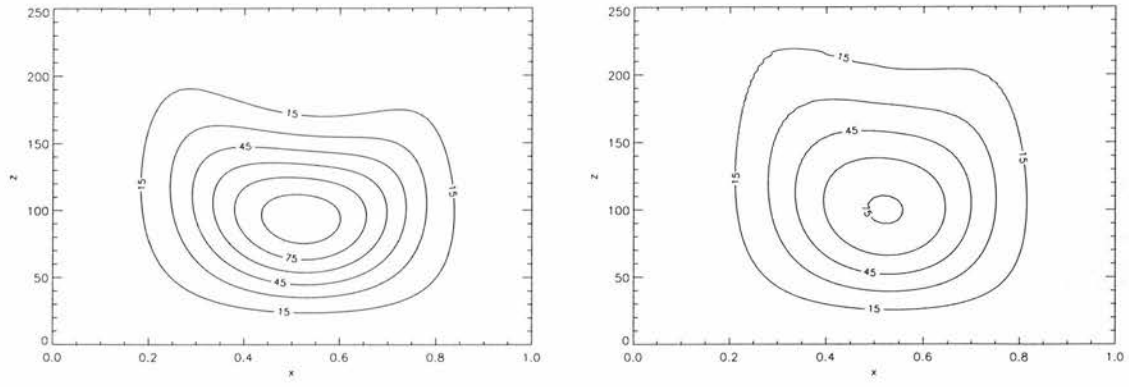

Figure 2.11: A contour plot of j^2 for the damping $\Lambda^2 = 10^{-4}$ with $\delta = 0.1$ in an unstratified plasma, $H = \infty$ (left) and in a stratified plasma, $H = 200$ (right).

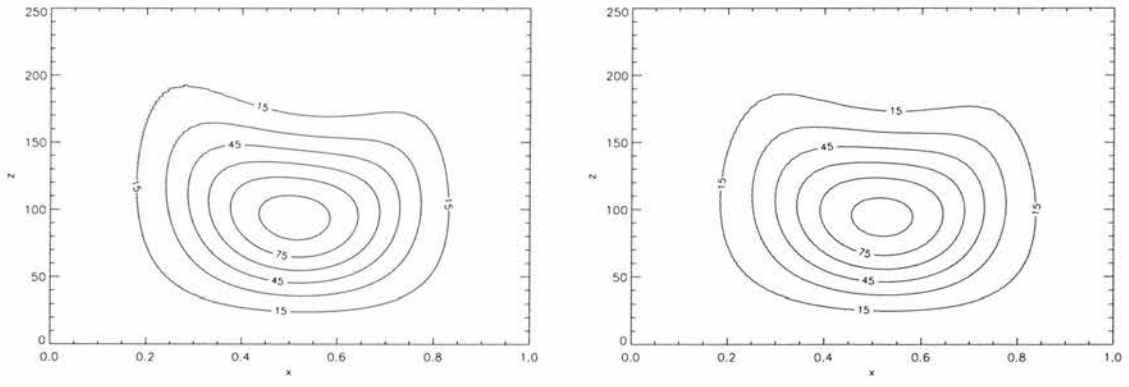

Figure 2.12: A contour plot of ω^2 for the damping $\Lambda^2 = 10^{-4}$ with $\delta = 0.1$ in an unstratified plasma, $H = \infty$ (left) and in a stratified plasma, $H = 200$ (right).

of the wavelengths and the maximum of the vorticity is almost the same as in the unstratified atmosphere. This different behaviour is due to the initial increase in the amplitude of the perturbed velocity and the fact that we considered the *dynamic* viscosity $\rho_0\nu$ to be constant, rather than the kinematic viscosity ν.

From Tables 2.3 and 2.4, we can conclude that the total amount of ohmic heating, $\eta \int_0^{z_{max}} j^2 dz$, and the total viscous heating, $\rho_0\nu \int_0^{z_{max}} \omega^2 dz$, at a certain value of x are more or less independent of the resistivity/viscosity, which confirms the result obtained by Hood et al. (1997a, 1997b). This table also indicates that the total ohmic/viscous heating stays constant as the scale height decreases or, that stratification does not seem to have an effect on the total amount of heat deposited into the plasma by either mechanism. But when the scale height H becomes very small in comparison with z_{max} and the phase mixing strength δ is weak, there seems to be a drastic drop in the total

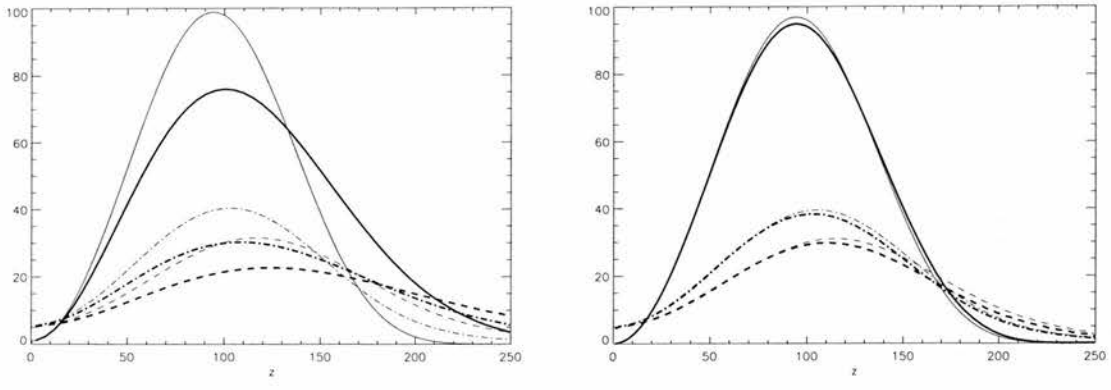

Figure 2.13: A cross-section of j^2 (left) and ω^2 (right) for the damping $\Lambda^2 = 10^{-4}$ in a stratified atmosphere for $H = 200$ with $\delta = 0.1$. The thin lines represent the solution in an unstratified plasma, i.e. $H = \infty$. Cross-sections at $x = 0.5$ (solid line), $x = 0.25$ (dashed line) and $x = 0.75$ (dot-dashed line)

	$\Lambda^2 = 10^{-3}$		$\Lambda^2 = 10^{-4}$		$\Lambda^2 = 10^{-5}$	
	$z_{max} = 250$		$z_{max} = 250$		$z_{max} = 500$	
	$\delta = 0.1$	$\delta = 0.5$	$\delta = 0.1$	$\delta = 0.5$	$\delta = 0.1$	$\delta = 0.5$
H = 10^6	0.724	0.927	0.9598	0.9711	0.9915	0.9658
H = 10^3	0.724	0.927	0.9598	0.9711	0.9907	0.9658
H = 200	0.724	0.927	0.9516	0.9711	0.8423	0.9658

Table 2.3: The total ohmic heating $\eta \int_0^{z_{max}} j^2 dz$, at $x = 0.5$ for different values of the scale height H and the phase mixing strength δ.

ohmic/visous heating. However this drop will vanish when we increase the height range over which the ohmic/viscous heating is integrated. For a strongly stratified medium with weak phase mixing, the waves damp very slowly so one has to go up to sufficiently large enough heights before the waves decay completely. So by going to higher z_{max}, the total ohmic/viscous heating will reach the same constant value even when stratification is large and δ small.

However, when the damping Λ^2 is strong and phase mixing weak, i.e. δ is small, we see that the total ohmic/viscous heating at $x = 0.5$ is substantially smaller than in all the other examined cases. This can be explained by Figure 2.14. Here we see that for the case $\Lambda^2 = 10^{-3}$, $\delta = 0.1$, the total ohmic/viscous heating at each value of x behaves quite different than the Poynting Flux at the base for each value of x. From the same figure we see that for e.g. $\Lambda^2 = 10^{-4}$, $\delta = 0.1$, the total ohmic/viscous heating at each value of x and the Poynting Flux at the base for each value of x behave quite similarly. The discrepancy for the strong damping, weak phase mixing case can therefore by

	$\Lambda^2 = 10^{-3}$		$\Lambda^2 = 10^{-4}$		$\Lambda^2 = 10^{-5}$	
	$z_{max} = 250$		$z_{max} = 250$		$z_{max} = 500$	
	$\delta = 0.1$	$\delta = 0.5$	$\delta = 0.1$	$\delta = 0.5$	$\delta = 0.1$	$\delta = 0.5$
H = 10^6	0.7122	0.9075	0.9454	0.9565	0.9767	0.9515
H = 10^3	0.7077	0.9075	0.9455	0.9573	0.9784	0.9536
H = 200	0.6859	0.9073	0.9462	0.9604	0.9831	0.9611

Table 2.4: The total viscous heating $\rho_0 \nu \int_0^{z_{max}} \omega^2 dz$, at $x = 0.5$ for different values of the scale height H and the phase mixing strength δ.

solved by calculating the total amount of ohmic heating, integrated over the volume of the plasma, $\eta \int_0^1 \int_0^{z_{max}} j^2 dz dx$ and the total viscous heating, $\rho_0 \nu \int_0^1 \int_0^{z_{max}} \omega^2 dz dx$ (see Tables 2.5 and 2.6). We now find that these values give good agreement for all examined cases. This result provides us with a check on the accuracy of the numerical code as we expect the total ohmic and viscous heating to be constant when d is taken large enough so that wave is completely damped. These calculations also confirmed that the Poynting flux at the base, which does not vary with the scale height, is balanced by the ohmic or viscous heating when the amplitudes of the perturbed magnetic field or velocity are decayed. This indicates that the total ohmic and viscous heating stays constant as the scale height decreases or, that stratification does not seem to have an effect on the total ohmic and viscous heating. So we found that in a stratified atmosphere the ohmic heating is spread out over

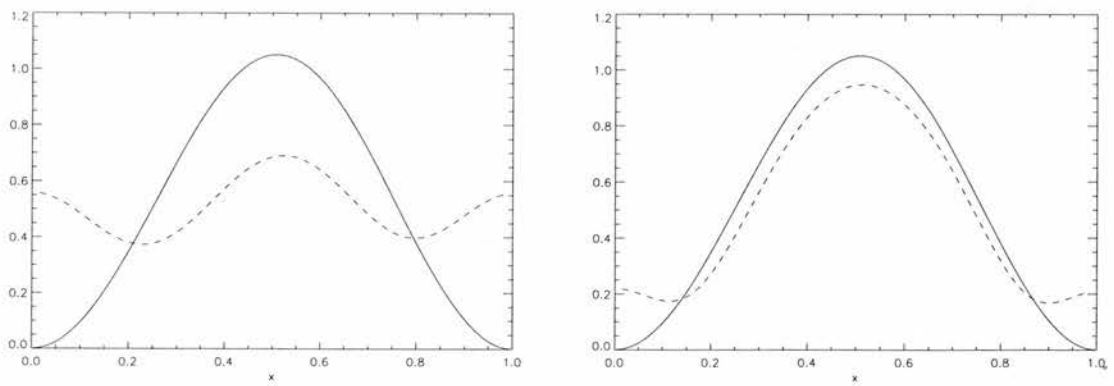

Figure 2.14: The Poynting flux at the base (solid line) and the total viscous heating $\rho_0 \nu \int_0^{z_{max}} \omega^2 dz$ at each value of x (dashed line) for $\delta = 0.1$, $H = 200$ and the damping $\Lambda^2 = 10^{-3}$ (left) and $\Lambda^2 = 10^{-4}$ (right).

a wider height range and the maximum does not build up as high as in the unstratified atmosphere. But despite these facts, the total amount of ohmic heat transferred to the plasma is independent

	$\Lambda^2 = 10^{-3}$		$\Lambda^2 = 10^{-4}$		$\Lambda^2 = 10^{-5}$	
	$z_{max} = 250$		$z_{max} = 250$		$z_{max} = 500$	
	$\delta = 0.1$	$\delta = 0.5$	$\delta = 0.1$	$\delta = 0.5$	$\delta = 0.1$	$\delta = 0.5$
H = 10^6	0.49	0.52	0.50	0.51	0.49	0.50
H = 10^3	0.49	0.52	0.50	0.51	0.49	0.50
H = 200	0.49	0.52	0.48	0.51	0.37	0.50

Table 2.5: The total ohmic heating $\eta \int_0^1 \int_0^{z_{max}} j^2 dx dz$, at $x = 0.5$ for different values of the scale height H and the phase mixing strength δ.

	$\Lambda^2 = 10^{-3}$		$\Lambda^2 = 10^{-4}$		$\Lambda^2 = 10^{-5}$	
	$z_{max} = 250$		$z_{max} = 250$		$z_{max} = 500$	
	$\delta = 0.1$	$\delta = 0.5$	$\delta = 0.1$	$\delta = 0.5$	$\delta = 0.1$	$\delta = 0.5$
H = 10^6	0.50	0.52	0.50	0.50	0.49	0.49
H = 10^3	0.50	0.52	0.50	0.50	0.49	0.49
H = 200	0.50	0.52	0.50	0.50	0.49	0.49

Table 2.6: The total viscous heating $\rho_0 \nu \int_0^1 \int_0^{z_{max}} \omega^2 dx dz$ for different values of the scale height H and the phase mixing strength δ.

of the resistivity and does not seem to be influenced very much by the stratification as long as d is sufficiently large enough. The viscous heating however is not influenced at all by the stratification. This shows that in a stratified medium, the viscous heating will dominate the ohmic heating at lower heights, under the assumption that the dynamic viscosity $\rho_o \nu$ is constant. However, the total amount of heat deposited into the plasma by either mechanism will be the same.

2.3.1 Energy

In this section we want to examine how the energy is transferred down to shorter lengthscales, for an Alfvén wave propagating up into the corona, both in a stratified and an unstratified atmosphere. We can do this by decomposing the numerical solution into orthogonal functions (Cally, 1991; Ireland & Priest, 1997). So the magnetic field is expanded as a Fourier sine series as

$$b(x,z) = \sum_{n=1}^{\infty} B_n(z) \sin\left(\frac{n\pi x}{L}\right) . \tag{2.22}$$

The q'th mode is then found to be:

$$B_q(z) = 2 \int_0^1 b(x,z) \sin\left(\frac{q\pi x}{L}\right) dx ,$$

and therefore the magnetic energy in the q'th mode is given by $M_q = \frac{1}{2\mu} B_q(z) B_q^*(z)$. Similarly, the kinetic energy in the q'th mode is given by $E_q = \frac{1}{2} \rho_0 V_q(z) V_q^*(z)$.

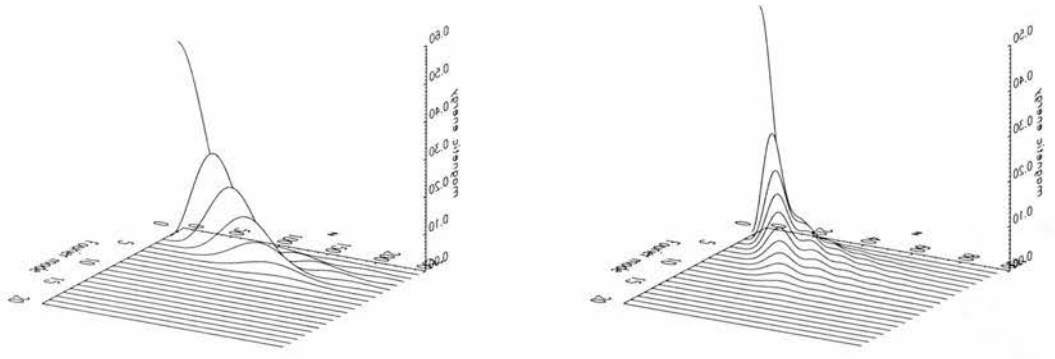

Figure 2.15: Energy-mode-height diagram for an Alfvén wave in an unstratified plasma with $\Lambda^2 = 10^{-4}$ and $\delta = 0.1$ (left) and $\delta = 0.5$ (right).

Figure 2.15 shows the excitation of increasing smaller Fourier modes with height z. As the waves propagate up, shorter length scales are being created as expected from Eqn. (2.1). When phase mixing is weak, the Alfvén wave does not develop short length scales very quickly as the plasma is almost uniform and therefore $\frac{dk}{dx}$ is much smaller in this case.

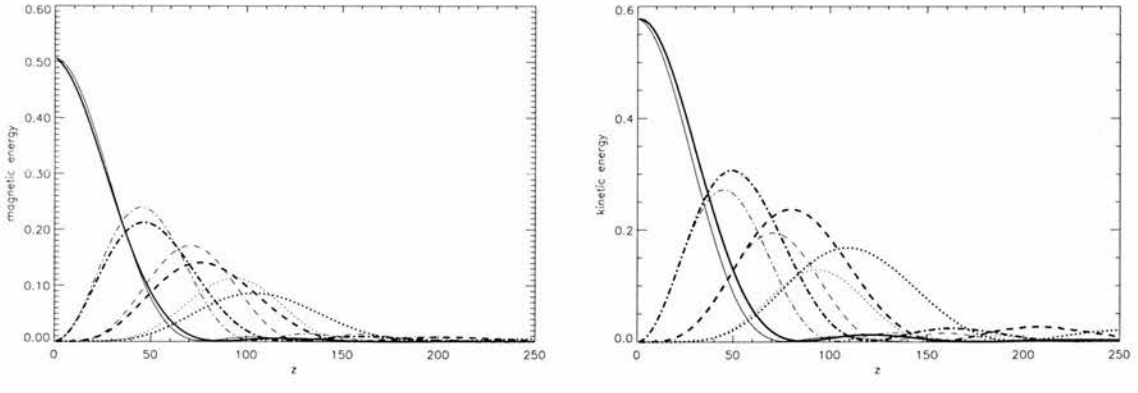

Figure 2.16: The lengthscale excitation of the Fourier modes $q = 1$ (solid line), $q = 2$ (dashed line), $q = 3$ (dot-dashed line), $q = 4$ (dotted line) in a stratified plasma, $H = 200$, with $\Lambda^2 = 10^{-4}$ and $\delta = 0.1$. The thin lines represent the solutions in an unstratified plasma, $H = \infty$.

Figure 2.16 examines the excitation of the first four Fourier modes in the plasma. As the waves propagate higher up into the atmosphere, shorter length scales are created and phase mixing carries significant amounts of energy down to smaller length scales where dissipation can be important.

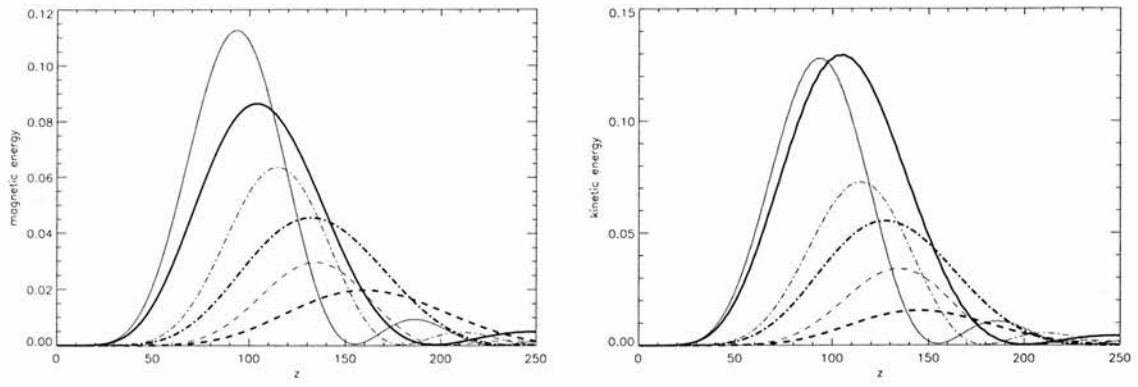

Figure 2.17: The lengthscale excitation of the Fourier modes $q = 4$ (solid line), $q = 5$ (dot-dashed line), $q = 6$ (dashed line) in a stratified plasma, $H = 200$, with $\Lambda^2 = 10^{-4}$ and $\delta = 0.1$. The thin lines represent the solutions in an unstratified plasma, $H = \infty$.

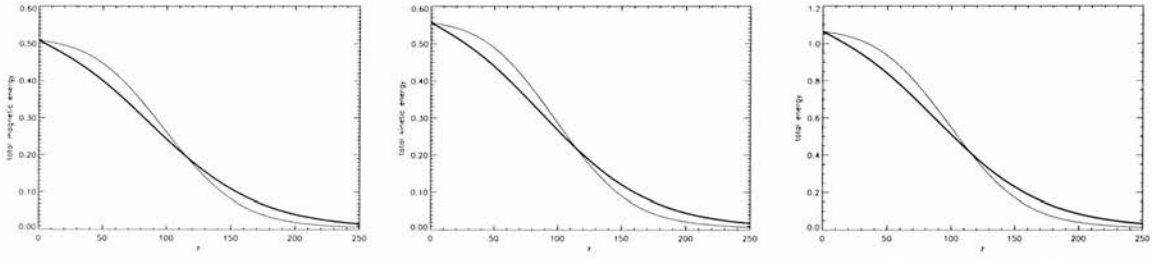

Figure 2.18: Evolution of the magnetic energy (left), the kinetic energy (middle) and the total energy (right) for an Alfvén wave in a stratified plasma ($H = 200$) with $\Lambda^2 = 10^{-4}$ and $\delta = 0.1$ when ohmic heating is considered. The thin lines represent the solutions in an unstratified plasma.

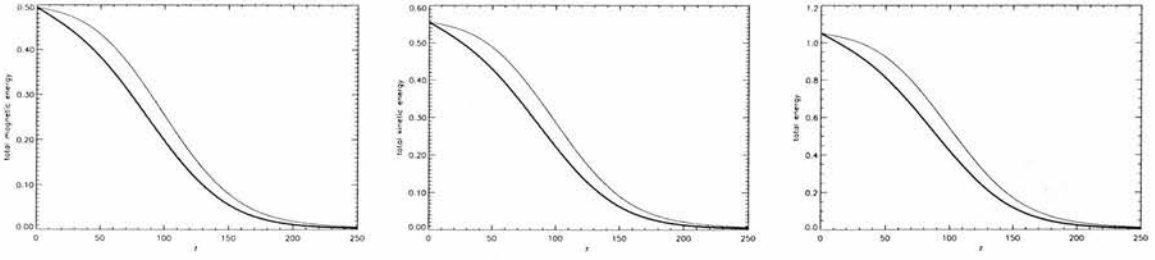

Figure 2.19: Evolution of the magnetic energy (left), the kinetic energy (middle) and the total energy (right) for an Alfvén wave in a stratified plasma ($H = 200$) with $\Lambda^2 = 10^{-4}$ and $\delta = 0.1$ when viscous heating is considered. The thin lines represent the solutions in an unstratified plasma.

We see however that the behaviour of the kinetic and the magnetic modes in the stratified and the unstratified plasma is quite different. Although the magnetic energy in the first mode initially falls off quicker in a stratified atmosphere, the energy has problems coming down to smaller length scales so it will take longer for the dissipative term in Eqn. (2.2) to have a large effect. The first four kinetic modes build up higher when stratification is included but if we look at Figure 2.17, we see again that the energy has problems coming down to smaller length scales.

The horizontal integrals of the magnetic and kinetic energies are given by $\int_0^1 \frac{B^2}{2\mu} dx$ and $\int_0^1 \frac{1}{2}\rho_0 v^2 dx$. The total energy is the sum of these magnetic and kinetic energies. From Figure 2.18 and Figure 2.19 we see that the behaviour of the total energy in a stratified medium changes, depending on whether we consider ohmic or viscous heating. When ohmic dissipation is considered, both the magnetic and the kinetic energy initially drop off faster in a stratified atmosphere. This can be understood by looking at Figure 2.7 which shows that the magnetic field drops off faster in a stratified atmosphere at lower heights when ohmic dissipation is considered. A similar behaviour is found for $\sqrt{\rho_0}v$ which explains the kinetic energy. When we consider viscous dissipation, the magnetic and kinetic energy both drop off quicker in the stratified atmosphere at all heights. From Figure 2.7 we see that the magnetic field decays faster in a stratified atmosphere than in an unstratified atmosphere at all heights. The same is true for $\sqrt{\rho_0}v$.

2.4 Two layer model

We now introduce a model with two different layers, a lower layer where the density decreases exponentially with height and an upper layer where the density remains constant. In this way we model an infinite atmosphere were the density drops off steeply at the base but stays constant above a certain height. Assuming that the density is constant above a fixed height allows the removal of the artificial upper boundary in the numerical code. From the above analysis we know that the wavelength will increase exponentially in the lower region but becomes constant once density is constant. We introduce a new parameter z_c which indicates the height of the boundary between the stratified and the non stratified atmospheres. To examine the behaviour of the wavelengths we consider weak phase mixing and no damping. Under these conditions, the effect of stratification is very strong.

By comparing the solid and the dotted curve in Figure 2.20 we clearly see that the behaviour of the magnetic field indeed changes at the critical height z_c. The wave dissipates faster once the density stays constant, which confirms again that phase mixing is less efficient in a stratified atmosphere. If we look at the evolution of the wavelength, it is obvious that in a partially stratified plasma the wavelengths stay constant once the critical value is reached while the wavelengths keep increasing

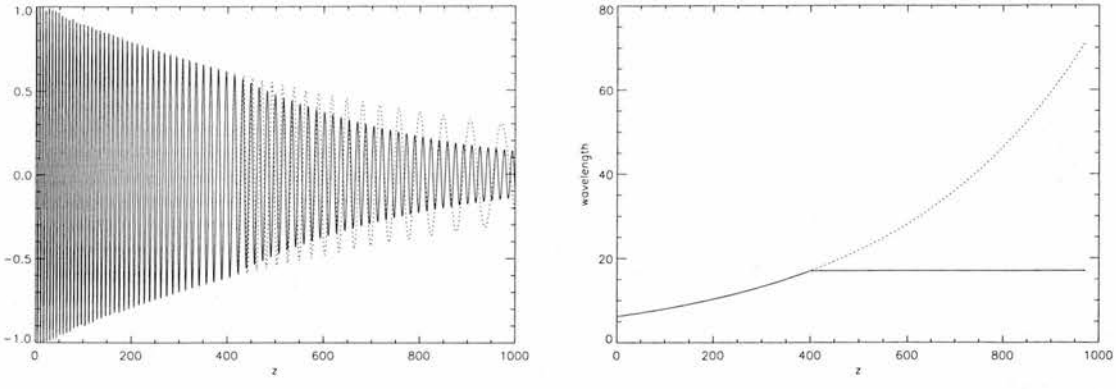

Figure 2.20: (left) A cross-section of the perturbed magnetic field in a partially stratified atmosphere ($H = 200$), $z_c = 400$, at $x = 0.5$ for $\Lambda^2 = 0.0$ and $\delta = 0.1$. The dotted line is the solution for a completely stratified atmosphere, $z_c = z_{max}$. (right) Behaviour of the wavelength with height at $x = 0.5$.

exponentially when the plasma is stratified completely.

2.5 Applications

In this paper we have studied the effect of stratification on phase mixing in an open atmosphere and we now put the obtained results into typical solar conditions. By considering the WKB solutions (2.19) for the magnetic field in a stratified atmosphere, we can obtain the following expression for the height z_{max} where most heat would be deposited,

$$z_{max} = \frac{v_{A0}}{\Omega}\left\{\left(\frac{2}{\Lambda^2 k'^2 k}\right)^{1/3} + \frac{v_{A0}}{6H\Omega}\left(\frac{2}{\Lambda^2 k'^2 k}\right)^{2/3}\right\}, \tag{2.23}$$

where $\Lambda^2 = \frac{\eta}{\Omega L^2}$ and $H = \frac{\mathcal{R}T}{\tilde{\mu}g}$. We have to remark here that we are working with dimensional variables in this section. Values obtained from expression (2.23) agree with the results shown in Figure 2.11. However, results for large heights are uncertain as the WKB solution (2.19) is only valid below certain heights. As the value of the resistivity in the solar corona is not exactly known, we consider η as a free parameter and use expression (2.23) to examine where the maximum of the ohmic heating would occur for a range of driving frequencies and temperatures. From expression (2.23) we see that the height of this maximum is influenced by several factors. When we increase the phase mixing parameter, δ, we see that the maximum will be situated at a lower height. If we, for example, assume that the plasma density inside a coronal plume is a factor 4 higher than the surrounding plasma, we find $\delta = 0.6$. If we further assume that the average coronal hole has a width of 10^8m, and that there are about 15 plumes in a coronal hole, we find $L \sim 7 \times 10^6$m. We notice

that the height of maximum ohmic heating would be reduced by reducing the background Alfvén speed. In the section we assume the background Alfvén velocity $v_{A0} \sim 500$ km/s in a coronal hole (Woo, 1996).

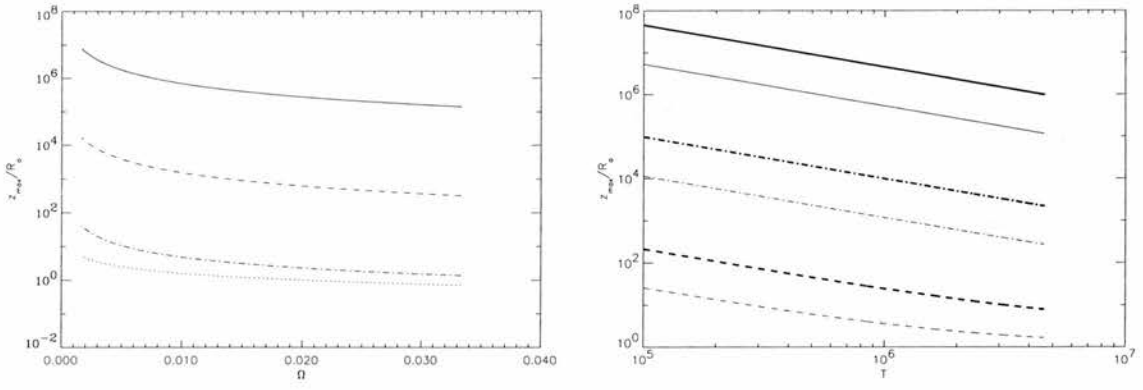

Figure 2.21: The height in solar radii at which the maximum of the ohmic heating is situated for different values of the resistivity, $\eta = 1$ (solid line), $\eta = 10^4$ (dot-dashed line), $\eta = 10^8$ (dashed line), for a range of driving frequencies (left) and temperatures (right). In the temperature-plot, the thick lines represent a driver with a 5-minute period while the thin lines represent a driver with a 1-minute period. In the frequency-plot, the dotted line represents the solution in an unstratified atmosphere for $\eta = 10^8$.

From Figure 2.21, we see how the height of maximum ohmic heating varies with temperature T and cyclic frequency $\Omega = \frac{1}{P}$ where P is the period, for different values of the resistivity. We consider a temperature range from 10^5 K up to 5×10^6 K and a frequency range which represents a period from 30 sec to 600 sec. When studying the effects of different temperatures we considered two different cases, a 5-minute oscillation and a 1-minute oscillation. When studying the effect of different frequencies, we consider T=1.5×10^6 K. From expression (2.23) we know that the height of maximum ohmic heating will decrease when η is increased, which is confirmed by the results shown in Figure 2.21. Furthermore we see that for a certain value of the resistivity, the height at which most heat will be deposited decreases when temperatures increase. For the 5-minute oscillation, we see that even for temperatures as high as 5×10^6 K and $\eta = 10^8$, the maximum will still occur at almost 10 solar radii. However, if we consider a driver with a shorter period, e.g 1 minute, we see that the maximum can be as low as a few solar radii. From Figure 2.21 we see that for a fixed value of the resistivity, the height of maximum heating increases when the period is increased. We find that for T=1.5×10^6 K, a 1 or 2-minute oscillation will deposit most heat within a few solar radii and could therefore be a candidate for heating the coronal holes, while e.g. a 5-minute oscillation might be a way to deposit heat in the solar wind. However, the results shown in Figure 2.21 and

the expression (2.23) show clearly that stratification increases the height at which the maximum of the ohmic heating occurs.

2.6 Conclusions

From this study of the effect of stratification on phase mixing in an open field region, we conclude that wavelengths lengthen when Alfvén waves propagate through a stratified plasma. So the main result is that a vertical stratification of the density makes phase mixing by ohmic heating less efficient as a coronal heating mechanism. In a stratified atmosphere, it will take longer to build up sufficiently small lengthscales for dissipation to play a role. Therefore, the ohmic heating is spread out over a wider height range and the maxima do not build up as high as in an unstratified atmosphere. However, the total ohmic heating deposited into the plasma is not affected by the stratification. We found that for viscous heating there was only a very slight difference between the stratified and the unstratified cases and the maximum builds up to a similar value in both cases. Just as the total ohmic heating, the total viscous heating does not seem to be influenced by the stratification. We can therefore conclude that in a stratified atmosphere, the heat will be deposited higher up than in an unstratified atmosphere and that the viscous heating will be the dominant component in the heating process at lower heights. Finally we can remark that when the inhomogeneity in the horizontal direction in the plasma is sufficiently large (i.e. for large values of δ), so that phase mixing is strong, stratification is unimportant. Due to the rapid phase mixing, energy can be dissipated before the effects of stratification build up. However, in section 4 we saw that, when considering likely coronal conditions, the effect of stratification on the efficiency of phase mixing in the solar corona would still be large as the height at which most heat would be deposited through ohmic dissipation was increased considerably by stratification for a range of driving frequencies and temperatures.

Chapter 3

Phase mixing of Alfvén waves in a diverging and open atmosphere

As far as the laws of mathematics refer to reality, they are not certain, and as far as they are certain, they do not refer to reality.
Albert Einstein

3.1 Introduction

Phase mixing was proposed by Heyvaerts & Priest (1983) as a mechanism for heating the plasma in the open magnetic field regions of coronal holes. We have investigated already the effect of a stratified atmosphere on phase mixing of Alfvén waves in an open field region. We found that wavelengths lengthen when Alfvén waves propagate through a stratified plasma and that ohmic dissipation would be less efficient as a coronal heating mechanism. Heat will be deposited higher up than in an unstratified atmosphere and the viscous heating will be the dominant component in the heating process at lower heights.

We now want to see what would be the effect of assuming a diverging background magnetic field. In a first step we consider a background magnetic field that is radially diverging and we assume that the density is only inhomogeneous in the horizontal direction. Ruderman et al. (1998), who considered phase mixing of Alfvén waves in planar two-dimensional open magnetic configurations using a WKB method, found phase mixing to be more efficient when the background field was radially diverging. We again restrict this study to travelling waves, generated by photospheric motions and propagating outwards from the Sun without total reflection.

3.2 Diverging magnetic field and no gravity, zero dissipation

3.2.1 Equilibrium and linearised MHD equations

To see how the general phase mixing picture is modified when we assume that the background magnetic field is radially diverging, spherical coordinates will be the most convenient choice and we therefore set up the equilibrium in spherical coordinates (Figure 3.1). Assuming a low-β-plasma and an isothermal atmosphere, i.e. T_0 uniform, the equilibrium is expanded in powers of β. Again following Del Zanna et al. (1997), the leading order solution is a radially diverging field, $\mathbf{B}_0 = B_0 \frac{r_0^2}{r^2}\hat{\mathbf{r}}$, where B_0 is the surface field strength and r_0 is the solar radius. Note that we can not assume a uniform field because of flux conservation, which tells us that $r^2 B_r$ has to be constant.

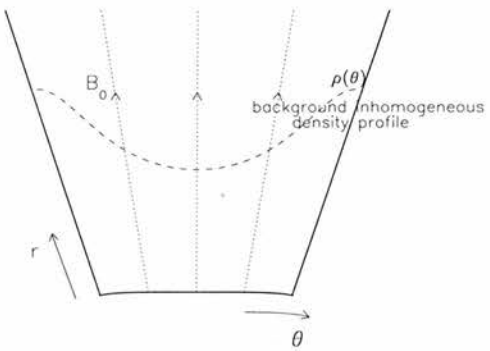

Figure 3.1: Model of phase mixing with a radially diverging background magnetic field $\mathbf{B}_0$ and an inhomogeneous density profile $\rho(\theta)$.

In this case the magnetohydrostatic force balance equations reduce to

$$\nabla p = \frac{1}{\mu}(\nabla \times \mathbf{B}) \times \mathbf{B} - \rho g \frac{r_0^2}{r^2}\hat{e}_r \,,$$

or, with $r = r_0 \bar{r}$, the pressure scale height $H = \frac{\mathcal{R}T}{\tilde{\mu} g}$ and $\beta = \frac{2\mu p_0}{B_0}$,

$$\frac{\beta}{2}\nabla p = \frac{1}{\mu}(\nabla \times \mathbf{B}) \times \mathbf{B} - \frac{\beta}{2}\frac{r_0}{H}\frac{1}{\bar{r}^2} p \hat{e}_r \,.$$

If we now assume $\mathbf{B} = \mathbf{B}_0 + \frac{\beta}{2}\mathbf{B}_0'$ and $p = p_0 + \frac{\beta}{2}p_0'$ we have

$$\nabla \times \mathbf{B}_0 = 0 \qquad \text{and} \qquad \nabla . \mathbf{B}_0 = 0$$

and, therefore,

$$\mathbf{B}_0 = \frac{B_0}{\bar{r}^2}\hat{e}_r \,.$$

We also find

$$\nabla p_0 = \frac{1}{\mu}\nabla \times \mathbf{B}_0' \times \mathbf{B}_0 - \frac{p_0 r_0}{H}\frac{1}{\bar{r}^2}\hat{e}_r \,,$$

or

$$\mathbf{B}_0.\nabla p_0 = \frac{dp_0}{d\bar{r}} B_r \,.$$

The only non-zero component is the radial component so we find

$$\frac{\partial p_0}{\partial \bar{r}} = -\frac{p_0 r_0}{H} \frac{1}{\bar{r}^2} \,,$$

and, therefore,

$$p_0 = p_0(\theta) e^{-\frac{r_0}{H}\left(1-\frac{1}{\bar{r}}\right)} \,,$$

and

$$\rho_0 = \rho_0(\theta) e^{-\frac{r_0}{H}\left(1-\frac{1}{\bar{r}}\right)} \,.$$

The force balance in the θ-direction determines the finite β correction to the magnetic field (see Section 2.2.1 or Del Zanna et al., 1997).

We now analyse Alfvén waves by considering perturbations v_ϕ and b_ϕ in the velocity and the magnetic field. Assuming a time dependence of the form $\exp(i\Omega t)$ for both the perturbed magnetic field $\mathbf{B}_1 = b(\theta, r) e^{i\Omega t} \hat{\boldsymbol{\phi}}$ and the velocity $\mathbf{v} = v(\theta, r) e^{i\Omega t} \hat{\boldsymbol{\phi}}$, we find that

$$\mathbf{j}_1 = \frac{1}{\mu} \left(\frac{1}{r \sin\theta} \frac{\partial}{\partial \theta} (\sin\theta \; b), -\frac{1}{r} \frac{\partial}{\partial r} (rb), 0 \right)$$

and that

$$\mathbf{j}_1 \times \mathbf{B}_0 = \frac{1}{\mu} \left(0, 0, B_{0r} \frac{1}{r} \frac{\partial}{\partial r} (rb) \right) \,.$$

The Alfvén waves does not generate variations in pressure and density so that $p_1 = \rho_1 = 0$. The only non-zero component to the linearised equation of motion is the ϕ-component, namely

$$i\Omega \rho_0 v = \frac{1}{\mu} B_0 \frac{r_0^2}{r^3} \frac{\partial}{\partial r} (rb) + \rho_0 \nu \nabla^2 v \,.$$

Similarly, the only non-zero component of the induction equation is

$$i\Omega b = B_0 \frac{r_0^2}{r} \frac{\partial}{\partial r} \left(\frac{v}{r} \right) + \eta \nabla^2 b \,.$$

Following Priest (1982) and taking the Coulomb logarithm as 20, the magnetic diffusivity $\eta = 10^{-9} T^{3/2} m^2 s^{-1}$, and the dynamic viscosity $\rho_0 \nu = 10^{-17} T^{5/2} kg m^{-1} s^{-1}$ only depend on the temperature and in the isothermal atmosphere are assumed constant. The Alfvén speed is given by

$$v_A^2(r, \theta) = v_A^2(\theta) \frac{1}{\bar{r}^4} \exp\left(\frac{r_0}{H} \left(1 - \frac{1}{\bar{r}} \right) \right) , \tag{3.1}$$

where $v_A^2(\theta) = B_0^2 / \mu \rho_0(\theta)$. These equations can be combined to give either one single equation for the perturbed magnetic field b,

$$b + \frac{v_A^2(\theta)}{\Omega^2} \frac{r_0^4}{r} \frac{\partial}{\partial r} \left(e^{\frac{r_0}{H}\left(1-\frac{1}{\bar{r}}\right)} \frac{1}{r^4} \frac{\partial}{\partial r} (rb) \right) + i \frac{\eta}{\Omega} \nabla^2 b = 0 \,, \tag{3.2}$$

where we neglect the dynamic viscosity $\rho_0\nu$, or to give an equation for the perturbed velocity v,

$$\frac{\Omega^2}{v_A^2(\theta)}e^{-\frac{r_0}{H}\left(1-\frac{1}{r}\right)}v + \frac{r_0^4}{r^3}\frac{\partial^2}{\partial r^2}\left(\frac{v}{r}\right) + i\frac{\rho_0\nu\Omega\mu}{B_0^2}\nabla^2 v = 0\,, \tag{3.3}$$

neglecting the resistivity η and where $v_A^2(\theta) = B_0^2/\mu\rho_0(\theta)$. Including both dissipation terms increases the order of the equations and obscures the physical effects of each term (see Chapter 2).

As it will be convenient to use dimensionless variables we set $r = r_0\bar{r}$ and $\theta = \theta_0\bar{\theta}$ and

$$v_A^2(\theta) = v_{A0}^2\left(1 + \delta\cos\left(m\pi\bar{\theta}\right)\right) = v_{A0}^2\bar{v}_A^2(\theta)\,, \tag{3.4}$$

where δ regulates the magnitude of the equilibrium density variations in the θ-direction for given radial disctance r, and m is the number of density inhomogeneities inside the coronal hole. This could be, for example, the number of coronal plumes. The equation for the perturbed magnetic field then becomes

$$b + \left(\frac{\lambda_0}{2\pi r_0}\right)^2\frac{\bar{v}_A^2}{\bar{\Omega}^2}\frac{1}{\bar{r}}\frac{\partial}{\partial\bar{r}}\left(e^{\frac{1}{\bar{H}}\left(1-\frac{1}{\bar{r}}\right)}\frac{1}{\bar{r}^4}\frac{\partial}{\partial\bar{r}}(\bar{r}b)\right) + i\frac{\Lambda_\eta^2}{\bar{\Omega}}\left(\frac{\theta_0^2}{\bar{r}^2}\frac{\partial}{\partial\bar{r}}\left(\bar{r}^2\frac{\partial b}{\partial\bar{r}}\right) + \frac{1}{\bar{r}^2\sin(\theta_0\bar{\theta})}\frac{\partial}{\partial\bar{\theta}}\left(\sin(\theta_0\bar{\theta})\frac{\partial b}{\partial\bar{\theta}}\right) - \theta_0^2\frac{b}{\bar{r}^2\sin^2(\theta_0\bar{\theta})}\right) = 0, \tag{3.5}$$

where

$$\lambda_0 = 2\pi\frac{v_{A0}}{\Omega_0} \tag{3.6}$$

is the basic wavelength , $\bar{H} = H/r_0$ is the pressure scale height meassured in units of the solar radius and $\Lambda_\eta^2 = \frac{\eta}{\Omega_0 r_0^2\theta_0^2}$. Similarly we can rewrite the equation for the perturbed velocity as

$$\frac{\bar{\Omega}^2}{\bar{v}_A^2}e^{-\frac{1}{\bar{H}}\left(1-\frac{1}{\bar{r}}\right)}v + \left(\frac{\lambda_0}{2\pi r_0}\right)^2\frac{1}{\bar{r}^3}\frac{\partial^2}{\partial\bar{r}^2}\left(\frac{v}{\bar{r}}\right) + i\Lambda_\nu^2\bar{\Omega}\left(\frac{\theta_0^2}{\bar{r}^2}\frac{\partial}{\partial\bar{r}}\left(\bar{r}^2\frac{\partial v}{\partial\bar{r}}\right) + \frac{1}{\bar{r}^2\sin(\theta_0\bar{\theta})}\frac{\partial}{\partial\bar{\theta}}\left(\sin(\theta_0\bar{\theta})\frac{\partial v}{\partial\bar{\theta}}\right) - \theta_0^2\frac{v}{\bar{r}^2\sin^2(\theta_0\bar{\theta})}\right) = 0, \tag{3.7}$$

where $\Lambda_\nu^2 = \frac{\rho_0\nu\Omega_0\mu}{B_0^2}\left(\frac{\lambda_0}{2\pi r_0\theta_0}\right)^2$.

We expect that the dominant damping terms are the second order derivatives in Eqns. (3.5) and (3.7). To obtain further (analytical) results we will therefore drop the other damping terms and work with

$$b + \left(\frac{\lambda_0}{2\pi r_0}\right)^2\frac{\bar{v}_A^2}{\bar{\Omega}^2}\frac{1}{\bar{r}}\frac{\partial}{\partial\bar{r}}\left(e^{\frac{1}{\bar{H}}\left(1-\frac{1}{\bar{r}}\right)}\frac{1}{\bar{r}^4}\frac{\partial}{\partial\bar{r}}(\bar{r}b)\right) + i\frac{\Lambda_\eta^2}{\bar{\Omega}}\left(\theta_0^2\frac{\partial^2 b}{\partial\bar{r}^2} + \frac{1}{\bar{r}^2}\frac{\partial^2 b}{\partial\bar{\theta}^2}\right) = 0, \tag{3.8}$$

and

$$\frac{\bar{\Omega}^2}{\bar{v}_A^2}e^{-\frac{1}{\bar{H}}\left(1-\frac{1}{\bar{r}}\right)}v + \left(\frac{\lambda_0}{2\pi r_0}\right)^2\frac{1}{\bar{r}^3}\frac{\partial^2}{\partial\bar{r}^2}\left(\frac{v}{\bar{r}}\right) + i\Lambda_\nu^2\bar{\Omega}\left(\theta_0^2\frac{\partial^2 v}{\partial\bar{r}^2} + \frac{1}{\bar{r}^2}\frac{\partial^2 v}{\partial\bar{\theta}^2}\right) = 0\,. \tag{3.9}$$

From now on we will drop the barred variables and work in terms of dimensionless variables. We consider either the ohmic heating, and solve Eqn. (3.8) with $\Lambda_\eta^2 = \eta/\Omega_0 r_0^2\theta_0^2$, or the viscous heating, and solve Eqn. (3.9) with $\Lambda_\nu^2 = \frac{\rho_0\nu\Omega_0\mu}{B_0^2}\left(\frac{\lambda_0}{2\pi r_0\theta_0}\right)^2$.

Similar to when we studied phase mixing in a stratified atmosphere, the boundary conditions are chosen as

$$v = 0, \qquad \theta = 0 \text{ and } \theta = 1, \tag{3.10}$$

$$v = \sin \pi\theta, \qquad r = 1, \tag{3.11}$$

on the photospheric base and an outward propagating wave on the upper boundary. To obtain this upper boundary condition we assume that the density remains constant with height and the dissipation is negligible outside the computational box. The solution corresponding to an outward propagating wave is

$$v \sim \exp\left(-ik(\theta)e^{-\frac{1}{H}(1-\frac{1}{r_{max}})}\frac{r^3-1}{3}\right),$$

and matching v and $\frac{\partial v}{\partial r}$ onto the solution inside the computational box gives

$$\frac{\partial v}{\partial r} = -ik(\theta)r^2 e^{-\frac{1}{H}(1-\frac{1}{r})}v, \qquad r = r_{max}, \tag{3.12}$$

where

$$k(\theta) = (1 + \delta\cos(m\pi\theta))^{-1/2}. \tag{3.13}$$

When dissipation is included and the height of the numerical box, i.e. r_{max}, is taken sufficiently large, the waves are damped and the actual choice of the upper boundary condition is unimportant.

To understand each physical effect clearly, we first examine the effect of a diverging field on the phase mixing of Alfvén waves. Hence, we eliminate gravitational effects by setting the pressure scale height to infinity, i.e. $1/H = 0$. In the rest of this chapter, we assume that the plasma is structured in the θ direction. When referring to stratification, we mean radial stratification due to gravity while a diverging atmosphere refers to the area change due to spherical geometry. The term 'Cartesian' is used to refer to a non-diverging atmosphere.

The spherical case allows the effect of flux tube area divergence to be studied. We can retrieve the Cartesian case in the following manner. If we assume

$$\bar{r} = 1 + \frac{\lambda_0}{2\pi r_0}\bar{z} \qquad \text{and} \qquad \bar{x} = \bar{r}\bar{\theta}, \tag{3.14}$$

we see that at low heights, i.e. $\bar{r} \approx 1$, and for small initial wavelengths λ_0 Eqns. (3.8) and (3.9) transform to

$$b + \frac{\bar{v}_A^2}{\bar{\Omega}^2}\frac{\partial^2 b}{\partial \bar{z}^2} + i\frac{\Lambda_\eta^2}{\bar{\Omega}}\left(\frac{x_0^2}{z_0^2}\frac{\partial^2 b}{\partial \bar{z}^2} + \frac{\partial^2 b}{\partial \bar{x}^2}\right) = 0, \tag{3.15}$$

and

$$\frac{\bar{\Omega}^2}{\bar{v}_A^2}v + \frac{\partial^2 v}{\partial \bar{z}^2} + i\Lambda_\nu^2\bar{\Omega}\left(\frac{x_0^2}{z_0^2}\frac{\partial^2 v}{\partial \bar{z}^2} + \frac{\partial^2 v}{\partial \bar{x}^2}\right) = 0, \tag{3.16}$$

with $\Lambda_\eta^2 = \eta/\Omega_0 x_0^2$ and $\Lambda_\nu^2 = \rho_0\nu\mu\Omega_0/B_0^2\left(\frac{z_0}{x_0}\right)^2$ where $x_0 = r_0\theta_0$ and $z_0 = \lambda_0/2\pi$ with λ_0 as in Eqn. (3.6). This shows that at low heights and for small λ_0, we recover the standard Heyvaerts and Priest case (Heyvaerts & Priest, 1983).

We note here that we are looking at torsional Alfvén waves, i.e. $v_r = 0, v_\theta = 0, v_\phi \neq 0$ and $\frac{\partial}{\partial \phi} = 0$, in open field regions. Examples of studies of torsional Alfvén waves in closed field regions such as coronal loops and arcardes, can be found in Ruderman et al. (1997a, 1997b). Furthermore, we remark that the choice of analysing torsional Alfvén waves excludes all possible coupling with slow and fast magneto-acoustic waves. Coupling of the different types of MHD waves and more complicated classes of motions are considered by e.g. Nakariakov et al. (1997, 1998); Berghmans & Tirry (1997); Tirry & Berghmans (1997); Ruderman (1999).

3.2.2 No dissipation

If we neglect dissipation, i.e. $\Lambda^2 = 0$, the exact solution of Eqns. (3.8) and (3.9) for the magnetic field and velocity perturbations are given by

$$b = \sin(\pi\theta)\left(\frac{r}{r_0}\right)^{3/2}\left[\frac{J_{5/6}\left(2\pi\frac{r_0}{\lambda_0}k(\theta)\frac{r^3}{3}\right) - iY_{5/6}\left(2\pi\frac{r_0}{\lambda_0}k(\theta)\frac{r^3}{3}\right)}{J_{5/6}\left(\frac{2\pi}{3}\frac{r_0}{\lambda_0}k(\theta)\right) - iY_{5/6}\left(\frac{2\pi}{3}\frac{r_0}{\lambda_0}k(\theta)\right)}\right], \tag{3.17}$$

and

$$v = \sin(\pi\theta)\left(\frac{r}{r_0}\right)^{3/2}\left[\frac{J_{1/6}\left(2\pi\frac{r_0}{\lambda_0}k(\theta)\frac{r^3}{3}\right) - iY_{1/6}\left(2\pi\frac{r_0}{\lambda_0}k(\theta)\frac{r^3}{3}\right)}{J_{1/6}\left(\frac{2\pi}{3}\frac{r_0}{\lambda_0}k(\theta)\right) - iY_{1/6}\left(\frac{2\pi}{3}\frac{r_0}{\lambda_0}k(\theta)\right)}\right], \tag{3.18}$$

where $k(\theta) = \frac{\Omega}{v_A(\theta)}$ and J is a Bessel function of order either $\frac{5}{6}$ or $\frac{1}{6}$.

The ideal MHD solutions in spherical coordinates may be approximated by a simple WKB solution of the form

$$b = \sin(\pi\theta)\exp\left(-2\pi i\frac{r_0}{\lambda_0}k(\theta)\psi\right) \quad \text{and} \quad v = \sin(\pi\theta)\exp\left(-2\pi i\frac{r_0}{\lambda_0}k(\theta)\psi\right), \tag{3.19}$$

where $3\psi = r^3 - 1$. Although the exact analytical solutions for the perturbed magnetic field and velocity differ, the approximate WKB solutions are both the same since the leading asymptotic terms of the Bessel functions agree on using the large argument approximation $J_\nu(\phi) \sim \sqrt{2/\pi\phi}\cos(\phi - \frac{1}{2}\nu\pi - \frac{1}{4}\pi)$ and $Y_\nu(\phi) \sim \sqrt{2/\pi\phi}\sin(\phi - \frac{1}{2}\nu\pi - \frac{1}{4}\pi)$ (Abramowitz & Stegun, 1965). The solutions (3.17) and (3.18) show that area divergence decreases the wavelength in agreement with the numerical solutions shown in Figures 3.2 and 3.3. Figures 3.3(a) and 3.3(b) confirm that the solutions for the perturbed magnetic field and the perturbed velocity are the same as predicted by solutions (3.19).

When $\Lambda^2 = 0$, Eqn. (3.16) becomes the standard wave equation for phase mixing in a Cartesian, non-dissipative system, i.e.

$$v + \frac{v_A^2}{\Omega^2}\frac{\partial^2 v}{\partial z^2} = 0\,. \tag{3.20}$$

Therefore, the solutions for the perturbed velocity and magnetic field in Cartesian coordinates are given by

$$v = \sin(\pi x)\exp(-ik(x)z) \qquad \text{and} \qquad b = \sin(\pi x)\exp(-ik(x)z)\,, \tag{3.21}$$

where $k(x) = \frac{\Omega}{v_A(x)}$.

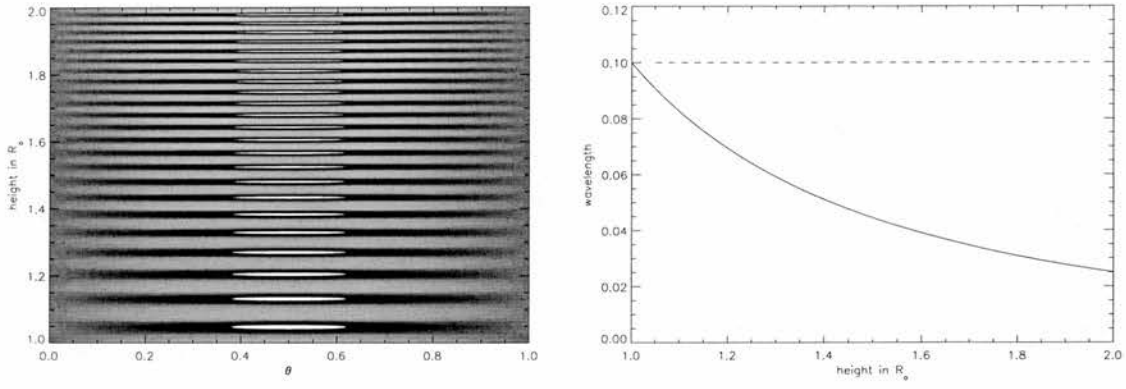

Figure 3.2: (left) A contour plot of the perturbed magnetic field in a diverging atmosphere, with $\delta = 0$. (right) The behaviour of the wavelength with height (at $\theta = 0.5$) with $\delta = 0$. The solid line is the solution for a diverging atmosphere, the dashed line corresponds to the Cartesian case.

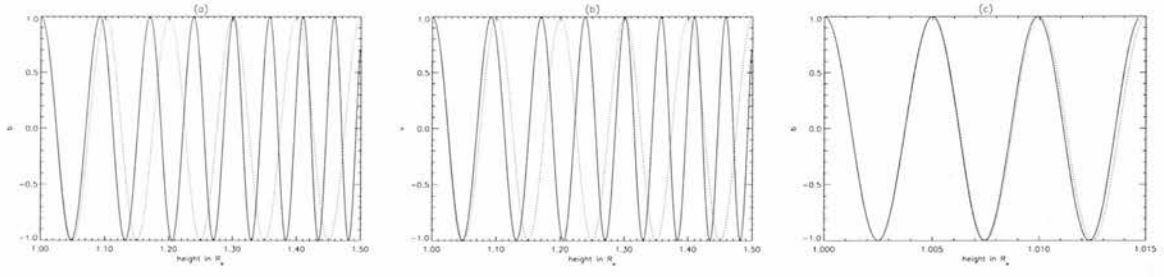

Figure 3.3: A cross-section of the perturbed (a) magnetic field and (b) velocity for a radially diverging background magnetic field at $\theta = 0.5$ with $\delta = 0.5$, $\lambda_0 = 0.1$ and $\theta_0 = 0.1$. (c) A cross-section of the perturbed magnetic field at $\theta = 0.5$ with $\delta = 0.5$, $\lambda_0 = 0.005$ and $\theta_0 = 0.1$.The dotted lines represent the corresponding solutions in Cartesian coordinates at $x = 0.5$.

From Figure 3.3(c) we see that low down, i.e. near $\bar{r} \approx 1$, and for small initial wavelengths λ_0 (see Eqn. (3.6)), the spherical and the Cartesian case indeed agree extremely well. The results in Figure 3.3 show that, unlike stratification which lengthens the wavelengths, area divergence shortens the wavelengths while the wavelengths remain constant in the Cartesian case. Indeed, in this case the Alfvén speed and the wavelength λ behave like $\frac{1}{r^2}$. The amplitude of both the perturbed magnetic field and the perturbed velocity are constant in height as we expected. Wright & Garman (1998) and Torkelsson & Boynton (1998) showed that in the large wavenumber limit the amplitudes of the Alfvén waves behave as $b \sim \rho_0^{1/4}$ and $v \sim \rho_0^{-1/4}$ and as ρ_0 is constant with height in this case, the result follows. This suggests that phase mixing will be more efficient in a diverging medium than in a non diverging medium as the short length scales, necessary for efficient dissipation, will be created

much faster. Therefore, heat could now be deposited at lower heights. Similar results were obtained by Ruderman et al. (1998). These results also show that, unlike the results due to stratification, the effect of the divergence of the background field is the same whether resistive or viscous heating is considered.

To obtain an estimate of where this heat would be deposited if dissipation were included, we now consider the current density, j^2. In spherical coordinates, only including the dominant terms, j^2 is given by

$$j^2 = \left(\frac{1}{r}\frac{\partial b}{\partial \theta}\right)^2 + \left(\frac{\partial b}{\partial r}\right)^2 = \frac{1}{r_0^2\theta_0^2}\left(\frac{1}{\bar{r}}\frac{\partial b}{\partial \bar{\theta}}\right)^2 + \frac{1}{r_0^2}\left(\frac{\partial b}{\partial \bar{r}}\right)^2, \tag{3.22}$$

while in Cartesian coordinates j^2 is given by

$$j^2 = \left(\frac{\partial b}{\partial x}\right)^2 + \left(\frac{\partial b}{\partial z}\right)^2 = \frac{1}{x_0^2}\left(\frac{\partial b}{\partial \bar{x}}\right)^2 + \frac{1}{z_0^2}\left(\frac{\partial b}{\partial \bar{z}}\right)^2, \tag{3.23}$$

where $x_0 = r_0\theta_0$ and $z_0 = \lambda_0/2\pi$. The numerical results obtained for both the magnetic field and the velocity indicate that the behaviour of the current density and the vorticity will be similar. Therefore we concentrate on the current density alone.

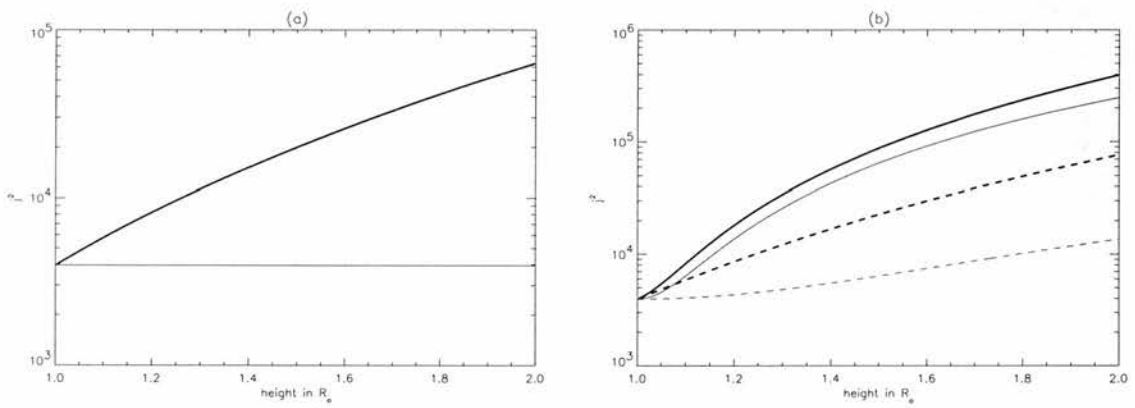

Figure 3.4: A cross-section of the current density j^2 for a diverging background magnetic field with $\lambda_0 = 0.1$ and $\theta_0 = 0.1$ at $\theta = 0.5$ for (a) $\delta = 0.0$ (b) different values of δ (solid line: $\delta = 0.5$, dashed line: $\delta = 0.1$) The thin lines represent the corresponding solutions in Cartesian coordinates at $x = 0.5$.

From Figure 3.4(a) we see that even when there is no phase mixing , i.e. $\delta = 0$, the current density builds up very rapidly in a diverging magnetic field. In the non-diverging atmosphere, i.e. the Cartesian case, this current density remains constant as gradients in the vertical or horizontal direction do not build up. As there is no phase mixing, the growth in j^2 in the diverging atmosphere is entirely due to the flaring out of the background field lines, i.e. the radial derivatives are building up. When we include phase mixing, i.e. $\delta > 0$, we see from Figure 3.4(b) that the build up of the current density, j^2, increases when δ increases. However, when the magnetic field is diverging, the

effect of increasing δ is larger than in the Cartesian case. Indeed, from comparing Eqns. (3.21) and (3.19), we see that a change in δ causes a bigger change in the spherical θ-derivatives than in the Cartesian x-derivatives. At $\theta = 0.5$ both the spherical r-derivatives and the Cartesian z-derivatives stay the same when the phase mixing parameter δ changes.

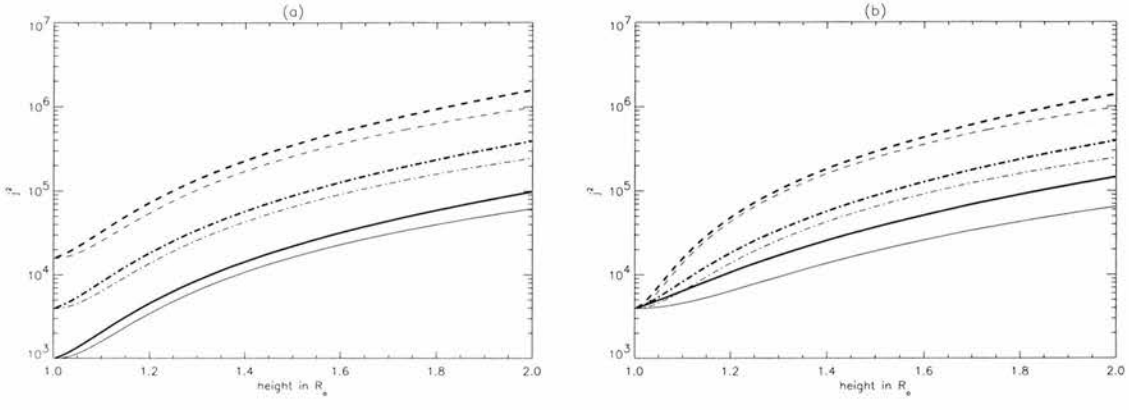

Figure 3.5: A cross-section of the current density j^2 for a diverging background magnetic field with $\delta = 0.5$ at $\theta = 0.5$ for (a) $\theta_0 = 0.1$ and different values of λ_0 (solid line: $\lambda_0 = 0.2$, dot-dashed line: $\lambda_0 = 0.1$, dashed line: $\lambda_0 = 0.05$) and (b) $\lambda_0 = 0.1$ and different values of θ_0 (solid line: $\theta_0 = 0.2$, dot-dashed line: $\theta_0 = 0.1$, dashed line: $\theta_0 = 0.05$). The thin lines represent the corresponding solutions in Cartesian coordinates at $x = 0.5$.

Figure 3.5(a) shows the change in the current density j^2 when we change the initial wavelength λ_0, through changes to either the frequency Ω_0 or the background Alfvén velocity v_{A0}. Since $\frac{\lambda_0}{2\pi} = \frac{v_{A0}}{\Omega_0}$, doubling λ_0 has the same effect as doubling v_{A0} or halving Ω_0 and so on. We therefore concentrate on the effect of varying just the one parameter λ_0. Changing λ_0 also causes z_0 to change as $z_0 = \frac{\lambda_0}{2\pi}$. We notice that j^2 starts off with a higher initial value when the initial wavelength λ_0 is smaller which is clear from Eqns. (3.19) and (3.21). We still see that the current density j^2 builds up faster in the spherical case and even that the difference between the spherical and the Cartesian case is more pronounced as the initial wavelength λ_0 gets smaller. From Eqns. (3.19) and (3.21) we see that all derivatives, apart from the Cartesian z-derivative, contain a $\frac{1}{\lambda_0}$ factor. From Eqn. (3.23), we see that, in the Cartesian case, the dimesionless variables introduce a factor $\frac{1}{\lambda_0^2}$ in front of the square of the z-derivative. These means that in both the spherical and Cartesian case, $j^2 \sim \frac{1}{\lambda_0^2}$ which implies that the difference between the spherical and Cartesian results gets 4 times bigger when we halve the initial wavelength λ_0. From Figure 3.5(b) we see that the current density builds up higher and that the difference between the spherical and the Cartesian case gets larger as we decrease the value of the parameter θ_0. However, from Eqns. (3.19) and (3.21) it is clear that all the derivatives remain unchanged when we vary θ_0. The parameter θ_0 only appears in expressions (3.22) and (3.23) for the

current density j^2. We see that the spherical θ-derivatives and Cartesian x derivatives are multiplied with a factor $\frac{1}{\theta_0^2}$ or that these derivatives will become 4 times larger when we halve θ_0. Again this implies that the difference between the spherical and Cartesian j^2 will get larger as θ_0 gets smaller.

From studying the non-dissipative case, we expect phase mixing to be enhanced when we increase the phase mixing parameter δ or decrease either the intial wavelength λ_0 or the parameter θ_0. We also expect more heat to be deposited into the plasma when we consider a diverging magnetic field compared to the Heyvaerts and Priest model in Cartesian coordinates. We now want to examine if these effects remain the same when we include dissipation in the system.

3.2.3 Energy

Combining the equation of motion and the induction equation gives the energy equation

$$\frac{\partial}{\partial t}\left(\frac{1}{2}\rho_0 v^2+\frac{b^2}{2\mu}\right)=\frac{B_0}{\mu}\frac{r_0^2}{r}\left(\frac{v}{r^2}\frac{\partial}{\partial r}(rb)+b\frac{\partial}{\partial r}\left(\frac{v}{r}\right)\right)+\rho_0\nu v\nabla^2 v+\frac{\eta}{\mu}b\nabla^2 b\,.$$

Using vector identities, we can rewrite this as

$$\frac{\partial}{\partial t}\left(\frac{1}{2}\rho_0 v^2+\frac{b^2}{2\mu}\right)=\frac{B_0}{\mu}\frac{r_0^2}{r^2}\frac{\partial}{\partial r}(v.b)+\rho_0\nu\nabla.(v\nabla v)-\rho_0\nu(\nabla v)^2 \\ +\frac{\eta}{\mu}\nabla.(b\nabla b)-\frac{\eta}{\mu}(\nabla b)^2\,.$$

Integrating over the volume of the plasma then gives

$$\begin{aligned}\frac{\partial}{\partial t}\left(\int\frac{1}{2}\rho_0 v^2+\frac{b^2}{2\mu}r^2\sin\theta dr d\theta\right)&=\frac{B_0}{\mu}r_0^2\int\frac{1}{r^2}\frac{\partial}{\partial r}(v.b)r^2\sin\theta dr d\theta\\&+\rho_0\nu\int\nabla.(v\nabla v)r^2\sin\theta dr d\theta+\frac{\eta}{\mu}\int\nabla.(b\nabla b)r^2\sin\theta dr d\theta\\&-\rho_0\nu\int\omega^2 r^2\sin\theta dr d\theta-\frac{1}{\sigma}\int j^2 r^2\sin\theta dr d\theta\,,\end{aligned}$$

as $(\nabla v)^2=\omega^2$, $(\nabla b)^2=\mu^2 j^2$ and $\eta\mu=\sigma^{-1}$.

So,

$$\begin{aligned}\frac{\partial}{\partial t}\int Er^2\sin\theta dr d\theta &= \frac{B_0}{\mu}r_0^2\int(v.b)_{r=\infty}\sin\theta d\theta-\frac{B_0}{\mu}r_0^2\int(v.b)_{r=0}\sin\theta d\theta\\&+\rho_0\nu\int\left(r^2 v\frac{\partial v}{\partial r}\right)_{r=\infty}\sin\theta d\theta-\rho_0\nu\int\left(r^2 v\frac{\partial v}{\partial r}\right)_{r=0}\sin\theta d\theta\\&+\rho_0\nu\int r\left(\sin\theta\frac{v}{r}\frac{\partial v}{\partial\theta}\right)_{\theta=\theta_0}dr-\rho_0\nu\int r\left(\sin\theta\frac{v}{r}\frac{\partial v}{\partial\theta}\right)_{\theta=0}dr\\&+\frac{\eta}{\mu}\int\left(r^2 b\frac{\partial b}{\partial r}\right)_{r=\infty}\sin\theta d\theta-\frac{\eta}{\mu}\int\left(r^2 b\frac{\partial b}{\partial r}\right)_{r=0}\sin\theta d\theta\\&+\frac{\eta}{\mu}\int r\left(\sin\theta\frac{b}{r}\frac{\partial b}{\partial\theta}\right)_{\theta=\theta_0}dr-\frac{\eta}{\mu}\int r\left(\sin\theta\frac{b}{r}\frac{\partial b}{\partial\theta}\right)_{\theta=0}dr\\&-\rho_0\nu\int\omega^2 r^2\sin\theta dr d\theta-\int\frac{j^2}{\sigma}r^2\sin\theta dr d\theta\,,\end{aligned}$$

where $E = \frac{1}{2}\rho_0(x,z)v^2 + \frac{1}{2\mu}b^2$ is the total energy. Applying the boundary conditions (3.10), (3.11) and (3.12) and neglecting $\nu\dfrac{\partial^2 v}{\partial r^2}$ and $\eta\dfrac{\partial^2 b}{\partial r^2}$, gives

$$\frac{\partial}{\partial t}\int Er^2\sin\theta dr d\theta = \frac{B_0}{\mu}r_0^2\int (v.b)_{r=\infty}\sin\theta d\theta - \frac{B_0}{\mu}r_0^2\int (v.b)_{r=0}\sin\theta d\theta$$
$$-\rho_0\nu\int \omega^2 r^2\sin(\theta)dr d\theta - \int\frac{j^2}{\sigma}r^2\sin(\theta)dr d\theta\,. \qquad (3.24)$$

Averaging over a period in time, it is clear that the difference between the energy flowing through the base and out through the upper boundary is dissipated as either viscous heating or ohmic heating. With dissipation, all the wave energy is dissipation before the upper boundary and so that all the energy propagating through the photospheric boundary goes into the ohmic and viscous heating terms.

3.3 Diverging atmosphere and no gravity, non-zero dissipation

In this section dissipation is included, i.e. $\Lambda^2 \neq 0$, but gravitational stratification is neglected and numerical results to Eqns. (3.5) and (3.7) are presented. We use the same numerical code as we used before to examine the effect of stratification on phase mixing of Alfvén waves. We therefore rewrite Eqn. (3.5) as

$$b + \frac{1}{(2\pi)^2}\frac{\lambda_0^2}{r_0^2}\frac{v_A^2}{\Omega^2}\left(\frac{1}{r^4}\frac{\partial^2 b}{\partial r^2} - \frac{2}{r^5}\frac{\partial b}{\partial r} - \frac{4}{r^6}b\right) + i\frac{\Lambda^2}{\Omega}\left(\theta_0^2\frac{2}{r}\frac{\partial b}{\partial r} + \theta_0^2\frac{\partial^2 b}{\partial r^2} + \right.$$
$$\left.\frac{1}{r^2}\frac{\partial^2 b}{\partial\theta^2} + \frac{\theta_0}{r^2}\frac{\cos(\theta_0\theta)}{\sin(\theta_0\theta)}\frac{\partial b}{\partial\theta} - \theta_0^2\frac{b}{r^2\sin^2(\theta_0\theta)}\right) = 0\,. \qquad (3.25)$$

To see the effect of the divergence of the field lines and dissipation it is useful to examine some approximate solutions, in both spherical and Cartesian coordinate systems.

When we consider resistivity, the WKB solutions in spherical coordinates, including the dominant damping terms $\theta_0^2\frac{\partial^2 b}{\partial r^2}$ and $\frac{1}{r^2}\frac{\partial^2 b}{\partial\theta^2}$ are

$$b = \sin(\pi\theta)\exp\left(-2\pi i\left(\frac{r_0}{\lambda_0}\right)k(\theta)\psi\right)\exp\left(-\frac{1}{2}\left(\frac{2\pi r_0}{\lambda_0}\right)^3\frac{\Lambda_\eta^2}{\Omega}\right.$$
$$\left.\left[\theta_0^2 k^3\frac{r^7-1}{7} + \frac{1}{9}k'^2 k\left(\frac{r^7}{7} - \frac{r^4}{2} + r - \frac{9}{14}\right)\right]\right)\,, \qquad (3.26)$$

with $3\psi = r^3 - 1$ and $\Lambda_\eta^2 = \frac{\eta}{\Omega_0 r_0^2\theta_0^2}$ and $k(\theta)$ as defined in Eqn. (3.13). Consider viscosity, the solution for the perturbed velocity becomes

$$v = \sin(\pi\theta)\exp\left(-2\pi i\left(\frac{r_0}{\lambda_0}\right)k(\theta)\psi\right)\exp\left(-\frac{1}{2}\left(\frac{2\pi r_0}{\lambda_0}\right)^3\Lambda_\nu^2\Omega\right.$$
$$\left.\left[\theta_0^2 k\frac{r^7-1}{7}+\frac{1}{9}\frac{k'^2}{k}\left(\frac{r^7}{7}-\frac{r^4}{2}+r-\frac{9}{14}r_0^7\right)\right]\right), \tag{3.27}$$

with $\Lambda_\nu^2 = \frac{\rho_0\nu\Omega_0\mu}{B_0^2}\left(\frac{\lambda_0}{2\pi r_0\theta_0}\right)^2$.

In Cartesian geometry we expect the horizontal derivatives to be more important than the vertical ones. So by only including the dominant damping term $\frac{\partial^2 b}{\partial x^2}$, corresponding WKB solutions in Cartesian coordinates are given by

$$b = \sin(\pi x)\exp(-ikz)\exp\left(-\frac{1}{6}\frac{\Lambda_\eta^2}{\Omega}k'^2kz^3\right), \tag{3.28}$$

with $\Lambda_\eta^2 = \frac{\eta}{\Omega_0 x_0^2}$ and

$$v = \sin(\pi x)\exp(-ikz)\exp\left(-\frac{1}{6}\Lambda_\nu^2\Omega\frac{k'^2}{k}z^3\right), \tag{3.29}$$

with $\Lambda_\nu^2 = \frac{\rho_0\nu\Omega_0\mu}{B_0^2}\left(\frac{z_0}{x_0}\right)^2$.

We note here that, although all the results presented here are numerical, the WKB solutions obtained in Appendix A give very good agreement in all cases considered.

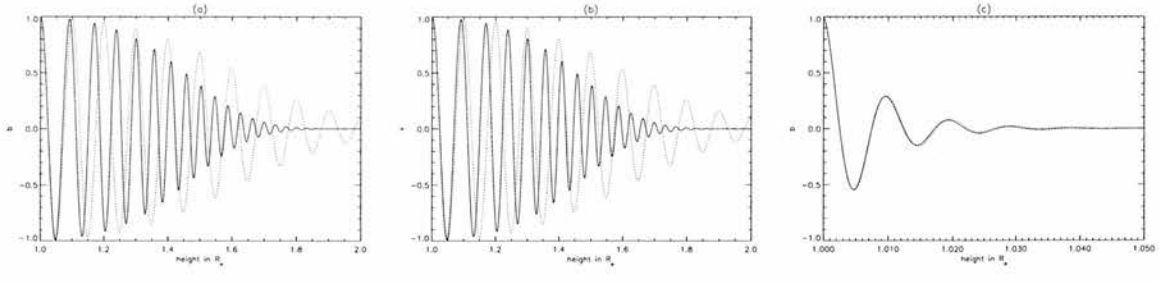

Figure 3.6: A cross-section of the perturbed (a) magnetic field and (b) velocity for a radially diverging background magnetic field at $\theta = 0.5$ with $\Lambda^2 = 10^{-4}$, $\delta = 0.5$ and $\lambda_0 = 0.1$. (c) A cross-section of the perturbed magnetic field at $\theta = 0.5$ with $\Lambda^2 = 10^{-4}$, $\delta = 0.5$ and $\lambda_0 = 0.01$. The dotted lines represent the corresponding solutions in Cartesian coordinates at $x = 0.5$.

From Figure 3.6, we see that including dissipation does not change the effect of an initially diverging magnetic field on the perturbed magnetic field. When the background field is radially diverging, wavelengths get shorter as the waves travel outward from the solar surface. This enhances the overall

damping of the wave amplitudes and therefore we expect heat to be deposited into the plasma at lower heights in a diverging atmosphere. From comparing Figures 3.6(a) and 3.6(b) we see again that the perturbed magnetic field and the perturbed velocity behave similarly when the resistive damping coefficient Λ_η^2 and the viscous damping coefficient Λ_ν^2 have the same value. However, we have to remark here that this is only the case at $\theta = 0.5$ (or $x = 0.5$ in the Cartesian case). At other values of θ there is a slight difference between the damping rate of the perturbed magnetic field and the perturbed velocity as Eqns. (3.26) and (3.27) show that for the magnetic field the damping term is proportional to k^3/Ω while for the velocity the damping term is proportional to $k\Omega$. Figure 3.6(c) confirms that at low heights, i.e. $\bar{r} \approx 1$, and for small initial wavelengths λ_0 there is a very good agreement between the spherical and the Cartesian case.

We now again look at the current density j^2 and the vorticity ω^2 to find out how the heat is deposited into the plasma through ohmic or viscous dissipation. From what we know about the no dissipation case and from the behaviour of the perturbed magnetic field, we expect strong current densities to build up when we consider a background field with radially diverging field lines.

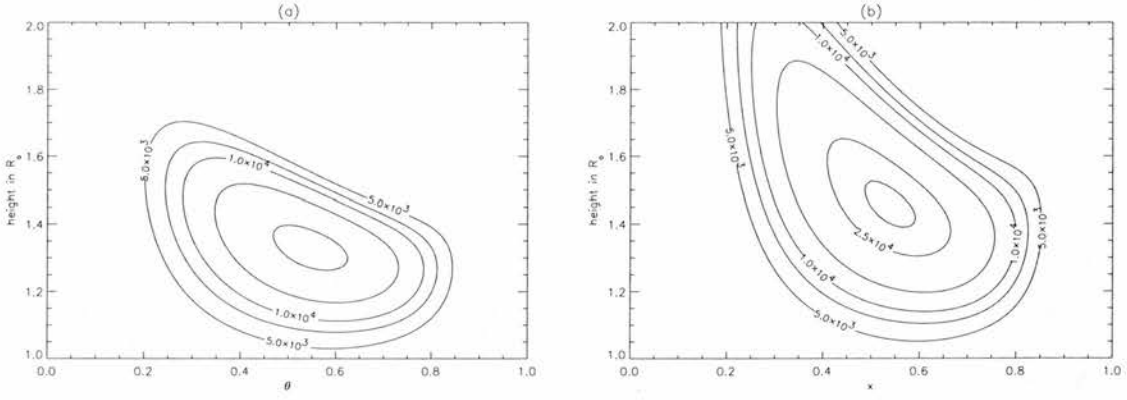

Figure 3.7: A contour plot of the current density j^2 with $\Lambda^2 = 10^{-4}$, $\delta = 0.5$, $\lambda_0 = 0.1$ and $\theta_0 = 0.1$ for (a) a diverging background magnetic field and (b) a non-diverging background magnetic field.

Figures 3.7 (a) and (b) are contour plots of the current density j^2 with a diverging and non-diverging background magnetic field. This figure shows clearly that the current density is concentrated at lower heights in the radially diverging geometry. However, although the maximum of the current density occurs at lower height in the spherical case, its value is less than the corresponding Cartesian case. Due to the combination of strong phase mixing and the shortening of the length scales caused by the divergence of the background magnetic field, the perturbed magnetic field is damped more quickly.

Figure 3.8 shows the behaviour of the current density j^2 for different values of the phase mixing parameter δ in both the spherical and Cartesian geometry. We see that when phase mixing is weak,

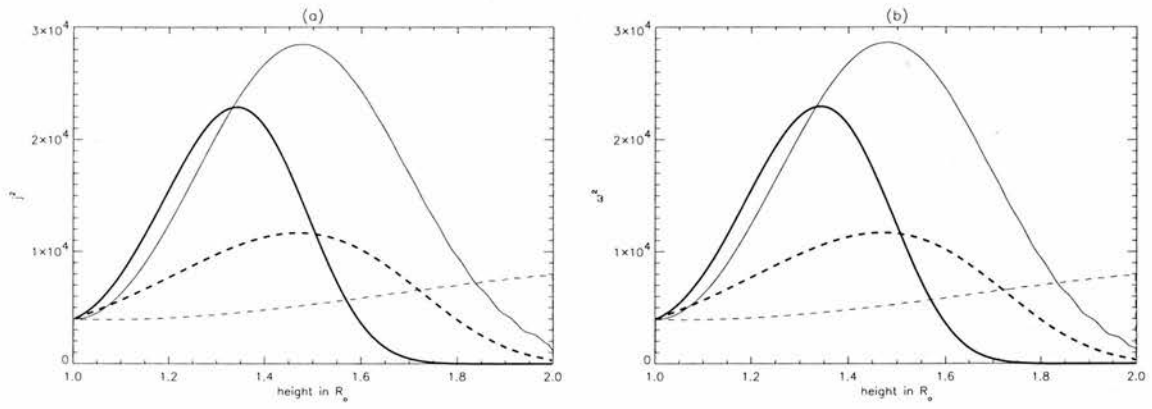

Figure 3.8: A cross-section of (a) the current density j^2 and (b) the vorticity ω^2 with $\Lambda^2 = 10^{-4}$ at $\theta = 0.5$ for different values of delta (solid line: $\delta = 0.5$, dashed line: $\delta = 0.2$). The thin lines represent the corresponding solutions in Cartesian coordinates at $x = 0.5$.

the results are the same as in the non-dissipative case. The current density builds up to a higher maximum, at a lower height when the background magnetic field is radially diverging. However, when phase mixing is stronger, i.e. $\delta = 0.5$, we see again that the maximum of the current density is situated at a lower height in the spherical case but reaches a higher maximum in the Cartesian case. The vorticity ω^2 behaves in a similar manner to the current density so that the deposition of heat into the plasma will occur at similar heights, whether we consider ohmic or viscous dissipation. Therefore we concentrate on the current density j^2 to see the effect of changing the plasma parameters.

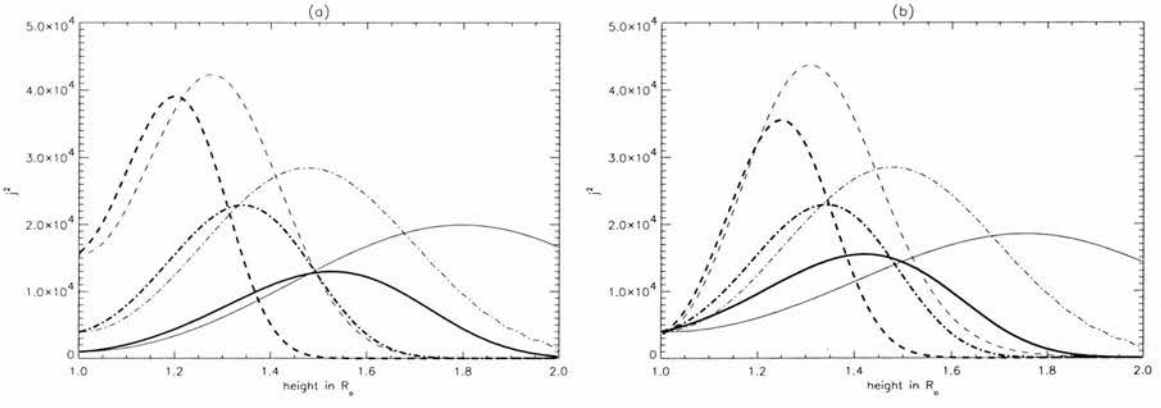

Figure 3.9: A cross-section at $\theta = 0.5$ of the current density j^2 for (a) different values of λ_0 (solid line: $\lambda_0 = 0.2$, dot-dashed line: $\lambda_0 = 0.1$, dashed line: $\lambda_0 = 0.05$) and (b) different values of θ_0 (solid line: $\theta_0 = 0.2$, dot-dashed line: $\theta_0 = 0.1$, dashed line: $\theta_0 = 0.05$). The thin lines represent the corresponding solutions in Cartesian coordinates at $x = 0.5$.

Figure 3.9(a) shows the variation in the current density j^2 when we change the initial wavelength

λ_0. Changing λ_0 causes the damping coefficient Λ^2 to change as $\Lambda^2 = \eta/\Omega_0 r_0^2 \theta_0^2$ and $\Omega_0 = 2\pi v_{A0}/\lambda_0$ and therefore $\Lambda^2 \sim \lambda_0$. The resistivity η is kept the same for all cases. From Figure 3.9(a) we see in both the spherical and the Cartesian case that the current density j^2 builds up stronger and quicker. Indeed, by starting off with a smaller initial wavelength, the small lengthscales needed for dissipation to be effective are created faster, i.e. the current density will build up at lower heights. However, although initially j^2 builds up faster and the maxima occur at lower heights in the spherical case, the maxima are smaller than in the corresponding Cartesian case.

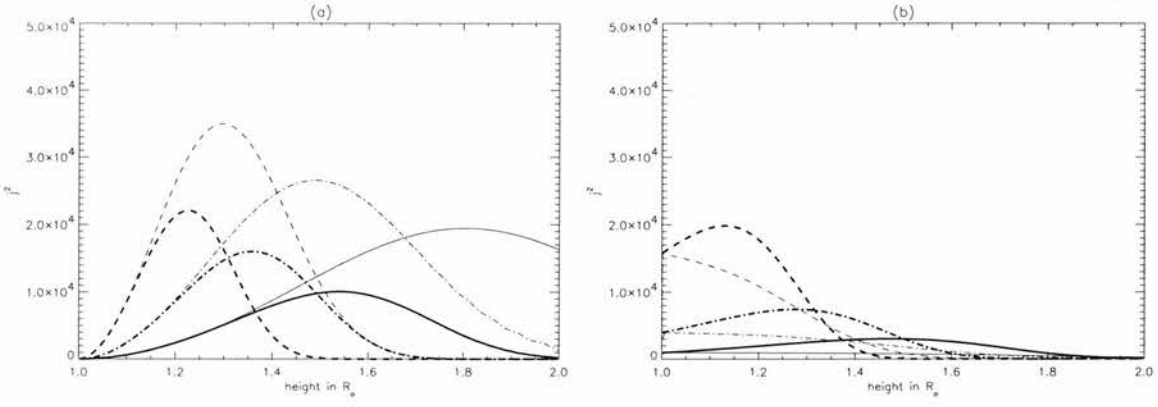

Figure 3.10: A cross-section at $\theta = 0.5$ of the current density j^2 taking into account only (a) the θ-derivatives or (b) the r-derivatives for different values of λ_0 (solid line: $\lambda_0 = 0.2$, dot-dashed line: $\lambda_0 = 0.1$, dashed line: $\lambda_0 = 0.05$). The thin lines represent the corresponding solutions in Cartesian coordinates at $x = 0.5$.

Figure 3.10 shows j^2 for different values of λ_0, only considering either of the derivatives to see the importance of the various terms in j^2. So for Figure 3.10(a) we took j^2 to be

$$j^2 = \frac{1}{r_0^2 \theta_0^2} \left(\frac{1}{\bar{r}} \frac{\partial b}{\partial \bar{\theta}} \right)^2 ,$$

i.e. not taking the radial derivatives into account, while for Figure 3.10(b)

$$j^2 = \frac{1}{r_0^2} \left(\frac{\partial b}{\partial \bar{r}} \right)^2 ,$$

i.e. not taking the θ-derivatives into account. From comparing the magnitude of the terms in j^2 in Figure 3.10 (a) and (b), we see that it is dominated by the θ-derivatives. In the spherical case, $\frac{1}{r}\frac{\partial b}{\partial \theta} \sim \frac{1}{r}\frac{r^3-1}{3} e^{-r^7/7}$ while in the Cartesian case, $\frac{\partial b}{\partial x} \sim z e^{-z^3/6}$ (see Eqns. (3.26) and (3.28)). So although the spherical θ-derivatives initially build up as r^2, the damping term $e^{-r^7/7}$ is significantly stronger than $e^{-z^3/6}$ explaining why j^2 initially builds up faster and why the maxima are situated at lower height and are less high in the spherical case. The initial increase in the radial derivatives in the spherical geometry we note in Figure 3.10(b) must be entirely due to the divergence of the

background magnetic field as the z-derivatives do not build up in the corresponding Cartesian case. So not only are the maxima of the θ-derivatives situated at lower heights than the maxima of the Cartesian x-derivatives, this initial increase in the radial derivatives will bring the maxima of the current density down to even lower heights. Figure 3.9(b) shows the change in the current density j^2 when we change the parameter θ_0. Again this causes other parameters to change as well. In this case the damping coefficient Λ^2 and x_0 will change as $\Lambda^2 \sim \theta_0^{-2}$ and $x_0 = r_0\theta_0$. The effect of changing θ_0 is largely the same as in the zero dissipation case. The current density builds up stronger at lower heights and again the maxima are higher in the Cartesian case.

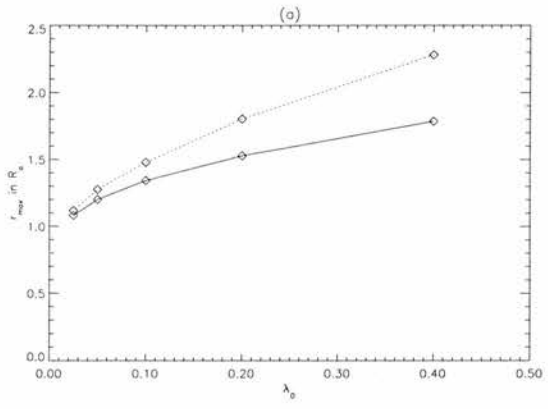

Figure 3.11: The height in solar radii at which the maximum of the current density is situated for different initial wavelengths λ_0. The dotted line represents the corresponding solution in Cartesian coordinates.

Figure 3.11 describes the height (in solar radii) at which the maximum of the current density would occur for different initial wavelengths λ_0. This figure confirms that the maxima are situated lower down in the spherical case but also shows that the difference gets smaller as the initial wavelength λ_0 gets smaller. If we look back at expression (3.14), we see that for small λ_0, the spherical and the Cartesian geometry will give the same results. As the maximum of j^2 is situated lower down as λ_0 gets smaller we can conclude that higher initial frequencies or a lower background Alfvén speed will cause the deposition of heat into the plasma to occur at lower heights.

The results in Table 3.1 are obtained for $\eta = 10^{-4}$ and the phase mixing parameter $\delta = 0.5$. By comparing the results for the total ohmic heating in the spherical and the Cartesian case for certain values of θ and x respectively we see that these results agree very well. This suggests that similar amounts of heat will be deposited through ohmic dissipation into the plasma in both cases and that the total amount of heat deposited does not depend on the geometry of the background magnetic field but only on the Poynting flux of magnetic energy through the photospheric base in response to footpoint motions. As expected, we also notice that the total ohmic heating $\eta \int_1^{r_{max}} j^2 r^2 dr$ does

	$\theta = 0.25$		$\theta = 0.5$		$\theta = 0.75$	
	spherical	Cartesian	spherical	Cartesian	spherical	Cartesian
$\lambda_0 = 0.1$, $\theta_0 = 0.1$	0.93	0.96	1.60	1.61	0.64	0.64
$\lambda_0 = 0.2$, $\theta_0 = 0.1$	0.94	0.98	1.60	1.62	0.64	0.64
$\lambda_0 = 0.05$, $\theta_0 = 0.1$	0.93	0.93	1.60	1.60	0.64	0.64
$\lambda_0 = 0.1$, $\theta_0 = 0.2$	0.93	0.94	1.59	1.60	0.64	0.64
$\lambda_0 = 0.1$, $\theta_0 = 0.05$	0.96	1.02	1.62	1.63	0.64	0.64

Table 3.1: The total ohmic heating $\eta \int_1^{r_{max}} j^2 r^2 dr$ (spherical) and $\eta \int_0^{z_{max}} j^2 dz$ (Cartesian), at different values of θ and x respectively, for different values of λ_0 and θ_0.

not depend on λ_0 or θ_0 (or z_0 and x_0 in the Cartesian case).

Overall, we can conclude that a diverging background magnetic field enhances phase mixing of Alfvén waves in the sense that wavelengths get shorter as the waves propagate up making the process of phase mixing more efficient as the small lengthscales needed for dissipation will build up lower down compared to a non-diverging atmosphere. A similar conclusion can be found in the Ruderman et al. solution for a uniform density in the vertical direction and an exponentially diverging magnetic field. We cannot make a direct comparison as we considered a truly open magnetic field, meaning that at no point the magnetic field lines connect back to the solar surface. However, we do reach the same conclusion that wave damping due to phase mixing will be faster in a diverging atmosphere.

3.4 Diverging atmosphere

3.4.1 Different background density profile

For all the results obtained above, we always considered the same background density profile, namely $\rho_0 = (1+\delta\cos(m\pi\theta))^{-1}$. We now want to study the effect of changing the background density profile. Consider the profile

$$\rho_0 = \rho_e + \frac{\rho_e - \rho_i}{2\tanh(\lambda\theta_*)}\left[\tanh(\lambda(\theta - \theta_*)) - \tanh(\lambda(\theta + \theta_*))\right], \tag{3.30}$$

where ρ_i is the density in the middle of the coronal hole and ρ_e approximately the density of the surrounding closed field, quiet Sun. λ controls the steepness of the transition from ρ_i to ρ_e and θ_* determines the position of this transition (Figure 3.12). In this section, we chose $\rho_i = 1.0$ and $\rho_e = 2.0$, i.e. we assumed that the density outside the coronal hole is twice as high as inside the coronal hole. As the differences between the spherical and Cartesian case are similar to the ones we

described above, we concentrate here on the effect of changing the density profile in the spherical geometry.

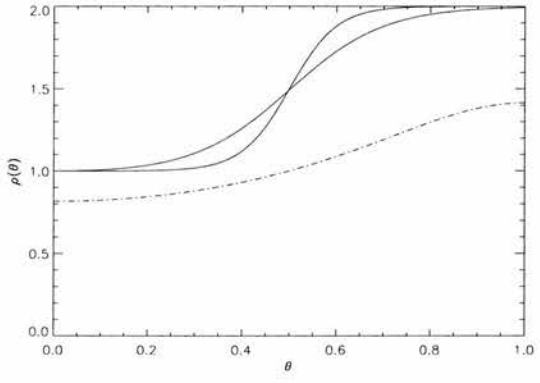

Figure 3.12: A plot of the density profile we will consider with $\rho_i = 1.0$, $\rho_e = 2.0$ and $\theta_* = 0.5$ for $\lambda = 5.0$ and $\lambda = 10.0$. The dot-dashed line is the density profile we considered before, i.e. $\rho_0 = (1 + \delta \cos(m\pi\theta))^{-1/2}$.

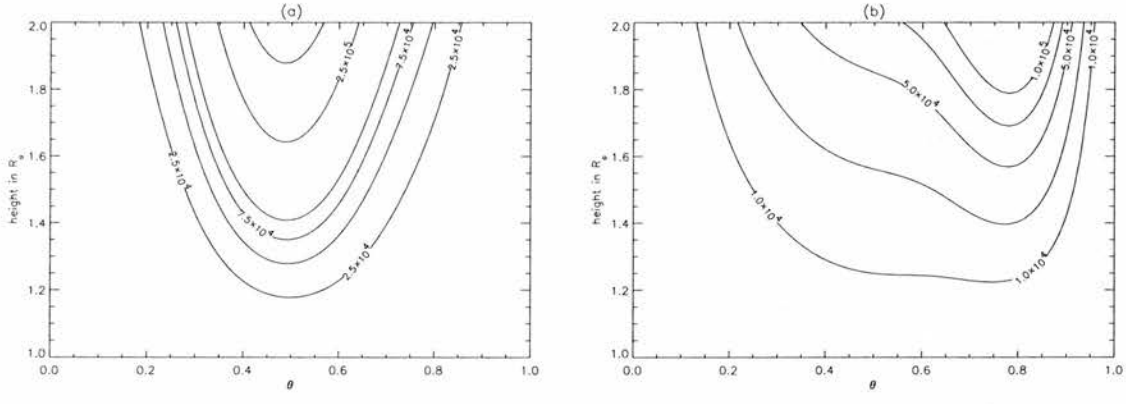

Figure 3.13: A contour plot of the current density j^2 for $\lambda = 5.0$ and (a) $\theta_* = 0.5$, (b) $\theta_* = 0.9$ for a radially diverging background magnetic field with $\Lambda^2 = 0.0$.

Figure 3.13 shows the current density j^2 for a radially diverging background in the non-dissipative case for different values of θ_*. Comparing Figures 3.13 (a) and (b), we see that j^2 is concentrated around the area where the gradient of the density profile is steepest. However, when θ_* is large we see that the current density also builds up where there is no or only a very small gradient in the background density profile. Rather than building up gradients by phase mixing, this build up is entirely due to the shortening of the wavelengths caused by the radially diverging field lines. This shortening of the wavelengths causes the radial derivatives to build up resulting in the increase of the current density that we see in Figure 3.13 (b) at, e.g., $\theta = 0.5$ where there is no gradient

in ρ_0. We also notice that when $\theta_* \neq 0.5$, the maximum of the current density does not occur exactly at θ_* but slightly to its left. However, Eqn. (3.19) tells us that $\frac{\partial b}{\partial \theta} \sim \sin(\pi\theta)k'(\theta)$, which has its maximum just next to θ_* when $\theta_* \neq 0.5$. When $\theta_* = 0.5$ both derivatives build up close to $\theta = 0.5$, as $\frac{\partial b}{\partial r} \sim \sin(\pi\theta)k(\theta)$, which explains why j^2 reaches higher values when $\theta_* = 0.5$ compared to $\theta_* = 0.9$ where both derivatives build up at different locations. When λ is increased so that the jump in the background density profile becomes steeper, the current density is confined to a smaller area around θ_*, where the gradient of the background density profile is steepest. Comparing with the corresponding Cartesian case tells us that in the non-dissipative case, j^2 builds up higher in the spherical case which agrees with the results we obtained earlier.

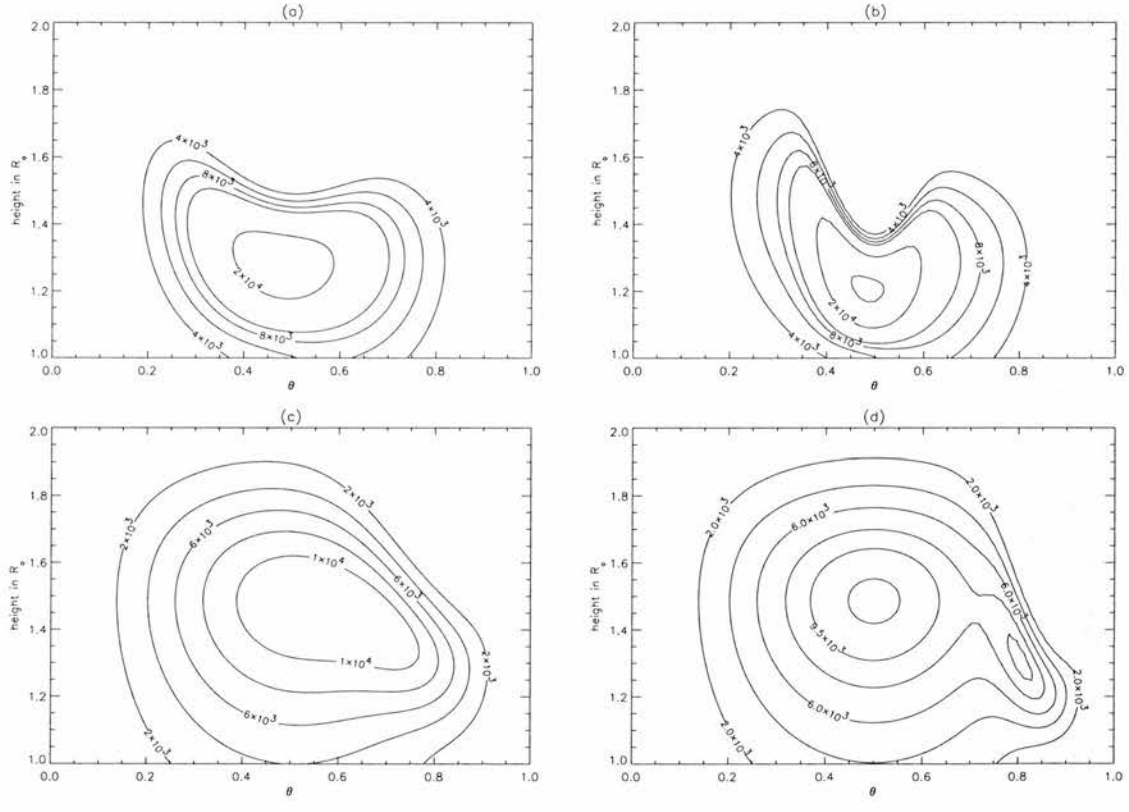

Figure 3.14: A contour plot of the current density j^2 for different values of λ and θ_* for a radially diverging background magnetic field with $\Lambda^2 = 10^{-4}$. (a) $\lambda = 5.0$, $\theta_* = 0.5$; (b) $\lambda = 10.0$, $\theta_* = 0.5$; (c) $\lambda = 5.0$, $\theta_* = 0.9$; (d) $\lambda = 10.0$, $\theta_* = 0.9$.

Figure 3.14 shows that the effects of changing λ or θ_* is similar when we include dissipation. Again we see that the current density j^2 is concentrated around the area where the gradients in the density profile are steepest. Figure 3.14 (d) shows that for large values of λ and θ_* it is even possible to get 2 separate maxima in the current density j^2. The maximum situated at θ_* is caused by 'normal' phase mixing i.e. gradients build up due to the inhomogeneous background density which causes

waves with the same frequency to move out of phase as they propagate up. The second maximum is entirely due to the shortening of the wavelengths caused by the diverging magnetic fieldlines. As the background density ρ_0 has a zero gradient at the location of this second maximum, the θ-derivatives do not build up. This explains why this does not occur in the Cartesian case. In this case neither of the derivatives build up when the background density is not inhomogeneous and therefore the current density does not build up. However, as before, the maxima of j^2 are located at a lower height in the spherical case but they are also less high than in the corresponding Cartesian case.

3.4.2 Different boundary condition at $r = r_0$

Till now, we used $b = \sin(n\pi\theta)$ at $r = r_0$ with $n = 1$ as a boundary condition on the base. We now study the effect on the current density j^2 of changing this boundary condition at the base by varying n. Note that we are using the original background density profile $\rho_0 = (1 + \delta\cos(m\pi\theta))^{-1}$ again. For the results in the section we chose $\delta = 0.5$ and $m = 1.0$.

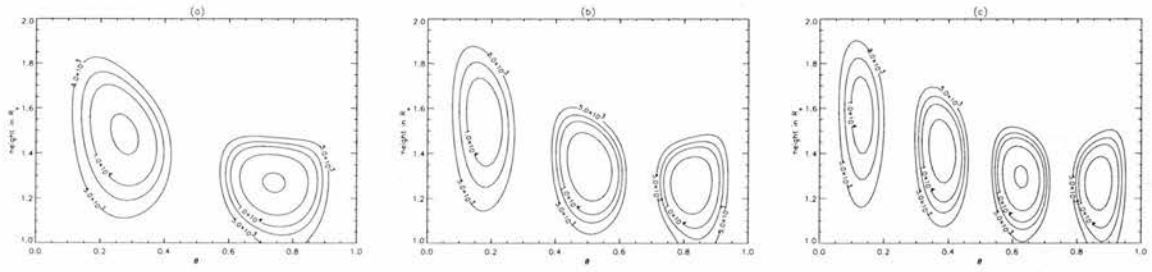

Figure 3.15: A contour plot of the current density j^2 with $\Lambda^2 = 10^{-4}$, $\delta = 0.5$, $\lambda_0 = 0.1$, $\theta_0 = 0.1$ and $b = \sin(n\pi\theta)$ at $r = r_0$, for (a) $n = 2$, (b) $n = 3$ and (c) $n = 4$.

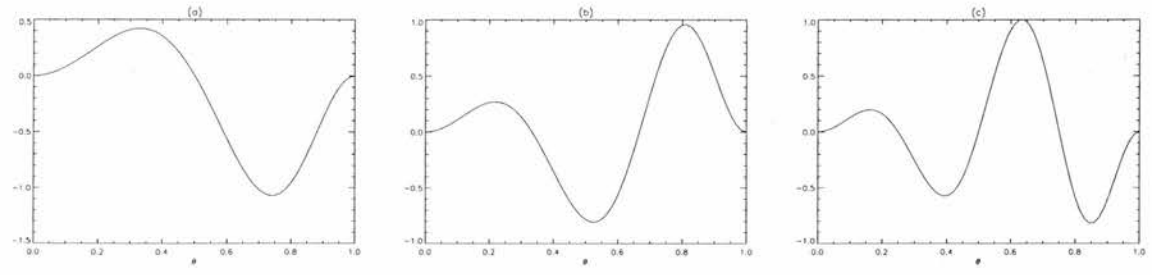

Figure 3.16: A plot of $\sin(n\pi\theta)k'(\theta)$ for (a) $n = 2$, (b) $n = 3$ and (c) $n = 4$.

From Figure 3.15 we see that we get quite a different distribution of the current density j^2 than in Figure 3.7 where we used $b = \sin(\pi\theta)$ as a boundary condition at $r = r_0$. This shows that the initial profile at $r = r_0$ of the perturbed magnetic field does influence where heat will be deposited into

the plasma. Comparing Figures 3.15 and 3.16, we see that the location of the current density j^2 is again given by the location of the peaks of $\sin(n\pi\theta)k'(\theta)$. We also notice that j^2 builds up higher and reaches its maximum lower down when $\sin(n\pi\theta)k'(\theta)$ reaches a higher value. In this case the maxima of $\sin(n\pi\theta)k(\theta)$ and $\sin(n\pi\theta)k'(\theta)$ are situated at roughly the same values of θ which means that both the radial derivatives and the θ-derivatives build up at the same place. Comparing with the Cartesian case we see again that the maxima occur lower down but are less high in the spherical case.

3.4.3 Effect of an individual plume

By adjusting the background density profile, we here try to model the effect of an individual plume in a solar coronal hole on the current density j^2. We therefore use the profile

$$\rho_0 = \rho_e + \frac{\rho_e - \rho_i}{2\tanh(\lambda\theta_*)}\left[\tanh(\lambda(\theta - \theta_*)) - \tanh(\lambda(\theta + \theta_*))\right], \tag{3.31}$$

where ρ_i is the density inside the plume and ρ_e approximately the density of the surrounding coronal hole. In this section we assume $\rho_e = 1.0$ and $\rho_i = 3.0$ or $\rho_i = 5.0$, i.e. the density inside the plume is 3-5 times as higher than the density in the surrounding coronal hole (Del Zanna et al., 1997). We used $b = \sin(\pi\theta)$ as boundary condition at $r = r_0$.

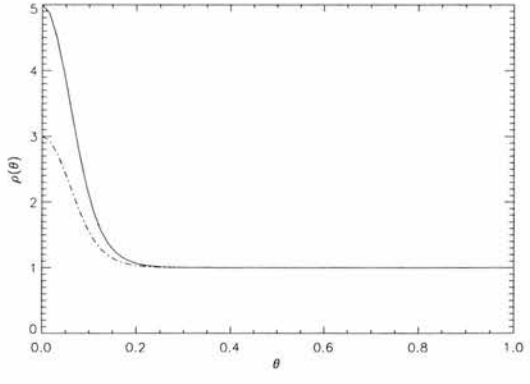

Figure 3.17: A plot of the density profile we will consider with $\rho_i = 5.0$ (solid line) and $\rho_i = 3.0$ (dot-dashed line), $\rho_e = 1.0$, $\theta_* = 0.05$ and $\lambda = 15.0$.

From Figure 3.18 we see largely the same phenomena as in Section 3.4.1. The current density j^2 builds up at 2 different locations as $\theta_* \neq 0.5$. Due to the shortening of the wavelengths the radial derivatives build up around $\theta = 0.5$ while the θ-derivatives build up close to θ_* due to phase mixing. This time the maximum of $\sin(\pi\theta)k'(\theta)$ is situated to the right of θ_* and from Figure 3.18 we see

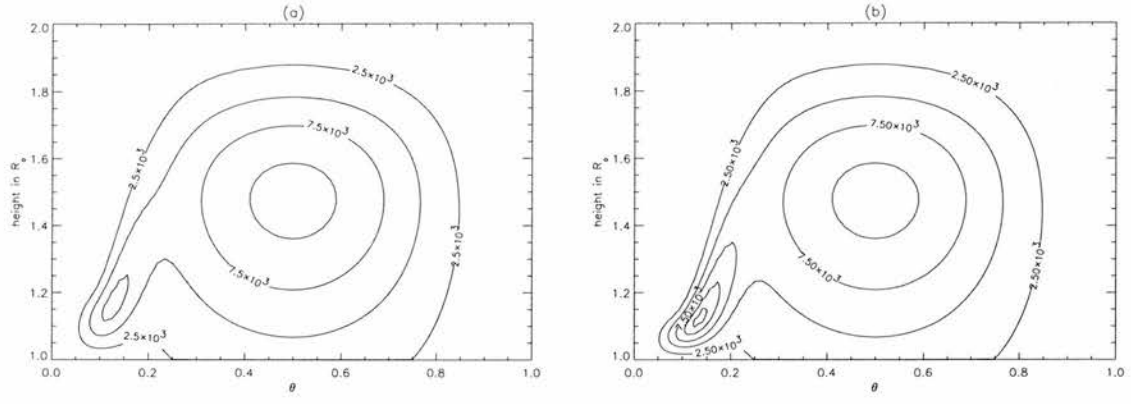

Figure 3.18: A contour plot of the current density j^2 for (a) $\rho_i = 3.0$ and (b) $\rho_i = 5.0$.

indeed that that is where the maximum of j^2 is located. When the jump in the density is not big enough, we see from Figure 3.18 (a) that the maximum of the current density outside the plume, caused by the build up of the radial derivatives, is higher than the one in the plume, caused by the θ-derivatives. This suggests that more heat will be deposited outside the plume than inside when the density of the plume is not much higher than the density of the surrounding coronal hole. Comparing Figure 3.17 and Figure 3.18 we see that the maximum of j^2 occurs low down and at the sides of the plume rather than inside the actual plume. In the Cartesian case, we only get heat deposited in the plume, not in the surrounding coronal hole as the z-derivatives do not build up in this case.

3.4.4 Effect of plumes in a coronal hole

To model a coronal hole with several plumes we consider the following background density profile,

$$\rho_0 = \rho_1 - \rho_2 + \rho_3 \,, \tag{3.32}$$

where

$$\rho_1 = \rho_{e1} + \frac{\rho_{e1} - \rho_i}{2\tanh(\lambda_1\theta_{*1})}\left[\tanh(\lambda_1(\theta - \theta_{*1})) - \tanh(\lambda_1(\theta + \theta_{*1}))\right] \,,$$

$$\rho_2 = \rho_{e2} + \frac{\rho_{e2} - \rho_i}{2\tanh(\lambda_2\theta_{*2})}\left[\tanh(\lambda_2(\theta - \theta_{*2})) - \tanh(\lambda_2(\theta + \theta_{*2}))\right] \,,$$

and

$$\rho_3 = \rho_e + \frac{\rho_e - \rho_i}{2\tanh(\lambda\theta_*)}\left[\tanh(\lambda(\theta - \theta_*)) - \tanh(\lambda(\theta + \theta_*))\right] \,,$$

where $\rho_i = 1.0$, $\rho_e = 4.0$, $\rho_{e1} = \rho_{e2} = 4.3$, $\lambda_1 = \lambda_2 = \lambda = 25.0$, $\theta_{*1} = 0.3$, $\theta_{*2} = 0.4$ and $\theta_* = 0.9$ (Figure 3.19).

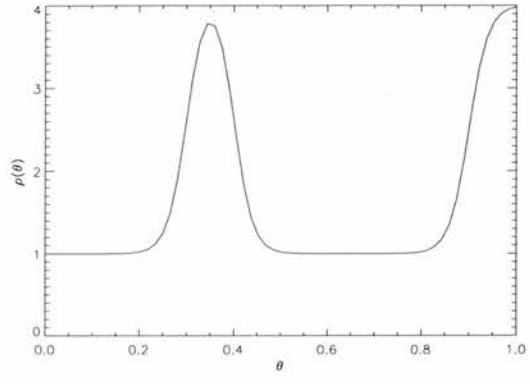

Figure 3.19: A plot of the density profile $\rho_0(\theta)$ we will consider to model plumes in a coronal hole.

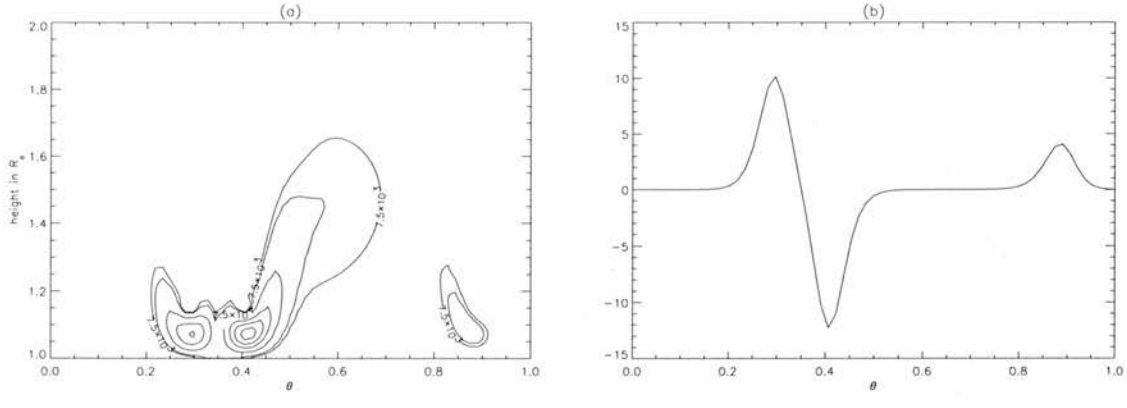

Figure 3.20: (a) A contour plot of the current density j^2 for the background density profile we specified above. (b) A plot of $\sin(\pi\theta)k'(\theta)$.

From Figure 3.20 we see that we can largely make the same conclusions as in Section 3.4.3. The behaviour of the current density j^2 is mainly determined by the behaviour of the θ-derivatives and as $\frac{\partial b}{\partial \theta} \sim \sin(\pi\theta)k'(\theta)$, we see that the maxima of j^2 coincide with the maxima of $\sin(\pi\theta)k'(\theta)$. Comparing Figure 3.19 and Figure 3.20 we see again that the maxima of j^2 occur low down and at the sides of the plumes rather than inside the actual plumes. The build up of current density in between the plumes and the boundary of the coronal hole is caused by the radial derivatives which build up at that location due to the shortening of the wavelengths. This, and the fact that j^2 builds up higher at the right hand side of the plume, is caused by the $\sin(\pi\theta)$-profile we chose for the perturbed magnetic field at the base. It is again this profile at the base which causes the amount of heat deposited at the boundary of the coronal hole to be small compared to the amount of heat

deposited at the sides of the coronal plumes as seen from Figure 3.20 (b). In the Cartesian case, we only get heat deposited at the edges of the plumes and at the boundary of the coronal hole.

3.5 Stratification in a diverging atmosphere

Stratification was shown to inhibit phase mixing but the results for a diverging field, obtained in the first half of this chapter, indicate an enhancement of energy dissipation. In this section we invesigate the effect of both gravitational stratification of the density and a radially diverging background magnetic field is on phase mixing of Alfvén waves. We therefore consider Eqn. (3.5),

$$b+\left(\frac{\lambda_0}{2\pi r_0}\right)^2\frac{\bar{v}_A^2}{\bar{\Omega}^2}\frac{1}{\bar{r}}\frac{\partial}{\partial\bar{r}}\left(e^{\frac{1}{H}\left(1-\frac{1}{\bar{r}}\right)}\frac{1}{\bar{r}^4}\frac{\partial}{\partial\bar{r}}(\bar{r}b)\right)+i\frac{\Lambda_\eta^2}{\bar{\Omega}}\left(\frac{\theta_0^2}{\bar{r}^2}\frac{\partial}{\partial\bar{r}}\left(\bar{r}^2\frac{\partial b}{\partial\bar{r}}\right)+\frac{1}{\bar{r}^2\sin(\theta_0\bar{\theta})}\frac{\partial}{\partial\bar{\theta}}\left(\sin(\theta_0\bar{\theta})\frac{\partial b}{\partial\bar{\theta}}\right)-\theta_0^2\frac{b}{\bar{r}^2\sin^2(\theta_0\bar{\theta})}\right)=0\,.$$

However, just as before we will only take into account the important damping terms and work with

$$b+\left(\frac{\lambda_0}{2\pi r_0}\right)^2\frac{v_A^2}{\Omega^2}\frac{1}{r}\frac{\partial}{\partial r}\left(e^{\frac{1}{H}\left(1-\frac{1}{r}\right)}\frac{1}{r^4}\frac{\partial}{\partial r}(rb)\right)+i\frac{\Lambda_\eta^2}{\Omega}\left(\theta_0^2\frac{\partial^2 b}{\partial r^2}+\frac{1}{r^2}\frac{\partial^2 b}{\partial\theta^2}\right)=0\,,\tag{3.33}$$

with $\Lambda_\eta^2=\eta/\Omega_0 r_0^2\theta_0^2$, for the perturbed magnetic field and

$$e^{-\frac{1}{H}\left(1-\frac{1}{r}\right)}\frac{\Omega^2}{v_A^2}v+\left(\frac{\lambda_0}{2\pi r_0}\right)^2\frac{1}{r^3}\frac{\partial^2}{\partial r^2}\left(\frac{v}{r}\right)+i\Lambda_\nu^2\Omega\left(\theta_0^2\frac{\partial^2 v}{\partial r^2}+\frac{1}{r^2}\frac{\partial^2 v}{\partial\theta^2}\right)=0\,,\tag{3.34}$$

with $\Lambda_\nu^2=\frac{\rho_0\nu\Omega_0\mu}{B_0^2}\left(\frac{\lambda_0}{2\pi r_0\theta_0}\right)^2$, for the perturbed velocity, to obtain analytical results.

In Cartesian coordinates the phase mixing equations are now given by,

$$b+\frac{v_A^2}{\Omega^2}\frac{\partial}{\partial z}\left(e^{\frac{z}{H_c}}\frac{\partial b}{\partial z}\right)+i\frac{\Lambda_\eta^2}{\Omega}\left(\frac{x_0^2}{z_0^2}\frac{\partial^2 b}{\partial z^2}+\frac{\partial^2 b}{\partial x^2}\right)=0\,,\tag{3.35}$$

and

$$e^{-\frac{z}{H_c}}\frac{\Omega^2}{v_A^2}v+\frac{\partial^2 v}{\partial z^2}+i\,\Lambda_\nu^2\Omega\left(\frac{x_0^2}{z_0^2}\frac{\partial^2 v}{\partial z^2}+\frac{\partial^2 v}{\partial x^2}\right)=0\,,\tag{3.36}$$

with $H_c=\frac{2\pi r_0}{\lambda_0}H$, $\Lambda_\eta^2=\eta/\Omega_0 x_0^2$ and $\Lambda_\nu^2=\rho_0\nu\mu\Omega_0/B_0^2\left(\frac{z_0}{x_0}\right)^2$ where $x_0=r_0\theta_0$ and $z_0=\lambda_0/2\pi$.

3.5.1 No dissipation

If we neglect dissipation, i.e. $\Lambda^2 = 0$, WKB solutions for the perturbed velocity and the perturbed magnetic field are given by

$$v = e^{\frac{1}{4H}\left(1-\frac{1}{r}\right)} \exp\left(-i\frac{2\pi r_0}{\lambda_0}k(\theta)R\right) , \tag{3.37}$$

and,

$$b = e^{\frac{-1}{4H}\left(1-\frac{1}{r}\right)} \exp\left(-i\frac{2\pi r_0}{\lambda_0}k(\theta)R\right) , \tag{3.38}$$

where $R = \int_1^r r^2 e^{-\frac{1}{2H}\left(1-\frac{1}{r}\right)} dr$.

The WKB solutions in Cartesian coordinates are given by,

$$v = e^{\frac{z}{4H_c}} \exp\left(-ik(x)Z\right) , \tag{3.39}$$

and,

$$b = e^{-\frac{z}{4H_c}} \exp\left(-ik(x)Z\right) , \tag{3.40}$$

where $Z = 2H_c\left(1 - e^{\frac{-z}{2H_c}}\right)$.

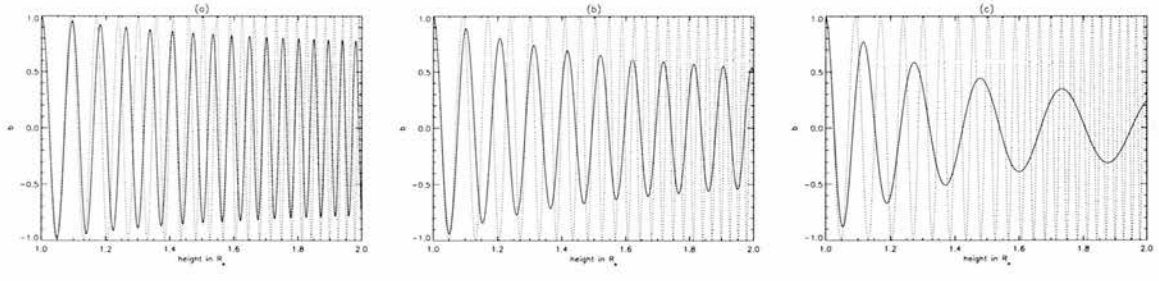

Figure 3.21: A cross-section of the perturbed magnetic field for a radially diverging background magnetic field at $\theta = 0.5$ with $\Lambda^2 = 0.0$, $\delta = 0.5$ and $\lambda_0 = 0.1$ for (a) $H = 0.5$, (b) $H = 0.2$ and (c) $H = 0.1$. The dotted lines represent the corresponding solution for $H = \infty$.

From Figures 3.21 and 3.23 we see that the gravitational stratification of the density has a very strong influence on the behaviour of both the perturbed magnetic field and velocity. Rather than staying constant, as in the radially diverging atmosphere, the amplitude of the magnetic field decreases

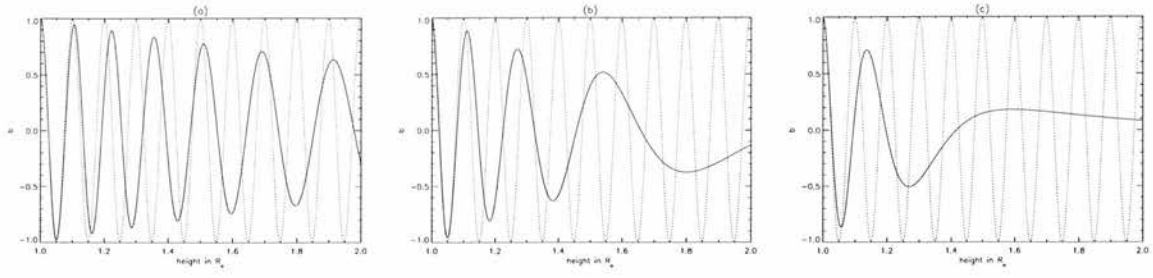

Figure 3.22: A cross-section of the (Cartesian) perturbed magnetic field at $x = 0.5$ with $\Lambda^2 = 0.0$, $\delta = 0.5$ and $\lambda_0 = 0.1$ for (a) $H = 0.5$, (b) $H = 0.2$ and (c) $H = 0.1$. The dotted lines represent the corresponding solution for $H = \infty$.

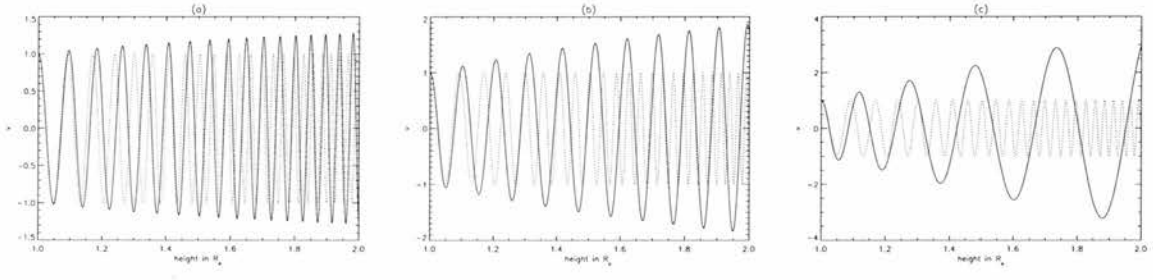

Figure 3.23: A cross-section of the perturbed velocity for a radially diverging background magnetic field at $\theta = 0.5$ with $\Lambda^2 = 0.0$, $\delta = 0.5$ and $\lambda_0 = 0.1$ for (a) $H = 0.5$, (b) $H = 0.2$ and (c) $H = 0.1$. The dotted lines represent the corresponding solution for $H = \infty$.

with height due to stratification. The amplitude of the velocity on the other hand, increases with height. This behaviour does not surprise us as this is exactly what we found when studying the effect of (just) stratification on phase mixing of Alfvén waves (Figures 3.22 and 3.24). We could also anticipate this effect from the behaviour of the density ρ_0. We know that in the non-dissipative case $b \sim \rho_0^{1/4}$ and $v \sim \rho_0^{-1/4}$, which in this case means that $b \sim e^{\frac{-1}{4H}\left(1-\frac{1}{r}\right)}$ or $b \sim e^{\frac{z}{4H_c}}$ in the Cartesian case. As the density decreases with height in a stratified atmosphere, this implies that the amplitude of b will decrease with height and that v will increase.

The Alfvén speed v_A and the wavelength λ now behave as $\frac{1}{r^2}e^{\frac{1}{2H}\left(1-\frac{1}{r}\right)}$ in the diverging case and as $e^{\frac{z}{2H_c}}$ in the Cartesian case. This means that the wavelength will increase everywhere in the Cartesian case, as we see from Figure 3.25(b) but that will only increase everywhere for $H < \frac{1}{4r_{max}}$ in the diverging case. This is all clearly seen in Figure 3.25(a). The wavelength only increases for all values of r for $H = 0.1$. When $H > \frac{1}{4}$, the wavelengths will decrease everywhere, which in Figure 3.25(a) happens for $H = \infty$ and $H = 0.5$. For $\frac{1}{4r_{max}} < H < \frac{1}{4}$, the wavelengths will increase till $r > \frac{1}{4H}$ and then decrease. Indeed, for $H = 0.2$, λ initially increases till $r = 1.0/(4H) = 1.25$ and

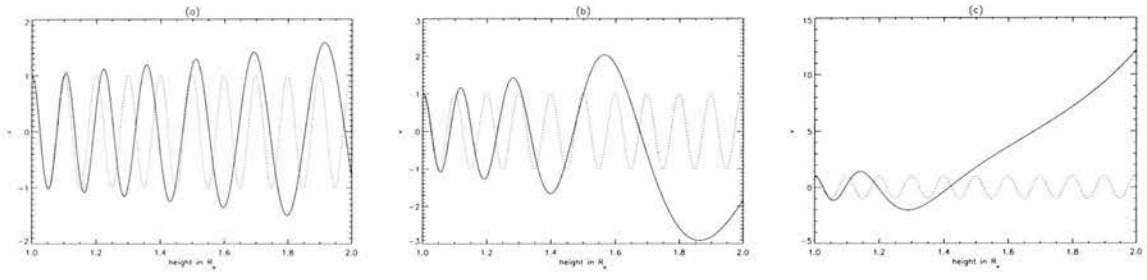

Figure 3.24: A cross-section of the (Cartesian) perturbed velocity at $x = 0.5$ with $\Lambda^2 = 0.0$, $\delta = 0.5$ and $\lambda_0 = 0.1$ for (a) $H = 0.5$, (b) $H = 0.2$ and (c) $H = 0.1$. The dotted lines represent the corresponding solution for $H = \infty$.

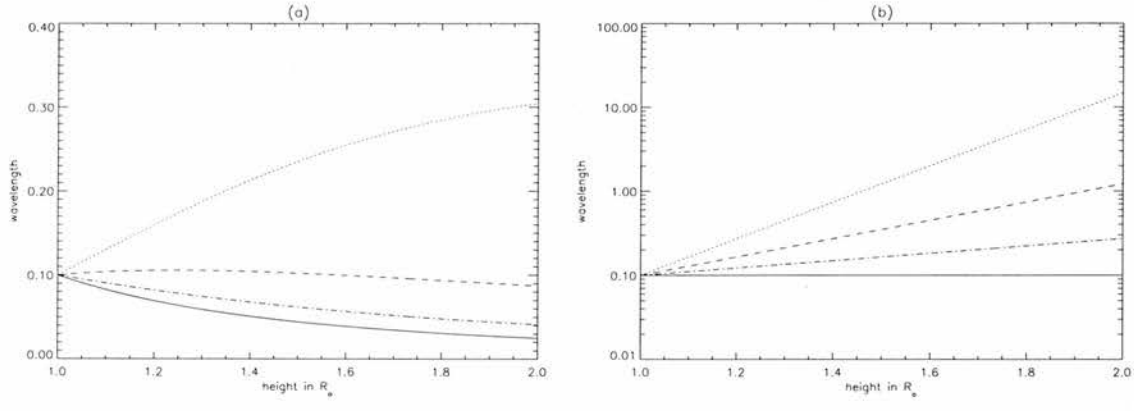

Figure 3.25: (a) Behaviour of the wavelength λ for a radially diverging background magnetic field at $\theta = 0.5$ with $\lambda_0 = 0.1$ for different values of the scale-height (solid line: $H = \infty$, dot-dashed line: $H = 0.5$, dashed line: $H = 0.2$, dotted line: $H = 0.1$). (b) Behaviour of the wavelength λ in the corresponding Cartesian case.

then decreases.

From Figures 3.26, 3.27, 3.28 and 3.29, it is clear that stratification introduces dramatic changes. When we look at the results for the ohmic heating j^2 (Figure 3.26) we retrieve the effects found when studying either a purely stratified or a diverging atmosphere. Despite the fact that the amplitude of b decreases due to the density stratification, j^2 still builds up for most values of the scale height H, due to the shorter wavelengths caused by the area divergence of the background magnetic field. It is only when stratification is very strong that j^2 decreases. We also see that j^2 builds up stronger in the diverging atmosphere than in the Cartesian case, a result already noted in the no stratification case. When the value of the initial wavelength λ_0 is decreased, we find that the current density reaches higher values, as found in the purely diverging atmosphere.

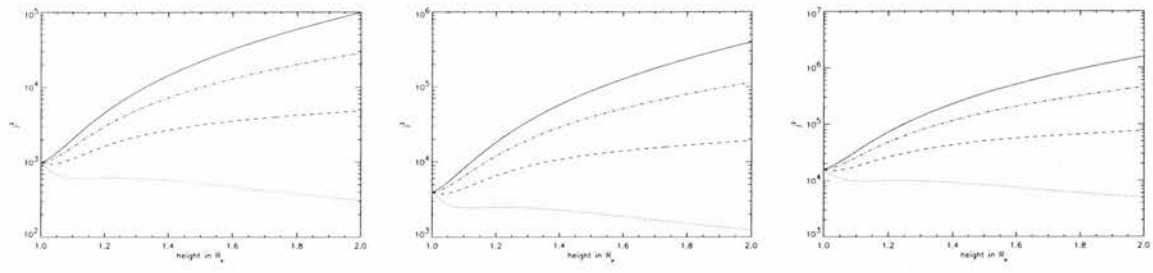

Figure 3.26: A cross-section of the current density for a radially diverging background magnetic field at $\theta = 0.5$ with (left) $\lambda_0 = 0.2$, (middle) $\lambda_0 = 0.1$ and (right) $\lambda_0 = 0.05$ for different values of the scale-height (solid line: $H = \infty$, dot-dashed line: $H = 0.5$, dashed line: $H = 0.2$, dotted line: $H = 0.1$).

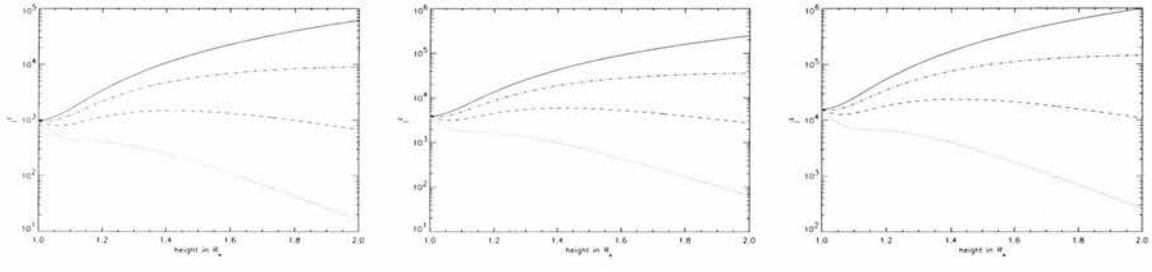

Figure 3.27: A cross-section of the (Cartesian) current density at $x = 0.5$ with (left) $\lambda_0 = 0.2$, (middle) $\lambda_0 = 0.1$ and (right) $\lambda_0 = 0.05$ for different values of the scale-height (solid line: $H = \infty$, dot-dashed line: $H = 0.5$, dashed line: $H = 0.2$, dotted line: $H = 0.1$).

The results are quite different when considering the viscous heating ω^2 (Figure 3.28). We see that the vorticity builds up higher than the corresponding current density and that the effect of changing the scale height is reduced. This different behaviour is due to the increase of the velocity amplitude, a result which we also found in the purely stratified atmosphere. The effect of the changing the value of the initial wavelength seems to be the same for the current density and the vorticity. If we compare these results with the corresponding Cartesian results in Figure 3.29, we see that, unlike the current density, the vorticity builds up higher in the Cartesian case. We also notice that while the vorticity decreases as the scale height is increased in the diverging atmosphere, the opposite happens in the Cartesian case. From Figure 3.29 we see that, as expected, the (Cartesian) vorticity initially builds up less high as the stratification increases. This is due to the lengthening of the wavelengths caused by the stratification and is in agreement with previous results. However, we see that very quickly the vorticity reaches higher values for stronger stratification due to the extremely rapid increase of the velocity amplitude caused by the decreasing density. The effect of changing the initial wavelength λ_0 is nevertheless maintained. Decreasing the initial wavelength causes the

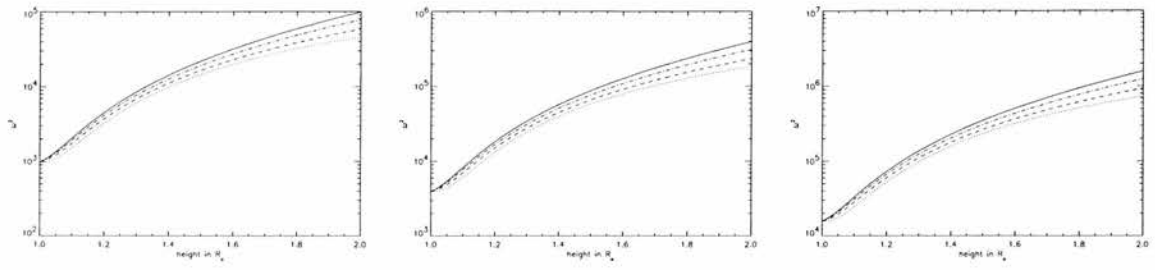

Figure 3.28: A cross-section of the vorticity for a radially diverging background magnetic field at $\theta = 0.5$ with (left) $\lambda_0 = 0.2$, (middle) $\lambda_0 = 0.1$ and (right) $\lambda_0 = 0.05$ for different values of the scale-height (solid line: $H = \infty$, dot-dashed line: $H = 0.5$, dashed line: $H = 0.2$, dotted line: $H = 0.1$).

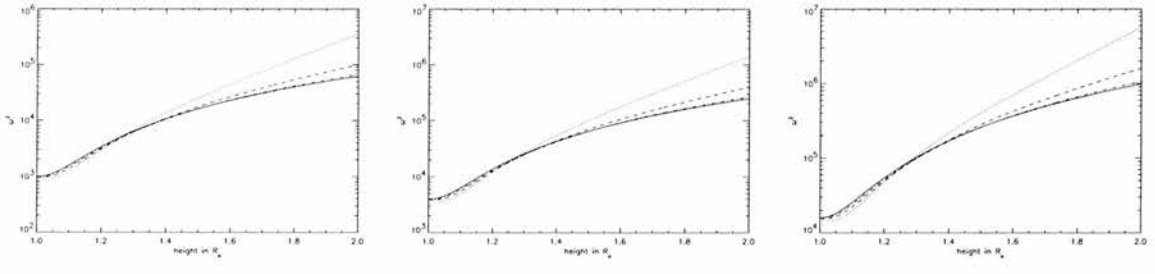

Figure 3.29: A cross-section of the (Cartesian) vorticity at $x = 0.5$ with (left) $\lambda_0 = 0.2$, (middle) $\lambda_0 = 0.1$ and (right) $\lambda_0 = 0.05$ for different values of the scale-height (solid line: $H = \infty$, dot-dashed line: $H = 0.5$, dashed line: $H = 0.2$, dotted line: $H = 0.1$).

vorticity to start of with a higher initial value and to reach higher values as the waves propagate up.

3.5.2 Stratified, diverging atmosphere, non-zero dissipation

We now consider $\Lambda^2 \neq 0$ and present numerical results to Eqns. (3.33) and (3.34). Again it is useful to examine some approximate solutions, in both spherical and Cartesian coordinate systems.

When we consider resistivity, the WKB solutions in spherical coordinates, including the dominant damping terms $\theta_0^2 \frac{\partial^2 b}{\partial r^2}$ and $\frac{1}{r^2}\frac{\partial^2 b}{\partial \theta^2}$ are

$$b = \sin(\pi\theta)\exp\left(-i\frac{2\pi r_0}{\lambda_0}k(\theta)R\right)\exp\left[-\frac{1}{4H}\left(1-\frac{1}{r}\right) - \frac{1}{2}\frac{\Lambda_\eta^2}{\Omega}\left(\frac{2\pi r_0}{\lambda_0}\right)^3 k^3 \int_1^r \left(\theta_0^2 r^6 e^{-\frac{3}{2H}\left(1-\frac{1}{r}\right)} + \frac{k'^2}{k^2}R^2 e^{-\frac{1}{2H}\left(1-\frac{1}{r}\right)}\right) dr\right], \qquad (3.41)$$

with $R = \int_1^r r^2 e^{-\frac{1}{2H}\left(1-\frac{1}{r}\right)} dr$ and $\Lambda_\eta^2 = \frac{\eta}{\Omega_0 r_0^2 \theta_0^2}$ and when we consider viscosity,

$$v = \sin(\pi\theta) \exp\left(-i\frac{2\pi r_0}{\lambda_0} k(\theta) R\right) \exp\left[\frac{1}{4H}\left(1-\frac{1}{r}\right) - \frac{1}{2}\Lambda_\nu^2 \Omega \left(\frac{2\pi r_0}{\lambda_0}\right)^3 k \int_1^r \left(\theta_0^2 r^6 e^{-\frac{1}{2H}\left(1-\frac{1}{r}\right)} + \frac{k'^2}{k^2} R^2 e^{\frac{1}{2H}\left(1-\frac{1}{r}\right)}\right) dr\right], \quad (3.42)$$

with $\Lambda_\nu^2 = \frac{\rho_0 \nu \Omega_0 \mu}{B_0^2} \left(\frac{\lambda_0}{2\pi r_0 \theta_0}\right)^2$.

The corresponding solutions in Cartesian coordinates are given by,

$$b = \sin(\pi x) e^{-\frac{z}{4H_c}} \exp(-ikZ) \exp\left(-\frac{1}{6}\frac{\Lambda_\eta^2}{\Omega} k^3 \left[\frac{x_0^2}{z_0^2} 2H_c (1 - e^{-3z/2H_c}) + \frac{k'^2}{k^2} Z^3\right]\right), \quad (3.43)$$

with $Z = 2H_c\left(1 - e^{\frac{z}{2H_c}}\right)$ and $\Lambda_\eta^2 = \frac{\eta}{\Omega_0 x_0^2}$ and

$$v = \sin(\pi x) e^{\frac{-z}{4H_c}} \exp(-ikZ) \exp\left(-\frac{1}{2}\Lambda_\nu^2 \Omega k \left[\frac{x_0^2}{z_0^2} Z - \frac{k'^2}{k^2} (2H_c)^3 \left(\frac{z}{H_c} - 2\sinh\left(\frac{z}{2H_c}\right)\right)\right]\right), \quad (3.44)$$

with $\Lambda_\nu^2 = \frac{\rho_0 \nu \Omega_0 \mu}{B_0^2} \left(\frac{z_0}{x_0}\right)^2$.

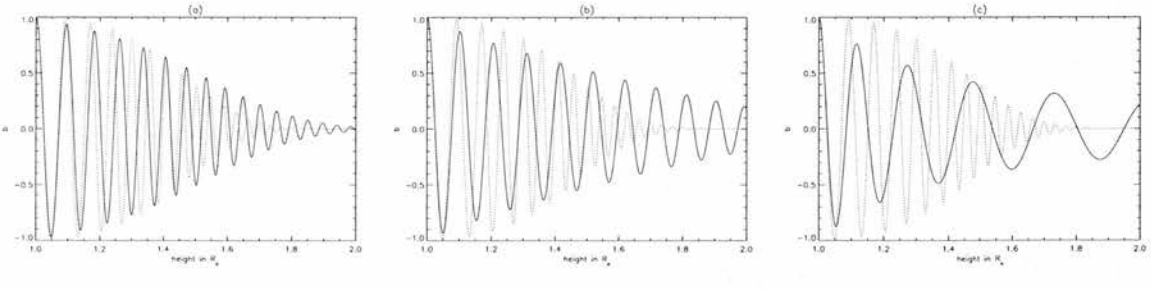

Figure 3.30: A cross-section of the perturbed magnetic field for a radially diverging background magnetic field at $\theta = 0.5$ with $\Lambda^2 = 10^{-4}$, $\delta = 0.5$ and $\lambda_0 = 0.1$ for (a) $H = 0.5$, (b) $H = 0.2$ and (c) $H = 0.1$. The dotted lines represent the corresponding solution for $H = \infty$.

Figures 3.30 and 3.31 show that including dissipation gives familiar results for the behaviour of the perturbed magnetic field. We see that, in both the spherical and the Cartesian case, the magnetic field initially decays faster when we include stratification. But, overall the damping rate is reduced in a stratified atmosphere. For weak stratification we see that the radial divergence of the background magnetic field still causes the waves to dissipate faster in the spherical case compared to the Cartesian case. We also notice that including dissipation has not changed the behaviour of the wavelength λ.

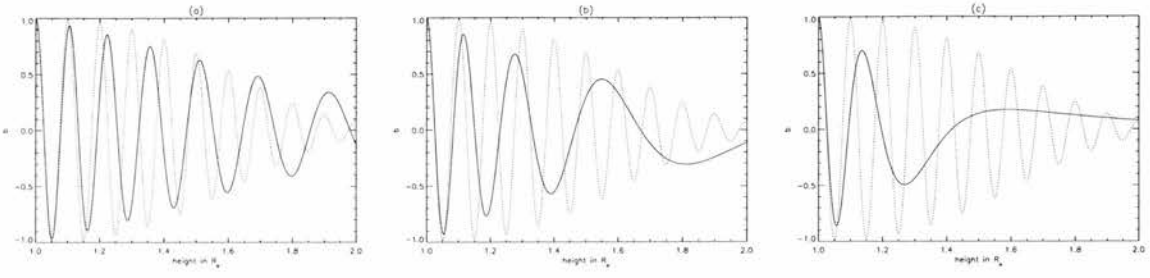

Figure 3.31: A cross-section of the (Cartesian) perturbed magnetic field at $x = 0.5$ with $\Lambda^2 = 10^{-4}$, $\delta = 0.5$ and $\lambda_0 = 0.1$ for (a) $H = 0.5$, (b) $H = 0.2$ and (c) $H = 0.1$. The dotted lines represent the corresponding solution for $H = \infty$.

From Figure 3.30 (a) we see that for $H = 0.5$ the wavelengths decrease as the wave propagates up with height. For $H = 0.2$ (Figure 3.30 (b)), λ initially increases and then decreases where as for $H = 0.1$ (Figure 3.30 (c)) the wavelengths increase for all heights. In the corresponding Cartesian cases (Figure 3.31) the wavelength increases everywhere due to the stratification.

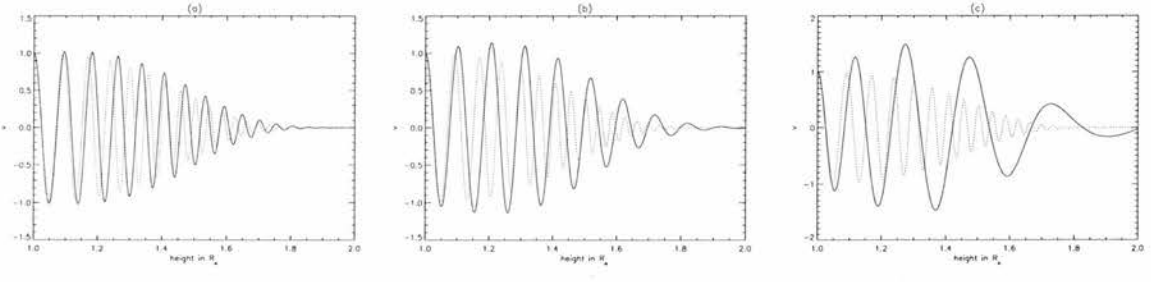

Figure 3.32: A cross-section of the perturbed velocity for a radially diverging background magnetic field at $\theta = 0.5$ with $\Lambda^2 = 10^{-4}$, $\delta = 0.5$ and $\lambda_0 = 0.1$ for (a) $H = 0.5$, (b) $H = 0.2$ and (c) $H = 0.1$. The dotted lines represent the corresponding solution for $H = \infty$.

Figures 3.32 and 3.33 show the behaviour of the perturbed velocity when we include dissipation in our model. And again the results do not surprise us. We notice an initial increase in the amplitude of the velocity in the stratified plasma which is the remnant of the amplitude increase of perturbed velocity noted in the zero dissipation case. We also see that the difference between the velocity results for the stratified and the unstratified atmosphere are considerably smaller than the magnetic field results. When considering viscous dissipation, we see that the perturbed velocity decays faster than the perturbed magnetic field damped by ohmic dissipation (Figure 3.30). However, in general the wave amplitudes decay faster in an unstratified atmosphere. The behaviour of the wavelength λ is the same as for the perturbed magnetic field.

For both the perturbed magnetic field and the perturbed velocity we mainly recover the results found

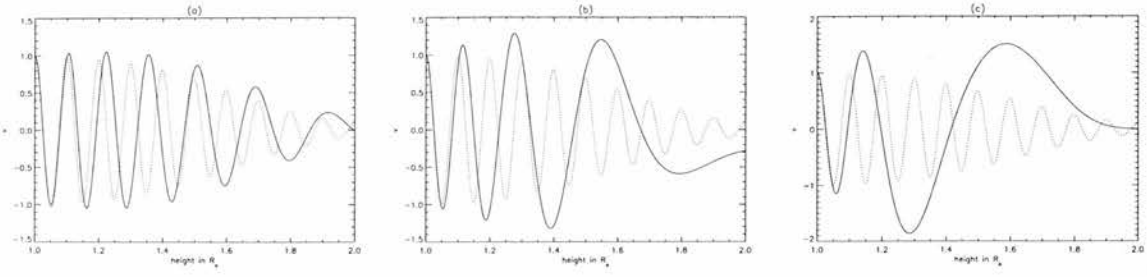

Figure 3.33: A cross-section of the (Cartesian) perturbed velocity at $x = 0.5$ with $\Lambda^2 = 10^{-4}$, $\delta = 0.5$ and $\lambda_0 = 0.1$ for (a) $H = 0.5$, (b) $H = 0.2$ and (c) $H = 0.1$. The dotted lines represent the corresponding solution for $H = \infty$.

when studying the effect of (only) stratification on phase mixing of Alfvén waves. The effect of a radially diverging background magnetic field on phase mixing does not seem to be strong enough to compensate for the stratification of the density when the dimensionless pressure scale height H is smaller than $1/4$.

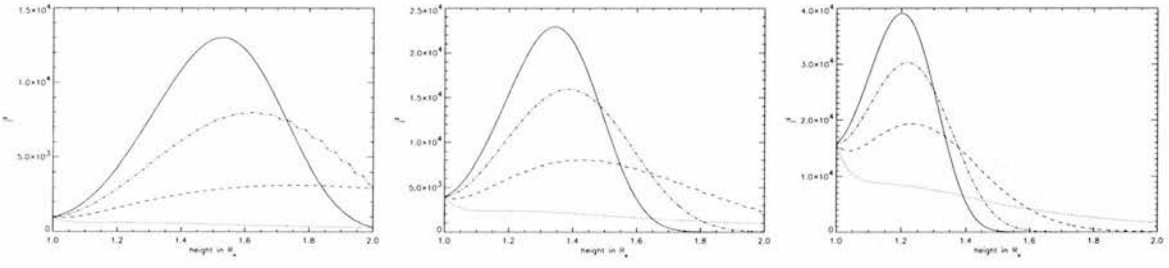

Figure 3.34: A cross-section of the current density for a radially diverging background magnetic field at $\theta = 0.5$ with (left) $\lambda_0 = 0.2$, (middle) $\lambda_0 = 0.1$ and (right) $\lambda_0 = 0.05$ for different values of the scale-height (solid line: $H = \infty$, dot-dashed line: $H = 0.5$, dashed line: $H = 0.2$, dotted line: $H = 0.1$).

The cross sections (Figures 3.34 and 3.35) of the current density j^2 only confirm the dominant effect of the stratified density. In both the spherical and the Cartesian case we see that the current density is spread out over a wider area when the pressure scale height is smaller. The maximum of j^2 is less high and situated higher up. However, we do see that the divergence of the background magnetic field still has some effect. When comparing corresponding different geometries we see that in the spherical case the maximum of the current density is situated at a lower height but is also smaller in magnitude, a result noticed and explained when studying the effect of divergence on phase mixing of Alfvén waves. We also recover the effect of changing the initial wavelength λ_0. When λ_0 is decreased, j^2 obtains a higher maximum at a lower height. We also found that, despite the

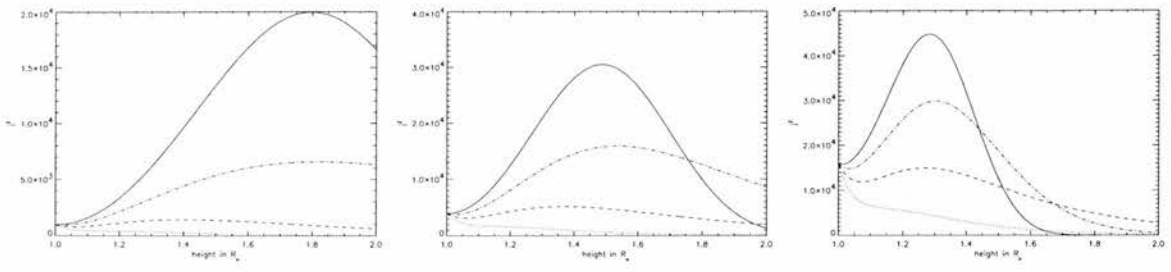

Figure 3.35: A cross-section of the (Cartesian) current density at $x = 0.5$ with (left) $\lambda_0 = 0.2$, (middle) $\lambda_0 = 0.1$ and (right) $\lambda_0 = 0.05$ for different values of the scale-height (solid line: $H = \infty$, dot-dashed line: $H = 0.5$, dashed line: $H = 0.2$, dotted line: $H = 0.1$).

different behaviours of the current density j^2 in different case, the total ohmic heating $\int_{r_0}^{r_{max}} j^2 r^2 dr$ at $\theta = 0.5$ is conserved in all cases. Overall we see that heat will be deposited higher up in a stratified atmosphere with a radially diverging background magnetic field. However, for the same amount of stratification heat will be deposited into the plasma at lower heights in the spherical case compared to the Cartesian case.

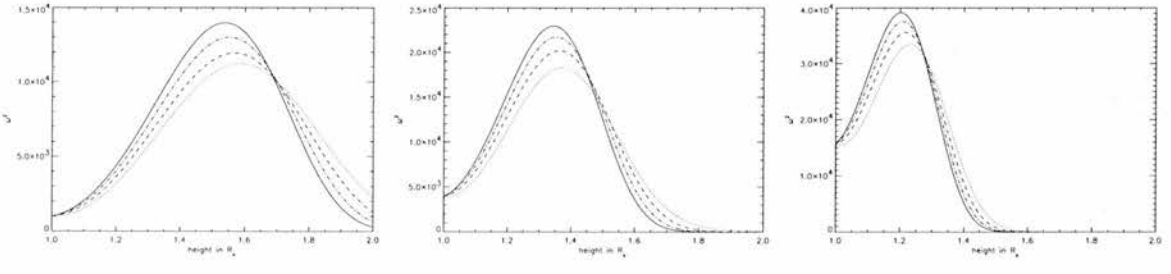

Figure 3.36: A cross-section of the vorticity for a radially diverging background magnetic field at $\theta = 0.5$ with (left) $\lambda_0 = 0.2$, (middle) $\lambda_0 = 0.1$ and (right) $\lambda_0 = 0.05$ for different values of the scale-height (solid line: $H = \infty$, dot-dashed line: $H = 0.5$, dashed line: $H = 0.2$, dotted line: $H = 0.1$).

Finally, Figures 3.36 and 3.37 show the behaviour of the vorticity ω^2 for both a radially diverging and a uniform background magnetic field for different values of the scale height H and the initial wavelength λ_0. Again we see that the effect of stratification on the vorticity is a lot smaller than the effect on the current density. The vorticity is only spread out very slightly due to the lengthening of the wavelengths in the stratified atmosphere. This different behaviour is due to the initial increase in the amplitude of the perturbed velocity and the fact that the *dynamic* viscosity $\rho_0 \nu$ is constant, rather than the kinematic viscosity ν. The effect of the divergence of the background magnetic field on the vorticity is similar to the effect on the current density. Compared to the Cartesian case

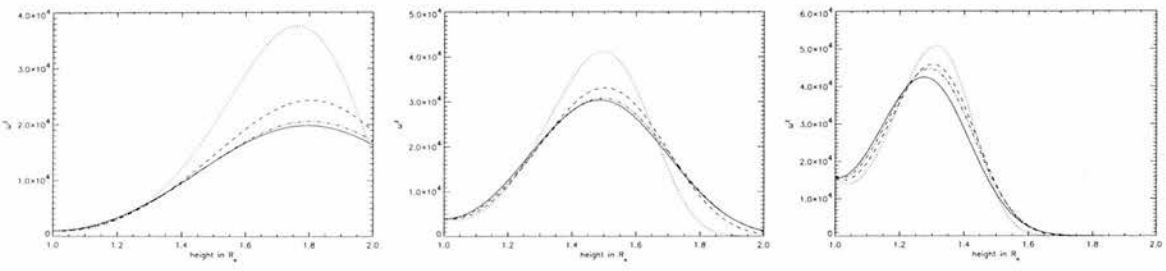

Figure 3.37: A cross-section of the (Cartesian) vorticity at $x = 0.5$ with (left) $\lambda_0 = 0.2$, (middle) $\lambda_0 = 0.1$ and (right) $\lambda_0 = 0.05$ for different values of the scale-height (solid line: $H = \infty$, dot-dashed line: $H = 0.5$, dashed line: $H = 0.2$, dotted line: $H = 0.1$).

the maximum of ω^2 occurs lower down in the spherical case but builds up less high. The effect of changing the initial wavelength λ_0 on the vorticity is again the same as for the current density. The maximum of the vorticity is situated at a lower height and builds up higher when λ_0 gets smaller.

Overall, we can make two conclusions about the combined effect of a density stratification and a radially diverging background magnetic field on the phase mixing of Alfvén waves. The stratification generates longer wavelengths, therefore phase mixing is less efficient and heat is deposited into the plasma at higher heights compared to a purely diverging atmosphere without stratification. At the same time the divergence results in shorter wavelengths which enhances phase mixing and heat is deposited at lower heights compared to a non-diverging atmosphere. So, compared to the original, uniform and unstratified Heyvaerts and Priest solution, phase mixing can be more or less efficient depending on the value of the scale height H. A similar conclusion can be found in Ruderman et al. (1998) but a direct comparison cannot be made. They assumed an exponentially diverging magnetic field and an exponentially decreasing density in such a manner that the resulting Alfvén velocity was depending on the horizontal coordinate only. In this study we have a different Alfvén speed and a truly open atmosphere in the sense that no magnetic field lines connect back to the solar surface. However, the general conclusions are broadly in agreement with Ruderman et al. (1998).

3.6 Conclusions

Let us put the results obtained in this paper into typical solar corona conditions. A coronal hole plasma is strongly inhomogeneous due to the presence of, for example, plumes, so phase mixing will occur when waves generated by photospheric motions travel outwards from the Sun. For example, if we assume that the plasma density inside a coronal plume is a factor of 4 higher than the surrounding plasma, we find $\delta \approx 0.5$. If we further assume a driver with a 1-minute period and assume the Alfvén

speed in a coronal hole to be 1000 km/s, we find that $\lambda_0 \approx 0.1$ solar radii. The pressure scale height $H = \frac{\mathcal{R}T}{\mu g}$ is found to be 0.2 solar radii for $T = 2 \times 10^6$K. With these values, we expect the maximum of the ohmic heating to occur at 1.4 solar radii and the maximum of the viscous heating at 1.35 solar radii (Figure 3.34). When we consider a driver with a 5-minute period, the initial wavelength will be longer, which will cause to maximum of the ohmic and viscous dissipation to be situated at larger heights. So we find that for T=2 $\times$ 10^6 K, a 1-minute oscillation will deposit most heat within a few solar radii and could therefore be a candidate for heating the coronal holes, while e.g. a 5-minute oscillation might be a way to deposit heat into the solar wind.

From studying the effect of a diverging background magnetic field on phase mixing of Alfvén waves in an open field region we conclude that wavelengths shorten when the waves propagate outwards. Due to these shortening wavelengths, phase mixing is more efficient as waves on neighbouring field lines become out-of-phase. Hence, sufficiently small lengthscales for dissipation to be important will now build up faster and the waves will therefore be dissipated quicker when compared to the standard non-diverging case. The divergence of the background magnetic field introduces two competing effects on the current density j^2. The shortening of the wavelengths causes the current density to build up faster and therefore the maxima of j^2 occur at lower heights in comparison to the Cartesian case. However, at the same time the shorter wavelengths cause phase mixing to be more efficient and, therefore, heat will be dissipated into the plasma at lower heights. Due to this combination the maxima of the current density j^2 occur at lower heights but are also lower than in the Cartesian case. We found that, unlike in a stratified atmosphere, the current density and the vorticity behave in a similar manner and that ohmic and viscous heating will have a similar importance in the heating process. From considering a different background density profile we can conclude that, in general, the maximum of the current density j^2 will occur where the gradient in the density profile is steepest as phase mixing will be most efficient there. By studying the effect of an individual plume in a coronal hole we found that more heat will be deposited outside the plume than inside when the density of the plume is not much higher than the density of the surrounding coronal hole and that the maximum of j^2 occurs low down at the sides of the plume rather than inside the actual plume. Looking at different boundary conditions at $r = r_0$ showed that the initial profile of the perturbed magnetic field does influence where heat will be deposited into the plasma through ohmic dissipation.

From our study of the combined effect of a stratified density and a radially diverging background magnetic field on phase mixing of Alfvén waves we found that the efficiency of phase mixing depends strongly on the particular geometry of the configuration. Finally, depending on the value of the scale height the wave amplitudes can damp either slower or faster than in the uniform non-diverging Heyvaerts and Priest (1983) solution.

Chapter 4

Wavelet Analysis and the determination of coronal plasma properties.

Science is the refusal to believe on the basis of hope.
C.P. Snow

4.1 Introduction

Recent observations of oscillations (e.g. DeForest & Gurman, 1998; Aschwanden et al., 1998) show that in most cases these wave motions are not steady harmonic waves but tend to be waves with only a few periods and either are of finite lifetime or are damped. Methods such as the Fast Fourier Transform calculate power at particular frequencies by analysing the entire time series at the same time. The Fourier transform provides information about the frequency domain, but all time localised information is essentially lost in this process. This information is not necessary for stationary signals but the method is inappropriate for non-stationary signals, as it is impossible to associate features in the frequency domain with their location in time. Therefore, Fourier analysis is not really appropriate for analysing observations of oscillatory signals, as it is unable to provide any information about the lifetime of the oscillations and can only indicate the dominant frequencies (or wavelengths) present.

However, wavelet analysis is an important extension of Fourier analysis as it provides the time local-

isation of the frequency components. This makes the wavelet analysis ideal for analysing time series where one expects localised variations of power. This analysing technique is used in many fields of physics that involve the study of (non-stationary) time series: acoustic, geophysics, helioseismology. Vigouroux & Delache (1993) make a comparison between Fourier and wavelet analysis of the solar diameter variability. Wavelet analysis is a powerful technique which allows a local decomposition of timescales in the time series of non-stationary processes. It is being applied increasingly to a range of astrophysical data.

Wavelet analysis has been used for analysing solar time series data before; Aschwanden et al. (1998) used wavelets to examine power law like behaviour in time series of hard X-ray solar flares, Frick et al. (1997) analysed the variability of the solar cycle in time while Bocchialini and Baudin (1994) examined the frequency and duration of chromospheric quiet Sun velocity oscillations. Komm (1994) applied a wavelet analysis to magnetograms of quiet and active Sun. More recently, Mészárosová et al. (1999) used a Fourier and wavelet analysis of type 42SER and 41F solar radio burst for which they found dominant periodicities in the 40-3 s interval. Gallagher et al. (1999) used a wavelet analysis to show an apparent periodicity in pulse like transient brightenings in the Quiet Sun network and the presence of a 3-minute oscillatory pattern in the intra-network regions, both in the chromospheric He I and the transition region O V lines. Ireland et al. (1999a) used wavelets to look for wave packets in active region CDS observations and Ireland et al. (1999b) analysed coronal heating events in high cadence TRACE data. Recently, Banerjee et al. (2000), used both Fourier and wavelet transforms to analyse spectral times series obtained by CDS and reported on the existence of oscillations with periods of 20–25 minutes in polar plumes.

In this chapter we investigate how a wavelet analysis can be used to find out more about the coronal plasma through which observed wave-like oscillations are propagating. The key point is that a detailed use of wavelet transforms can provide valuable diagnostic information through coronal seismology. We base this study on the results of the previous chapters. There phase mixing of Alfvén waves in a stratified and radially diverging, open atmosphere was studied in detail. Although slow magneto-acoustic waves seem to be observed more frequently, theoretical details of propagation of Alfvén waves are better known and many of its properties should transfer to slow waves propagating along magnetic field lines. We will start with a brief introduction to wavelet analysis and more details on some basic properties.

4.1.1 Comparison with the Fourier transform

The Fourier transform decomposes any periodic function into a set of orthonormal basis functions of sines and cosines. The coefficients of the basis functions represent the contribution of the sine

and cosine components of the function at all frequencies. The Fourier transform of a function $f(x)$ is defined as

$$F(s) = \int_{-\infty}^{\infty} f(x) \exp(-i2\pi sx) dx \,, \tag{4.1}$$

where the inverse transform is given by

$$f(x) = \int_{-\infty}^{\infty} F(s) \exp(i2\pi sx) ds \,, \tag{4.2}$$

so that

$$f(x) = \int_{-\infty}^{\infty} \left[\int_{-\infty}^{\infty} f(u) \exp(-i2\pi su) du \right] \exp(i2\pi sx) ds \,. \tag{4.3}$$

However, as we will usually be working with discrete data f_j, $j = 0, \ldots, N-1$, it is useful to introduce the discrete Fourier transform (DFT),

$$F_q = \frac{1}{N} \sum_{j=0}^{N-1} f_j \exp(-i2\pi jq/N) \,, \tag{4.4}$$

which estimates the Fourier transform of a function from a finite number of sampled points. Its inverse is given by

$$f_j = \frac{1}{N} \sum_{q=0}^{N-1} F_q \exp(i2\pi jq/N) \,. \tag{4.5}$$

The fast Fourier transform (FFT) is a DFT (computational) algorithm, developed by Cooley and Turkey in 1965, which reduces the number of computations from the order of N^2 to $N \log N$.

So both the FFT and the wavelet transform of a function can be thought of as a transformation to a different domain. For the FFT, the basis functions of this new domain are sines and cosines and for the wavelet transform, the basis functions are more complicated functions called wavelets. Before we explain the wavelet analysis in more details, we illustrate the difference between the fast Fourier transform and the wavelet analysis using the following signals (Figure 4.1),

$$\text{signal1} = \cos(2\pi 10t) + \cos(2\pi 25t) + \cos(2\pi 50t) + \cos(2\pi 100t) \tag{4.6}$$

$$\text{signal2} = \begin{cases} \cos(2\pi 10t) & 0 \le t \le 1/4 \\ \cos(2\pi 25t) & 1/4 < t \le 2/4 \\ \cos(2\pi 50t) & 2/4 < t \le 3/4 \\ \cos(2\pi 100t) & 3/4 < t \le 1 \end{cases} . \tag{4.7}$$

Signal1 is a stationary signal, because it has frequencies 10, 25, 50 and 100 Hz at any given instant in time. Signal2 is a non-stationary signal with the same frequencies occurring at different time intervals.

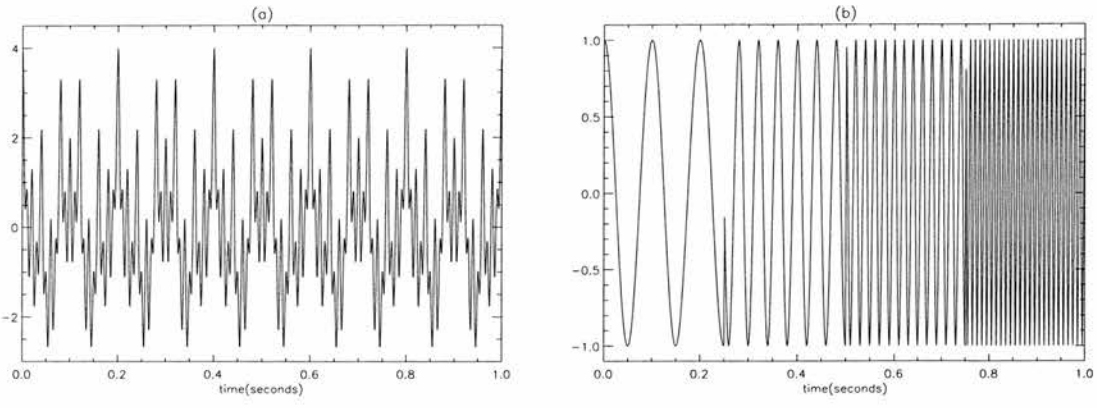

Figure 4.1: Plot of (a) signal1 and (b) signal2.

To work out the Fourier transform of signal1, we work out the transform of a general function $f(t) = \cos lt$,

$$\begin{aligned} F(s) &= \int_{-\infty}^{\infty} f(t)e^{-2\pi its}dt \\ &= \int_{-\infty}^{\infty} \cos(lt)e^{-2\pi its}dt \\ &= \frac{1}{2}\int_{-\infty}^{\infty} (e^{ilt} + e^{-ilt})e^{-2\pi its}dt \\ &= \frac{1}{2}\int_{-\infty}^{\infty} (e^{2\pi it(\frac{l}{2\pi}-s)} + e^{-2\pi it(\frac{l}{2\pi}+s)})dt\,. \end{aligned} \tag{4.8}$$

The second term on the right hand side is very small compared to the first term and only reaches its maximum value for $s = -l$ which is negative. As s represents the period, we are only interested in positive values and thus, we will only consider the first term on the right hand site. Although we cannot solve this integral explicitly, we can get an idea of its behaviour from the following integral,

$$\begin{aligned} I &= \int_{-a}^{a} e^{2\pi i(\frac{l}{2\pi}-s)t}dt \\ &= \int_{-a}^{a} \cos(2\pi(\frac{l}{2\pi} - s)t)dt + 0 \\ &= \frac{2}{2\pi}(\frac{l}{2\pi} - s)^{-1} \sin 2\pi(\frac{l}{2\pi} - s)a\,. \end{aligned}$$

Therefore, when $s \neq \frac{l}{2\pi}$,

$$-\frac{1}{\pi}(\frac{l}{2\pi} - s)^{-1} \leq I \leq \frac{1}{\pi}(\frac{l}{2\pi} - s)^{-1}\,, \tag{4.9}$$

independently of the value of a. When $s = \frac{l}{2\pi}$,

$$I = 2a \to \infty \quad \text{as} \quad a \to \infty\,. \tag{4.10}$$

From Eqns. (4.9) and (4.10), we see that

$$I \sim \delta(\frac{l}{2\pi} - s)\,. \tag{4.11}$$

Combining Eqns. (4.8) and (4.11), we find that the Fourier transform of signal1 is given by

$$FT(signal1) \sim \delta(10-s) + \delta(25-s) + \delta(50-s) + \delta(100-s)\,. \tag{4.12}$$

For signal2, the Fourier transform is given by

$$\begin{aligned} F(s) &= \int_0^{1/4} \cos(2\pi 10t) e^{-2\pi its} dt + \int_{1/4}^{1/2} \cos(2\pi 25t) e^{-2\pi its} dt + \\ &\qquad \int_{1/2}^{3/4} \cos(2\pi 50t) e^{-2\pi its} dt + \int_{3/4}^{1} \cos(2\pi 100t) e^{-2\pi its} dt\,. \end{aligned}$$

Using Equation (4.8), we calculate this transform by solving the following integral,

$$\begin{aligned} I &= \int_a^b e^{2\pi i(\frac{l}{2\pi} - s)t} dt \\ &= \int_a^b \cos(2\pi(\frac{l}{2\pi} - s)t) dt + i \int_a^b \sin(2\pi(\frac{l}{2\pi} - s)t) dt \\ &= \frac{1}{2\pi}(\frac{l}{2\pi} - s)^{-1} \left[\sin 2\pi(\frac{l}{2\pi} - s)b - \sin 2\pi(\frac{l}{2\pi} - s)a - i\cos 2\pi(\frac{l}{2\pi} - s)b + i\cos 2\pi(\frac{l}{2\pi} - s)a \right]. \end{aligned}$$

Therefore, the Fourier transform of signal2 is given by

$$\begin{aligned} FT(signal2) = \frac{1}{2\pi} \Bigg\{ & (10-s)^{-1} \left[\sin\frac{2\pi}{4}(10-s) - i\cos\frac{2\pi}{4}(10-s) + i \right] \\ + \; & (25-s)^{-1} \left[\sin\pi(25-s) - \sin\frac{\pi}{2}(25-s) - i\cos\pi(25-s) + i\cos\frac{\pi}{2}(25-s) \right] \\ + \; & (50-s)^{-1} \left[\sin\frac{3\pi}{2}(50-s) - \sin\pi(50-s) - i\cos\frac{3\pi}{2}(50-s) + i\cos\pi(50-s) \right] \\ + \; & (100-s)^{-1} \Bigg[\sin 2\pi(100-s) - \sin\frac{3\pi}{2}(100-s) \\ & \qquad - i\cos 2\pi(100-s) + i\cos\frac{3\pi}{2}(100-s) \Bigg] \Bigg\}\,. \end{aligned} \tag{4.13}$$

Figure 4.2 shows the frequency spectrum for both signals from a Fourier analysis and confirms the results of Eqns. (4.12) and (4.13) The dotted line in Figure 4.2(b) is the analytically calculated Fourier Transform of signal2 (see Eqn. (4.13)). Both plots show the same frequencies, i.e. 10, 25, 50 and 100 Hz for both signals which is indeed correct as both signals have the same frequency components. However, the first signal has these frequencies at all times where as the second signal has these frequencies at different time intervals. The Fourier analysis gives us no information on the time localisation of the frequency components, except for the broadening of the peaks. For a non-stationary signal, a time-frequency analysis is needed and the wavelet transform is a transform of this type.

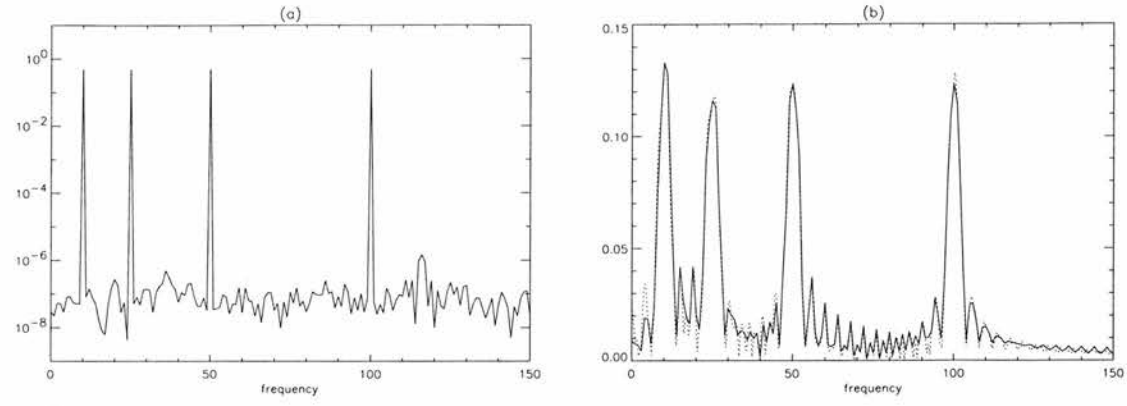

Figure 4.2: Fourier analysis of (a) signal1 and (b) signal2. The dotted line is the analytical result from Eqn. (4.13).

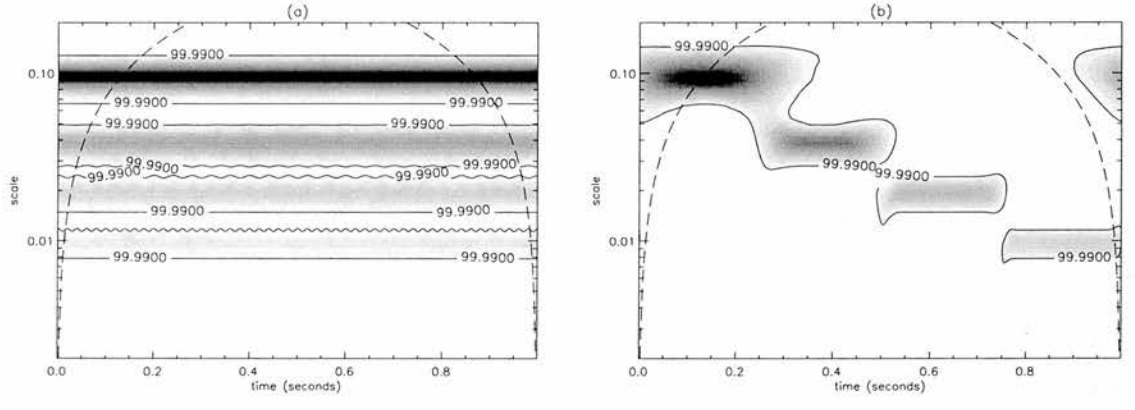

Figure 4.3: Wavelet analysis of (a) signal1 and (b) signal2.

Figure 4.3 shows the results of a wavelet analysis of the 2 signals. The scale on the vertical axis corresponds to the inverse of the frequency. It is now clear that the four frequency components are present at all times in signal1 but occur at different time intervals in signal2. So the wavelet analysis does tell us which frequency components are present in a given signal and when these components occur in time.

4.2 Wavelet Transform

In this section, we will give an overview of the method of wavelet analysis but for further details we refer the reader to Farge (1992) and Torrence & Compo (1998). The continuous wavelet transform of a function $f(t)$ is defined as the convolution of $f(t)$ with an analysing function $\psi(\eta)$. To be called

a wavelet, the analysing function must be localised both in time and frequency space and should be admissible, which, for an integrable function, means that its average should be zero (Farge 1992). We also assume that ψ is normalised, i.e. $\int_{-\infty}^{\infty} \psi\psi^* d\eta = 1$, where ψ^* is the complex conjugate. For $\eta = (t' - t)/s$ we have

$$W(t,s) = \int_{-\infty}^{\infty} f(t') \frac{1}{\sqrt{s}} \quad \psi^* \left[\frac{(t'-t)}{s} \right] dt' \,, \tag{4.14}$$

where t is time and s is the wavelet scale. The factor $\frac{1}{\sqrt{s}}$ is necessary to satisfy the normalisation condition taken as

$$\int_{-\infty}^{\infty} \psi \left[\frac{(t'-t)}{s} \right] \psi^* \left[\frac{(t'-t)}{s} \right] dt' = s \,.$$

For a discrete time series x_n of N observations with sample interval δt, the wavelet transform is given by

$$W_n(s) = \sum_{n'=0}^{N-1} x_{n'} \sqrt{\frac{\delta t}{s}} \psi^* \left[\frac{(n'-n)\delta t}{s} \right] \,, \tag{4.15}$$

where s is the wavelet scale and n allows us to translate the analysing wavelet in time. In this case, the factor $\sqrt{\frac{\delta t}{s}}$ ensures that the normalisation condition is satisfied. The wavelet transforms at each scale s are now directly comparable to each other and to transforms of other time series. By varying s and n, one can build up a picture of any features in the time series as a function of the scale s and the localised time index n. If a Fourier transform is taken of the data, so that

$$\hat{x}_j = \frac{1}{N} \sum_{n=0}^{N-1} x_n e^{-2\pi i j n/N} \,, \tag{4.16}$$

where $j = 0 \ldots N-1$ is the frequency index, then the wavelet transform can also be written as,

$$W_n(s) = \sum_{k=0}^{N-1} \hat{x}_j \sqrt{\frac{2\pi s}{\delta t}} \hat{\psi}^*(s\omega_j) e^{i\omega_j n \delta t} \tag{4.17}$$

where $\hat{\psi}$ is the Fourier transform of the function ψ and where the angular frequency is defined as

$$\omega_j = \begin{cases} \frac{2\pi j}{N\delta t} & \text{if } j \leq \frac{N}{2} \\ -\frac{2\pi j}{N\delta t} & \text{if } j > \frac{N}{2} \,. \end{cases} \tag{4.18}$$

Using Eqn. (4.17) and a standard Fast Fourier Transform (FFT) routine, the continuous wavelet transform for a given s can be calculated at all n simultaneously. The wavelet power spectrum is defined as $|W_n(s)|^2$. Ranging through s and n will build up a two-dimensional time-frequency transform of the original time series (Figure 4.5). As the Fourier transform in Eqn. (4.17) assumes the data is periodic, 'wrap around' errors will occur at both edges of the transform when one is dealing with time series of finite length. One possible solution to this problem is to pad the end of

the time series with zeros before doing the wavelet transform. Unless otherwise stated, all solutions in this chapter are obtained using a numerical code, based on Eqn. (4.17), as numerically it is considerably faster to do the calculations for all n simultaneously in Fourier space. Whenever analytical approximations are calculated, they are based on Eqn. (4.15).

The choice of the appropriate analysis (or mother) wavelet depends on the nature of the signal and on the kind of information we want to extract from the signal. In our analysis, we will use the (complex-valued) Morlet wavelet,

$$\psi(\eta) = \pi^{-1/4} \exp(ik\eta) \exp\left(-\frac{\eta^2}{2}\right), \tag{4.19}$$

consisting of a plane wave modulated by a Gaussian, as our mother wavelet (Figure 4.4).

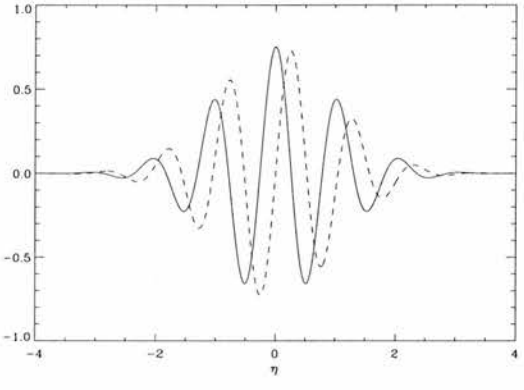

Figure 4.4: Real (solid line) and imaginary (dashed line) part of the Morlet wavelet with $k = 6$.

Now we have chosen a mother wavelet, we need to choose a set of scales s to use in the wavelet transformation. Following Torrence & Compo (1998), we take

$$s_j = s_0 2^{j\delta j}, \qquad j = 0, 1, \ldots, J \tag{4.20}$$

where,

$$J = \delta j^{-1} \log_2(N\delta t/s_0)\,. \tag{4.21}$$

Here $s_0 = 2\delta t$ is the smallest scale and J determines the largest scale. The value of δj is chosen to be 0.125.

Because we work with finite time series, the wavelet transform suffers from edge effects at both ends of the time series. This results in a *cone of influence* in the transform, indicated as a dashed line in all the figures. The cone of influence represents a measure of where the edge of the finite sample data has affected the analysis. As in Torrence & Compo (1998), the COI is defined so that the wavelet power for a discontinuity at the edges decreases by a factor e^{-2}. Portions of the transform

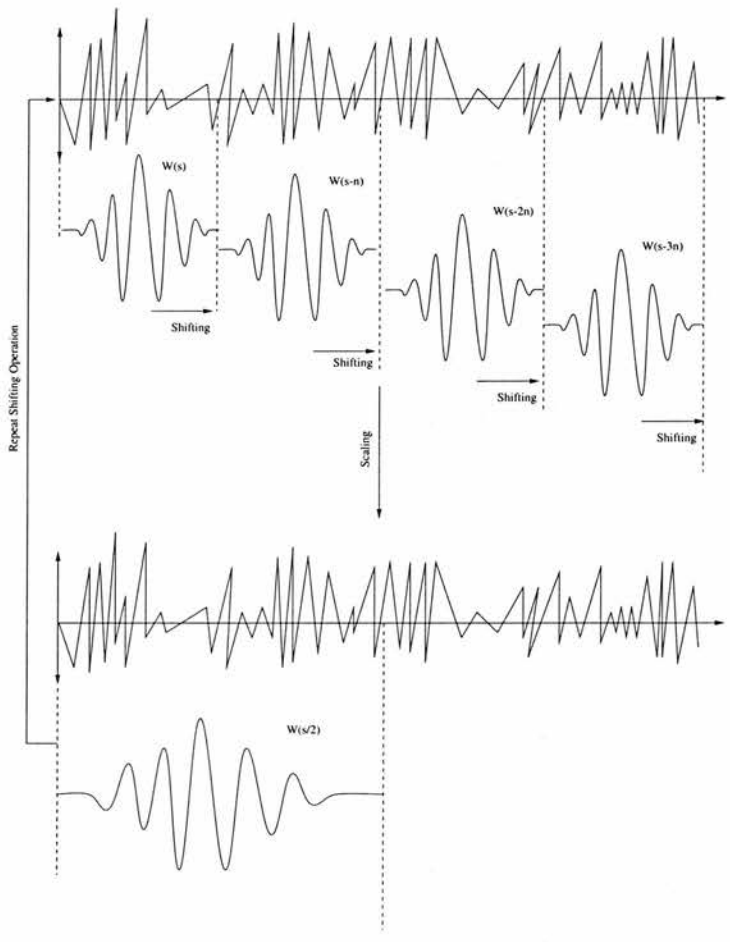

Figure 4.5: The scaling and shifting process of the wavelet transform.

that are outside the area formed by the 'time' axis and the cone of influence are subject to these edge effects and are therefore unreliable. The edge effects are more pronounced at larger scales as the influence of each wavelet extends further in time and larger parts of the discontinuities will enter the analysis. Overall, errors in the transform near the edges will be a combination of edge effects and the wrap-around of the Fourier transform.

4.2.1 Significance levels

To put a confidence level in the analysis, we assume that the noise in our TRACE data (see Chapter 5) follows a Poisson distribution, i.e. if N counts are observed then the Poisson noise in such measurement is $\sigma_{noise} = \sqrt{N}$. Assuming a Poisson distribution for the noise in the data, it can be shown (Doyle et al. 1997; Torrence & Compo 1998) that the distribution for the local wavelet power is

$$\frac{|W_n(s)|^2}{\sigma^2_{noise}} \rightarrow \frac{1}{2}\chi^2_2 ,$$

at each time n and scale s, where χ^2_2 is the χ^2-distribution with two degrees of freedom. The probability that the noise power level P_{noise} exceeds a threshold power level $P_{treshold}$ is (Doyle et al. 1997)

$$\text{Prob}(P_{noise} > P_{treshold}) = Q(P_{treshold}|2)\,,$$

with Q the integral probability of the χ^2-distribution

$$Q(\chi^2|v) = \left(2^{v/2}\Gamma(\frac{v}{2})\right)^{-1} \int_{\chi^2}^{\infty} t^{v/2-1}e^{-t/2}dt\,.$$

Now define $(1-\epsilon)$ as the probability that the local wavelet power exceeds a detection level P_{det} and is *not* caused by noise. This means that the chance for some power to exceed P_{det} and to be caused by noise is $1-(1-\epsilon)$ and it follows that the detection level is given by

$$\epsilon = Q(P_{det}|2)\,,$$

or that $P_{det} - 2\ln(1/\epsilon)$. We chose a 99.0% (or 99.9%) confidence level in our analysis above which we consider any wavelet power as real. Therefore, when

$$\frac{|W_n(s)|^2}{\sigma^2_{noise}} > \ln(1/\epsilon)\,,$$

there is a 1.0% (or 0.1%) chance that this is due to chance. This allows us to calculate 99% confidence contour level in the wavelet transform, indicated as a solid line in all the figures. A more detailed explanation of these statistical properties can be found in Leahy et al. (1983).

4.2.2 Frequency and temporal resolution

We now try to get a deeper understanding of the wavelet analysis and its basic properties, such as its time and scale resolution. Therefore, we calculate the wavelet transform of some basic and simple functions analytically. This will tell us how the value of the parameter k in Eqn. (4.19) affects the resolution of the transform, which will help us chosing an appropriate value for k. We start by working out the wavelet power spectrum $|W|^2$ for the harmonic wave $f(t) = \cos lt$.

$$W(t,s) = \frac{\pi^{-1/4}}{\sqrt{s}}\frac{1}{2}\int_{-\infty}^{\infty}(e^{ilt'} + e^{-ilt'})e^{-ik\frac{(t'-t)}{s}}e^{-\frac{(t'-t)^2}{2s^2}}dt'\,. \tag{4.22}$$

Now set $\eta = \frac{t'-t}{s}$, which implies $dt' = sd\eta$ and $t' = t + s\eta$.

$$\begin{aligned}
W(t,s) &= \frac{\pi^{-1/4}}{\sqrt{s}}\frac{s}{2}\int_{-\infty}^{\infty}(e^{ilt}e^{ils\eta} + e^{-ilt}e^{-ils\eta})e^{-ik\eta}e^{-\eta^2/2}d\eta \\
&= \pi^{-1/4}\frac{\sqrt{s}}{2}e^{ilt}\int_{-\infty}^{\infty}e^{i(ls-k)\eta}e^{-\eta^2/2}d\eta + \frac{s}{2}e^{-ilt}\int_{-\infty}^{\infty}e^{-i(ls+k)\eta}e^{-\eta^2/2}d\eta \\
&= \pi^{-1/4}\frac{\sqrt{s}}{2}\sqrt{2\pi}\left[e^{ilt}e^{-(ls-k)^2/2} + e^{-ilt}e^{-(ls+k)^2/2}\right] \\
&= \pi^{-1/4}\frac{\sqrt{s}}{2}\sqrt{2\pi}\left[\cos lt\left(e^{-(ls-k)^2/2} + e^{-(ls+k)^2/2}\right) + i\sin lt\left(e^{-(ls-k)^2/2} - e^{-(ls+k)^2/2}\right)\right]
\end{aligned}$$

The wavelet power is then given by

$$\begin{aligned}
|W|^2 &= \pi^{-1/2}\frac{s}{4}2\pi\left[\cos^2 lt\left(e^{-(ls-k)^2/2}+e^{-(ls+k)^2/2}\right)^2+\sin^2 lt\left(e^{-(ls-k)^2/2}-e^{-(ls+k)^2/2}\right)^2\right] \\
&= \pi^{1/2}\frac{s}{2}\left[e^{-(ls-k)^2}+e^{-(ls+k)^2}+(\cos^2 lt-\sin^2 lt)e^{-(ls-k)^2/2-(ls+k)^2/2}\right] \\
&= \pi^{1/2}\frac{s}{2}\left[e^{-(ls-k)^2}+e^{-(ls+k)^2}+\cos 2lt \quad e^{-l^2s^2-k^2}\right] \\
&\approx \pi^{1/2}\frac{s}{2} \quad e^{-(ls-k)^2}. \qquad (4.23)
\end{aligned}$$

For positive scales, this function has a maximum at $s=\frac{k+\sqrt{k^2+2}}{2l}$. The period will then be given by

$$P=\frac{2\pi}{l}=Fs\,, \qquad (4.24)$$

with $F=\frac{4\pi}{k+\sqrt{k^2+2}}$. So to extract the period of the signal from the wavelet analysis, we have to multiply the scales used in the analysis by this factor F. From this result, we also see that we will get a better scale (or frequency) resolution for larger values of k as the wavelet power behaves like a Gaussian function, centered around $s=\frac{k}{l}$. As illustrated in Figure 4.6, the Gaussian gets narrower for larger values of k which will results in a more accurate resolution of the period. As k gets smaller, the Gaussian curve becomes wider which implies a loss of scale resolution.

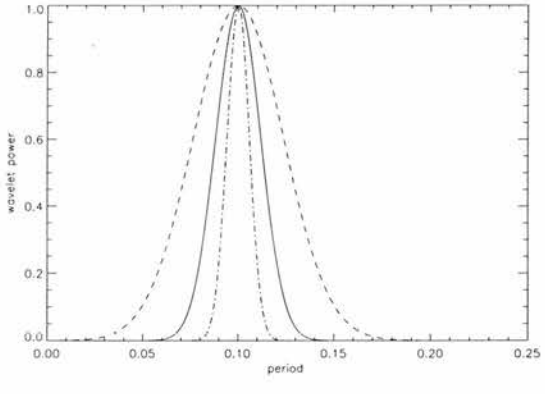

Figure 4.6: Wavelet power for $f(t)=\cos lt$ with $l=2\pi 10$ for different values of k; $k=3$ (dashed line), $k=6$ (solid line), $k=12$ (dot-dashed line).

As stated above, the analysing function must have zero mean to be admissible as a wavelet (Farge 1992). The Morlet wavelet is only marginally admissible as its average is given by $\sqrt{2}\pi^{1/4}e^{-k^2/2}$, which is never exactly zero. However, for $k=6$, the average is of the order of 3×10^{-8}. For larger values of k, the scale resolution is improved but at the same time, the temporal resolution is lost, which is why we choose the smallest value for k that makes the function admissible.

To illustrate this loss of temporal resolution analytically, we work out the wavelet power of the

function $f(t) = \cos(lt)$ for $0 \leq t \leq a$ and $f(t) = 0$ elsewhere,

$$W(t,s) = \frac{\pi^{-1/4}}{\sqrt{s}} \frac{1}{2} \int_0^a (e^{ilt'} + e^{-ilt'}) e^{-ik\frac{(t'-t)}{s}} e^{-\frac{(t'-t)^2}{2s^2}} dt' . \tag{4.25}$$

Again setting $\eta = \frac{t'-t}{s}$, we find

$$\begin{aligned}
W(t,s) &= \pi^{-1/4}\frac{\sqrt{s}}{2} \int_{-\frac{t}{s}}^{\frac{a-t}{s}} (e^{ilt}e^{ils\eta} + e^{-ilt}e^{-ils\eta}) e^{-ik\eta} e^{-\eta^2/2} d\eta \\
&= \pi^{-1/4}\frac{\sqrt{s}}{2} \left\{ e^{ilt} \int_{-\frac{t}{s}}^{\frac{a-t}{s}} e^{i(ls-k)\eta} e^{-\eta^2/2} d\eta + e^{-ilt} \int_{-\frac{t}{s}}^{\frac{a-t}{s}} e^{-i(ls+k)\eta} e^{-\eta^2/2} d\eta \right\} \\
&= \pi^{-1/4}\frac{\sqrt{s}}{2} \left\{ e^{ilt} \int_{-\frac{t}{s}}^{\frac{a-t}{s}} e^{-(ls-k)^2/2} e^{-\frac{(-i(ls-k)+\eta)^2}{2}} d\eta + e^{-ilt} \right. \\
&\qquad \left. \int_{-\frac{t}{s}}^{\frac{a-t}{s}} e^{-(ls+k)^2/2} e^{-\frac{(i(ls+k)+\eta)^2}{2}} d\eta \right\} \\
&= \pi^{-1/4}\frac{\sqrt{s}}{2} \left\{ e^{ilt} e^{-(ls-k)^2/2} \int_{-\frac{t}{s}}^{\frac{a-t}{s}} e^{-\frac{(-i(ls-k)+\eta)^2}{2}} d\eta + e^{-ilt} e^{-(ls+k)^2/2} \right. \\
&\qquad \left. \int_{-\frac{t}{s}}^{\frac{a-t}{s}} e^{-\frac{(i(ls+k)+\eta)^2}{2}} d\eta \right\} .
\end{aligned}$$

From now on we will ignore the second term on the left hand side as it will be very small compared to the first term and only reach its maximum value for $s \approx -\frac{k}{l}$ which is negative. As the scale represents the period, we are only interested in positive values of s. By setting $u = -i(ls-k) + \eta$ we find,

$$\begin{aligned}
W(t,s) &= \pi^{-1/4}\frac{\sqrt{s}}{2} e^{ilt} e^{-(ls-k)^2/2} \int_{-i(ls-k)-\frac{t}{s}}^{-i(ls-k)+\frac{a-t}{s}} e^{-u^2/2} du \\
&= \pi^{-1/4}\frac{\sqrt{s}}{2} e^{ilt} e^{-(ls-k)^2/2} \left[\int_0^{-i(ls-k)+\frac{a-t}{s}} e^{-u^2/2} du - \int_0^{-i(ls-k)-\frac{t}{s}} e^{-u^2/2} du \right] \\
&= \pi^{-1/4}\frac{\sqrt{s}}{\sqrt{2}} e^{ilt} e^{-(ls-k)^2/2} \frac{2}{\sqrt{\pi}} \left[\mathrm{erf}\left(-i\frac{ls-k}{\sqrt{2}} + \frac{a-t}{\sqrt{2}s} \right) \right. \\
&\qquad \left. -\mathrm{erf}\left(-i\frac{ls-k}{\sqrt{2}} - \frac{t}{\sqrt{2}s} \right) \right] \\
&= \sqrt{s}(\cos lt + i \sin lt) e^{-(ls-k)^2/2} \frac{\sqrt{2}}{\pi^{3/4}} \left[\mathrm{erf}\left(-i\frac{ls-k}{\sqrt{2}} + \frac{a-t}{\sqrt{2}s} \right) \right. \\
&\qquad \left. -\mathrm{erf}\left(-i\frac{ls-k}{\sqrt{2}} - \frac{t}{\sqrt{2}s} \right) \right] ,
\end{aligned}$$

where $\mathrm{erf}(x)$ is the Error function (Abramowitz & Stegun, 1965). As we are interested in the effect the value of k has on the temporal resolution of the maximum of the wavelet power, we set $s \approx \frac{k}{l}$. The wavelet power is then given by,

$$|W|^2 = \frac{k}{l} \frac{2}{\pi^{3/2}} \left[\mathrm{erf}\left(l\frac{a-t}{\sqrt{2}k} \right) + \mathrm{erf}\left(\frac{lt}{\sqrt{2}k} \right) \right]^2 .$$

In Figure 4.7(a) and (b), we have plotted the wavelet power for the function $f(t) = \cos(lt)$ for $0 \leq t \leq a$ and $f(t) = 0$ elsewhere, for different values of k and a. We see that as k gets smaller, the Error function gets narrower which implies that the time resolution gets better. For larger values of k, the Error function becomes more and more spread out and the estimated time can be wrong with a factor of 2 or more. We also note that the loss of temporal resolution for larger k is stronger for smaller values of a.

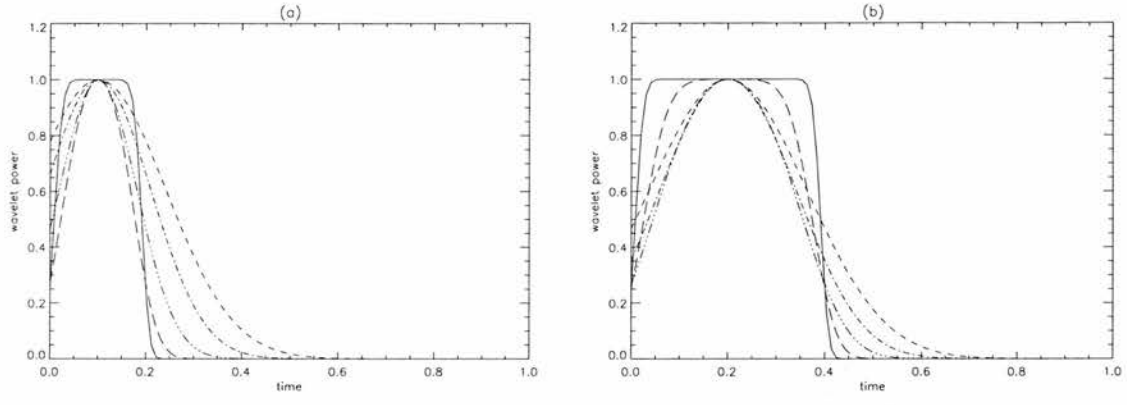

Figure 4.7: Normalised wavelet power for $f(t) = \cos lt$ for $0 \leq t \leq a$ and $f(t) = 0$ elsewhere with (a) $a = 0.2$ and (b) $a = 0.4$, with $l = 2\pi 10$ for different values of k; $k = 1$ (solid line), $k = 3$ (long dashed line), $k = 6$ (dot-dot-dashed line), $k = 9$ (dot-dashed line), $k = 12$ (dashed line).

The loss of the scale resolution for small k and the temporal resolution for large k is illustrated using signal2 (see above) in Figure 4.8. From Figure 4.8(a) we see that we have a very accurate time resolution for small values of k while a larger value of k (Figure 4.8(c)) gives a very good scale resolution. Taking k=6 (Figure 4.8(b)) gives us a suitable compromise between time and scale resolution. So, from now on we will set $k = 6$ in the Morlet wavelet (Eq. 4.19).

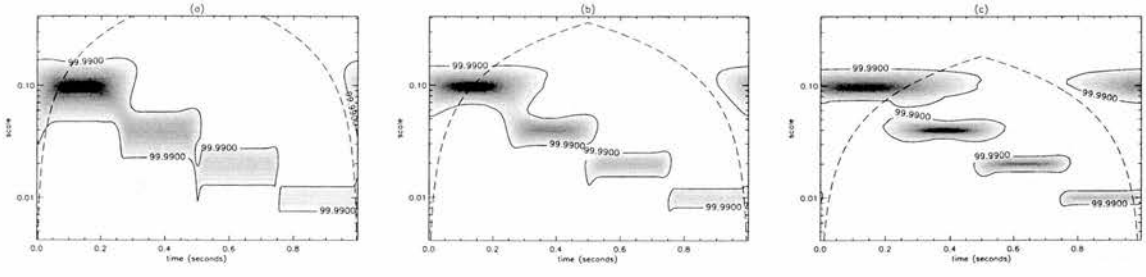

Figure 4.8: Wavelet analysis of the signal2 (Eqn. (4.7)) for different values of k; (a) $k = 3$, (b) $k = 6$ and (c) $k = 12$.

4.2.3 Wavelet analysis of Solar Cycle

As a final example, we investigate the wavelet transform of the annual sunspot numbers, from which we expect to find the well known 11-year solar cycle.

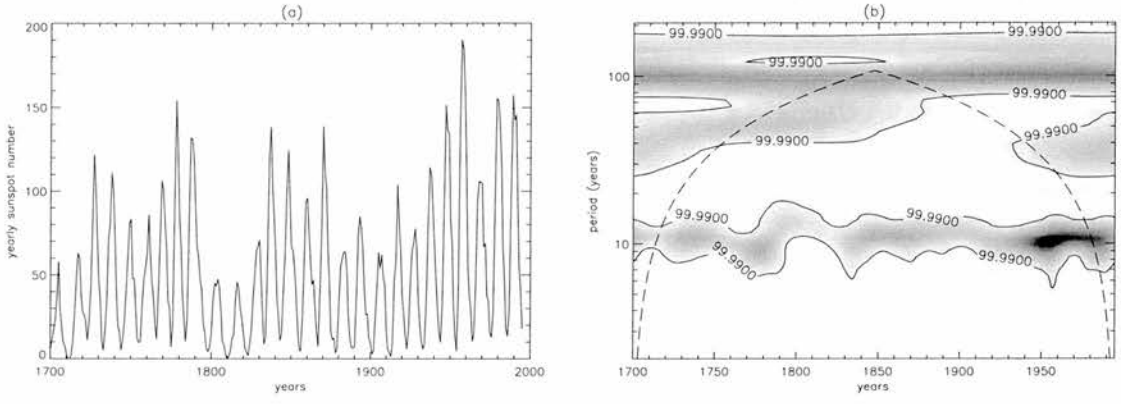

Figure 4.9: (a) Overview of yearly sunspot numbers between 1700 and 1995 and (b) results of the wavelet analysis

In Figure 4.9(a) we have plotted the annual sunspot numbers between 1700 and 1995. Figure 4.9(b), shows the results of the wavelet analysis of this timeseries. We notice that there are 2 distinct regions of wavelet power, one which corresponds to the 11-year (or Schwabe) cycle and a second one that indicates the 100-year (or Gleissberg) cycle. The deviation of the 11-year cylce length that is present around 1800, occurs during the so-called Dalton minimum (1790 – 1820). For a more detailed (wavelet) analysis of the solar cylce, see Frick et al. (1997). However, this simple and well known example illustrates that wavelet analysis could be a very useful tool to analyse observational data.

4.3 Wavelet analysis of phase mixed Alfvén waves

Till now, we have analysed the wavelet transforms of a time series $f(t)$. However, it is also possible to take the wavelet transform of functions depending on spatial variables, rather than time. All results with respect to time and frequency resolution still apply and can now be though of as space and wavelength resolution. Using a wavelet analysis on phase mixed Alfvén waves, we now demonstrate that there is a distinct signature of phase mixing in the wavelet transform. Using this signature, it is possible to extract information from the wavelet transform about the physical surroundings in which the waves are propagating. Phase mixing in a stratified and radially diverging, open atmosphere was studied in detail in the previous chapters of this thesis. The effect of dissipation, stratification

and divergence on phase mixing of Alfvén waves was described using both numerical and WKB solutions. In this chapter we will use the approximate WKB solutions for phase mixed Alfvén waves in a diverging and gravitationally stratified atmosphere. For the derivation of these solutions, we refer the reader to appendix A. What is important here is not that we are analysing Alfvén waves as such but to show how wavelet analysis can provide valuable information about the coronal plasma. Slow and fast MHD waves will exhibit similar characteristics but cannot be treated in such a simple manner.

Including viscosity, the WKB solution for the perturbed velocity $\mathbf{v}$, in spherical (dimensionless) coordinates, is given by

$$v \approx \exp\left(-i\frac{2\pi r_0}{\lambda_0}K(\theta)R\right)\exp\left[\frac{1}{4H}\left(1-\frac{1}{r}\right)-\right.$$
$$\left.\frac{1}{2}\Lambda_\nu^2\Omega\left(\frac{2\pi r_0}{\lambda_0}\right)^3 K(\theta)\int_1^r\left(\theta_0^2 r^6 e^{-\frac{1}{2H}\left(1-\frac{1}{r}\right)}+\frac{K'(\theta)^2}{K(\theta)^2}R^2 e^{\frac{1}{2H}\left(1-\frac{1}{r}\right)}\right)dr\right], \quad (4.26)$$

with $R = \int_1^r r^2 e^{-\frac{1}{2H}\left(1-\frac{1}{r}\right)}dr$ and $\Lambda_\nu^2 = \frac{\rho_0\nu\Omega_0\mu}{B_0^2}\left(\frac{\lambda_0}{2\pi r_0\theta_0}\right)^2$ and where, for example, $K(\theta) = (1+\delta\cos(m\pi\theta))^{-1/2}$. The parameter δ regulates the magnitude of the equilibrium density variation, which causes phase mixing to occur. The radial distance r and the pressure scale height H are measured in units of the solar radius r_0. All the results described in this paper are obtained with $\delta = 0.5$. If one wants to study each physical effect separatly, gravitational stratification can be eliminated by setting the pressure scale height to infinity, i.e. $1/H = 0$. The spherical geometry allows the effect of flux tube divergence to be studied. If necessary, at low heights, i.e. $r \approx 1$ and for small initial wavelengths λ_0 the non-diverging Cartesian case can be retrieved by setting

$$r = 1 + \frac{\lambda_0}{2\pi r_0}z \qquad \text{and} \qquad x = r\theta\,. \quad (4.27)$$

The solution is in Cartesian coordinates is thus given by,

$$v = \sin(\pi x)e^{\frac{-z}{4Hc}}\exp(-iKZ)\exp\left(\frac{1}{2}\Lambda_\nu^2\Omega\frac{K'^2}{K}(2H_c)^3\left[\frac{z}{H_c}-2\sinh\left(\frac{z}{2H_c}\right)\right]\right), \quad (4.28)$$

with $Z = 2H_c\left(1-e^{\frac{z}{2H_c}}\right)$ and $\Lambda_\nu^2 = \frac{\rho_0\nu\Omega_0\mu}{B_0^2}\left(\frac{z_0}{x_0}\right)^2$. The Cartesian coordinates have been made dimensionless by setting $x_0 = r_0\theta_0$ and $z_0 = \lambda_0/2\pi$. We will calculate the WKB solution between $r = 1$ and $r = r_{max}$ in solar radii, or in Cartesian coordinates, between $z = 0$ and $z = z_{max}$ and θ (or x) between 0 and 1. As we are mainly interested in the behaviour of the waves as they propagate up in height, we will be looking at cross sections of the wavefront at $\theta = 0.5$ or, in Cartesian coordinates, $x = 0.5$.

Gravitational stratification was found to generate longer wavelengths and therefore phase mixing is less efficient and heat is deposited into the plasma at higher heights compared to a purely diverging

atmosphere without stratification. At the same time the divergence results in shorter wavelengths which enhances phase mixing and heat is deposited at lower heights compared to a non-diverging atmosphere. So, compared to the original, uniform and unstratified Heyvaerts & Priest (1983) solution, phase mixing can be more or less efficient depending on the value of the scale height H. Finally, as an example we show the Fourier transform of a phase mixed Alfvén wave in a gravitationally stratified atmosphere in Figure 4.10 (for the original signal, see Figure 4.15). It is clear that the Fourier transform is not able to tell us anything about the basic wavelength or about the way the wavelength changes as the wave propagates up with height. It will become clear in the next sections that a wavelet analysis can provide a lot more information.

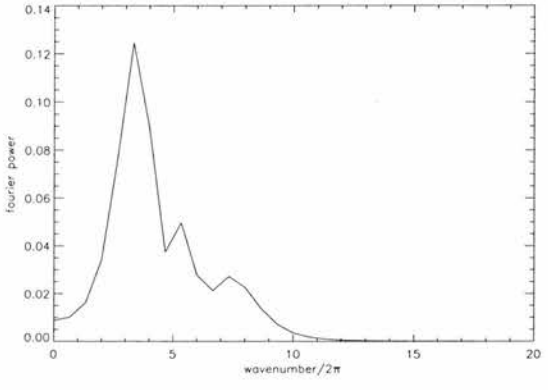

Figure 4.10: Fast Fourier transform of the perturbed velocity at $x = 0.5$ in a stratified, non-dissipative plasma, with $H = 0.5$.

4.3.1 Finite wave Trains

Considering the wavelet transform of a phase mixed wave in a uniform and unstratified plasma, i.e. with no gravitational stratification or radially divergence, as studied by Heyvaerts & Priest (1983). As the wave propagates up in height, dissipation by phase mixing will occur and the amplitude of wave will decrease to zero and the signal can thus be thought of as a finite wave. The perturbed velocity can be obtained from Eqn. (4.26) by taking the Cartesian limit and setting $1/H = 0$ and is given by

$$v \approx \exp(-iK(x)z) \exp\left(-\frac{\Lambda_\nu^2}{6}\frac{K'(x)^2}{K(x)}z^3\right), \tag{4.29}$$

The wavelet power is calculated by working out the integral

$$W(z,s) = \frac{\pi^{-1/4}}{\sqrt{s}} \int_0^{z_{max}} e^{-iK(x)z'} e^{-\varepsilon z'^3} e^{-ik\frac{(z'-z)}{s}} e^{-\frac{(z'-z)^2}{2s^2}} dz', \tag{4.30}$$

where $\varepsilon = \frac{\Lambda_\nu^2}{6}\frac{K'(x)^2}{K(x)}$ and z_{max} is the upper boundary of the computational or observational window. Rewritting this integral as

$$W(z,s) = \frac{\pi^{-1/4}}{\sqrt{s}} e^{-iK(x)z} \int_0^{z_{max}} e^{-iK(x)s\frac{z'-z}{s}} e^{-\varepsilon s^3\left(\frac{z'-z}{s}+\frac{z}{s}\right)^3} e^{-ik\frac{z'-z}{s}} e^{-\frac{(z'-z)^2}{2s^2}} dz' , \tag{4.31}$$

and setting $\eta = \frac{z'-z}{s}$, we find,

$$W(z,s) = \pi^{-1/4}\sqrt{s} e^{-iK(x)z} \int_0^{\frac{z_{max}-z}{s}} e^{-i(k+K(x)s)\eta} e^{-\varepsilon s^3(\eta+\frac{z}{s})^3} e^{-\frac{\eta^2}{2}} d\eta . \tag{4.32}$$

As

$$e^{-3\varepsilon z^2 s\eta} \ll e^{-i(k+K(x)s)\eta} \qquad \text{and} \qquad e^{-3\varepsilon\ s^2\eta^2} \ll e^{-\frac{\eta^2}{2}} , \tag{4.33}$$

and

$$e^{-\varepsilon s^3\eta^3} \approx 1 , \tag{4.34}$$

we can set

$$e^{-\varepsilon s^3(\eta+\frac{z}{s})^3} \approx e^{-\varepsilon z^3} . \tag{4.35}$$

The wavelet power is then approximately given by

$$W(z,s) \approx \pi^{-1/4}\sqrt{s} e^{-iK(x)z} e^{-\varepsilon z^3} \int_0^{\frac{z_{max}-z}{s}} e^{-i(k+K(x)s)\eta} e^{-\frac{\eta^2}{2}} d\eta . \tag{4.36}$$

The integral we are now left with is the one we worked out for the finite harmonic wave. As above, the wavelet power will reach its maximum at $s_{max} \approx \frac{k}{K(x)}$ and is given by

$$|W|^2 \approx \frac{k}{K(x)}\frac{4}{\pi^{3/2}} e^{-2\varepsilon z^3}\left[\mathrm{erf}\left(\frac{(z_{max}-z)K(x)}{\sqrt{2}k}\right) + \mathrm{erf}\left(\frac{zK(x)}{\sqrt{2}k}\right)\right]^2 , \tag{4.37}$$

where $k = 6$. We want to compare these damped waves with a truly finite wave, i.e. a harmonic oscillation with the same wavelength $\lambda = 0.1$, that is cut off after a certain height. If there are distinct signatures in the wavelet transform that tell us the difference between both 'finite' signals, it might be possible to find out more about the involved dissipation mechanism when finite wave-like perturbations are observed.

Figure 4.11 show the two finite signals we will be comparing. The harmonic signal in Figure 4.11 (a) is cut off after a height $1.75R_o$ while the signal in Figure 4.11 (b) is dissipated by phase mixing, i.e. by setting the dissipation coefficient $\Lambda_\nu^2 = 10^{-4}$ in Eqn. (4.29) and taking a cross-section at $x = 0.5$. We now investigate whether the wavelet transform can indicate the difference between these two different signals.

The wavelet transform of the two different finite signals is displayed in Figure 4.12. Both transforms indicate that an oscillation with a wavelength $\lambda = 0.1$ is present in the lower half of the region. As expected, we see that the wavelet power in the case of the damped wave (Figure 4.12 (b)) decreases more gradually than in the case of the finite harmonic wave (Figure 4.12 (a)).

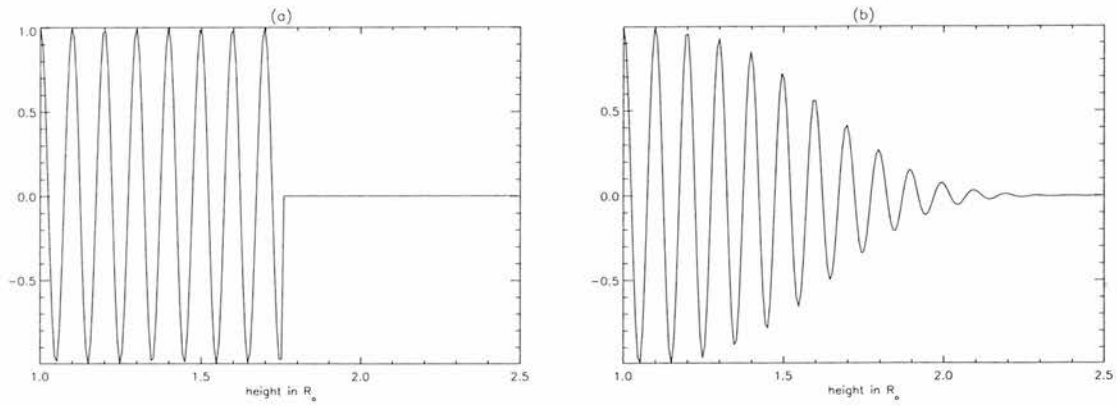

Figure 4.11: (a) A harmonic oscillation with basic wavelength $\lambda = 0.1$, cut off after a height $1.75R_o$. (b) A cross-section at $x = 0.5$ of the perturbed velocity, calculated from Eqn. (4.29), with $\Lambda_\nu^2 = 10^{-4}$.

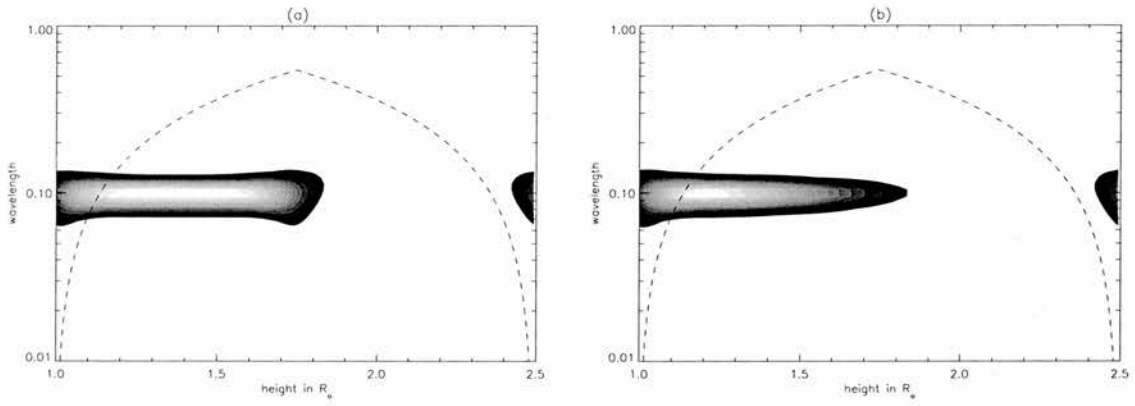

Figure 4.12: (a) and (b) Corresponding wavelet transforms of the signals displayed in Figure 4.11. The dashed lines indicate the cone of influence.

But although there is some difference between the respective transforms, this difference is much clearer in Figure 4.13. Here we plot a cross-section of the wavelet transform as a function of height, at its maximum power, i.e. at a wavelength $\lambda = 0.1$. The wavelet power in these figures has been normalised with respect to its maximum value. The power in Figure 4.13 (a) drops steeply to zero once the signal is cut off, while the power in Figure 4.13 (b) decreases more gradually as the amplitude of the signal is damped. Using the wavelet transform, it is possible to distinguish between a signal that switches off suddenly and a signal that is damped more gradually. Additionally, the steepness of the slope of the transform in Figure 4.13 (b) indicates how strongly the wave is damped.

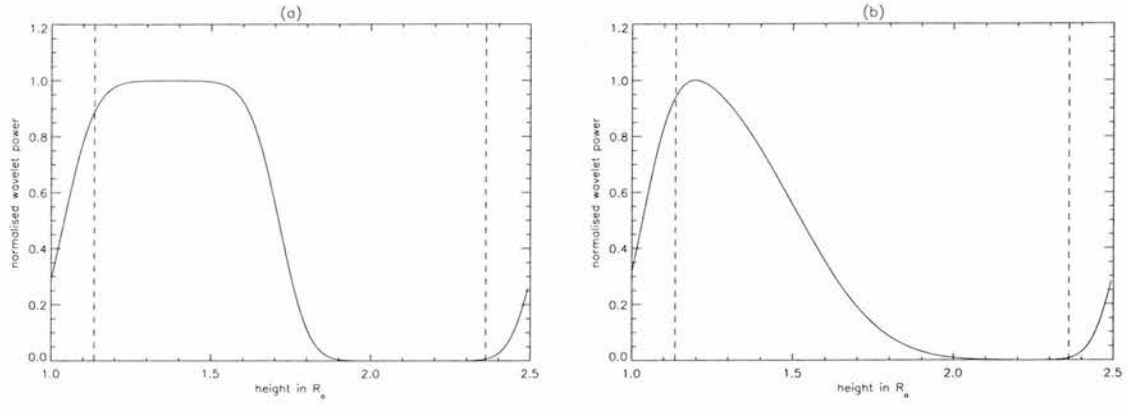

Figure 4.13: Cross-section of the (normalised) wavelet power at maximum wavelet power, i.e. at $\lambda = 0.1$ for (a) the finite harmonic wave and (b) for the phase mixed Alfvén wave. The dashed lines indicate the cone of influence.

4.3.2 Wave dissipation

In the previous section we have seen it is possible to tell from the wavelet transform that a signal is dissipated. We now try to find out more about the involved dissipation mechanism, from the wavelet analysis. If we look carefully at Eqn. (4.37), we see that the wavelet power is approximately damped as $-\varepsilon z^3$, exactly the same as the phase mixed wave. If we can fit this analytical expression to the wavelet transform of an observed signal, this might imply that the observed signal is dissipated by phase mixing which means there must be an inhomogeneity in the background density. It will then also be possible to extract the value of the dissipation coefficient from the slope of the cross-section at the basic wavelength of the wavelet transform. As the value of the coronal viscosity and resistivity are still not exactly known, an estimate of their value will have important implications for many suggested coronal heating mechanisms.

The phase mixed signal plotted in Figure 4.14 (a) is obtained by setting $\Lambda_\nu^2 = 10^{-5}$ in the WKB solution (Eqn. (4.29)) and taking a cross-section at $x = 0.5$. As the waves propagate up with height, the basic wavelength stays constant but the amplitude of the oscillation is damped as phase mixing occurs. Both these properties are visible in the wavelet transform (Figure 4.14 (b)). At all heights, the wavelet power is situated at the basic wavelength $\lambda = 0.1$. At larger heights, we see that the amplitude of the transform decreases, consistent with the decreasing amplitude of the original signal. The slight increase at the right hand edge is a consequence of the wrap-around effect, caused by the Fourier transform. However, this increase occurs outside the COI and should therefore not be taken into account anyway. In Figure 4.14 (c), we have plotted a cross-section of the wavelet power at a constant wavelength $\lambda = 0.1$. The solid line corresponds to the numerical

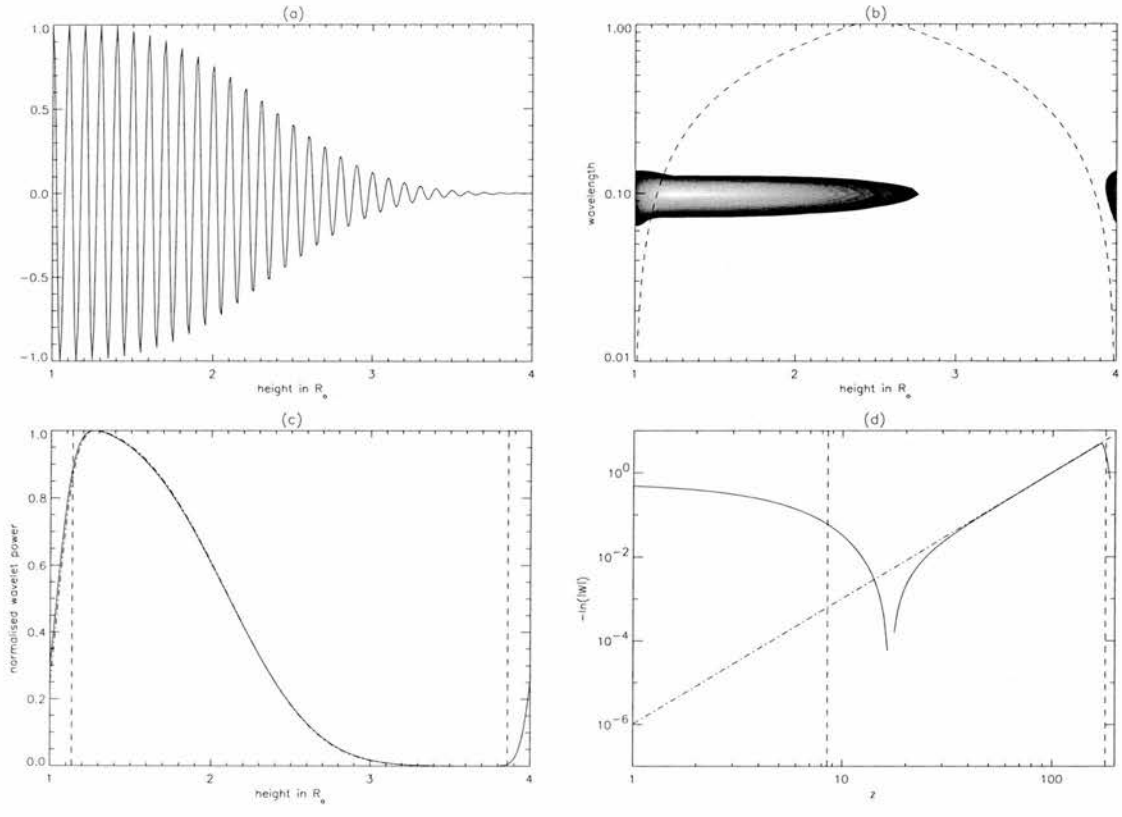

Figure 4.14: (a) A cross-section at $x = 0.5$ of the perturbed velocity in a stratified, dissipative plasma, with $\Lambda_\nu^2 = 10^{-5}$. (b) Corresponding wavelet transform of the velocity at $x = 0.5$. (c) Cross-section of the (normalised) wavelet power at maximum wavelet power, i.e. at $\lambda = 0.1$. The dot-dashed line corresponds to the analytical approximation (4.37) with $\varepsilon = 10^{-6}$. (d) Logarithmic plot of the cross-section of the wavelet power as a function of the Cartesian height z. The relation between r, the height in solar radii R_o, and z is given by Eqn. (4.27). The dot-dashed line corresponds to $\ln(\exp(\varepsilon z^3))$.The dashed lines indicate the cone of influence.

solution for the wavelet transform, whereas the dot-dashed line was obtained from the analytical approximation (Eqn. (4.37)), setting $\varepsilon = 10^{-6}$. When comparing the expression for the dissipation coefficient Λ_ν^2, used in Eqn. (4.29), with the expression for the parameter ε, used in Eqn. (4.37), we see that $\Lambda_\nu^2 = 10^{-5}$ implies $\varepsilon \approx 10^{-6}$, at $x = 0.5$. The agreement between the numerical solution and the analytical expression is quite good. The difference near the edges is caused be the wrap-around error, coming from the Fourier transform that is used to obtain the numerical solution. The agreement at the edges can be improved by padding the signal with zeroes, before taking the wavelet transform. However, the $e^{-\varepsilon z^3}$ slope, which is a characteristic signature of phase mixing, is clearly present in the transform. Additionally, the steepness of this slope will give us an estimate for the value of the dissipative coefficient Λ_ν^2. Finally, Figure 4.14 (d) is a logarithmic version of Figure

4.14 (c), plotted against the Cartesian height z (see Eqn. (4.27)), rather than the height in R_o we have used so far. The dot-dashed line is simply $\ln(\exp(\varepsilon z^3))$, with $\varepsilon = 10^{-6}$. Inside the COI, the agreement between both solutions is remarkable and as $\ln(\exp(\varepsilon z^3)) = \varepsilon$ at $z = 1$, the value of the parameter ε is directly given by the intersection of εz^3 and the vertical axis. The gradient of the slope is three, corresponding to the power in the exponential damping due to phase mixing (see Eqn. (4.29)). Alternative damping mechanisms would have a different slope in such a logarithmic plot.

From a wavelet analysis of this signal, we extracted a lot more information than just the wavelength(s) of the oscillations. The fact that $e^{-\varepsilon z^3}$ is an excellent fit implies that phase mixing is occuring, and hence, that there is a substantial density inhomogeneity present in the plasma. Furthermore, it is possible to estimate the value of the coronal dissipation coefficient from a logarithmic plot of the wavelet transform. It is important to note here that phase mixing is merely used as an example of a dissipation mechanism. Other dissipation mechanisms have their own characteristic damping profile, which will be present in the wavelet transfrom.

4.3.3 Gravitational stratification

In this section we neglect dissipation (by setting the dissipative coefficient $\Lambda_\nu^2 = 0$) and look at the effect of a gravitationally stratified atmosphere. We again use Cartesian coordinates. When a density inhomogeneity is present in both the horizontal and vertical direction, phase mixing will occur and as the phase mixed Alfvén waves propagate up with height, the amplitude of the perturbed velocity will increase as $\rho_0^{-1/4}$, due to the decreasing density ρ_0 (Wright & Garman, 1998; Torkelsson & Boynton, 1998). Additionally, the wavelength λ will increase as $e^{z/2H}$, as the Alfvén speed v_A depends on height as $e^{z/2H}$, where H is the pressure scale height (see Chapter 2). For the results presented in this section, we set $H = 0.5$. Again, we want to find out if the wavelet transform indicates that gravitational stratification is present in the surroundings where oscillations are observed. Although the pressure scale height H can be calculated from temperature estimates, it would be nice to confirm this value from the wavelet transform.

In Figure 4.15 (a), we plotted a cross-section of the perturbed velocity, again at $x = 0.5$. It is clear that both the amplitude and the wavelength increase as the wave propagates up with height. The wavelet transform (Figure 4.15 (b)) confirms that increasingly longer wavelengths are present with increasing height. The strongly increasing amplitude of the wavelet transform is caused by the amplitude increase of the perturbed velocity at larger heights. The fact that the transform starts decreasing again is purely caused by the wrap-around error of the Fourier transform. In this figure, we also plot (dot dashed line) $e^{z/2H}$ as a function of height, the wavelength variation we expect from previous studies. We see that, apart from outside the cone of influence, where edge effects become

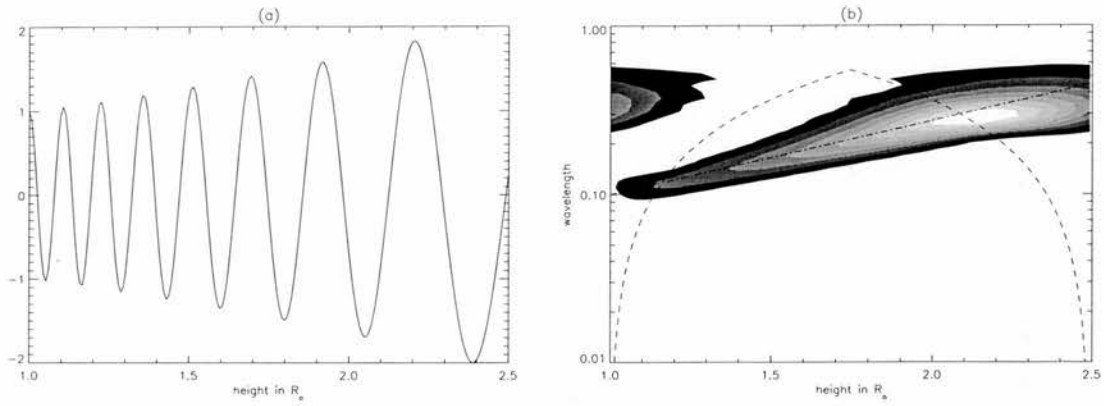

Figure 4.15: (a) A cross-section at $x = 0.5$ of the perturbed velocity in a stratified, non-dissipative plasma, with $H = 0.5$. (b) Corresponding wavelet transform of the velocity at $x = 0.5$. The dot-dashed line represents $e^{z/2H}$. The dashed lines indicate the cone of influence.

to large to trust the transform, the $e^{z/2H}$ variation of the wavelength is remarkably well represented in the wavelet power. So when an increase in wavelength is present in the wavelet transform of observed oscillations, the pressure scale height H can be obtained by fitting an $e^{z/2H}$ curve through the wavelet power. Unfortunately, as the wavelength increases when the waves propagate up with height, an increasingly larger portion of the transform will fall outside the COI. So for a strongly stratified atmosphere, i.e. for small values of the pressure scale height H, it might be difficult to fit the $e^{z/2H}$ curve to the transform. However, despite this, there clearly is a lot more information in the wavelet transform then there is in the Fourier transform of the same signal (Figure 4.10).

4.3.4 Diverging atmosphere

Finally, we study the effect of a radially diverging background magnetic field. We exclude dissipation ($\Lambda_\nu^2 = 0$) and gravitational stratification ($H \to \infty$) from the model and work with spherical coordinates, as they will be the most convenient choice. As a density inhomogeneity is still present in the horizontal direction, phase mixing of Alfvén will again occur as the waves propagate up with height. In Chapter 3, we found that, unlike gravitational stratification which lengthens the wavelength, area divergence shortens the wavelength. Indeed, both the Alfvén speed and the wavelength λ will decrease as $\frac{1}{r^2}$. As the background density is independent of height, the amplitude of the perturbed velocity remains constant.

The cross-section of the perturbed velocity in Figure 4.16 (a) shows the constant amplitude and the rapidly decreasing wavelength with increasing height. As the wavelengths decrease continuously, it is important to include a sufficiently high number of scales in the wavelet analysis, to ensure that all

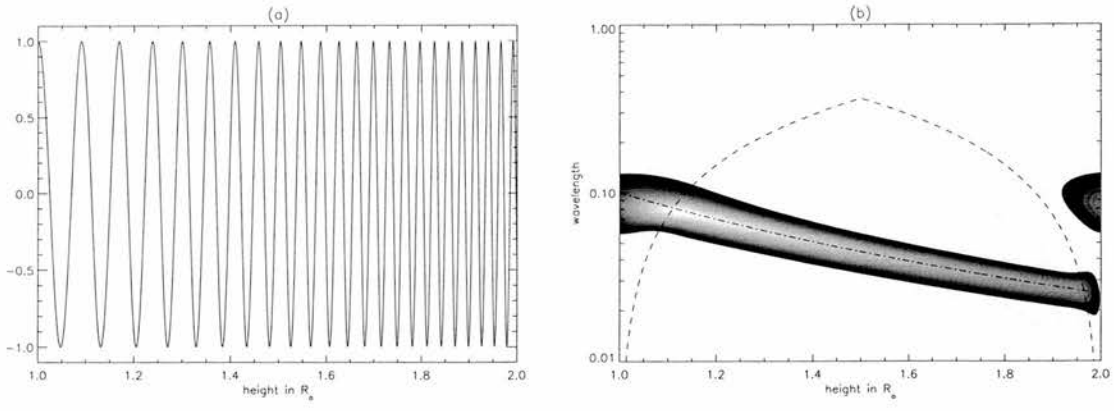

Figure 4.16: (a) A cross-section at $\theta = 0.5$ of the perturbed velocity in a non-dissipative plasma, with a radially diverging background magnetic field (b) Corresponding wavelet transform of the velocity at $\theta = 0.5$. The dot-dashed line represents $\frac{1}{r^2}$. The dashed lines indicate the cone of influence.

wavelengths are fully resolved. Therefore, we decrease the value of δj, which determines the number of scales included in the wavelet analysis, to 0.025 in this section. The wavelet transform (Figure 4.16 (b)) confirms the decreasing wavelength as wavelet power is present at continuously smaller wavelengths for larger heights. The dot-dashed line overplotted is the expected wavelength change $\frac{1}{r^2}$. Just as in the gravitational stratification case, the wavelet transform follows the theoretically predicated change in wavelength extremely well, inside the cone of influence. As for smaller scales (or wavelengths in this case) larger portions of the transform fall inside the COI, the $\frac{1}{r^2}$ change in wavelength can be followed for almost the entire duration of the signal. When this $\frac{1}{r^2}$ curve fits the transform, and there is no (radial) change in the background density, this implies that the backround magnetic field is radially diverging.

4.4 Discussion and Conclusions

In this chapter we applied a wavelet analysis to phase mixed Alfvén waves in various physical circumstances. We briefly introduced the wavelet analysis and then discussed its resolution properties in more detail. In a first stage we compared two finite signals, dissappearing at a similar height. The first one being a simple harmonic wave, cut off at this height, and the second one being an Alfvén wave, dissipated by phase mixing. Apart from indicating the wavelength present in the signals, the wavelet transform is distinctly different for a truly finite oscillation and for a gradually damped oscillation. Thus, when observing oscillations of finite lifetime, one can use a wavelet analysis to determine whether the signal is simply cut off, or gradually dissipated. Additionally, it is possible to have an estimate for the value of the dissipation coefficient by fitting an analytical approximation

to the numerical solution for the wavelet transform. As the εz^3 slope of the analytical fit is a typical characteristic of phase mixing, a good fit between this approximation and the transform of the analysed signal could imply that the signal is dissipated by phase mixing. Other dissipation mechanisms will have their own characteristic slope, which will be evident in the wavelet transform. When applying these results to observational data, this could supply us with information on which dissipation is involved in the damping of the observed oscillation. The same method was followed in studying phase mixing of Alfvén waves in a gravitationally stratified or a radially diverging atmosphere. The $e^{z/2H}$ lengthening of the wavelengths that occurs when Alfvén waves propagate through a vertically stratified plasma, is clearly evident in the wavelet transform. From this a value for the pressure scale height can be estimated and, when possible, compared to values obtained by different methods, e.g. when the temperature of the surroundings is known. Similarly, the $\frac{1}{r^2}$ behaviour of the wavelength in an atmosphere with a radially diverging background magnetic field, is also present in a wavelet transform of such an oscillation. In general, the wavelength is given by $2\pi v_A/\omega$. Thus, the variation in wavelength with height, as given by the wavelet analysis, provides information about the coronal Alfvén speed. Hence, we have a measure of both the coronal density and the coronal magnetic field variation.

Although this first study considered phase mixing of Alfvén waves, because they can be described by a single WKB expression, and not the much more frequently observed slow magneto-acoustic waves, it indicates that a wavelet analysis of observed wave-like oscillations can provide important information about the physical surroundings in which the oscillations are found. An obvious next step is to apply the methods and results presented in this chapter to oscillations observed in the solar corona. Due to its high spatial and temporal resolution, TRACE data provides an excellent opportunity to investigate waves in the solar corona and, through a wavelet analysis, provide estimates for local coronal plasma properties. Examples of the implications of the results we presented here on the analysis of observational data will be presented in the next chapter.

Chapter 5

Observation of oscillations in large active region loops

I don't have any solutions, but I certainly admire the problem.
A. Brilliant

5.1 Introduction

Despite the widespread occurrence of hot coronae in the Sun and other stars, the coronal heating mechanism is still not fully understood. The study of coronal oscillations is important in this aspect since these oscillations could be associated with dissipating wave motions that could be heating the solar corona (Porter et al. 1994a, 1994b; Roberts et al. 1984). Possible magnetohydrodynamic wave heating theories include mechanisms such as phase mixing and resonant absorption. Obviously, the detection of oscillations in the corona is a crucial step in determining the presence and relevance of these wave heating mechanisms. A short overview of observations of oscillations in the solar atmosphere is given in the introduction to this thesis.

During the last few years, there have been several reports of observations of periodic and quasi-periodic oscillations in different coronal structures. DeForest & Gurman (1998) reported on quasi-periodic compressive waves in solar polar plumes which Ofman et al. (1999) consider to be slow magneto-acoustic waves. Berghmans & Clette (1999), Berghmans et al. (1999a) and Robbrecht et al. (1999) found propagating disturbances in coronal loops, observed on 13th May 1998, in the TRACE 171 Å and EIT (SOHO) 195 Å passband. Aschwanden et al. (1999) report the first detection of spatial displacement oscillations of coronal loops, observed for the first time due to the high spatial

resolution of the *Transition Region and Coronal Explorer* (TRACE) telescope. Nakariakov et al. (1999) analysed the transverse loop oscillations induced by a flare observed with TRACE in the 171 Å and 195 Å passband and estimated the damping time. From the damping time Nakariakov et al. (1999), estimated that the coronal dissipation coefficient could be as much as eight or nine orders of magnitude larger than the theoretically predicted classical value. This larger dissipation coefficient may solve some of the existing difficulties with wave heating and reconnection theories. However, Schrijver and Brown (2000) argued that rocking motions of the photosphere (associated with a flare) could cause loops to oscillate. If this is the case, the period and decay rate of the oscillations will be largely determined by the characteristics of the photosphere, saying very little about the properties of the corona.

In this chapter, we report on the detection of propagating disturbances along a loop structure close to an active region as observed in 171 Å by TRACE. A first report on small scale EUV brightenings in the same high cadence (9 s) TRACE data was given by Ireland et al. (1999b). As in Ireland et al. (1999a, 1999b), we employ a wavelet analysis to investigate significant periodicity in the observed oscillations. As described in the previous chapter, wavelet analysis is a powerful technique which allows a local decomposition of timescales in the time series of non-stationary processes. It is being applied increasingly to a range of astrophysical data. We will also show examples of comparable propagating oscillations that were found in similar datasets. The observation of coronal oscillations has important consequences as it could provide us with useful information for many numerical or analytical models of wave heating in the solar corona.

5.2 Analysis and Results for 23 March 1999

5.2.1 Observations

The analysis in the first half of this chapter is based upon TRACE 171 Å (Fe IX) and 195 Å (Fe XII) observations of active region AR 8496, a large, stable active region present in the southwest quadrant, on 23 March 1999. The data is taken as part of Joint Observing Programme 83 - *High cadence activity studies and the heating of coronal loops.* The aim of this study was to reduce the cadence of the TRACE observations to as low a value as possible while still retaining enough counts that events of interest would not be lost in the noise. A more detailed and technical description of JOP 83 can be found in Appendix C. The first sequence, start time 0651 UT, consists of 157 512×512 pixel images in the TRACE 171 Å passband with a 9 s cadence and with a pixel size of $1''$. The data is run through the Solarsoft TRACE routine TRACE_PREP (provided by the SOHO and TRACE teams) and subsequently cleaned using TRACE_DESPIKE (removing spikes in the

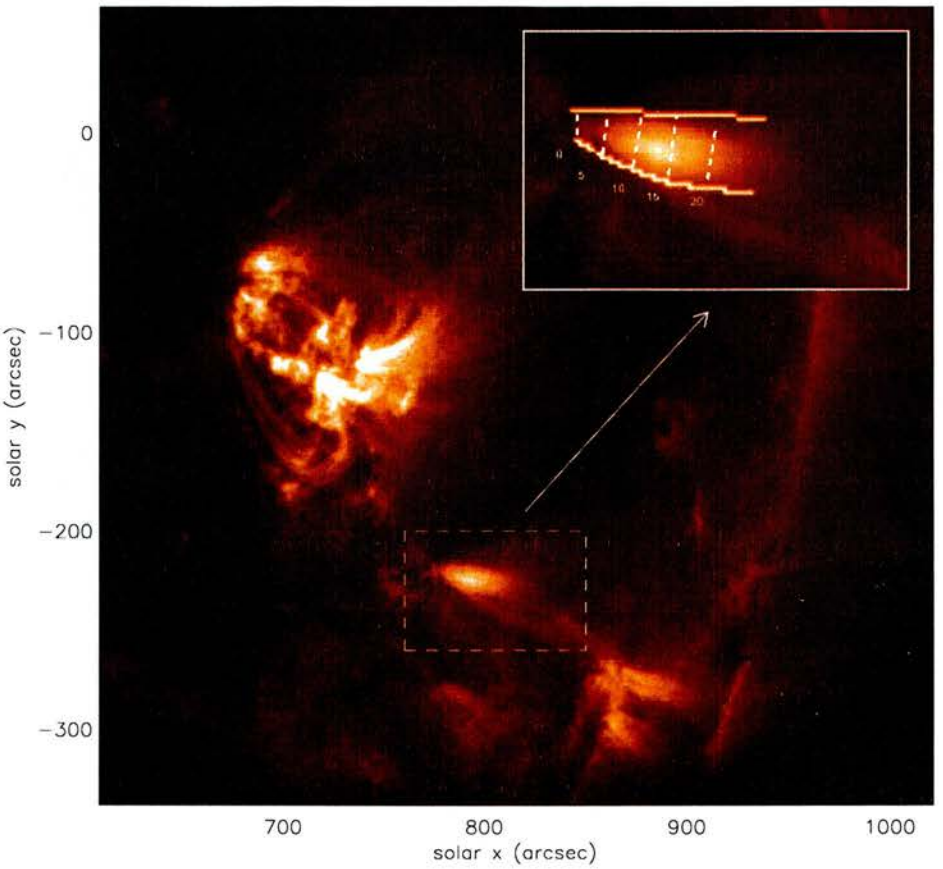

Figure 5.1: Typical image in the 0651 UT 171 Å dataset. Inset is a blow up of the area supporting the oscillatory signal.

datacube), TRACE_CLEANJPG (removing JPEG compression artifacts) and TRACE_DESTREAK (removing cosmic ray and particle streaks). As the data only covers a relatively short period, they have not been corrected for solar rotation. Figure 5.1 shows an image of the active region AR 8496. This is the first of the 0651 UT sequence on which we will be concentrating in this chapter. The tube-like area that is indicated in the inset in Figure 5.1 shows the region we will be looking at in detail. The bright footpoint is about 40 arcsec (29 000 km) in length.

5.2.2 Propagating disturbances in a large coronal loop near AR 8496

The 0651 UT dataset

To obtain results above a satisfactory confidence level, it is necessary to sacrifice some of the spatial and temporal resolution of this dataset. The original datacube consisted of 157 images with a 9

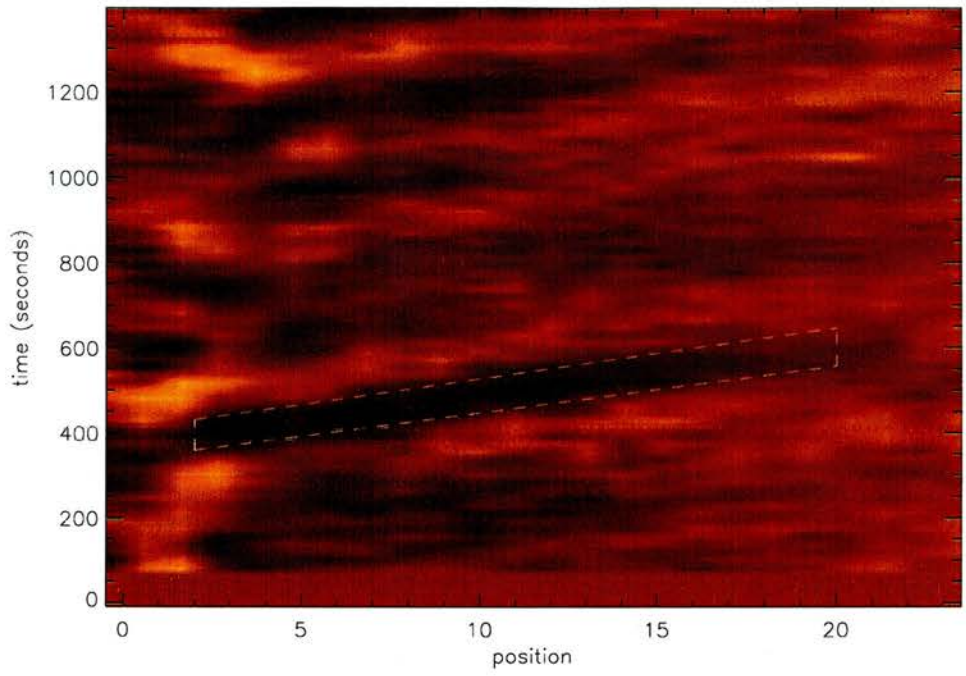

Figure 5.2: A plot of the running difference between the average time series for each position along the inner arc.

second cadence. To increase the signal-to-noise ratio, a datacube with 78 images with a 18 second cadence was created by summing over consecutive images. To analyse the evolution of the region's brightness, we divide the region into 50 cross-sections. Both arcs that form the tube are normalised and cross-sections are then defined by connecting corresponding positions as is shown in the inset in Figure 5.1. To emphasise the time-variable aspect of the behaviour of the region, we create a running-difference image of the average time series for each position. From each frame we subtracted the frame taken 90 seconds earlier. As we are mainly interested in the time-variability of the intensity along the loop, we added all the unique datacounts along two consecutive cross-sections. In order to obtain a uniform normalisation, we divided by the number of counts. This is then defined to be the *average* timeseries for each of the 25 positions along the tube, each of the positions covering a distance of roughly $2''$. We note here that the datacube now has half of the time and spatial resolution of the original.

In the running-difference image (Figure 5.2), some bright and dark features can be seen clearly running across the image with positive gradients. These diagonal ridges represent outward travelling regions of slightly higher (bright) or lower (dark) intensity. This indicates that a disturbance is travelling along the structure. These outward propagating disturbances seem to be triggered by

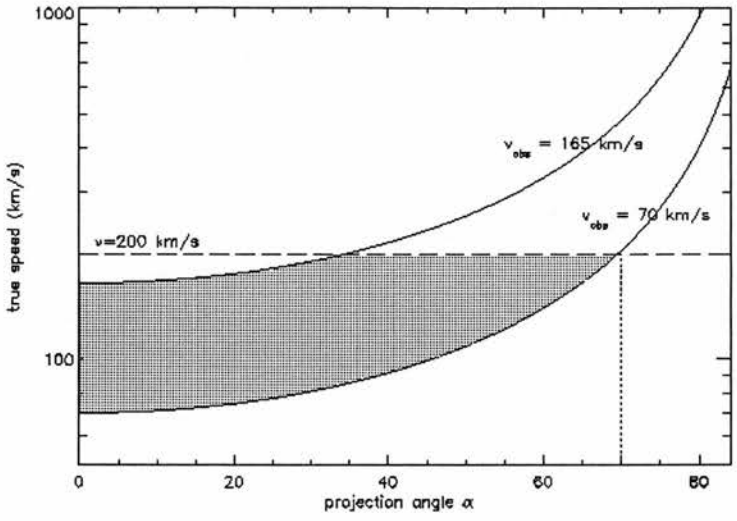

Figure 5.3: Dependence of the true propagation speed of the disturbance upon the projection angle α.

small scale brightenings at the footpoint of the loop. The propagation speed of these features can be estimated by measuring their slope in the running-difference image. This speed has been calculated to be between 70–165 km s^{-1} throughout the time sequence. There is no significant deceleration or acceleration of the features as they propagate, since the gradients in the running-difference are relatively constant. This apparent velocity is perpendicular to the line-of-sight. Taking into account line-of-sight projections, the true speed would be given by

$$v_{\rm true} = \frac{v_{\rm obs}}{\cos\alpha}\,, \tag{5.1}$$

where $v_{\rm obs}$ is the speed estimated from the observations and α is the projection angle between the loop and the disk (Robbrecht et al., 1999). As α is most likely to be between 0 and 90 degrees, the above range of apparent speeds gives us a lower limit for the real propagation speed of the disturbances. Estimating the exact value of the angle α is difficult from the observations as the loops are not observed on the limb. By using the apparent speeds $v_{\rm obs}$ and assuming $v_{\rm true} \lesssim 200$ km s^{-1}, we can get an idea of a reasonable range of values for the projection angle α. In Figure 5.3 we plotted the upper and lower limits for the true speed $v_{\rm true}$ by setting $v_{\rm obs} = 165$ km s^{-1} and $v_{\rm obs} = 70$ km s^{-1} respectively in Equation (5.1). For $v_{\rm true} \lesssim 200$ km s^{-1}, this gives us a range $0° \leq \alpha \leq 70°$ for the projection angle α. A discussion of the inclination of large coronal loops observed by TRACE can be found in Reale (1999).

These oscillations are real time variations in intensity since motions of bright features due to solar rotation would result in much slower variations. For the first half of the region, the amplitude of

the disturbance is a variation of 2%-4% compared to the background brightness, which is more than twice the amplitude of the expected noise level. The signal gets weaker as it propagates along the structure; there is about a 0.6%-2% variation in the background brightness which is only just above the noise level when the signal reaches the end of the analysed region. Thus, there appears to be evidence that the amplitude of the disturbances decreases as they travel along the structure. However, attempts to calculate a damping length from this data do not yield conclusive results.

Wavelet analysis of the disturbances

To determine an oscillation timescale in the data, we use a wavelet analysis at different positions along the tube. The left plot of Figure 5.4 shows the original data at position 4 along the tube like region as defined in Figure 5.1. The right plot shows the "processed" data at this position; that is, a linear polynomial is fitted to the original data and subtracted subsequently from the original data. Just from a visual inspection, we already see that at this position, there is a signal with a period of roughly 300 seconds for the entire duration of the observation. The results from the wavelet analysis for position 4 are shown in Figure 5.5. A clear band of strong wavelet power, situated between about 200 and 400 seconds, above the 99.0% confidence level, is detected running throughout the entire time interval. The maximum of the wavelet power occurs around 300 seconds.

The raw and processed data at position 6 are shown in Figure 5.6. Although still clearly visible, the oscillation at this position is less regular. The period seems to change and the oscillation only starts after about 400 seconds. However, it is exactly in such a case that the strength of the wavelet transform will become evident. The wavelet transform for position 6 is shown in Figure 5.7. Two distinct maxima occur; the first one is situated more or less in the middle section of the time sequence, with maximum power at about 260 seconds whereas the second one occurs near the end of the time sequence, with a maximum at roughly 200 seconds. The longer 260 second period is comparable with the periods found at position 4 but the 200 second period occuring near the end is slightly shorter than what we found before. Part of the power at 200 seconds falls outside the COI, as the oscillations occured near the end of the time sequence. From the description of the wavelet analysis technique we made earlier, we know that the decay of the amplitude of the wavelet power near the edges has to be treated cautiously. It could be a true decay or a side effect of the wavelet transform. From looking at the oscillation at position 6 (Figure 5.6, right), it is clear that the decay is an artefact of the transform as the amplitude of the oscillation in the timeseries does not appear to be decaying. When comparing the transforms at positions 4 (Figure 5.5) and 6 (Figure 5.7), we see that in both cases there is some wavelet power between 200–250 seconds, which corresponds to the clear black diagonal band that can be seen in the running-difference image (Figure 5.2, box).

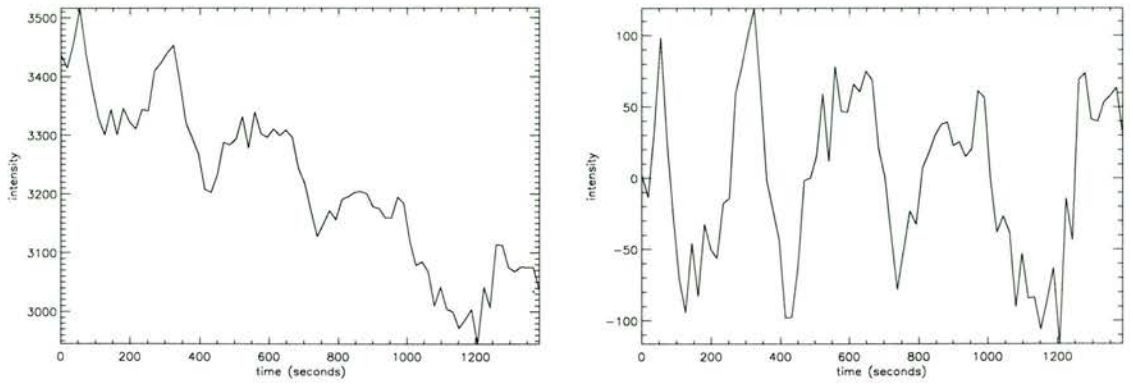

Figure 5.4: An overview of the raw (left) and processed (right) intensity variations at position 4 along the region shown in Figure 5.1

We now look at position 14, at bit further along the structure. The left plot of Figure 5.8 again shows the original data whereas the right plot shows the processed data. We see that a signal with more or less the same period as before (roughly 300 seconds) is present. From the wavelet analysis (Figure 5.9), we see there is strong wavelet power between 230 and 380 seconds (maximum again around 300 seconds), above the 99.0% confidence level, although not for the entire duration of the time sequence. From looking at Figure 5.8, it seems to be a true decay of the oscillation in the signal.

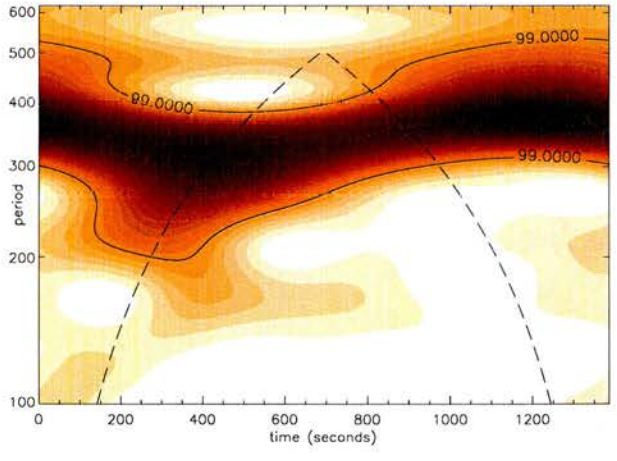

Figure 5.5: Wavelet analysis at position 4 along the tube (confidence level=99.0 %). Darker colours correspond to higher wavelet power. The dashed line indicates the cone of influence.

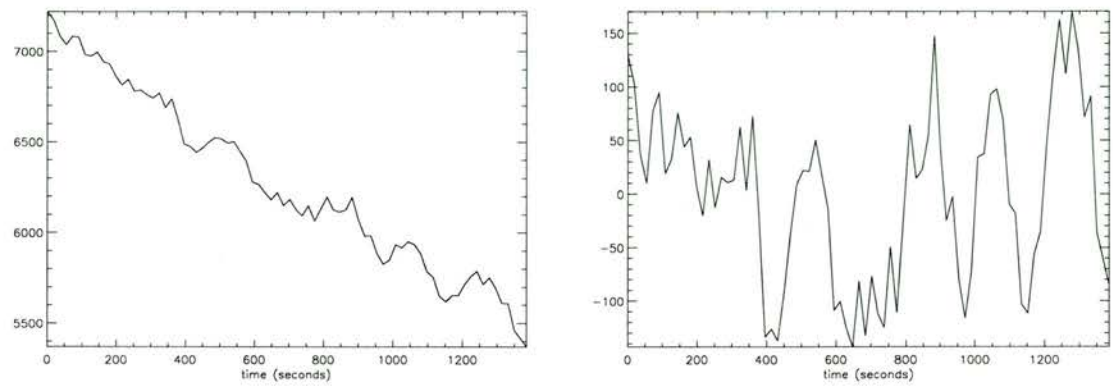

Figure 5.6: An overview of the raw (left) and processed (right) intensity variations at position 6 along the region shown in Figure 5.1

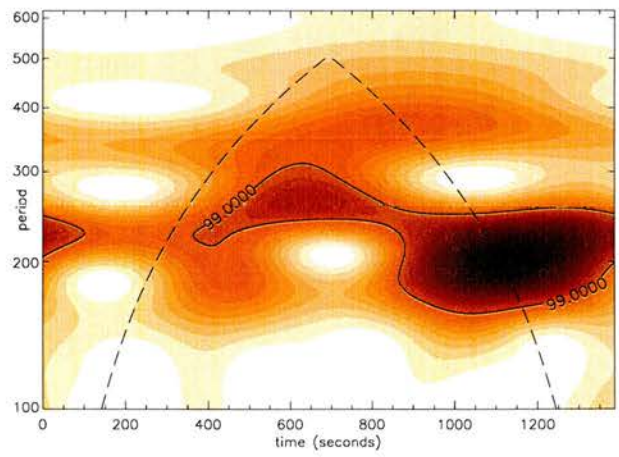

Figure 5.7: Wavelet analysis at position 6 along the tube (confidence level=99.0 %). Darker colours correspond to higher wavelet power. The dashed line indicates the cone of influence.

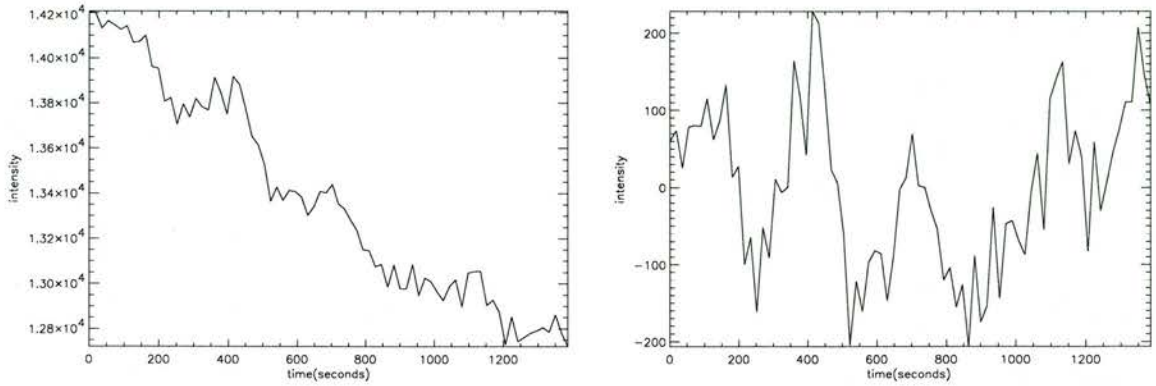

Figure 5.8: An overview of the raw (left) and processed (right) intensity variations at position 14 along the region shown in Figure 5.1

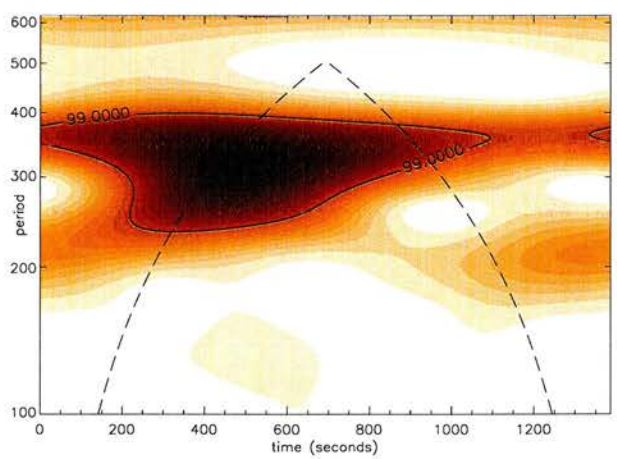

Figure 5.9: Wavelet analysis at position 14 along the tube (confidence level=99.0 %). Darker colours correspond to higher wavelet power. The dashed line indicates the cone of influence.

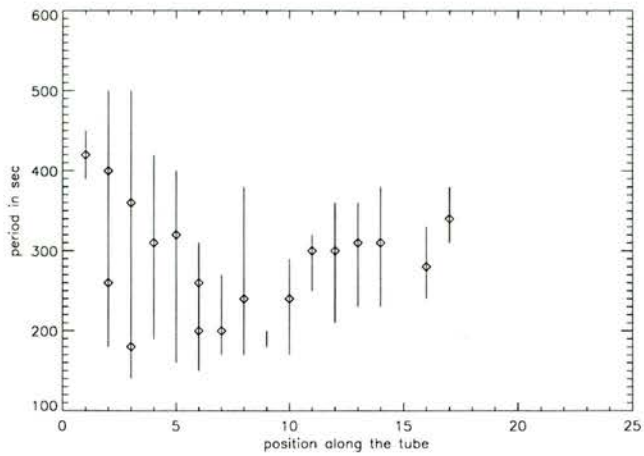

Figure 5.10: An overview of the range of periods found at each positions along the tube (confidence level=99.0 %)

This analysis was repeated for all the positions along the tube and an overview of the results is given in Figure 5.10. This figure shows the range of periods that are picked up for each position, above the 99.0 % confidence level. From this we see that the periods are situated between 140 s and 500 s. The diamonds in Figure 5.10 indicate where the strongest wavelet power is situated for each position, which ranges from 180 s to 420 s.

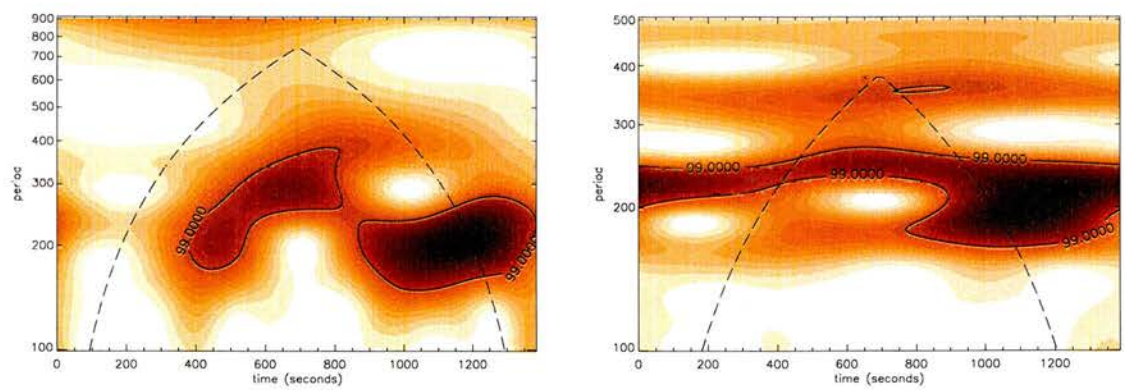

Figure 5.11: Wavelet analysis with (left) k=4 and (right) k=8, at position 6 along the tube (confidence level=99.0 %). Darker colours correspond to higher wavelet power. The dashed line indicates the cone of influence.

Finally, we repeat the wavelet analysis at position 6, using different values of the parameter k in the Morlet wavelet. From studying the wavelet analysis in the previous chapter, we know that a smaller value of k will give a better temporal resolution, whereas a larger value will give a better resolution

of the periods. In the left hand side in Figure 5.11 we set $k = 4$, on the right hand side, $k = 8$. Both the improved temporal resolution and the improved resolution of the periods are evident in these transforms. When $k = 4$ (Figure 5.11, left), there is a clear distinction between when different periods are found. Between about 375 and 825 seconds after the start of the signal, periods in the 180–390 range are found. Between 860 seconds and the end of the signal, periods in the 150–280 range are found. When comparing this with Figure 5.7 (where $k = 6$), we notice that a wider range of periods is found above the 99.0 % confidence level but, at the same time, their location in time is a lot better determined for smaller values of k. When $k = 8$ (Figure 5.11, right), the range of periods above the 99.0% confidence level is narrowed considerably. A period between 200 and 270 seconds is found for the entire duration of the sequence, with the additional shorter period (170–260 seconds) starting at 775 seconds, till the end of the signal. A comparison with Figure 5.7 shows clearly that although the range of periods found above the confidence level is smaller, a lot of the temporal resolution is lost for larger values of k.

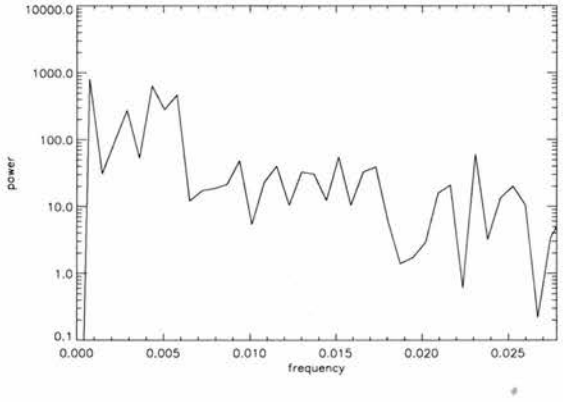

Figure 5.12: Fourier transform of the oscillation at position 6 along the tube.

As a last illustration of the advantages of wavelet analysis, we calculate the Fourier transform (FFT) of the signal at position 6 (see Figure 5.6 for the actual signal). The results are shown in Figure 5.12. It is very clear that a standard Fourier transform is not appropriate to analyse this signal, as the FFT does not manage to pick up any period in particular.

Discussion of the propagating disturbances

In the magnetically dominated corona, structures are expected to undergo three types of oscillations, driven by different restoring forces: non-compressional Alfvén waves, where the restoring force is provided by the magnetic tension, and slow and fast magneto-acoustic waves, where the magnetic and kinetic pressures are the restoring forces (Porter et al. 1994a, 1994b; Roberts et al. 1984).

While Alfvénic oscillations are essentially velocity oscillations and do not cause any variation in the intensity, the compressional waves cause density changes. Therefore, they could be observed in the form of intensity variations, provided there are no associated temperature changes big enough to push the material outside the 171 Å passband.

Since the data displays propagating variations in the intensity (Figure 5.2), these could be interpreted as magneto-acoustic modes. The moving features that are visible in the loop footpoint region travel at a constant speed throughout our field of view, i.e. there appears to be no significant deceleration or acceleration. As they are travelling at the order of the coronal sound speed ($c_s \sim 150$ km s^{-1}), we consider these propagating oscillations to be good candidates for being propagating slow magneto-acoustic waves, similar to the propagating features found in polar plumes by DeForest and Gurman (1998). Ofman et al. (1999) calculated the acoustic cutoff frequency to be $\omega_{\rm cutoff} \approx 1.5 \times 10^{-3}$ rad s^{-1} and consequently, waves with periods over 70 minutes would be evanescent. As the oscillations we observed have much shorter periods, the waves are travelling into the corona. Following Ofman et al. (1999), we can estimate the energy flux carried by the slow magneto-acoustic waves as $\rho[(\delta v)^2/2]v_s$, where δv is the wave velocity amplitude and $v_s \approx c_s = 150$ km s^{-1} in the corona. For slow magneto-acoustic waves, the velocity amplitude δv is directly related to the change in density $\delta\rho$ which we found to be of the order of 2%. Using $\rho = 5 \times 10^{-16}$ g cm^{-3} (Priest 1982) and $\delta v = 3$ km s^{-1}, we get an upper bound for the wave energy flux $\sim 3.5 \times 10^2$ ergs cm^{-2} s^{-1}. For weak active region loops, a wave flux of 5000 W m^{-2} or $\sim 5 \times 10^6$ ergs cm^{-2} s^{-1} is needed to heat them (Priest 1982). Therefore we conclude that the energy flux carried by the disturbances is only a very small fraction of the total energy required to heat coronal loops. The above interpretation is only valid if we assume the loop to be linear and homogeneous. For a non-linear, non-homogeneous medium, there could be other possible interpretations involving nonlinear waves and mode coupling.

Signatures of compressional waves in polar plumes were first detected by the White Light Channel of the UVCS instrument on SOHO high above the limb by Ofman et al. (1997). Unlike the observations done by Aschwanden et al. (1999), no flare occurred during or just before our observations. Similar propagating disturbances along coronal loops near an active region (AR 8218), with parameters almost identical to ours, were found by Berghmans & Clette (1999), Berghmans et al. (1999a) and Robbrecht et al. (1999). It seems that the compressive waves found in polar plumes by Ofman et al. (1997) and DeForest & Gurman (1998) do not only occur in (open) polar plumes but can also be found in large, coronal loops. These loops originate from compact sources near active regions and fan out to end in remote quiet Sun regions. So although they are closed magnetic structures, they appear to have much in common with plumes and perhaps can be treated locally as open magnetic structures.

The small microflare-like brightenings that trigger the outward propagating disturbances were also

seen by Berghmans & Clette (1999) and could be related to the results of Porter et al. (1998). They found that bright extended coronal features, whether rooted in active or quiet regions, are heated from active compact features at their feet. The large coronal loops are rooted in predominantly unipolar regions, which include small islands of the opposite polarity and the magnetic field lines along the neutral lines surrounding these islands are highly sheared. They suggest that shear-driven reconnection at the footpoints might generated MHD waves. Surprisingly though, they found a very poor correlation between the intensity changes at these footpoints to the changes in emission in the large scale structures extending away from them. Therefore they conclude that the heating of the loops is connected to some form of activity that is too cool to be seen as X-ray microflaring (several 10^6 K). However, in the cooler TRACE 171 Å line (10^6K), we do observe weak brightenings at the footpoints of large loops that trigger outward propagating intensity changes in the loops. Unfortunately, as AR8496 was situated too far away from disk center at the time of the observations, no clear MDI data is available to pick out the magnetic root of the loop we analysed.

Temperature and density of the loop footpoint

The left image on the top row in Figure 5.13 is a close up plot of the intensity in the 171 Å passband of the region we are studying. As the intensity scales as the square of the density, this provides a way of studying the density behaviour of the structure at that specific temperature. It appears that along as well as across the structure, the density profile in the 171 Å passband, i.e. the material at about 1 MK, resembles a Gaussian profile. The right plot in Figure 5.13 is the average intensity along the loop from its footpoint; for each position we summed all the datacounts between the boundaries of the tube defined by the white lines and divided by the number of pixels of each cross section. We see that the intensity initially increases, reaching a maximum at around position 12, i.e. about 17 500 km from the base of the loop before decreasing again (each position in the right images of Figures 5.13 and 5.14 roughly covers 2″). The intensity increases by a magnitude of 2 compared to the value of the intensity at the base of the structure. This implies that the density is increasing by a factor of approximately $\sqrt{2}$. Comparing this plot of the average intensity along the footpoint with the running-difference image (Figure 5.2), we see that the oscillations are most pronounced in the lower half of the region, i.e. where the density is increasing.

The left image on the bottom row in Figure 5.13 is an intensity plot of the region in the 195 Å passband. This image was taken at 0645 UT on 23rd March 1999, i.e. just before the start of the high cadence sequence we have been studying. Comparing this image with the top row, we see that there is a considerable difference between the structure in 171 Å (or at 1 MK) and in 195 Å (or at 1.5 MK). Apart from a bright part right near the base, the structure is hardly visible in 195 Å. The plot of the average intensity along the loop (bottom right image in Figure 5.13) confirms that

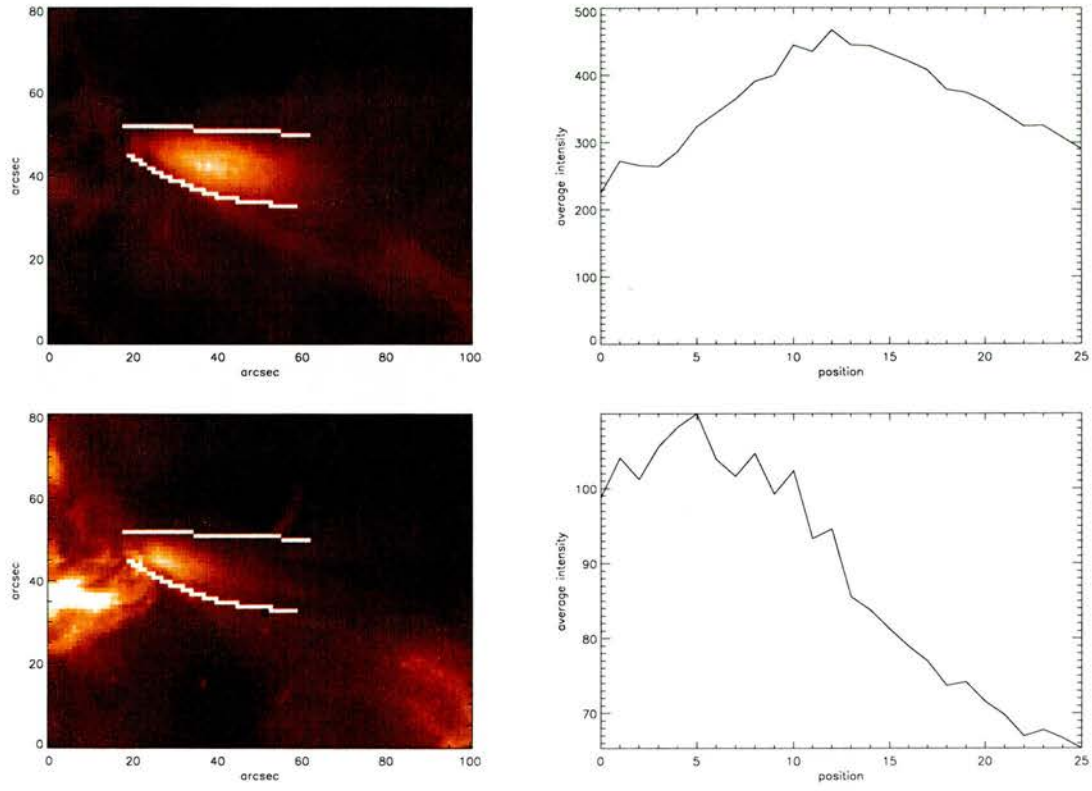

Figure 5.13: (left) A plot of the intensity (in the (left) 171 Å and (right) 195 Å passbands) of the loop footpoint. Brighter colours correspond to higher values. (right) The average intensity (in the (left) 171 Å and (right) 195 Å passbands) for each position along the structure.

the hotter material is concentrated in the first 7 or 8 positions (5000 or 6000 km) of the loop. The intensity decreases by about 30 % along the loop.

Figure 5.14 gives an indication of the temperature of the loop footpoint. The left image was obtained by taking the ratio of a 195 Å and 171 Å image, taken only a few seconds apart at 0645 UT on 23rd March 1999. The actual values quoted in the image have to be treated cautiously and the image only gives us a basic idea of the relative temperature changes in the structure. The profile of the temperature resembles an inverted Gaussian profile, both along and across the fluxtube. So as opposed to the intensity and density in 171 Å the temperature reaches a minimum along the structure. The right image in Figure 5.14 shows the average temperature along the structure, obtained in a similar way to the average intensity along it. As expected from the behaviour of the density in 171 Å and 195 Å along the footpoint, the temperature indeed decreases in the lower half of the region, before increasing again. However, the increase in the temperature at the end cannot necessarily be trusted as counts in both the 171 Å and 195 Å passband are too low. The minimum

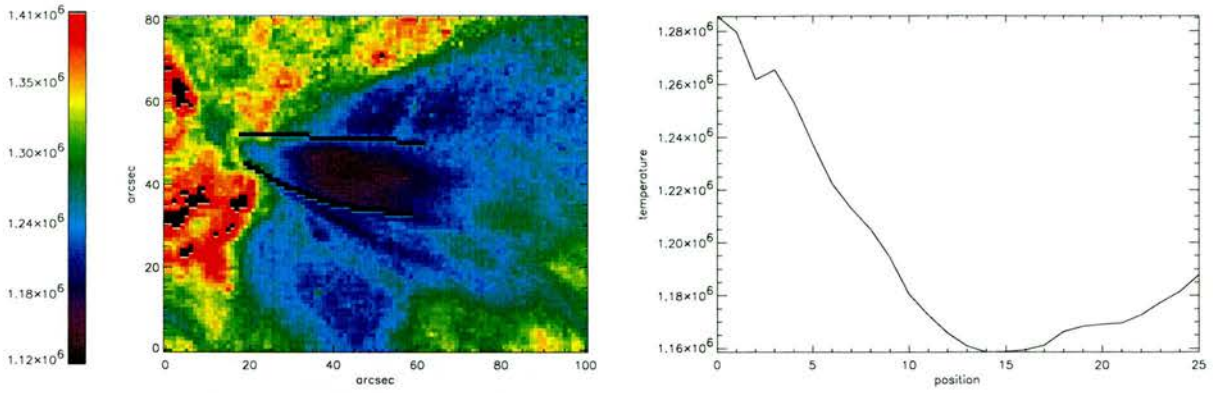

Figure 5.14: (left) A plot of the temperature of the loop footpoint. (right) The average temperature for each position along the structure.

in temperature seems to occur a few arcseconds further along than the 171 Å density maximum, i.e. at position 14 (roughly 20 000 km from the base). At its minimum, the temperature has decreased by about 10% compared to its value at the base. Therefore, the decrease in temperature seems considerably smaller than the increase in 171 Å density along the loop footpoint.

The 0750 UT and 0827 UT datasets

Following on from the high cadence (9 s) data, starting at 0651 UT, the observations continued with a cadence of roughly 60 seconds for about 1 hour until another high cadence run starts at 0826 UT. From this hour, we chose a sequence, starting at 0750 UT, of 32 1024×1024 pixel images in the TRACE 171 Å passband with a pixel size of $0.5''$. The data is prepared and cleaned (i.e. despiked and the pedestal read-out subtracted) in the same way as the 0651 UT sequence and is not corrected for solar rotation. Due to the longer exposure times in this set of observations, it was not necessary to sum over consecutive images. We create a running-difference image of the average time series by subtracting the previous frame, i.e. the one taken 60 seconds earlier, from each frame. We again summed over two consecutive cross-sections but because of the higher spatial resolution, each position now covers a distance of roughly $1''$.

Figure 5.15 shows the running difference of the tube like area (see Figure 5.1) between 0750 UT and 0820 UT. We see that there are some diagonal bright and dark bands with positive gradients, as in the 0651 UT running-difference image (Figure 5.2). The bands are less clear and continuous, which is due to the 60 second cadence rather than the very high 9 second cadence we obtained previously. However, the propagating, outward travelling disturbances appear to persist throughout the sequence. From the slopes in this running-difference image, the propagation speed has been

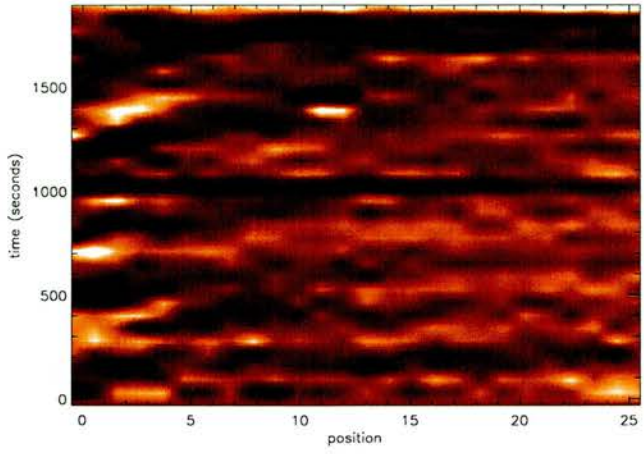

Figure 5.15: Running difference between 0750 UT and 0820 UT.

calculated to be between 40 and 105 km s^{-1}, again without a significant deceleration or acceleration. These speeds overlap with the results found in the high cadence 0651 UT sequence. The amplitude of the intensity disturbance is a variation of 2%-5% compared to the background brightness, which is between two and three times the amplitude of the expected noise level. Once again the signal is strongest in the first half of the region and gets weaker as it propagates along the structure. From a visual inspection, we found periods between 200 and 500 seconds, but due to the lower temporal resolution, these are only a rough estimate.

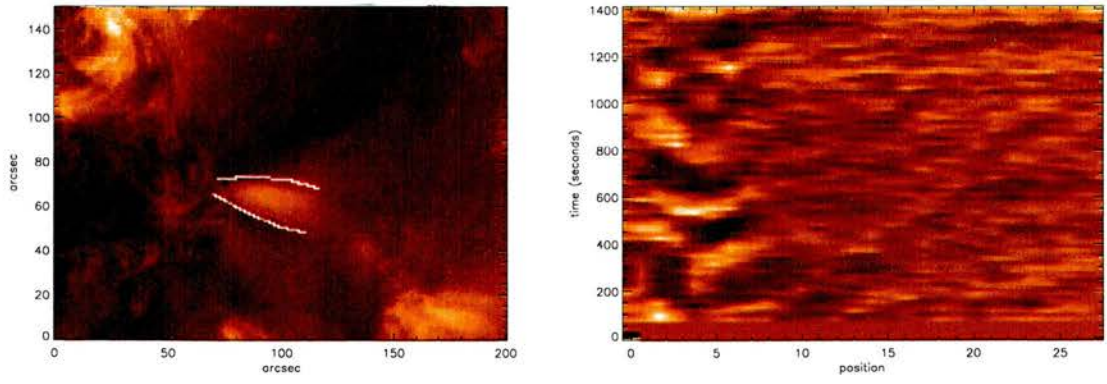

Figure 5.16: (left) Typical image in the 0827 UT 171 Å dataset and (right) running-difference image of the tube like area.

A second high cadence observational sequence, starting at 0827 UT, consists of 79 images in the TRACE 171 Å passband and 80 images in the 195 Å passband. Both sequences have an 18 second cadence and 512×512 pixel images with a $1''$ pixel size. The data is again prepared and cleaned as

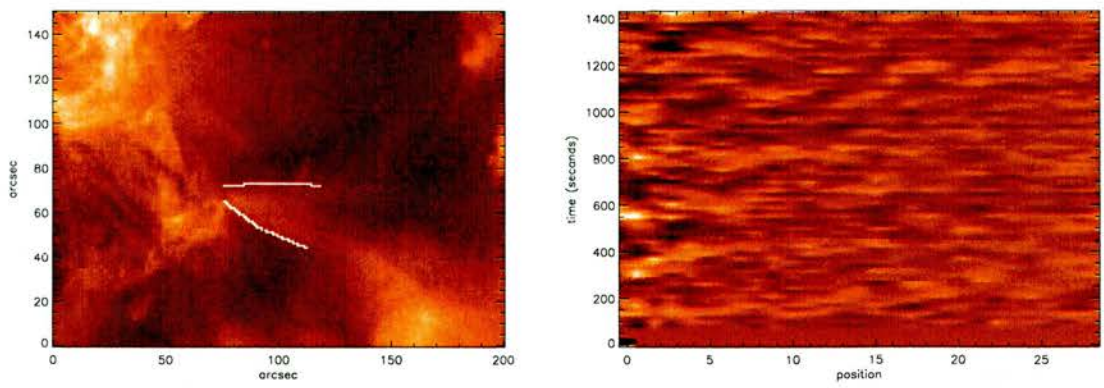

Figure 5.17: (left) Typical image in the 0827 UT 195 Å dataset and (right) running-difference image of the tube like area.

before. Although these images had relatively short exposure times, we did not sum over consecutive images to retain the 18 second cadence. The running-difference image is created by subtracting the frame taken 90 seconds earlier. Again we summed over two consecutive cross-sections so each position now covers a distance of roughly 2″.

Figure 5.16 shows the first of the 171 Å images in the 0827 UT sequence taken by TRACE. The tube like region we indicated is less pronounced and bright, compared with the same region in the 0651 UT sequence. The running-difference image still shows bright and dark diagonal bands and the propagating disturbances have similar properties but seem to be confined to the lower half of the structure. The propagation speed has been estimated to be $\sim 60 - 140$ km s^{-1} and the amplitude of the intensity variations amounts to 2% – 5% of the background intensity in the lower half of the tube, which is about twice the level of the expected noise. The periods are of the order 200 – 500 seconds. It is unclear whether the disturbances are less pronounced because the intensity of the structure is decreasing or because the signal is weakening. In the 195 Å dataset (Figure 5.17), the region we are looking at is barely visible and features in the running-difference image are too faint to be conclusive.

Overall, the quasi-periodic signal we found in the 0651 UT data sequence seems to persist between 0651 UT and 0851 UT. The disturbance consists of a 2% – 5% variation in the intensity compared to the background intensity and seems to be most pronounced in the lower half of the structure. We found periods between 200 and 400 seconds and velocities of the order of roughly 100 km s^{-1}.

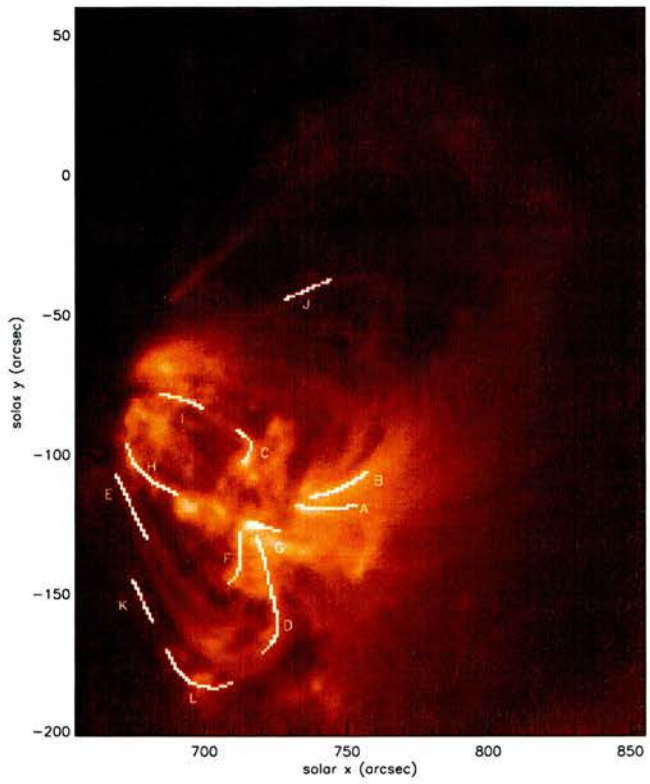

Figure 5.18: Image of the active region AR 8496. Overplotted are the loops A – L where we found quasi-periodic transient brightenings.

5.2.3 Transient brightenings in active region AR8496

This section investigates the active region that is present in this dataset. From earlier space missions like Skylab, Solar Maximum Mission and Yokhoh, it was found that impulsive, localised variations in intensity occur nearly continuously in active regions. From SMM UV emission lines, Porter et al. (1984) found frequent brightening events of modest amplitude, localised in space and short lived (40 – 60 seconds) within an active region. Withbroe et al. (1985) and Habbal et al. (1985) investigate the temporal and spatial variation of EUV emission lines from Skylab data. They report frequent, localised brightenings, lasting between 5 and 15 minutes and with spatial scales between 5″ and 15″ and suggest that the coronal plasma in small-scale magnetic loops is heated by an intermittent impulsive heating mechanism, most likely involving the rapid release of magnetic energy. In a deep survey of solar nanoflares with Yokhoh, Shimizu & Tsuneta (1997) found similar short-time, small scale brightness enhancements in X-rays (microflares), which appear fainter than transient

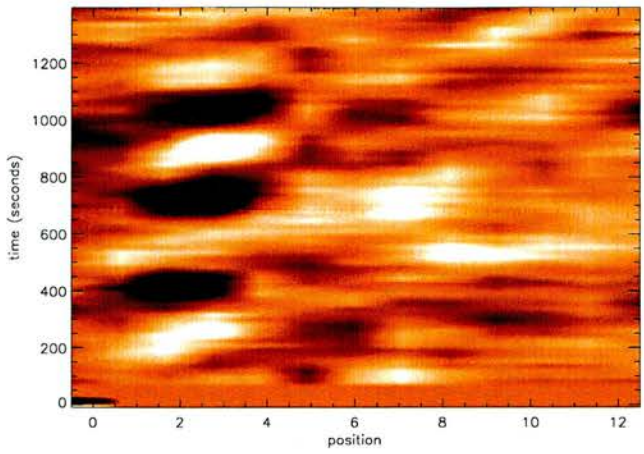

Figure 5.19: A plot of the running difference between the average time series for each position along loop I (Figure 5.18).

brightenings of localised parts of long loop structures. Instruments like EIT (Extreme-Ultraviolet Imaging Telescope) or CDS (Coronal Diagnostic Spectrometer) on board SOHO frequently observe localised, short-lived brightenings in active regions. They were noted in early CDS observations by Mason et al. (1997) as compact, intense brightenings in transition region lines. Brekke et al. (1997) and Kjeldseth-Moe et al. (1998) observed very rapid time variability in active regions with CDS and found that large Doppler shifts occur only in parts of a loop, not along its entire length. From EIT observations, Berghmans & Clette (1999) and Berghmans et al. (1999a) find various types of active region EUV brightenings, ranging from a B3.5 flare to EUV versions of active region transient brightenings as previously observed by SXT (Yohkoh).

In Figure 5.18 we have indicated the loops in the active region (A to L) where we found some kind of localised, quasi-periodic brightening. We now have a closer look at the brightenings seen in loop I. In the running difference image (Figure 5.19) we clearly see a quasi-periodic pulse at the start of this loop. However, it is not known whether this pulse causes a disturbance to travel along the loop. Figure 5.20 shows (a) the intensity variation and (b) the wavelet analysis at position 2 along the loop, where the pulse seems to be strongest. We find that at this position, the brightenings amount to a 8% variation in intensity compared to the background intensity and have a period of 300 – 400 seconds. The signal is well above the expected noise level. The strong pulse appears be to very localised and only about 4 arcsec wide (the positions indicated in Figure 5.19 are roughly $2''$ apart). In all of the loops indicated in Figure 5.18 we found similar pulses and Table 5.1 gives an overview of the periods and amplitudes of these brightenings. Most periods are of the order of 200 – 400 seconds while the amplitudes on average amount to a 3% – 7% variation compared to the

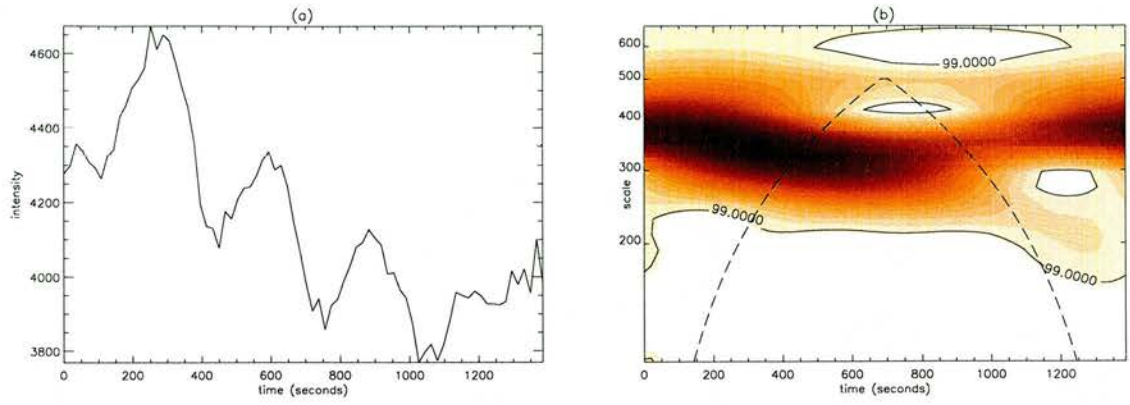

Figure 5.20: (a) An overview of the raw intensity variations at position 2 along loop I and (b) wavelet analysis at this position (confidence level=99.0 %). Darker colours correspond to higher wavelet power. The dashed line indicates the cone of influence.

loop	period (sec)	amplitude (%)
A	200 – 300	4.5 – 5
B	200 – 250	3 – 4
C	200	5
D	200	3
E	200 – 400	5 – 9.5
F	300 – 400	4 – 5
G	300 – 400	5 – 7
H	250	10
I	300 – 400	5 – 8
J	500	10 – 20
K	300	15
L	300 – 400	7

Table 5.1: An overview of the periods (sec) and amplitudes of the quasi-periodic brightenings found in the loops of active region AR 8496, as indicated in Figure 5.18.

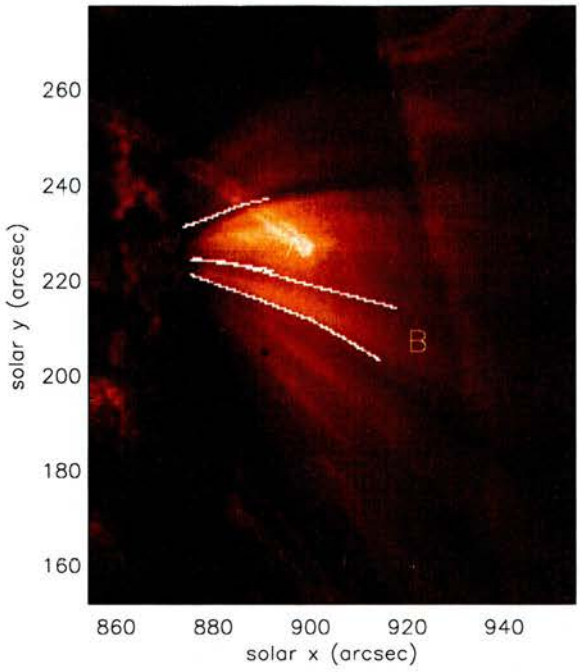

Figure 5.21: Typical image of the 171 Å dataset of 19th August 1998.

background intensity. Occasionally peaks up to 20% are detected. Similar to loop I, most of the pulses are very localised and only a few arcseconds wide. Although the amplitudes of the brightenings we found are smaller in size, they are not unlike the active region core brightenings discussed by Berghmans & Clette (1999) and Berghmans et al. (1999a). They point out the similarities to active region brightenings found by Shimizu (1995) using Yokhoh SXT data and they suggest these events might be the weaker and cooler EUV counterparts of the SXT active region transient brightenings.

5.3 Analysis and Results for 19 August 1998

5.3.1 Observations

We now consider a set of TRACE 171 Å (Fe IX) images of the north-west limb taken on 19th August 1998. The sequence we investigate started at 0143 UT and finished at 0715 UT. The dataset consists of 244 1024 × 1024 pixel 171 Å images with a pixel size of 0.5″. The images predominantly have a 60 second cadence but during the time sequence, 5 minute or longer breaks occurred to allow TRACE to observe in the White Light Channel. The data has been despiked and the pedestal read-out has been subtracted. To compare like with like, the images are normalised with respect to the exposure

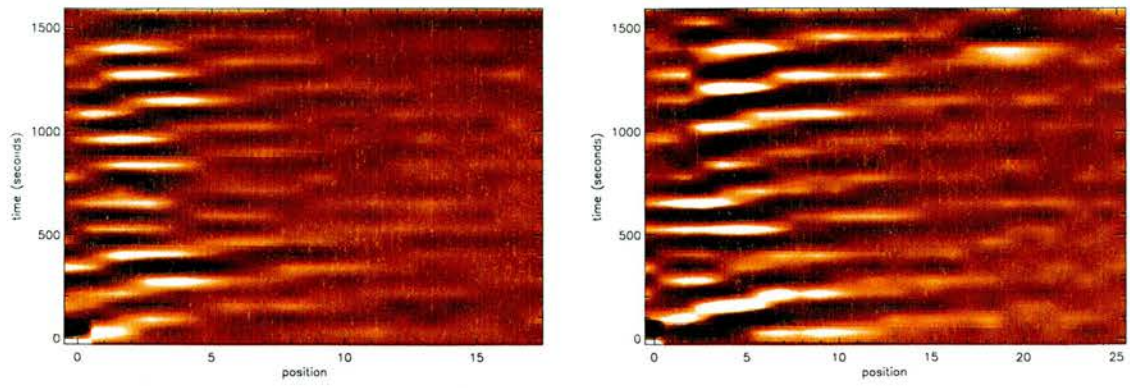

Figure 5.22: A running difference between the average time series for each position along the region A (left) and B (right) indicated in Figure 5.21 between 0404 UT and 0430 UT on 19th August 1998.

times. Figure 5.21 shows an image of the observed region. The tube-like areas that are indicated seem to be the bright base of a large,diffuse coronal loop, similar to the region near AR 8496 in which we previously found propagating disturbances (Section 5.2.2). We will now study this region in more detail and create running difference images of this region to see whether we can find similar propagating disturbances.

5.3.2 Discussion of the running difference and the propagating disturbances

We start with looking at loop A (see Figure 5.21), for the entire duration of the dataset. To build up a running-difference image of this very long time sequence, we created running-differences of 9 consecutive sequences of roughly 30 images. To keep the (already very low) 60 second cadence, we did not sum over consecutive images. From every frame we subtracted the previous frame, i.e. the one taken 60 seconds earlier. As we only analysed short intervals at a time, the data was not corrected for solar rotation. Once again we summed over two consecutive cross-sections, and thus, each position in the running-difference images covers a distance of roughly $1''$. By joining all the 'short' running-difference images together, we constructed a large running-difference image (shown in Figure 5.23) which stretches over a time interval of just over 5.5 hours. The black bands in this running-difference image are 5 minute gaps in the observational sequence or images where the pedestal read-out was extremely high and which therefore could not be used.

In the running-difference we see bright and dark bands appearing for the entire duration of the sequence. However, due to the very long period of time, this image is not detailed enough to understand what is happening. Therefore, we now concentrate on a part of the sequence, running

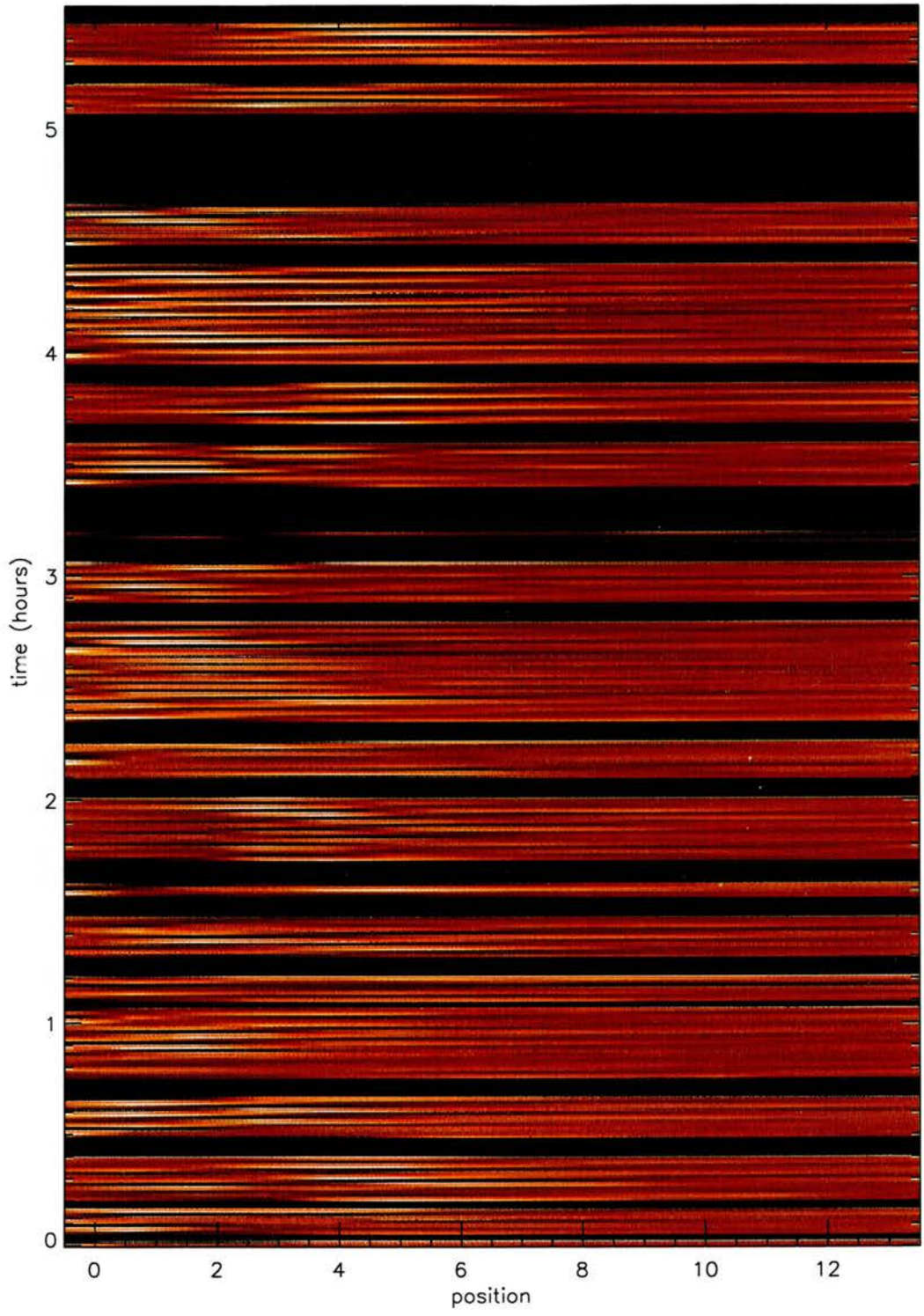

Figure 5.23: A running difference between the average time series for each position along the region indicated in Figure 5.21 between 0143 UT and 0715 UT on 19th August 1998.

from 0404 UT till 0430 UT. This is the longest interval in the dataset without a 5-minute gap or a high pedestal read-out. From this detailed running-difference image (Figure 5.22, left), it becomes clear that the bright and dark bands are diagonal bands, not unlike the ones we detected in the observations of the footpoint of the large coronal loop on 23rd march 1999 (Section 5.2.2). From the slopes in this running-difference image, the propagation speed has been calculated to be between 55 and 95 km s^{-1}. In the first half of the region, the amplitudes of the disturbance are about 5% – 8% and are 3 to 5 times higher than the level of the noise. As the disturbance travels along the tube, the amplitudes go down to about 2% before disappearing below the noise level. Due to the 60 second cadence, the diagonal bands appear stepwise rather then continuous. Because of this low temporal resolution, it is hard to make an estimate of the periodicity or to perform a wavelet analysis of this data. From a visual inspection, the disturbances appear similar to the ones observed before and from the full running-difference (Figure 5.23) it is clear that the signal is present for the entire duration of the dataset.

For loop B (see Figure 5.21), we only consider the 'clean' section of the dataset, i.e. the sequence between 0404 UT and 0430 UT where no 5-minute gape or high pedestal read-out occured. In the running-difference image (Figure 5.22, right) we see very strong dark and bright diagonal bands that are easily distinguishable for 20 positions, i.e. 14 000 km. Propagation speeds are calculated to be between 55 – 165 km s^{-1}. The amplitudes of the disturbance were estimated to be 5% – 8%, although peaks as high as 10% occurred as well. The amplitudes became weaker near the end of the tube and at position 20, they are only about a 1% variation compared to the background intensity.

Temperature and density of the loop footpoint

From Figure 5.21, we see that there appears to be another coronal structure behind loop A; this might interfer with the observational analysis. With this in mind, as well as the fact that the oscillations are more pronounced in loop B, the rest of the discussion of the density and temperature variation will concentrate on loop B.

The left image on the top row in Figure 5.24 is a plot of the intensity of the region we are studying. The Gaussian shape of the intensity along and across the loop is very similar to what we found in the 171 Å data of 23rd March 1999 (Figure 5.13). The average intensity along the loop shows the same increase and decrease, with the intensity increasing by a magnitude of just over 2 compared to the value of the intensity at the base of the structure. The maximum value occurs around position 24 along the loop, or, as each position now covers about 1″, about 24″ (17500 km) from the base. When comparing this with the running-difference image (left image in Figure 5.22), we again see that the oscillations are strongest in the lower half of the tube, where the intensity and density are

increasing. The left image on the bottom row in Figure 5.24 is a plot of the region in the 195 Å passband. This image was taken at 0404 UT on on 19th August 1998. Comparing this with the top row, the same conclusions can be drawn as for 23rd March 1999. The hotter material is concentrated right at the base of the structure; further along, the feature is hardly visible in the 195 Å passband.

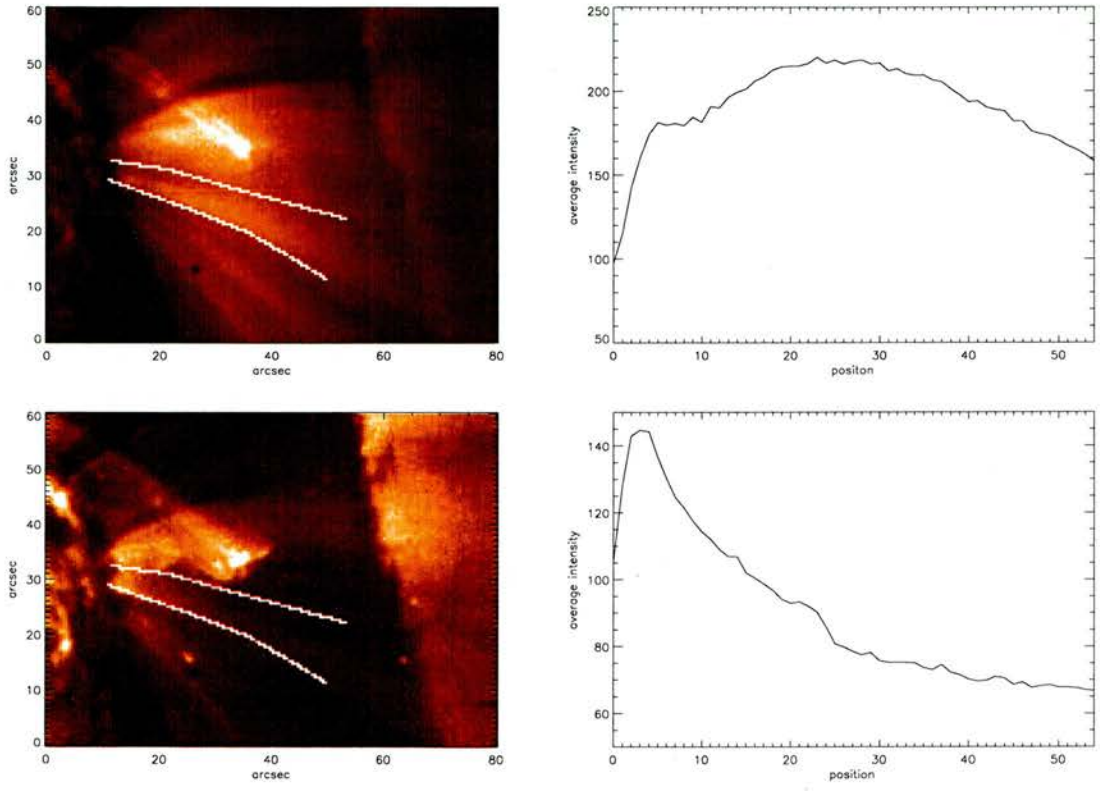

Figure 5.24: (left) A plot of the intensity (in the (left) 171 Å and (right) 195 Å passbands) of the loop footpoint. Brighter colours correspond to higher values. (right) The average intensity (in the (left) 171 Å and (right) 195 Å passbands) for each position along the structure.

The left image in Figure 5.25 was obtained by taking the ratio of a 195 Å and 171 Å image, taken at 0404 UT on 19th August 1998. It indicates that the temperature profile resembles an inverted Gaussian profile, both along and across the structure. The average temperature along the base of the loop decreases by about 7% before increasing and again, the minimum in temperature seems to occur a little further along than the 171 Å density maximum.

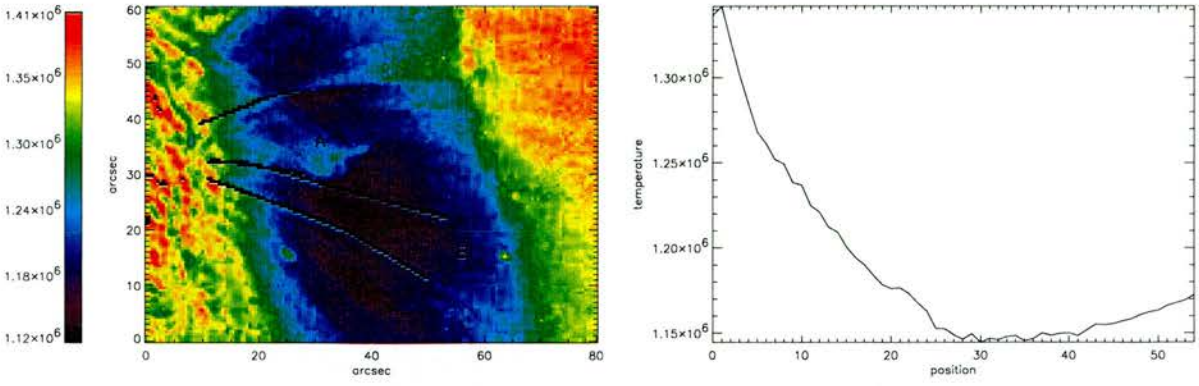

Figure 5.25: (left) A plot of the temperature of the loop footpoint. (right) The average temperature for each position along the structure.

5.4 Analysis and Results for April 2000

5.4.1 Observations

During April 2000, Joint Observing Programme 83 - *High cadence activity studies and the heating of coronal loops* - was run for a second time. With the results presented so far in this chapter and, at the same time, increased solar activity, in mind, we concentrated on regions which were displaying some signs of activity, rather than the 'quiescent' active regions that were observed in the March 1999 JOP 83 campaign. However, we did not explicitly look for regions that were flaring or erupting, partly due to technical constraints on mainly the TRACE instrument. TRACE observations were combined with SXT onboard Yohkoh and the CDS, EIT and MDI instruments onboard SOHO. For the more technical details of this observational campaign, see Appendix C. In the course of three weeks, we observed four different active regions. AR 8939 was observed as it crossed the disk, from 4 till 10 April 2000. During this period, there was no flaring activity of any significance in this active region. AR 8948 was observed between 11 and 16 April, although due to technical reasons, JOP 83 was not run on 14 April 2000. Initially, this region showed significantly more activity but quietened down in the second half of the week ; EIT observed M1 flares on 11 and 12 April and a C2 flare on 13 April. Finally, AR 8954 was observed on 17 April and AR 8955 on 18 and 19 April 2000.

The data we present in this section was taken by TRACE in the 171 Å passband. The various sequences are roughly about 20–25 minutes long, consisting of 512 × 512 pixel images, with a pixel size of 1″. The cadence varies between 7 and 11 seconds. The data is prepared in the same way as described in Section 5.2.1.

5.5 Results for April 2000

In Table 5.2, we give a summary of the properties of the oscillations found in this data. An actual overview of the analysis for each of the loops can be found in Appendix D. In this appendix, we show 4 different figures for each case of an observed oscillation; an actual image on which the loop footpoint is marked, a running-difference image, the average intensity (in the 171 Å passband) along the structure and an overview of the range of periods that were obtained above a 99.0 % confidence level from a wavelet analysis of the time series at each position. A range of amplitudes of the disturbance, compared to the background intensity is also given. In Table 5.2 we give a range of propagations speeds, amplitude variations and periods for each loop. The propagations speeds were calculated from the slopes in the running-difference images and the periods that are quoted are the ones where wavelet power was strongest.

The ranges of parameters of the examples of oscillations in Table 5.2 are very similar to what we found before. Disturbances propagate outwards with a velocity between 80 and 150 km/s. The variations in intensity are of the order of 2%-5% compared to the background brightness in the first half of the structure and then get weaker, of the order of 1%-2%, as they propagate along the structure. All periods found are again mainly in the 200–400 second range. The average intensity along each of the loops follows more or less the same profile as we found in the 23 March 1999 and 19 August 1998 loops. The 171 Å density initially increases, reaching a maximum somewhere between 6000 and 15 000 km from the base of the loops, before decreasing again. In some cases, a different profile was found for the intensity along the loop. However, a comparison with the actual image shows that in those cases, the base of the loop was unclear or obscured by another structure. Therefore, the intensity profile for the lower half of the loops could be alternated by material before or behind the loop we actually want to analyse. Comparing the average intensity along the footpoints with the running-difference images, we note again that the oscillations are most pronounced in the lower half of the region where the density is increasing.

Disturbances were often found in the same location for several consecutive days. However, although the overall shape of the structures showed little variation, it was usually not possible to identify exactly the same loops on different days. Finally, we remark here that a lot more examples of propagating disturbances were found in AR 8939 in comparison with the other active regions. Obviously this region was observed for a longer period of time than the other ones but, additionaly, this was also the more quiescent of the observed regions. Although similar disturbances were found in the other active regions, they were usually less clear and persistent. In general, examples of well defined, outward propagating disturbances are more often found in the larger loops that show very little variation or activity over extended periods of time.

Loop	Velocities (km/s)	Amplitudes (%)	Max Periods (s)
AR 8939			
4 April - Loop A	95–125	0.9–3.6	240–470
4 April - Loop A	95–125	0.9–3.6	240–470
4 April - Loop B	75–110	1.5–5.3	210–490
4 April - Loop C	100–195	0.7–5.7	170–520
4 April - Loop D	75–110	1.2–4.8	210–430
5 April - Loop A	135–180	1.5–4.8	230–470
7 April - Loop A	125–170	1.2–5.8	190–420
7 April - Loop B	90–145	0.9–4.9	210–340
7 April - Loop C	75–125	1.3–4.9	255–290
7 April - Loop D	85–125	1.0–4.0	300–410
8 April - Loop A	60–85	0.7–4.2	160–170
9 April - Loop A	95–155	1.1–3.5	170–185
9 April - Loop B	90–200	1.6–5.4	210–420
AR 8948			
11 April - Loop A	60–90	1.1–4.5	280–370
11 April - Loop B	90–140	1.1–4.2	220–370
11 April - Loop C	95–140	0.9–6.4	345–440
13 April - Loop A	120–185	0.8–4.1	250–370
AR 8954			
17 April - Loop A	130–200	1.3–5.0	210–480
17 April - Loop B	55–70	1.4–4.8	270–470
AR 8955			
18 April - Loop A	75–140	1.0–5.0	210–470
18 April - Loop B	100–165	1.0–5.0	255–390
19 April - Loop A	60–80	1.9–9.4	170–360

Table 5.2: Overview of oscillations found in April 2000 TRACE data.

5.6 Conclusions

We have analysed intensity variations in the base of a large,diffuse active region coronal loop, observed by TRACE on 23rd March 1999 in the 171 Å passband. We interpreted these oscillations as propagating slow magneto-acoustic waves, carrying an estimated energy flux of 4×10^2 ergs cm^{-2} s^{-1}. We found periods with the strongest power in the 180-420 s range and velocities of the order of 70 - 165 km s^{-1}. Due to the coincidence with the photospheric 5-minute period, there could be some form of coupling between the photosphere and the coronal loop, e.g. in the form of photospheric driving of the loop footpoints. The oscillations appeared strongest in the lower half of the structure. From an analysis of the density and temperature of the region, we found that in this lower half, i.e. the first about 17 000 km, the density in the 171 Å passband increased by a factor $\sim \sqrt{2}$. In the 195 Å pass band we found that most of the material was concentrated in the first 5000 or 6000 km. The temperature decreased by about 10%, with its minimum occuring slightly further along the structure than the 171Å density maximum.

In the running difference images of many of the small-scale loops of the active region itself, quasi-periodic brightenings are seen. The intensity variations are about 3% – 5% of the background intensity and from the wavelet analysis we found periods of the order of 200 – 400 seconds. These brightenings appear similar to the ones found by Berghmans & Clette (1999) and Berghmans et al. (1999a), which they interpret to be the EUV counterparts of the SXT active region transient brightenings.

From an analysis of TRACE 171 Å data, taken on 19th August 1998, we again found quasi-periodic disturbances in a region with similar density and temperature characteristics as the one in the 23rd March 1999 observations. In this case, the signal lasted for several hours and the amplitudes and velocities of the perturbations were of the same order as the oscillations described above. However, as the data had a low temporal resolution (60 second cadence), it was not possible to perform a detailed (wavelet) analysis.

All additional examples (April 2000) of oscillations in the footpoints of large coronal loops discussed here display a very similar range of parameters. The disturbances travel outward with a propagation speed between 80 and 150 km s^{-1}. The variations in intensity are of the order of 2%-5%, compared to the background brightness and these get weaker as the disturbance propagates along the structure. From a wavelet analysis at different positions along the structures, periods in the 200–400 seconds range are found.

Chapter 6

Conclusions

Results! Why, man, I have gotten a lot of results. I know several thousand things that won't work.
Thomas Edison

In this thesis we investigated various aspects, both theoretical and observational, of wave propagation in the solar corona. We restricted the theoretical study to travelling waves, generated by photospheric motions and propagating outwards from the Sun without total reflection.

In Chapters 2 and 3, we modified the standard Heyvaerts and Priest (1983) model to include a gravitationally stratified density and a radially diverging background magnetic field. When considering phase mixing of Alfvén waves in open field regions with a gravitationally stratified background density, we found that wavelengths lengthen when Alfvén waves propagate up in height. Therefore, it will take longer in a stratified atmosphere to build up the small lengthscales that are necessary for dissipation to be effective. When considering the resulting ohmic heating, we found that it is spread out wider than in an unstratified atmosphere and the maxima do not build up as high. This implies that a vertical stratification of the density makes phase mixing less efficient as a coronal heating mechanism in regions where the magnetic field is open. On the other hand, there are only very slight differences between the stratified and unstratified model for viscous heating. Heat is deposited over a similar range of heights and maxima reach almost identical values. However, the total amount of ohmic and viscous heating deposited into the plasma is not influenced by the gravitational stratification of the density. Therefore, we conclude that in a stratified atmosphere, the heat will be deposited higher up than in an unstratified atmosphere and that the viscous heating will be the dominant component in the heating process at lower heights. Additionally, we found that for a certain value of the resistivity, the height at which most heat will be deposited decreases when

temperatures increases or when the period decreases; a 1 or 2-minute oscillation can deposit most heat within a few solar radii and could therefore be a candidate for heating the coronal holes, while e.g. a 5-minute oscillation might be a way to deposit heat in the solar wind. Finally we remark that when the inhomogeneity in the horizontal direction, which causes phase mixing to occur, is sufficiently large, the effect of stratification is greatly reduced. Due to the rapid and strong phase mixing, energy can be dissipated at low heights, before the effects of stratification build up. However, when putting the obtained results into typical solar conditions, we had to conclude that the effect of stratification on the efficiency of phase mixing in the solar corona would still be large as the height at which most heat would be deposited through ohmic dissipation was increased considerably by stratification for a range of driving frequencies and temperatures.

In a next step (Chapter 3), we considered a background magnetic field that is radially diverging and we assumed that the density is only inhomogeneous in the horizontal direction. From this study of the effect of a diverging background magnetic field on phase mixing of Alfvén waves in an open field region we found that wavelengths shorten when the waves propagate up in height. Unlike stratification, a diverging background magnetic field enhances phase mixing and makes it more efficient, as waves on neighbouring field lines become out-of-phase quicker than in the uniform area case. Therefore, the lengthscales small enough for dissipation to be important will now build up faster and the waves will be dissipated quicker, i.e. at lower heights, when compared to the standard non-diverging case. Unlike in a stratified, non-diverging atmosphere, the current density and the vorticity behave in a similar manner and ohmic and viscous heating will have a similar importance in the heating process. The divergence of the background magnetic field introduces two competing effects on the current density or vorticity. The current density/vorticity builds up faster due to the shortening of the wavelengths, causing the maxima of the ohmic/viscous heating to occur at lower heights in comparison to the Cartesian case. Simultaneously, the shorter wavelengths cause phase mixing to be more efficient and due to this combination the maxima of the current density or vorticity occur at lower heights but are also lower than in the Cartesian case.

When considering different profiles for the background density, we found that in general, the maximum of the current density or vorticity occurs where the gradient in the density profile is largest as phase mixing is most efficient there. A profile modelling an individual plume in a coronal hole showed that more heat will be deposited outside the plume than inside when the density of the plume is not much higher than the density of the surrounding coronal hole. The maximum of the ohmic or viscous dissipation occurs low down at the sides of the plume rather than inside the actual plume. Finally, looking at different boundary conditions at $r = r_0$ showed that the initial profile of the perturbed magnetic field does influence where heat will be deposited into the plasma through ohmic or viscous dissipation.

As a last step, we studied the combined effect of a stratified density and a radially diverging background magnetic field on phase mixing of Alfvén waves. We calculated a WKB solution that incorporates both the density stratification and the divergence of the magnetic field. This approximate solution agrees very well with our numerical solutions and, when taking the appropriate limits, reduces to the solution for either a stratified density or a diverging magnetic field. We found that the efficiency of phase mixing depends strongly on the particular geometry of the configuration. Depending on the value of the scale height phase mixing can be either more or less efficient in comparison with the uniform non-diverging Heyvaerts and Priest solution.

In chapter 4, we introduced a technique called 'wavelet analysis'. We investigated how wavelet analysis can be used to determine properties of observed wave-like oscillations and, through coronal seismology, provide diagnostic information about the coronal plasma through which the oscillations are propagating. Based on the results of the previous chapters, we studied the wavelet transform of phase mixed Alfvén waves in various physical circumstances. In this thesis, we used the complex-valued Morlet wavelet, $\psi(\eta) = \pi^{-1/4} \exp(ik\eta) \exp\left(-\eta^2/2\right)$, consisting of a plane wave modulated by a Gaussian, as the basic wavelet. Working out the transform of simple harmonic functions analytically indicated a loss of the scale resolution for small values of the parameter k and a reduction in the temporal resolution for large k. Firstly, we made a comparison between two finite signals; a truly finite signal, i.e. a simple harmonic wave, cut off at a certain height and an Alfvén wave, dissipated by phase mixing. We demonstrated that, using a wavelet transform, it is possible to distinguish between these two 'finite' signals; the wavelet transform of a truly finite oscillations is distinctly different from the transform of a gradually damped oscillation. Therefore, one can use a wavelet analysis to determine whether an observed signal of finite lifetime is simply cut off, or gradually dissipated. Additionally, we showed that it is possible to extract an estimate for the value of the dissipation coefficient by fitting an analytical approximation to the numerical solution for the wavelet transform. As each dissipation mechanism has its own characteristic slope, a good fit between the analytical approximation and the transform of the observed oscillation could supply us with information on which dissipation is involved in the damping of the observed oscillation. In a next stage, we studied the wavelet transform of Alfvén waves in a gravitationally stratified atmosphere. The typical $e^{z/2H}$ lengthening of the wavelengths we found in Chapter 2, is clearly evident in the wavelet transform, thus providing an independent estimate of the value of the pressure scale height. When possible, this estimate can be compared to values obtained by different methods, e.g. when the temperature of the surroundings is known. Finally, the $\frac{1}{r^2}$ shortening of the wavelengths of Alfvén waves propagating in an atmosphere with a radially diverging background magnetic field is also present in a wavelet transform of such an oscillation. As the wavelength is directly related to the Alfvén speed, the variation of the wavelength with height provides information about both the coronal density and the magnetic field variation.

Our final Chapter 5 contains the observational part of this thesis. We reported on the detection of propagating disturbances along loop structures close active region as observed in the 171 Å passband by TRACE. The data we used was taken as part of JOP 83 - *High cadence activity studies and the heating of coronal loops*; an observational campaign that aimed to reduce the cadence of the TRACE observations to as low a value as possible while still retaining enough counts that events of interest would not be lost in the noise. A large fraction of this chapter was dedicated to a study of active region AR 8496, a large, stable active region present in the southwest quadrant, on 23 March 1999. In the footpoint of a large,diffuse coronal loop near this active region, we found quasi-periodic intensity variations. From a running-difference image of the 25-minute long time sequence, we found velocities of the order of 70–165 km s^{-1}. We employed a wavelet analysis to investigate significant periodicity in the observed oscillations and detected periods with the strongest power in the 180-420 s range. The oscillations appeared strongest in the lower half of the footpoint, where the density of the material observed in the TRACE 171 Å passband was found to increase. In the 195 Å pass band we found that most of the material was concentrated in the first 5 or 6 Mm along the loop. Since the propagating disturbances were found as variations in the intensity, they could be interpreted as magneto-acoustic modes. Additionally, they were found to travel at the order of the coronal sound speed, and thus we consider these oscillations to be good candidates for propagating slow magneto-acoustic waves. We estimated that the disturbances carried an energy flux of the order of 4×10^2 ergs cm^{-2} s^{-1}, which is only a very small fraction of the total energy required to heat coronal loops.

We note here that the above interpretation is only valid if we assume the loop to be linear and homogeneous and that for a non-linear, non-homogeneous medium, there could be other possible interpretations. In many of the small-scale loops of the active region itself, quasi-periodic brightenings were seen, which appear similar to the ones found by Berghmans & Clette (1999)

In 171 Å TRACE data, taken on 19th August 1998 and during April 2000, we found several more examples of quasi-periodic propagating disturbances in the footpoints of large, diffuse coronal loops. All oscillations displayed a very similar range of parameters; propagation speeds were generally found in the 80– 150 km s^{-1} range. The variations in intensity amounted to about 2%-5%, compared to the background brightness and typically got weaker as the disturbance propagated along the structure. A wavelet analysis at different positions along the structures, indicated periods in the 200–400 seconds range. Obviously, the observation of coronal oscillations has important consequences as it could provide us with useful information for many numerical or analytical models of wave heating in the solar corona.

6.1 Suggestion for future work

In this thesis, we investigated the effect of a radially diverging background magnetic field on phase mixing of Alfvén waves. However, in reality, the magnetic field in the photosphere is strongly concentrated at supergranule boundaries and expands super-radially due to the rapidly decreasing density in the chromosphere and transition region. This super-radial divergence of the magnetic field could have important effects on Alfvén waves as they propagate up in height and on the efficiency of phase mixing as a coronal heating mechanism. Additionally, it would be interesting to investigate the effect of a random as opposed to a periodic driver on phase mixing of Alfvén waves. Both the aspect of a super-radially diverging background magnetic field and a random photospheric driver will probably have to be studied using numerical simulations.

Our study of wavelet analysis considered phase mixing of Alfvén waves, only because they can be described by a single WKB expression. We found that a wavelet analysis of observed wave-like oscillations can provide important information about the physical surroundings in which the oscillations are found. However, slow magneto-acoustic waves seem to be observed much more frequently. Although we expect a lot of the properties of Alfvén waves to transfer to slow waves propagating along magnetic field lines, there will be considerable differences. It would be worthwhile studying the wavelet transform of propagating slow magneto-acoustic waves, in different physical circumstances. Results from such a study could then be applied to wave-like intensity variations similar to the ones we discussed in Chapter 5. Although the spatial and temporal resolution of the present generation spacecrafts might not be sufficient to perform an analysis as detailed as the one described in Chapter 4, it will be possible to obtain an estimate for some of the coronal parameters. In this way, wavelet analysis could be used as an alternative approach to 'coronal seismology'. Obviously, the applications of wavelet analysis do not have to be restricted to solar observational data. Often the signal-to-noise ratio in magneto-spheric data is a lot better, which could provide us with an opportunity to perform a 'full' wavelet analysis.

The observational analysis in this thesis was entirely based on observations taken by TRACE in the 171 Å passband. However, as described in Appendix C, JOP 83 (April 2000) involved a lot more instruments. A brief comparison between images in the 171 Å ($\sim$ 1MK) and 195 Å ($\sim$1.5 MK) passbands, both taken by TRACE, indicated considerable differences between the loop footpoints at the respective temperatures. During the April 2000 campaign, the EIT instrument observed mainly in the 195 Å passband. A detailed analysis of this data is necessary to obtain a better understanding of the propagating disturbances found in the TRACE sequences. Co-temporal and co-spatial data taken by CDS and Yohkoh will enable us to analyse the same loop footpoint in a temperature range that covers a considerable part of the solar atmosphere. An analysis of the MDI data could

provide us with information on the driver of the propagating disturbances. However, to obtain a full understanding of the observed wave-like disturbances, it will be necessary to set up an analytical model. Such a model would have to account for the observed periods and propagation speeds. Additionally, it would have to explain why the amplitudes of the oscillations appear strongest in the lower part of the loops and consequently decrease as they propagate up along the loop. Only a combination of the observational results and a theoretical model will determine why the propagating disturbances are found in some loops and not in others, and whether the oscillations have any significance in relation to the coronal heating problem.

Appendix A

Calculation of the WKB-solutions

If mathematically you end up with the wrong answer, try multiplying [by] the page number.
Finagle's Corollary

The phase mixing equation for the perturbed velocity in a stratified atmosphere with a radially diverging background magnetic field is given by

$$k^2(\theta)e^{-\frac{1}{H}\left(1-\frac{1}{r}\right)}v+\left(\frac{\lambda_0}{2\pi r_0}\right)^2\frac{1}{r^3}\frac{\partial^2}{\partial r^2}\left(\frac{v}{r}\right)+i\Lambda_\nu^2\Omega\left(\theta_0^2\frac{\partial^2 v}{\partial r^2}+\frac{1}{r^2}\frac{\partial^2 v}{\partial\theta^2}\right)=0, \tag{A.1}$$

where $k^2(\theta)=\frac{\Omega^2}{v_A^2(\theta)}$ and $\Lambda_\nu^2=\frac{\rho_0\nu\Omega_0\mu}{B_0^2}\left(\frac{\lambda_0}{2\pi r_0\theta_0}\right)^2$.

Now set $\chi=\frac{v}{r}$ so that

$$k^2(\theta)e^{-\frac{1}{H}\left(1-\frac{1}{r}\right)}\chi+\left(\frac{\lambda_0}{2\pi r_0}\right)^2\frac{1}{r^4}\frac{\partial^2\chi}{\partial r^2}+i\Lambda_\nu^2\Omega\left(\frac{\theta_0^2}{r}\frac{\partial^2 r\chi}{\partial r^2}+\frac{1}{r^2}\frac{\partial^2\chi}{\partial\theta^2}\right)=0\,.$$

Setting $\chi=g(r)X(R,\theta)$ with $R=f(r)$ and only taking into account second order derivatives in the damping term we get

$$\begin{aligned}gf'^2\frac{\partial^2 X}{\partial R^2}+(gf''+2g'f')\frac{\partial X}{\partial R}+g''X+r^4k^2\left(\frac{2\pi r_0}{\lambda_0}\right)^2e^{-\frac{1}{H}\left(1-\frac{1}{r}\right)}gX\\ +i\Lambda_\nu^2\Omega\,r^4\left(\frac{2\pi r_0}{\lambda_0}\right)^2\left(\theta_0^2gf'^2\frac{\partial^2 X}{\partial R^2}+\frac{1}{r^2}g\frac{\partial^2 X}{\partial\theta^2}\right)=0\,,\end{aligned} \tag{A.2}$$

or,

$$\begin{aligned}\frac{\partial^2 X}{\partial R^2}+\left(k^2\left(\frac{2\pi r_0}{\lambda_0}\right)^2\frac{r^4e^{-\frac{1}{H}\left(1-\frac{1}{r}\right)}}{f'^2}+\frac{g''}{gf'^2}\right)X+\left(\frac{f''}{f'^2}+\frac{2g'}{gf'}\right)\frac{\partial X}{\partial R}\\ +i\Lambda_\nu^2\Omega\left(\frac{2\pi r_0}{\lambda_0}\right)^2\left(\theta_0^2r^4\frac{\partial^2 X}{\partial R^2}+r^2\frac{1}{f'^2}\frac{\partial^2 X}{\partial\theta^2}\right)=0\,.\end{aligned} \tag{A.3}$$

To obtain a second order partial differential equation with constant coefficients, we eliminate the first order derivative by settings its coefficient equal to zero:

$$\frac{f''}{f'^2} + \frac{2g'}{gf'} = 0 \qquad \Rightarrow \quad g = (f')^{-1/2} .$$

To leading order, the coefficient of X is constant in R if:

$$f'^2 = r^4 e^{-\frac{1}{H}\left(1-\frac{1}{r}\right)} ,$$

or,

$$R = f(r) = \int_1^r r^2 e^{-\frac{1}{2H}\left(1-\frac{1}{r}\right)} dr ,$$

where we have chosen the positive square root to match the outgoing wave condition. We then find

$$g = r^{-1} e^{\frac{1}{4H}\left(1-\frac{1}{r}\right)} .$$

Neglecting the second term in the coefficient of X which is of smaller order, Eq. (A.3) becomes:

$$\frac{\partial^2 X}{\partial R^2} + \left(\frac{2\pi r_0}{\lambda_0}\right)^2 k^2 X + i\Lambda_\nu^2 \Omega \left(\frac{2\pi r_0}{\lambda_0}\right)^2 \left(\theta_0^2 r^4 \frac{\partial^2 X}{\partial R^2} + \frac{1}{r^2} e^{\frac{1}{H}\left(1-\frac{1}{r}\right)} \frac{\partial^2 X}{\partial \theta^2}\right) = 0 . \tag{A.4}$$

We now see that the WKB-solution in the zero dissipation case is given by

$$X = \exp\left(-ik(\theta)\frac{2\pi r_0}{\lambda_0} R\right) , \tag{A.5}$$

and to obtain a solution to the non-zero dissipation case, we set

$$X = \exp\left(-ik(\theta)\frac{2\pi r_0}{\lambda_0} R_0\right) F(R_1) , \tag{A.6}$$

where $R_0 = R$ and $R_1 = \varepsilon R_0$. From Eq. (A.4) we then get

$$\begin{aligned} &\left[\left(-ik\frac{2\pi r_0}{\lambda_0}\right)^2 F + 2\varepsilon\left(-ik\frac{2\pi r_0}{\lambda_0}\right)\frac{\partial F}{\partial R_1} + \varepsilon^2 \frac{\partial^2 F}{\partial R_1^2}\right] + k^2 \left(\frac{2\pi r_0}{\lambda_0}\right)^2 F \\ &\quad + i\Lambda_\nu^2 \Omega \left(\frac{2\pi r_0}{\lambda_0}\right)^2 \left\{\theta_0^2 r^4 \left(-ik\frac{2\pi r_0}{\lambda_0}\right)^2 F + \frac{e^{\frac{1}{H}\left(1-\frac{1}{r}\right)}}{r^2}\left(-ik'\frac{2\pi r_0}{\lambda_0} R_0\right)^2 F\right\} = 0 , \end{aligned} \tag{A.7}$$

or,

$$\varepsilon \frac{1}{F}\frac{\partial F}{\partial R_1} = -\frac{1}{2}\Lambda_\nu^2 \Omega \left(\frac{2\pi r_0}{\lambda_0}\right)^3 k \left(\theta_0^2 r^4 + r^{-2} e^{\frac{1}{H}\left(1-\frac{1}{r}\right)} \frac{k'^2}{k^2} R_0^2\right) .$$

And with

$$\frac{\partial F}{\partial R_1} = \frac{\partial F}{\partial r}\frac{\partial r}{\partial R_1} = \varepsilon^{-1}\frac{\partial F}{\partial r}\frac{\partial r}{\partial R_0} = \varepsilon^{-1}\left(f'(r)\right)^{-1}\frac{\partial F}{\partial r} ,$$

we find,

$$\ln F = -\frac{1}{2}\Lambda_\nu^2 \Omega \left(\frac{2\pi r_0}{\lambda_0}\right)^3 k \int_1^r \theta_0^2 r^6 e^{-\frac{1}{2H}\left(1-\frac{1}{r}\right)} + e^{\frac{1}{2H}\left(1-\frac{1}{r}\right)} \frac{k'^2}{k^2} R^2 dr .$$

The full solution for the perturbed velocity then becomes:

$$\begin{aligned} v = \sin(\pi\theta) \exp\left(-i\frac{2\pi r_0}{\lambda_0} k(\theta) R\right) \exp\Bigg[&\frac{1}{4H}\left(1-\frac{1}{r}\right) - \\ &\frac{1}{2}\Lambda_\nu^2 \Omega \left(\frac{2\pi r_0}{\lambda_0}\right)^3 k \int_1^r \left(\theta_0^2 r^6 e^{-\frac{1}{2H}\left(1-\frac{1}{r}\right)} + \frac{k'^2}{k^2} R^2 e^{\frac{1}{2H}\left(1-\frac{1}{r}\right)}\right) dr\Bigg] , \end{aligned} \tag{A.8}$$

with $R = \int_1^r r^2 e^{-\frac{1}{2H}\left(1-\frac{1}{r}\right)} dr$ and $\Lambda_\nu^2 = \frac{\varrho_0 \nu \Omega_0 \mu}{B_0^2} \left(\frac{\lambda_0}{2\pi r_0 \theta_0}\right)^2$.

The solution for the perturbed magnetic field can be obtained in a similar manner. When we consider a model with a radially diverging background magnetic field but no stratification of the density, we can either repeat the method described above or we can simply take the limit $H \to \infty$ in Eq. (A.8). To obtain a solution with a uniform background field and stratification, we set $r = 1 + \frac{\lambda_0}{2\pi r_0} z$ and $x = r\theta$ in Eq. (A.8).

Appendix B

Emission lines and temperatures

T	log T	Helium	Oxygen	Neon	Magnesium	Silicon	Iron
1.6×10^4	4.20	He I	-	-	-	-	-
9.1×10^4	4.96	-	O III	-	-	-	-
1.8×10^5	5.25	-	O IV	Ne IV	-	-	-
2.3×10^5	5.37	-	O V	Ne V	-	-	-
2.5×10^5	5.4	-	-	-	Mg V	-	-
4.3×10^5	5.63	-	-	Ne VI	Mg VI	-	-
5.0×10^5	5.7	-	-	Ne VII	-	-	-
6.3×10^5	5.8	-	-	-	Mg VII	-	-
7.9×10^5	5.9	-	-	-	Mg VIII	Si VIII	-
9.6×10^5	5.98	-	-	-	Mg IX	Si IX	Fe X
1.4×10^6	6.14	-	-	-	Mg X	Si X	Fe XI Fe XII
1.6×10^6	6.2	-	-	-	-	Si XI	Fe XIII
1.9×10^6	6.27	-	-	-	-	Si XII	Fe XIV Fe XV
2.7×10^6	6.43	-	-	-	-	-	Fe XVI
7.9×10^6	6.9	-	-	-	-	-	Fe XIX

Table B.1: A selection of frequently used lines and their corresponding temperatures (Mason et al., 1997; Kjeldseth-Moe & Brekke, 1998).

Appendix C

SOHO/TRACE Joint Observing Programme 083 - High Cadence Activity Studies and the Heating of Coronal Loops

Authors: Robert Walsh (St Andrews),
Jack Ireland (ESA/GSFC),
Ineke De Moortel (St Andrews).

Contacts: Ted Tarbell (TRACE),
Richard Harrison (CDS),
Julia Saba (MDI),
Sarah Matthews (Yohkoh).

E-mail Addresses: robert@mcs.st-and.ac.uk,
ireland@esa.nascom.nasa.gov,
ineke@mcs.st-and.ac.uk,
tarbell@sag.space.lockheed.com,
harrison@solg2.bhnsc.rl.ac.uk,
sam@msslac.mssl.ucl.ac.uk.

Progress:	First Draft	March 1998
	Second Draft	February 2000
	Latest revision	March 2000

Objective:

Our aim is to investigate rapid time variation (down to the order of seconds) around and within a target coronal loop system and relate these dynamical changes to theoretical models for various dynamic coronal loop heating mechanisms.

Conditions Necessary to Run:

Occurrence of a suitably well defined coronal loop system (on either the disk or limb) and involvement of at minimum TRACE.

Scientific Case:

One of the principle objectives of the TRACE, SOHO and Yohkoh Missions is to tackle the difficult problem of how the solar corona is heated. With the wide variety of structures present in this dynamic environment, it is likely that several different mechanisms play their role in the energy deposition. However, as to which mechanism dominates in a particular solar region is under debate. Coronal loop structures are believed to outline the Sun's magnetic field as it rises through the dense photosphere and spreads out into the rarefied corona. These loops are amongst the hottest regions of the corona (typically 1 10 MK) and appear to show changes down to the cadence threshold of current instrumentation (Strong 1994). This Joint Observing Programme between TRACE, SOHO and Yohkoh seeks to investigate, through a selection of differing observing sequences over a range of timescales, the dynamic heating properties of coronal loops.

This JOP was first run sucessfully in March 1999. Results from that observing campaign are given in the following.

A: Oscillations in Coronal Loops

Wave heating mechanisms are thought to play an important role in the heating of coronal loops. The resonant absorption of MHD waves in loop type cavities predicts narrow regions of significant energy deposition: phase mixing of Alfvén waves predicts a strongly time dependent amplitude damping. The unambiguous detection of these mechanisms would be a great leap forward in our understanding the role of MHD wave dynamics in coronal loops. Estimates of the wave periods generated by inputing typical coronal parameters to these models suggest that high cadence observations will be very important in the search for conclusive evidence.

Fundamentally, we wish to determine the characteristic behaviour of oscillations in coronal loops.

EUV coronal oscillations have been found before; for example, a 262s period oscillation is described by Chapman et al. 1972); Antonucci et al. (1984) see both 117s and 141s. Harrison (1987) sees a 20 minute oscillation in a loop system which could be slow standing magnetoacoustic waves as described by Roberts et al. (1984). Recently, Ireland et al. (1999a) describe a wavelet analysis of spatially restricted CDS data in which they find co-temporal 300s period oscillations at chromospheric and transition region temperatures.

TRACE permits multi temperature views of target loop systems at high cadence over fields of view bigger than those available with CDS. Using JOP 83 observations from March 23rd 1999, De Moortel, Ireland & Walsh (see Chapter 5) investigate a set of TRACE 171 A observations of a bright loop footpoint of a diffuse coronal loop structure. A wavelet analysis displays outward propagating perturbations with periods 180-42 0 s at approx. 70 - 165 km s^{-1}. These authors suggest that the osc illations are slow magneto-acoustic waves.

B: Small scale transient EUV brightenings

Recent interest has centred on the concept that the corona is the result of the cumulative effect of many small scale, localised heating bursts. With improved spatial and temporal resolution, the observed evolution of many discrete brightenings over a wide range of temperatures has been estab lished.

Bocchialini, Vial and Einaudi (1997) perform a statistical analysis on SUMER data of an EUV bright point and deduce that self-similiar structures exist with scales much smaller that the instrument resolution. Shimizu and Tsuneta (1997) provide a survey of intensity changes in an active region viewed by SXT. They relate the small brightenings to localised regions within loops. Shimizu (1995) describes many frequent flare-like brightenings, mostly in the form of single and multiple loops observed by the Soft X-ray Telescope (SXT) on Yohkoh. The loop heating appears to occur at either the footpoints or loop intersection and he terms these events "Active Region Transient Brightenings" (ARTBs). EUV transient brightenings in coronal loops are described by Berghmans and Clette (1999) - their statistical analysis leads them to conclude that these "loop events" are EUV counterparts of ARTBs (Berghmans et al., 1999b).

In the previous run of JOP 83, Ireland, Wills-Davey and Walsh (1999b) made a study of 27 small dynamic brightening events in 171 A line with 9s cadence and 1" resolution. Their results showed the brightenings displayed quite complex structures consisting of small scale loops with hot, dense plasma flowing along them, often over 100 km s^{-1}.

C: Emission and Temperature Variations along a Coronal Loop

The temperature profile along a magnetic loop is very sensitive to the position in the loop where

the heat is deposited, the lengthscale of the energy deposition and the lifetime of the event (Walsh, 1999). Priest (1998) applies a very simple analytical model to compare the temperature structure for several different heating profiles with SXT temperature measurements along a large (> 100 Mm) loop. Ireland et al. (1999a) analyses CDS, low cadence (approx. 1 hour) observations to derive loop temperature via line ratio techniques. Kano and Tsuneta (1996) measure the temperature along X-ray active region loops and find that the temperature profile has several small fluctuations which were larger that the observational error. These variations may reflect actual spatial fluctuations of the heat input to the loop. Walsh and Georgoulis (1999) introduce a coronal loop model to examine the plasma response to energy deposition events over a range of lengthscales and timescales. They show that the spatial fluctuations in temperature can be reproduced by small scale, localised heating events. However, the heating must be dynamic in nature. Static heating models cannot reproduce these types of spatial variation. In fact, Walsh, Bell and Hood (1996) demonstrate that even a simple sinusoidal variation in the heat input with respect to time yields an apex temperature that can differ widely from that expected with a static model. These spatial heating simulations could be used to "recreate" the observed, evolving temperature profile along a loop. Thus, a constraint would be placed on the lengthscale, location and lifetime of the heat input and consequently upon the possible heating mechanism itself. The superior cadence abilities of the TRACE instrument would invaluable in this context with EUV observations of bright loops down to the order of tens of seconds (see Basic Method below). The diagnostic capabilities of CDS will also be utilised to determine a range of plasma parameter values and velocity measurements.

D : Other Instrument Involvement

Complementary to the TRACE observations, the spectral capabilities of CDS (plasma density, velocity, turbulent nature and "average" temperature measurements) will be essential, as will coincident MDI magnetograms when the target system is on the disc. Yohkoh will provide coverage in higher temperature lines. EIT will provide information on any significant events that occur exterior to the TRACE/CDS field of view (for example, a prominence eruption).

Basic Method:

The JOP should be run as a target of opportunity programme - i.e. listed for a period of about 3-4 weeks.

The TRACE component of this JOP is split into three related observing sequences which together form a thorough examination of the activity within coronal loops. These sequences are graded with regard to increasing cadence. They are:

- TJOP1 - Variations in Loop Structure (minutes),
- TJOP2 - High Cadence Temperature Measurements along Loops (orders of tens of seconds) ,

- TJOP3 - Rapid Variations of Loop Emission (order of seconds).

For each run of the JOP either one TJOP or a selection of the TJOPs will be used - dependent on the target and the choice of the JOP leaders. The instrumental support from SOHO and Yohkoh for each TJOP is given below in Operating Details.

Pointing and Target Selection:

Both disk and limb target loop systems will be considered where apparent loop structure is well defined in EIT and SXT images. With increased solar activity at time of writing (February 2000) the JOP leaders will on this occasion concentrate upon loop systems which are displaying some clear signs of activity (microflaring for example) as compared to the "static, quiescent" loops examined in the March 1999 JOP 83 campaign. However, see the note under TJOP3 for certain constraints on this. The JOP leaders are not looking a region that is flaring and/or erupting.

Note that the CDS LOOPS_3 sequence has a specfic need for precise pointing. For example, within one run, the LOOPS_3 slit could be placed on the apex of the loops and then at the footpoint areas. For on disc targets, MDI magnetograms will be of immense help in target positioning assuming that for a simple on-disk bipolar region, the loop apex lies between the areas of opposite polarity while the footpoints are essentially the areas of strong magnetic field. (see Operating Details below).

On disk targets would involve all the instruments as indicted below. It would be nice to select region within the MDI high resolution field. Limb targets would be studied using TRACE, CDS, EIT and SXT only.

Operating Details:

(i) TRACE - studies to be run for each TJOP:

TJOP1 : High cadence EUV (195, 171, 284) and Ly alpha exposures with intermittent CIV for transition region monitoring.
Area : 1024 × 1024 at 0.5"
Cadence : approx. 30s-60s

TJOP2 : Higher cadence EUV Observations in two wavelengths (195, 171) alternatively to produce "temperature along loop" measurements.
Area : 512 × 512 at 1.0"
Cadence : approx 10-15 s with 3-5 compression.

TJOP3 : Rapid imaging of part of loop structure with one line (brightest of 195 or 171) producing fastest cadence possible with TRACE for oscillation analysis and brightening study.

Area : 512 × 512 at 1.0"

Cadence : 9 s for approx. 25 minute period

NOTE: The clearest way of understanding how this cadence was achieved would be to look back to the last run on March 23rd 1999. In brief, Ted Tarbell put together some experimental runs using 2 × 2 binning of the CCD which would only run during the radiation-free portions of the TRACE orbit ie for about 25 minutes at a time. In that way, the radiation testing was skipped and AEC (Automatic Exposure Control) was trusted to keep us at good exposures and avoids using too much mass memory. Ted Tarbell calculated the .utim files for the 4 wavelength combinations for the specific day of observations, computed the HLZ's and checked the mass memory with the timeline program. However, this means that you are relying on AEC (not safeframe) for lumogen protection and thus probably should not be pointed at a very hot active region.

(ii) CDS - Studies to be run in conjunction with the observing sequences introduced in JOP59. This study is split into three sub-JOPS as indicated below (see actual JOP for more details).

Sub-JOP1: LARGEBP2 (CDS Study 10, Variations 25 or 26)

NIS (Normal Incidence Spectrometer), 2 × 240 slit, 240 × 240 area, 120 locations

Exposure 45s (Var 25) or 20s (Var 26 - if very bright)

Duration 6949s (Var 25) or 6579s (Var 26).

Lines: He I 584, O III 599, O V 629, Ca X 557, Mg IX 368, Mg X 625, Si X 346, 356, Fe XII 364, Fe XIII 348, Fe XIV 333, Fe XVI 360, Si XII 520, background 355, 335.

Sub-JOP2: Run EJECT_V3 once followed by a series of LOOPS_2 and a final EJECT_V3. Total duration should be several hours - the longer the better.

EJECT_V3 (CDS Study 11, Variation 18)

NIS, 4 × 240 slit, 240 × 240 area, 60 locations,

Exposure 10s, Duration 991s.

Lines: He I 584, O V 629, Si X 347, 356, Mg IX 368, Fe XVI 360.

LOOPS_2 (CDS Study 12, Variation 7)

NIS, 2 × 240 slit, 10 × 240 area, 5 locations

Exposure 20s. Duration 134 per raster.

Lines: He I 584, O V 629, Mg IX 368, Fe XVI 360.

Sub-JOP3: Run EJECT_V3 once followed by a series of LOOPS_3 and a final EJECT_V3. Total duration should be several hours - the longer the better.

EJECT_V3 - see above.

LOOPS_3 (CDS Study 123, Variation 1)

NIS, 4 × 240 slit, 4 × 120 area, 1 location

Exposure 10s - 50 rasters. Duration 707s.

Lines: He I 584, O V 639, Mg IX 368, Fe XVI 360.

SPECIAL CASE : When TJOP2 is being run, the CDS PROFILE study should be given priority for producing the temperature along the loop for comparison with TRACE runs.

PROFILE (CDS Study 283)

NIS, 2x240 slit, 240x240 area, 120 location

Exposure 30s - 120 rasters. Duration 1hr14m22s.

Lines: He I 584, O V 639, Mg IX 368, Fe XVI 360, Fe XVI 335, Fe XIV 334, Fe XIV 353, Fe XII 352, Fe XII 364.

(iii) EIT - Ensure that there are full-Sun images in Fe IX/X, Fe XII within the TRACE/CDS Study timeframe. Ensure in both cases that there is a He II image near in time for alignment with CDS He I.

(iv) MDI - Minimum requirement is one minute cadence magnetograms which cover the target active region, at least for the times TRACE is running at its highest cadence. If the target active region is in the MDI high res FOV then high res magnetograms are preferred to full disk if at all possible, particularly during the TRACE high-cadence times.

(v) Yohkoh (SXT) - Ensure at a minimum SXT synoptic observations during JOP and, if possible, home in on selected region for higher cadence observation.

Appendix D

Overview of oscillations found in TRACE data taken with JOP83 - April 2000

D.1 Introduction

In this appendix, we give an overview of oscillations found in footpoints of long, diffuse coronal loops. The observations were taken by TRACE, as part of JOP 83, from 04 until 19 April 2000. For each case of an observed oscillation, we show 4 different figures. A first figure is a typical image of the observational sequence in which the oscillation was found. The structure that is indicated in this figure shows the region that supports the disturbance. The second figure is a running-difference image of the average time series for each position. From each frame we subtracted the frame taken approximately 90 seconds earlier. The propagation speeds are estimated from the slope of the bright and dark, diagonal ridges in this running-difference image. The average intensity, plotted in the third figure, is the average intensity along the structure, at the start of the observational sequence. To obtain an average intensity, we added all the data counts along a cross-section, and divided by the number of pixels. The final figure shows the range of periods that were obtained from a wavelet analysis of the time series at each position. These periods are situated above the 99.0 % confidence level and inside the cone of influence. The diamonds in this figure indicate where the strongest wavelet power is situated for each position. A range of amplitudes of the disturbance, compared to the background intensity is also given.

D.2 Active Region AR 8939

D.2.1 4 April 2000

Loop A - 0928 UT

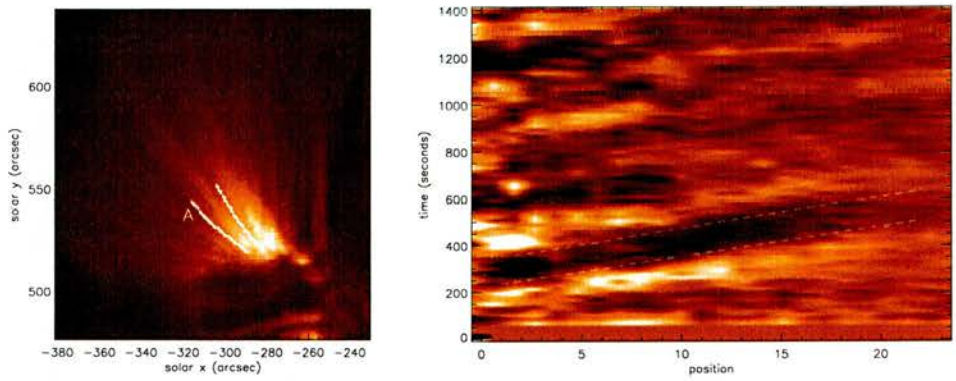

Figure D.1: image and running difference, 4 April 2000 - 0928 UT

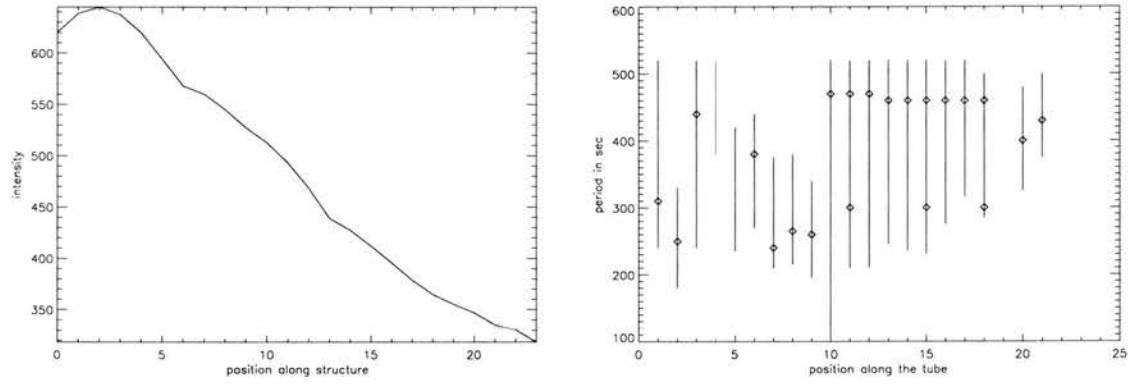

Figure D.2: Average intensity and periods along loopA, 4 April 2000 - 0928 UT

- 178 images, with a cadence of 8 seconds
- velocity estimate from the running difference, 95–125 km/s
- amplitudes between 0.9% and 3.6%
- periods between 100 and 520 sec (max between 240 and 470 sec)

Loop B - 0928 UT

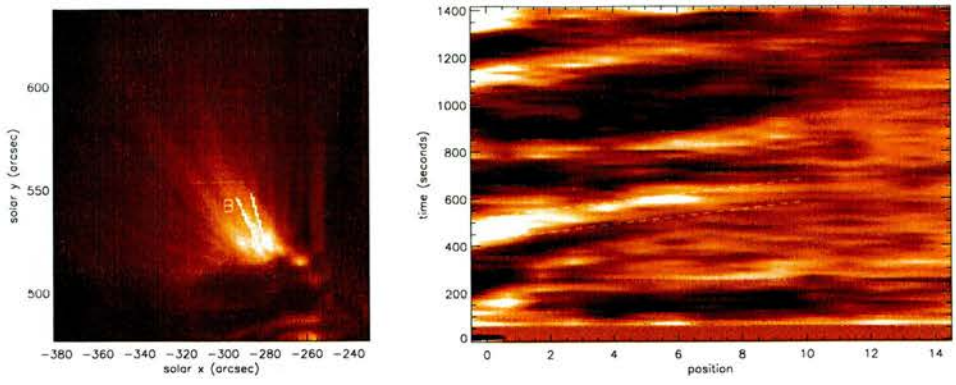

Figure D.3: image and running difference, 4 April 2000 - 0928 UT

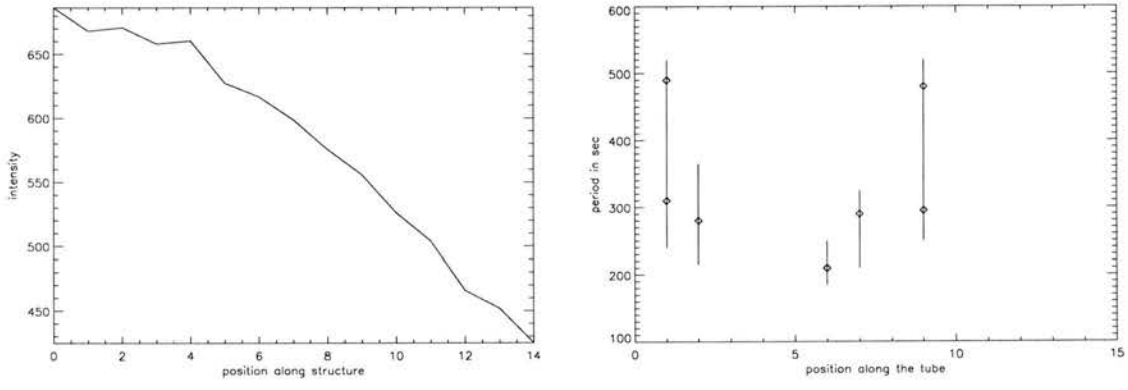

Figure D.4: Average intensity and periods along loop B, 4 April 2000 - 0928 UT

- 178 images, with a cadence of 8 seconds
- velocity estimate from the running difference, 75–110 km/s
- amplitudes between 1.5% and 5.3%
- periods between 185 and 520 sec (max between 210 and 490 sec)

Loop C - 0928 UT

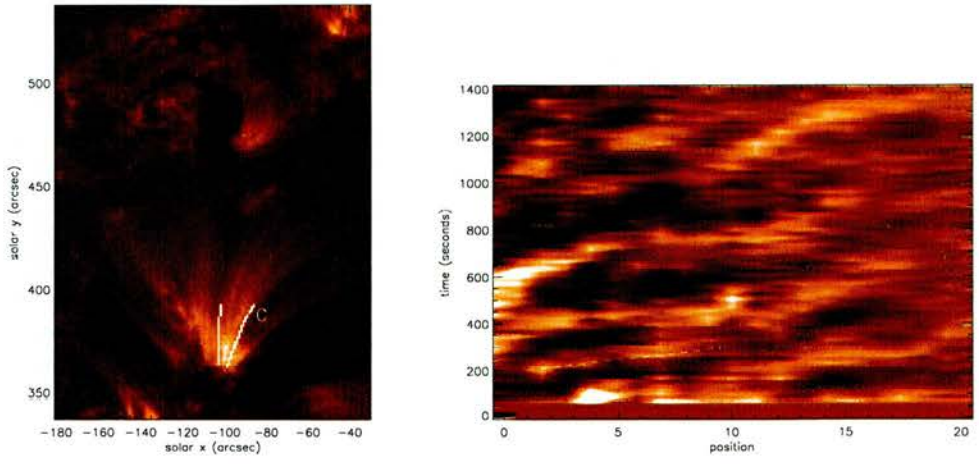

Figure D.5: image and running difference, 4 April 2000 - 0928 UT

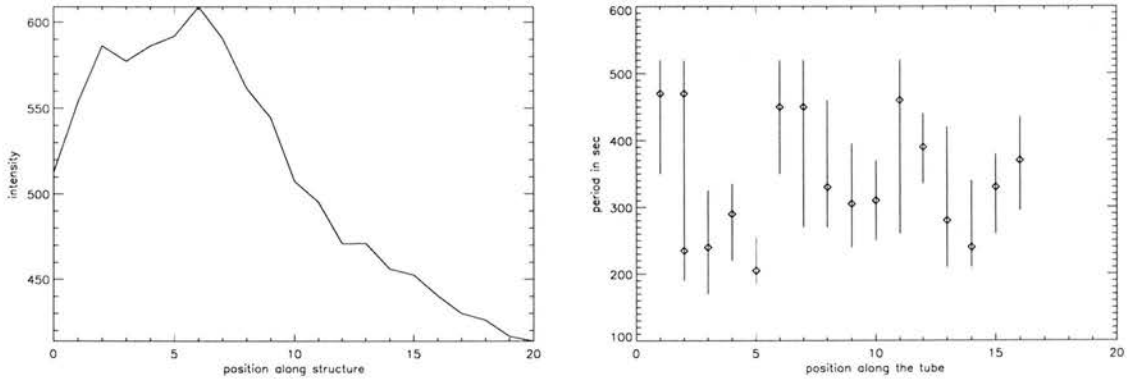

Figure D.6: Average intensity and periods along loop C, 4 April 2000 - 0928 UT

- 178 images, with a cadence of 8 seconds
- velocity estimate from the running difference, 100–195 km/s
- amplitudes between 0.7% and 5.7%
- periods between 170 and 520 sec (max between 205 and 470 sec)

Loop D - 0928 UT

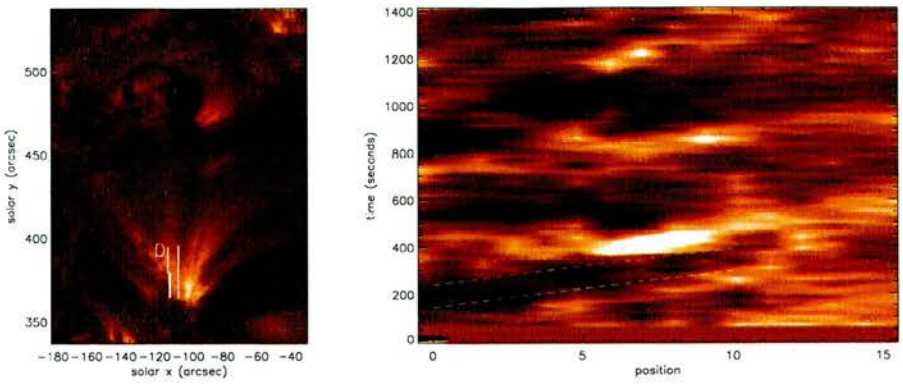

Figure D.7: image and running difference, 4 April 2000 - 0928 UT

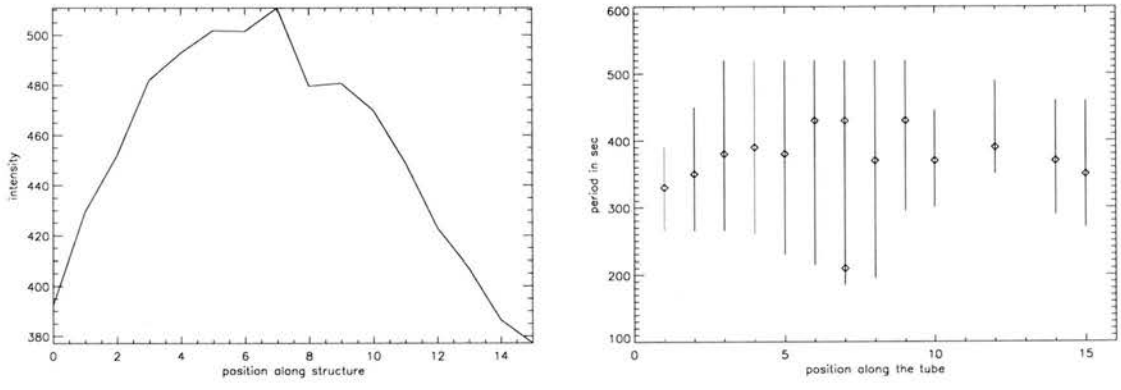

Figure D.8: Average intensity and periods along loop D, 4 April 2000 - 0928 UT

- 178 images, with a cadence of 8 seconds
- velocity estimate from the running difference, 75–110 km/s
- amplitudes between 1.2% and 4.8%
- periods between 185 and 520 sec (max between 210 and 430 sec)

D.2.2 5 April 2000

Loop A - 0230 UT

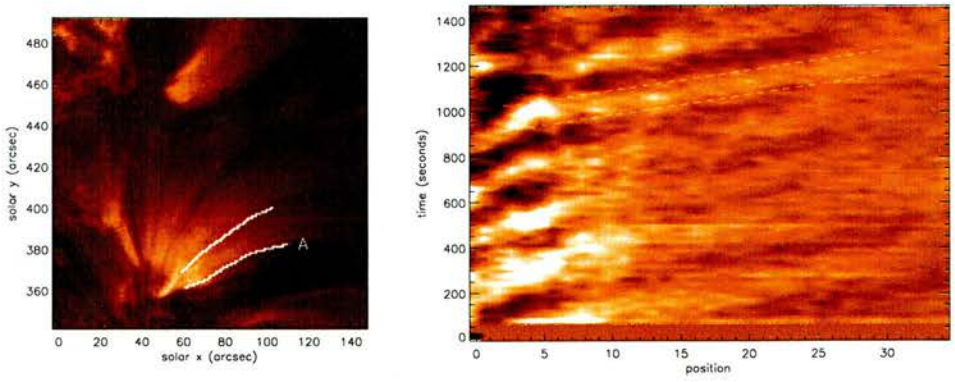

Figure D.9: image and running difference, 5 April 2000 - 0230 UT

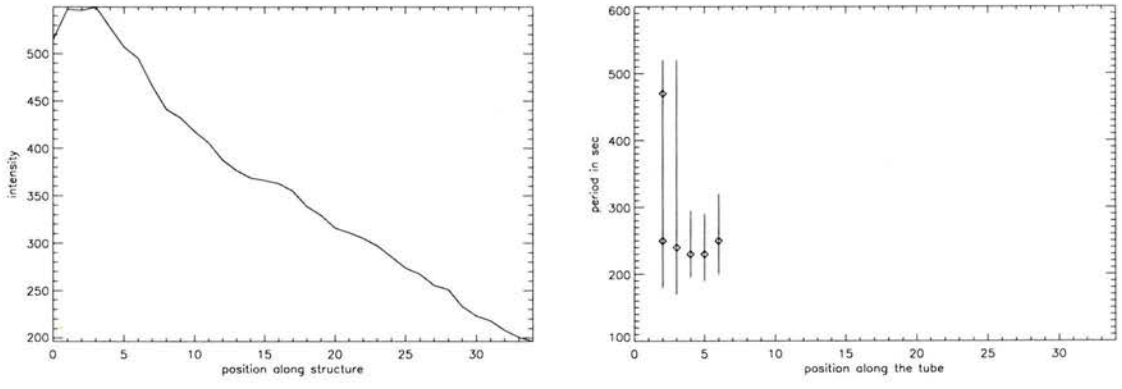

Figure D.10: Average intensity and periods along loop A, 5 April 2000 - 0230 UT

- 164 images, with a cadence of 9 seconds
- velocity estimate from the running difference, 135–180 km/s
- amplitudes between 1.5% and 4.8%
- periods between 170 and 520 sec (max between 230 and 470 sec)

D.2.3 7 April 2000

Loop A - 1328 UT

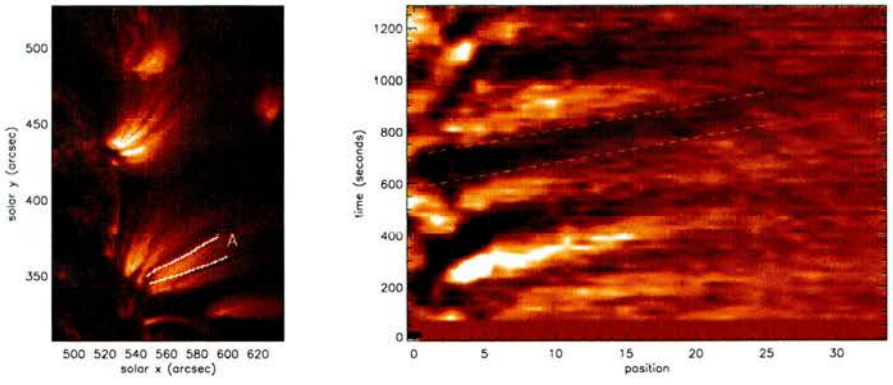

Figure D.11: image and running difference, 7 April 2000 - 1328 UT

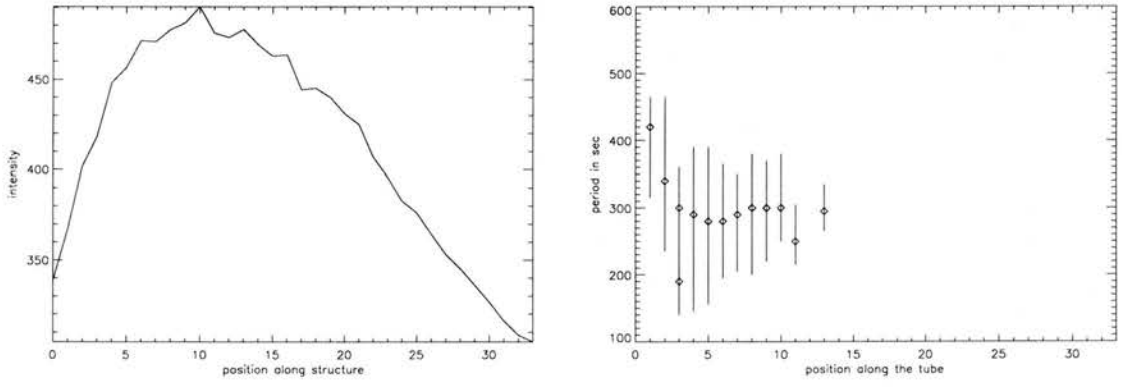

Figure D.12: Average intensity and periods along loop A, 7 April 2000 - 1328 UT

- 144 images, with a cadence of 9 seconds
- velocity estimate from the running difference, 125–170 km/s
- amplitudes between 1.2% and 5.8%
- periods between 140 and 465 sec (max between 190 and 420 sec)

Loop B - 1151 UT

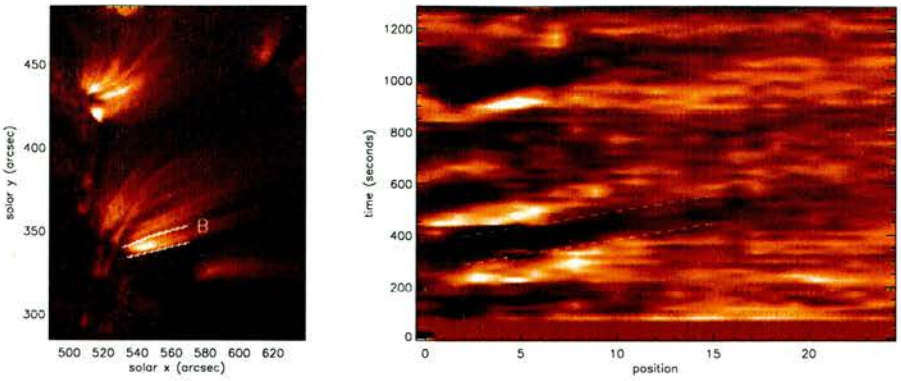

Figure D.13: image and running difference, 7 April 2000 - 1151 UT

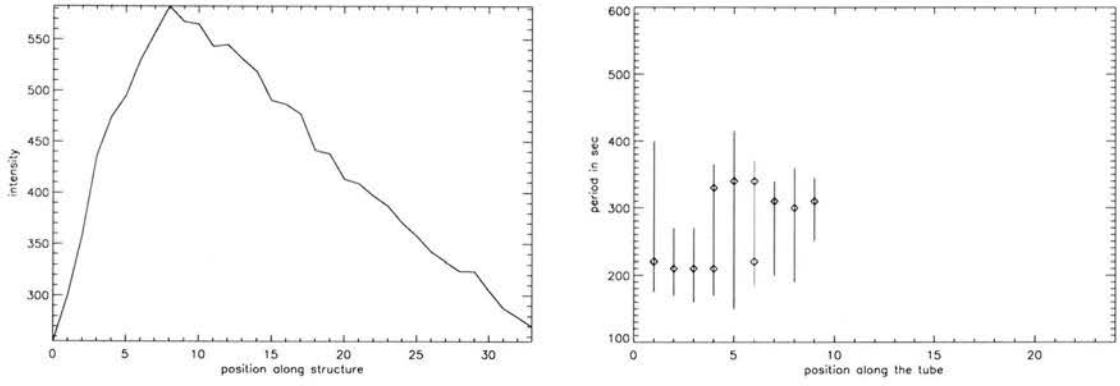

Figure D.14: Average intensity and periods along loop B, 7 April 2000 - 1151 UT

- 144 images, with a cadence of 9 seconds
- velocity estimate from the running difference, 90–145 km/s
- amplitudes between 0.9% and 4.9%
- periods between 150 and 415 sec (max between 210 and 340 sec)

Loop C - 1242 UT

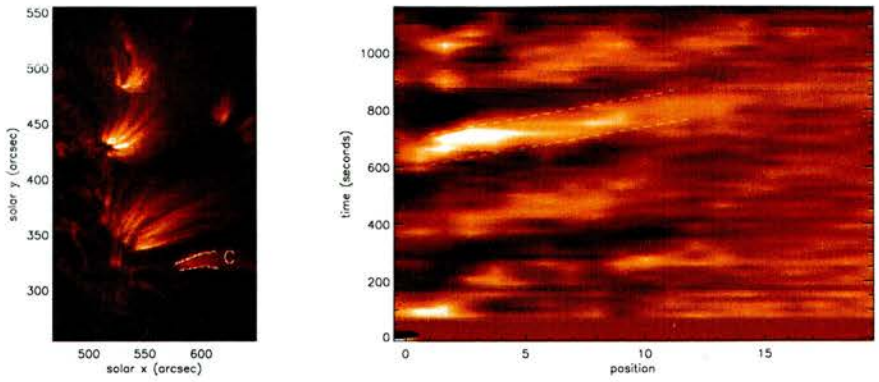

Figure D.15: image and running difference, 7 April 2000 - 1242 UT

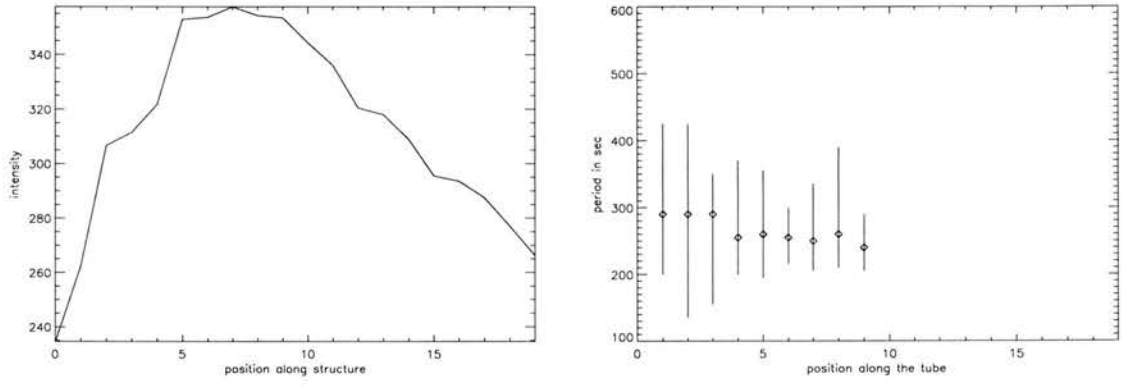

Figure D.16: Average intensity and periods along loop C, 7 April 2000 - 1242 UT

- 130 images, with a cadence of 9 seconds
- velocity estimate from the running difference, 75–125 km/s
- amplitudes between 1.3% and 4.9%
- periods between 135 and 425 sec (max between 255 and 290 sec)

Loop D - 1328 UT

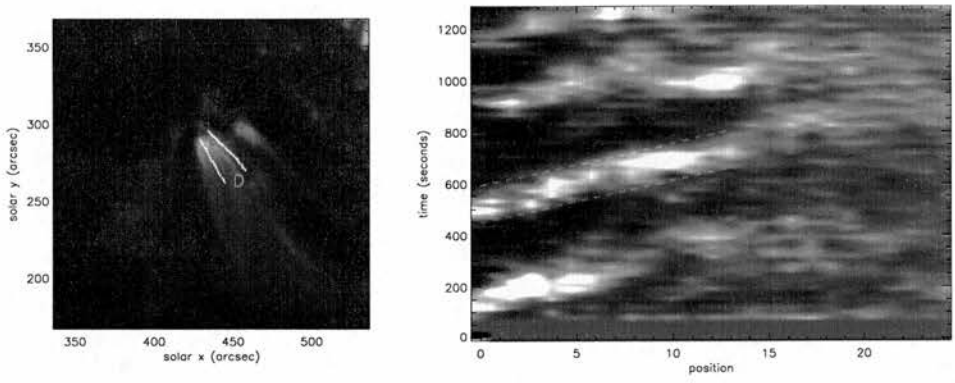

Figure D.17: image and running difference, 7 April 2000 - 1328 UT

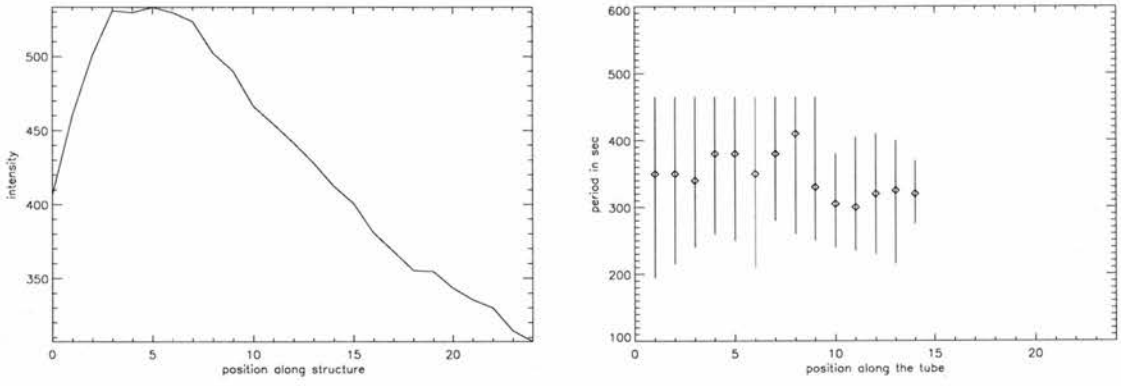

Figure D.18: Average intensity and periods along loop D, 7 April 2000 - 1328 UT

- 144 images, with a cadence of 9 seconds
- velocity estimate from the running difference, 85–125 km/s
- amplitudes between 1% and 4%
- periods between 195 and 465 sec (max between 300 and 410 sec)

D.2.4 8 April 2000

Loop A - 1204 UT

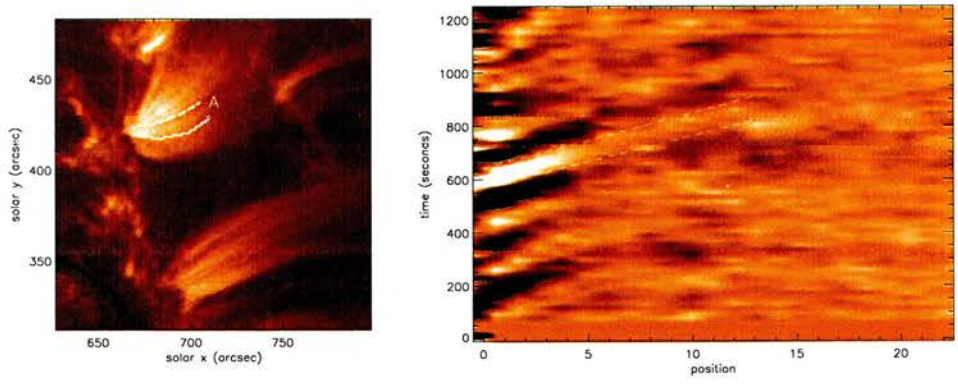

Figure D.19: image and running difference, 8 April 2000 - 1204 UT

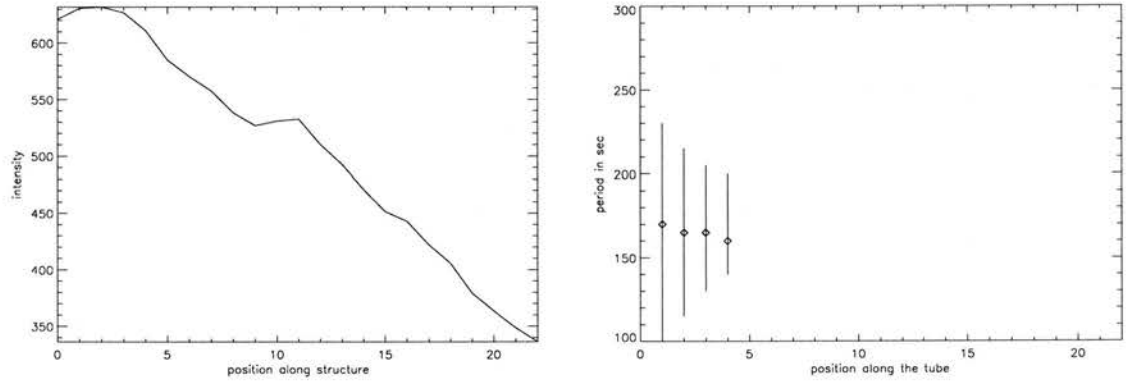

Figure D.20: Average intensity and periods along loop A, 8 April 2000 - 1204 UT

- 140 images, with a cadence of 9 seconds
- velocity estimate from the running difference, 60–85 km/s
- amplitudes between 0.7% and 4.2%
- periods between 100 and 230 sec (max between 160 and 170 sec)

D.2.5 9 April 2000

Loop A - 1354 UT

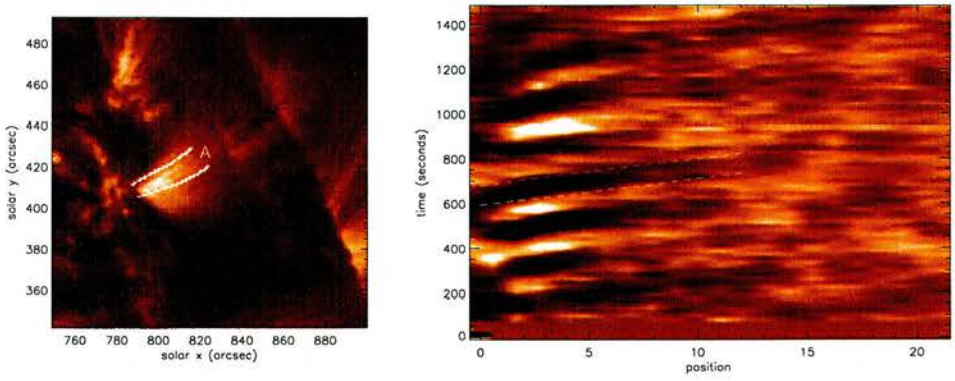

Figure D.21: image and running difference, 9 April 2000 - 1354 UT

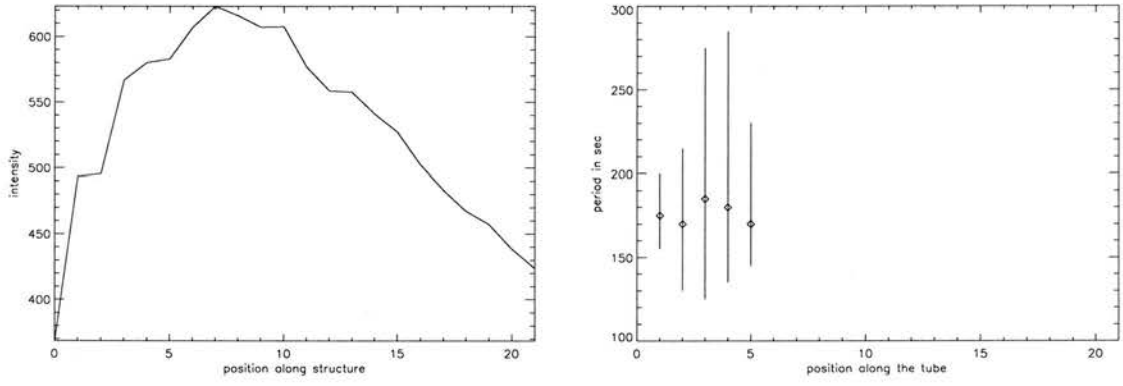

Figure D.22: Average intensity and periods along loop A, 9 April 2000 - 1354 UT

- 166 images, with a cadence of 9 seconds
- velocity estimate from the running difference, 95–155 km/s
- amplitudes between 1.1% and 3.5%
- periods between 125 and 285 sec (max between 170 and 185 sec)

Loop B - 0904 UT

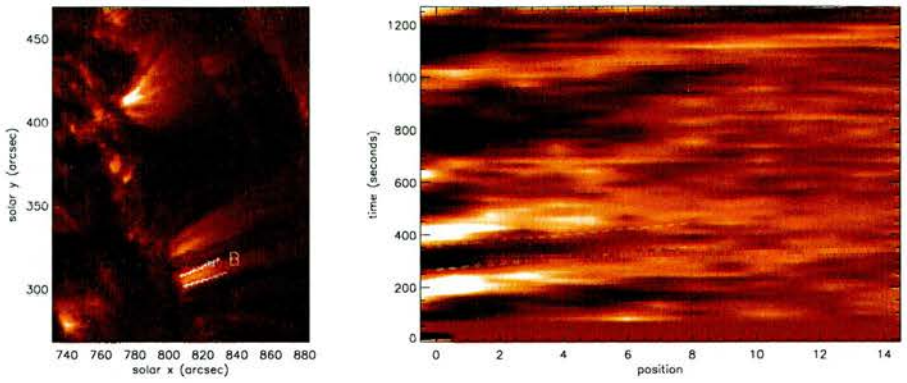

Figure D.23: image and running difference, 9 April 2000 - 0904 UT

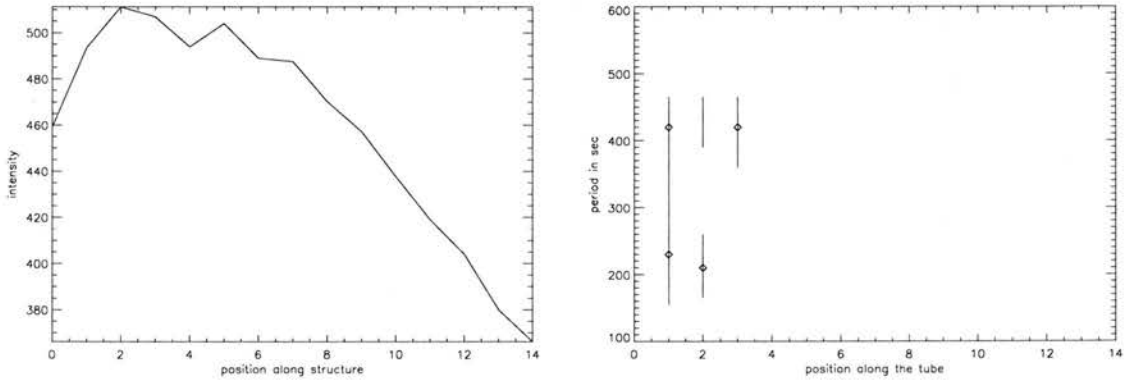

Figure D.24: Average intensity and periods along loop B, 9 April 2000 - 0904 UT

- 142 images, with a cadence of 9 seconds
- velocity estimate from the running difference, 90–200 km/s
- amplitudes between 1.6% and 5.4%
- periods between 155 and 465 sec (max at 210 and 420 sec)

D.3 Active Region AR 8948

D.3.1 11 April 2000

Loop A - 1514 UT

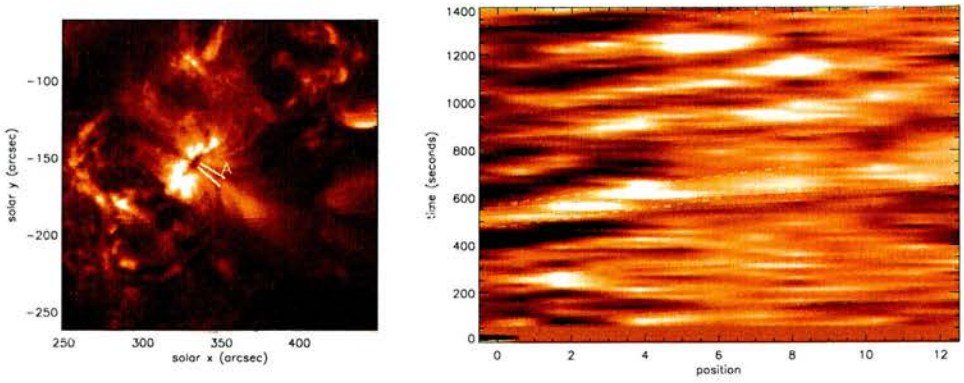

Figure D.25: image and running difference, 11 April 2000 - 1514 UT

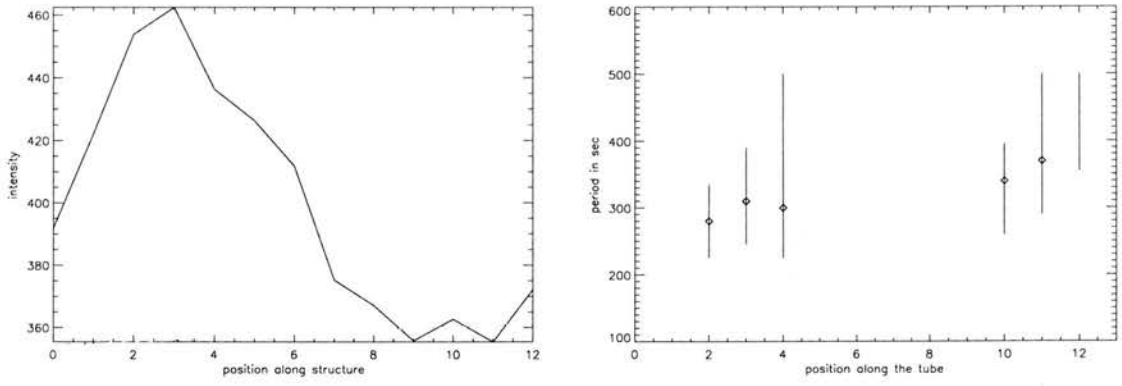

Figure D.26: Average intensity and periods along loop A, 11 April 2000 - 1514 UT

- 176 images, with a cadence of 8 seconds
- velocity estimate from the running difference, 60–90 km/s
- amplitudes between 1.1% and 4.5%
- periods between 225 and 500 sec (max between 280 and 370 sec)

Loop B - 1514 UT

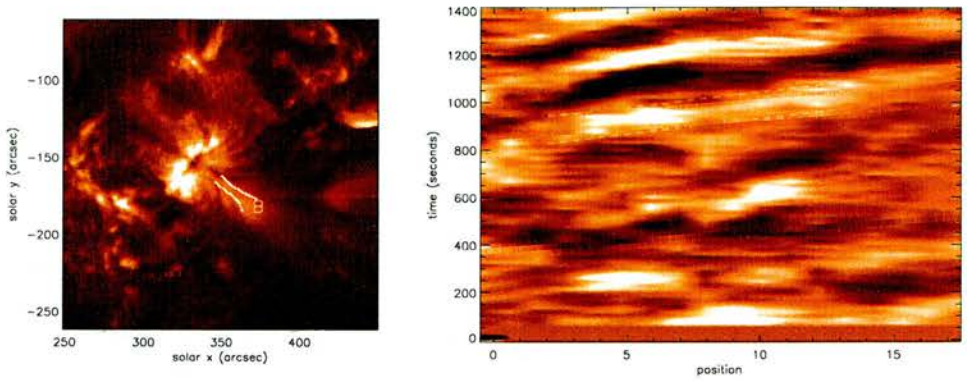

Figure D.27: image and running difference, 11 April 2000 - 1514 UT

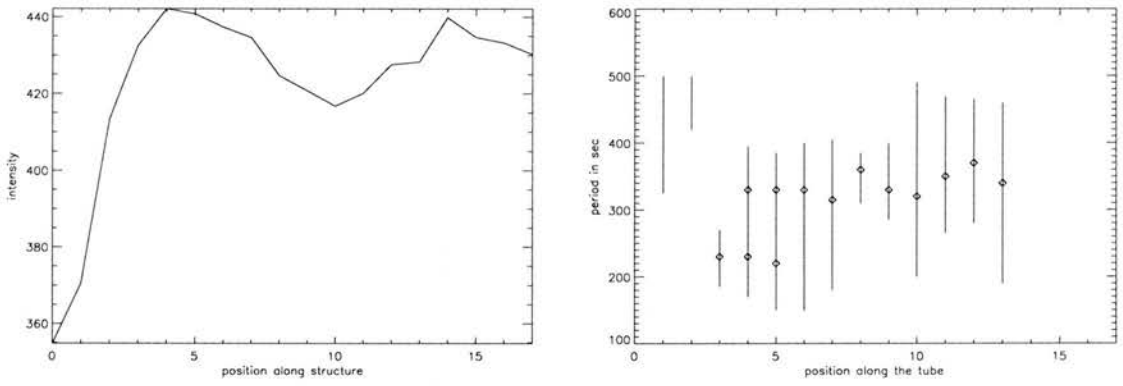

Figure D.28: Average intensity and periods along loop B, 11 April 2000 - 1514 UT

- 176 images, with a cadence of 8 seconds
- velocity estimate from the running difference, 90–140 km/s
- amplitudes between 1.1% and 4.2%
- periods between 150 and 500 sec (max between 220 and 370 sec)

Loop C - 1514 UT

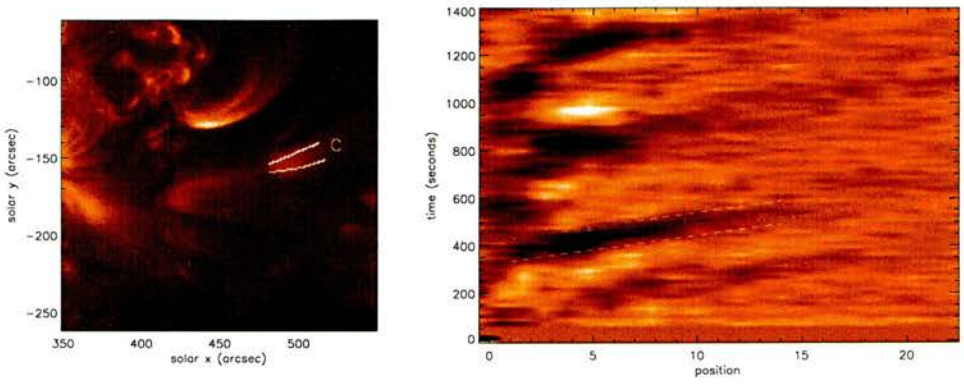

Figure D.29: image and running difference, 11 April 2000 - 1514 UT

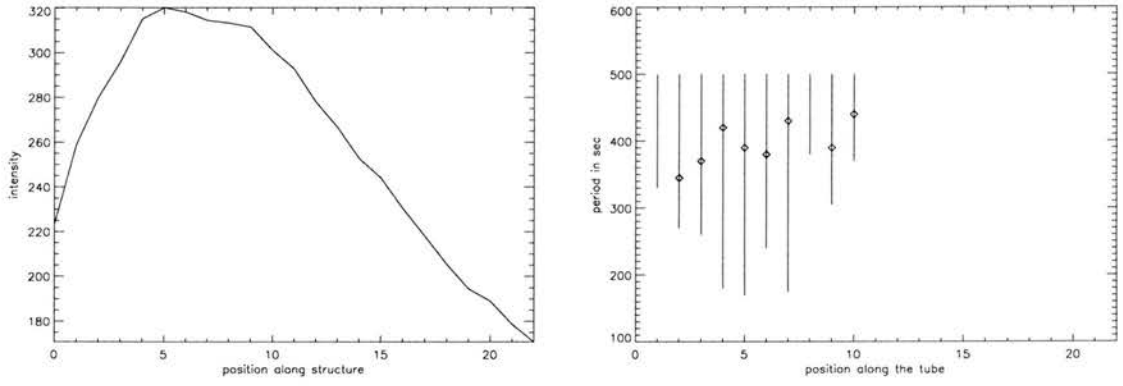

Figure D.30: Average intensity and periods along loop C, 11 April 2000 - 1514 UT

- 176 images, with a cadence of 8 seconds
- velocity estimate from the running difference, 95–140 km/s
- amplitudes between 0.9% and 6.4%
- periods between 170 and 500 sec (max between 345 and 440 sec)

D.3.2 13 April 2000

Loop A - 1405 UT

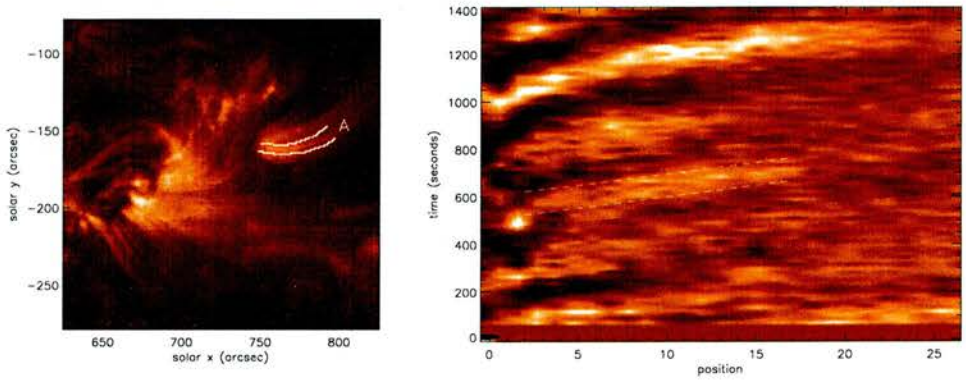

Figure D.31: image and running difference, 13 April 2000 - 1405 UT

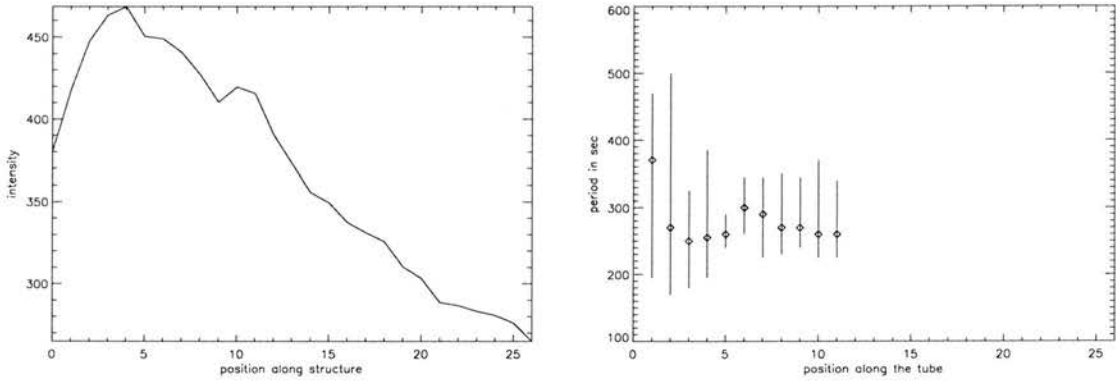

Figure D.32: Average intensity and periods along loop A, 13 April 2000 - 1405 UT

- 176 images, with a cadence of 8 seconds
- velocity estimate from the running difference, 120–185 km/s
- amplitudes between 0.8% and 4.1%
- periods between 170 and 500 sec (max between 250 and 370 sec)

D.4 Active Region AR 8954

D.4.1 17 April 2000

Loop A - 1325 UT

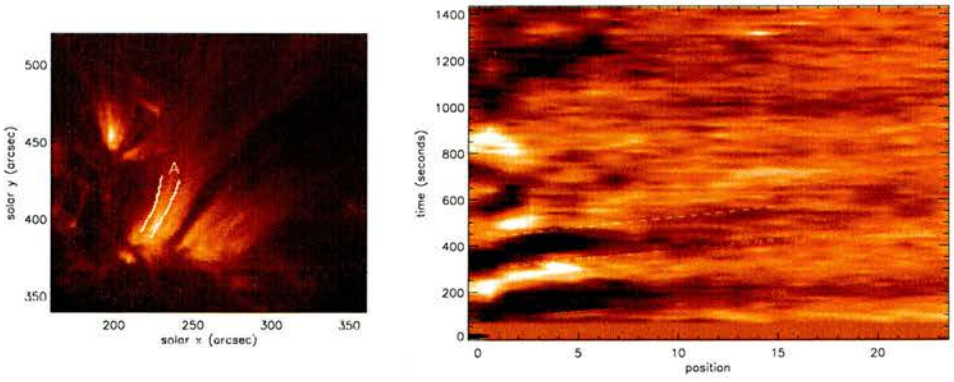

Figure D.33: image and running difference, 17 April 2000 - 1325 UT

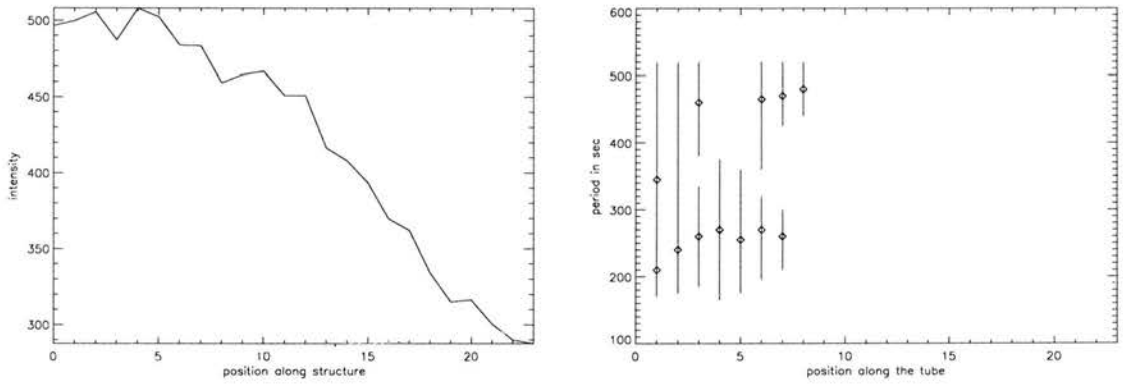

Figure D.34: Average intensity and periods along loop A, 17 April 2000 - 1325 UT

- 206 images, with a cadence of 7 seconds
- velocity estimate from the running difference, 130–200 km/s
- amplitudes between 1.3% and 5%
- periods between 165 and 520 sec (max between 210 and 480 sec)

Loop B - 1325 UT

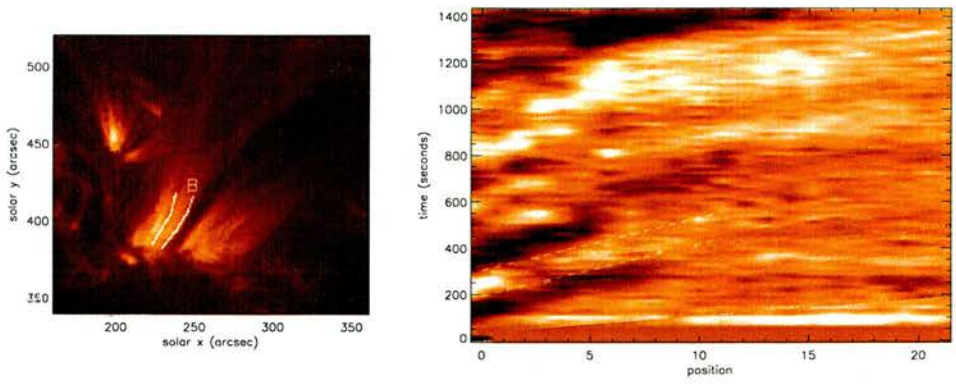

Figure D.35: image and running difference, 17 April 2000 - 1325 UT

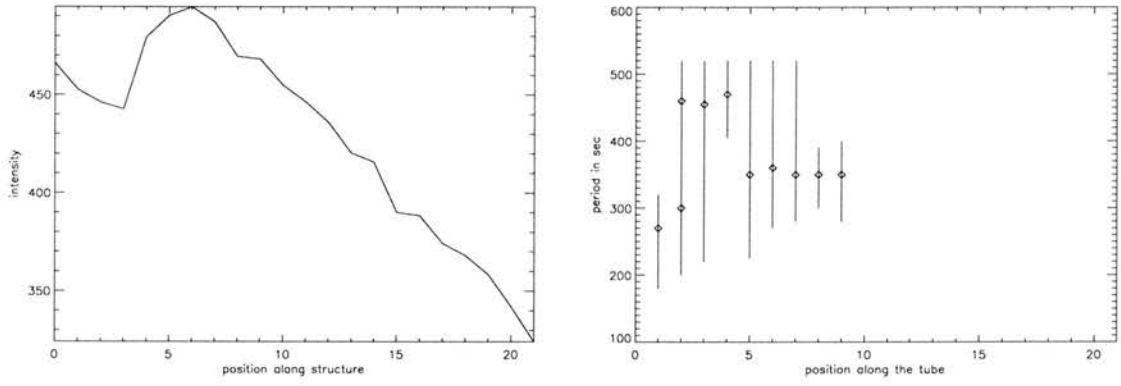

Figure D.36: Average intensity and periods along loop B, 17 April 2000 - 1325 UT

- 206 images, with a cadence of 7 seconds
- velocity estimate from the running difference, 55–70 km/s
- amplitudes between 1.4% and 4.8%
- periods between 180 and 520 sec (max between 270 and 470 sec)

D.5 Active Region AR 8955

D.5.1 18 April 2000

Loop A - 2330 UT

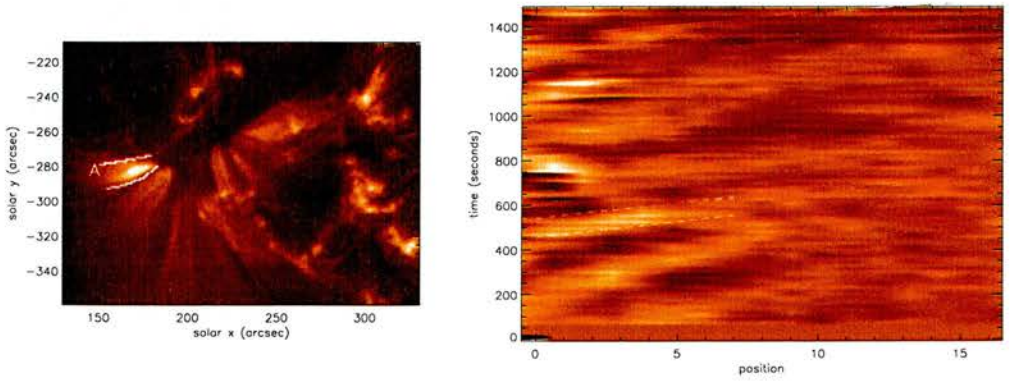

Figure D.37: image and running difference, 18 April 2000 - 2330 UT

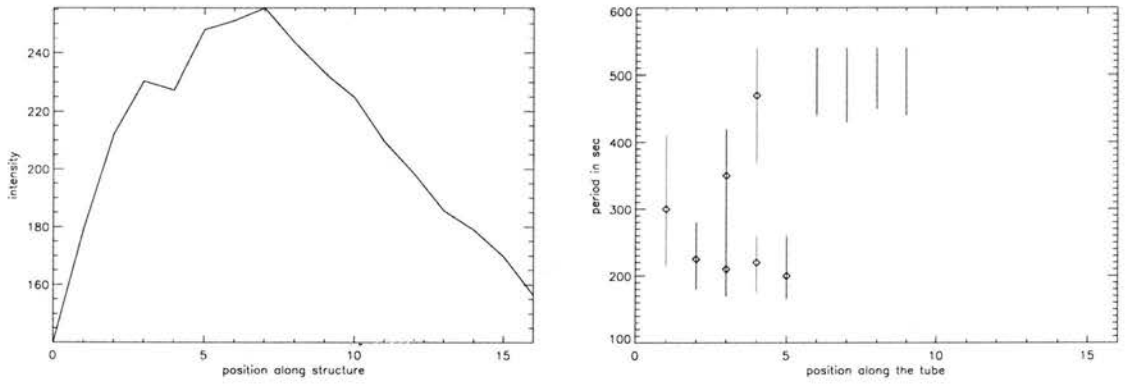

Figure D.38: Average intensity and periods along loop A, 18 April 2000 - 2330 UT

- 107 images, with a cadence of 14 seconds
- velocity estimate from the running difference, 75–140 km/s
- amplitudes between 1% and 5%
- periods between 165 and 540 sec (max between 210 and 470 sec)

Loop B - 2330 UT

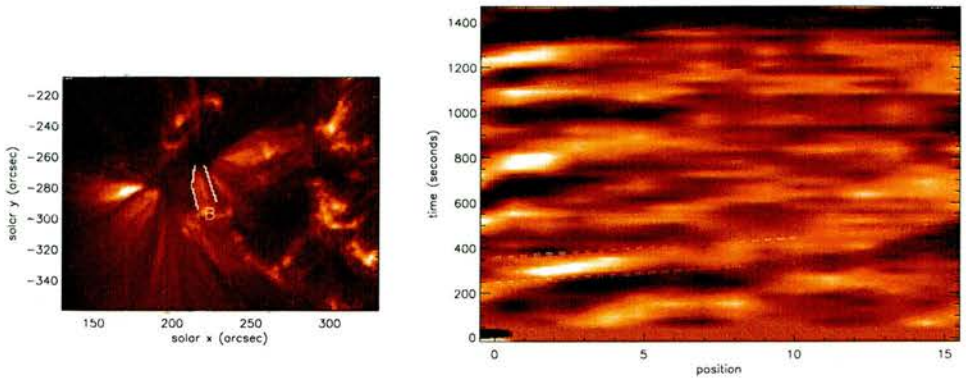

Figure D.39: image and running difference, 18 April 2000 - 2330 UT

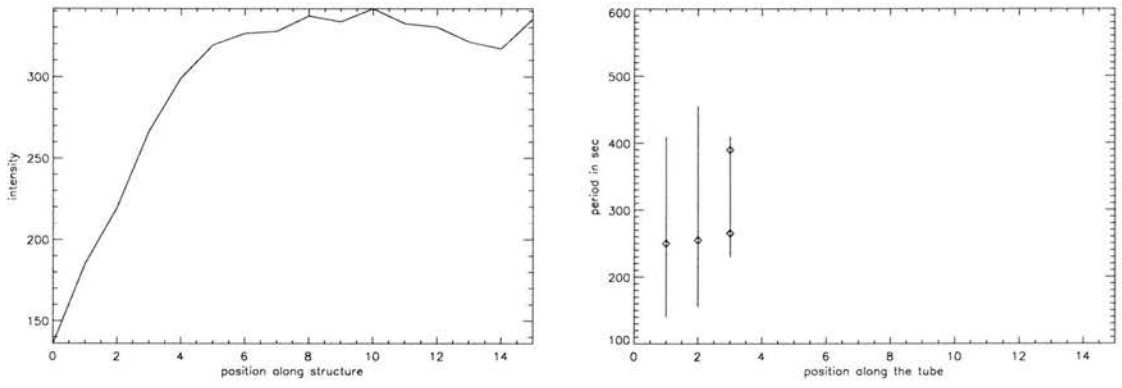

Figure D.40: Average intensity and periods along loop B, 18 April 2000 - 2330 UT

- 107 images, with a cadence of 14 seconds
- velocity estimate from the running difference, 100–165 km/s
- amplitudes between 1% and 5%
- periods between 140 and 455 sec (max at 255 and 390 sec)

D.5.2 19 April 2000

Loop A - 1535 UT

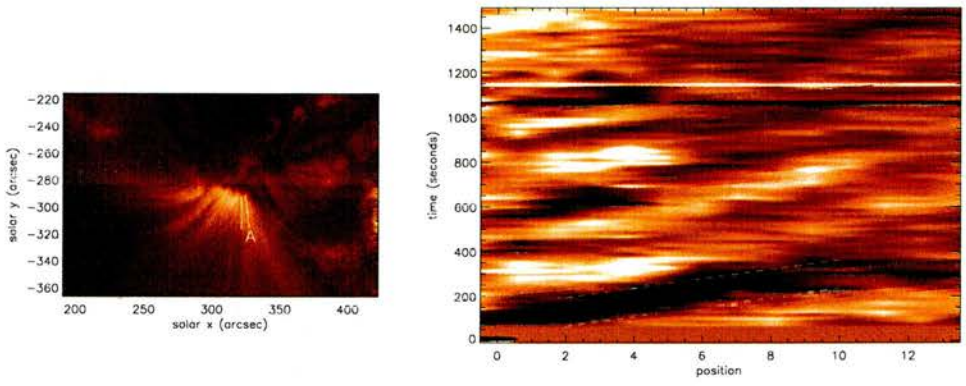

Figure D.41: image and running difference, 19 April 2000 - 1535 UT

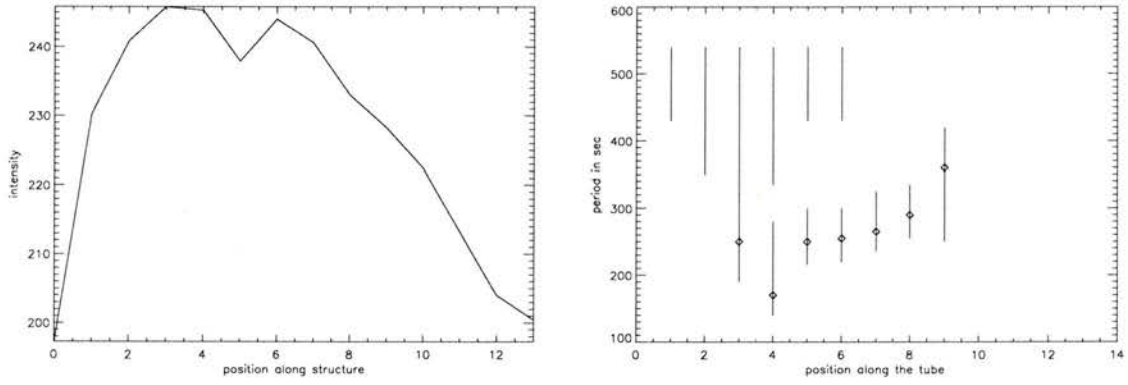

Figure D.42: Average intensity and periods along loop A, 19 April 2000 - 1535 UT

- 107 images, with a cadence of 14 seconds
- velocity estimate from the running difference, 60–80 km/s
- amplitudes between 1.9% and 9.4%
- periods between 140 and 540 sec (max between 170 and 360 sec)

References

Abdelatif, T.E., 1987, ApJ 322, 494

Abramowitz, M. and Stegun, I.A., 1965, Handbook of mathematical functions, Dover

Antonucci, E., Gabriel, A.H., Patchett, B.E., 1984, Solar Physics 93, 85

Aschwanden, M.J., 1987, Solar Physics 111, 113

Aschwanden, M.J., Kliem, B., Schwarz, U., Kurths, J., Dennis, B.R., Schwartz, R.A, 1998, ApJ 505, 941

Aschwanden, M.J., Fletcher, L., Schrijver, C.J., Alexander, D., 1999, ApJ 520, 880

Athay, R.G., White, O.R., 1979a, ApJS, 39, 333

Athay, R.G., White, O.R., 1979b, ApJ, 229, 1147

Banerjee, D., O'Shea, E., Doyle, J.G., 2000, A&A 355, 1152

Beliën, A.J.C., Poedts, S., Goedbloed, J.P., 1997, A&A 322, 995

Berghmans, D., Tirry, W.J., 1997, A&A 325, 318

Berghmans, D., Clette, F., 1999, Solar Physics 186, 207

Berghmans, D., Clette, F., Robbrecht, E., McKenzie, D., 1999a, ESA-SP 446

Berghmans, D., McKenzie, D., Clette, F., 1999b, ESA-SP 448

Bocchialini, K., Baudin, F., 1994, A&A 299, 893

Bocchialini, K., Vial, J.-C., Einaudi, G., 1997, ESA-SP 404, 211

Botha, G.J.J., Arber, T.D., Nakariakov, V.M., Keenan, F.P., 2000, A&A *in press*

Boynton, G.C., Torkelsson, U., 1996, A&A 308, 299

Braginskii, S.I., 1965 in *Reviews of Plasma Physics*, Ed. Leontovich, M.A., Consultants Bureau, New York

Bray, R.J., Cram, L.E., Durrant, C.J., Loughead, R.E., 1991, *Plasma Loops in the Solar Corona*, Cambridge University Press, Cambridge

Brekke, P., Kjeldseth-Moe, O., Harrison, R.A., 1997, Solar Physics 175, 511

Browning, P.K., Priest, E.R., 1984, A&A 131, 283

Browning, P.K., 1991, Plasma Phys. and Controlled Fusion 33, 539

Brynildsen, N., Leifsen, T., Kjeldseth-Moe, O., Maltby, P., 1999a, ApJ 511, L121

Brynildsen, N., Kjeldseth-Moe, O., Maltby, P., 1999b, ApJ 517, L159

Cally, P.S., 1991, J.Plasma Phys. 45, 453

Chapman, R.D., Jordan, S.D., Neupert, W.M., Thomas, R.J., 1972, ApJ 174, L97

Chiuderi-Drago, F., Landi, E., Fludra, A., Kerdraon, A., 1999, A&A 348, 261

Cranmer, S.R. et al., 1999, ApJ 511, 481

Das, T.K., Chatterjee, T.N., Sen, A.K., 1993, Solar Physics 148, 61

David, C., Gabriel, A.H., Bely-Dubau, F., Fludra, A., Lemaire, P., Wilhelm, K., 1998, A&A 336, L90

Davila, J.M., 1987, ApJ 317, 514

DeForest, C.E., Hoeksema, J.T., Gurman, J.B., Thompson, B.J., Plunkett, S.P., Howard, R., Harrison, R.C., Hassler, D.M., 1997, Solar Physics 175, 393

DeForest, C.E., Gurman, J.B. 1998, ApJ 501, L217

Del Zanna, L., Hood, A.W., Longbottom, A.W., 1997, A&A 318, 963

Doyle, J.G., van den Oord, G.H.J., O'Shea, E., 1997, A&A 327, 365

Doyle, J.G., Teriaca, L., Banerjee, D., 1999, A&A 349, 956

Egan, T.F, Schneeberger, T.J., 1979, Solar Physics 64, 223

Erdélyi, R., Doyle, J.G., Perez, M.E., Wilhelm, K., 1998, A&A 337, 287

Esser, R., Fineschi, S., Dobrzycka, D., Habbal, S.R., Edgar, R.J., Raymond, J.C., Kohl, J.L., Guhathakurta, M., 1999, ApJ 510, L63

Farge, M., 1992, Annu. Rev. Fluid Mech. 24, 395

Frick, P., Galyagin, D., Hoyt, D.V., Nesme-Ribes, E., Schatten, K.H., Sokoloff, D., Zakharov, V., 1997, A&A 328, 670

Gallagher, P.T., Phillips, K.J.H., Harra-Murnion, L.K., Baudin, F., Keenan, F.P., 1999, A&A 348, 251

Giordano, S., Antonucci, E., Noci, G., Romoli, M., Kohl, J.L., 2000, ApJ 531, L79

Goedbloed, J.P., Halberstadt, G., 1994, A&A 286, 275

Golub, L. and Pasachoff, J.M., 1997, *The Solar Corona*, Cambridge University Press, Cambridge

Golub, L., Maxson, C., Rosner, R., Serion, S., Vaiana, G.S., 1980, ApJ 238, 343

Habbal, S.R., Ronan, R., Withbroe, G.L., 1985, Solar Physics 98, 323

Handy, B.N. et al., 1999, Solar Physics 187, 229

Harra-Murnion, L.K., Matthews, S.A., Ichimoto, K., 1999, A&A 345, 1011

Harrison, R.A., 1987, A&A 182, 337

Halberstadt, G., Goedbloed, J.P., 1993, A&A 280, 647

Halberstadt, G., Goedbloed, J.P., 1995a, A&A 301, 559

Halberstadt, G., Goedbloed, J.P., 1995b, A&A 301, 577

Heyvaerts, J., Priest, E.R., 1983, A&A 117, 220

Hollweg, J.V., 1978, Solar Physics 56, 305

Hollweg, J.V., 1981, Solar Physics 70, 25

Hollweg, J.V., Jackson, S., Galloway, D., 1982, Solar Physics 75, 35

Hood, A.W., Ireland, J., Priest, E.R., 1997a, A&A 318, 957

Hood, A.W., Gonzalés-Delgado, D., Ireland, J., 1997b, A&A 324, 11

Ionson, J.A., 1978, ApJ 226, 650

Ionson, J.A., 1984, ApJ 276, 357

Ireland, J., 1996, Ann. Geophys. 14, 485

Ireland, J., Priest, E.R., 1997, Solar Physics 173, 31

Ireland, J., Walsh, R.W., Harrison, R.A., Priest, E.R., 1999a, A&A 347, 355

Ireland, J., Wills-Davey, M., Walsh, R.W., 1999b, Solar Physics 190, 207

Kano, R., Tsuneta, S., 1996, PASJ, 48, 535

Kjeldseth-Moe, O., Brekke, P., 1998, Solar Physics 182, 73

Komm, R.W., 1994, ASP Conference Series 68, 24

Koutchmy, S., Zugzda, Y.D., Locans, V., 1983, A&A 120, 185

Leahy, D.A., Darbro, W., Elsner, R.F., Weisskopf, M.C., Sutherland, P.G., Kahn, S., Grindlay, J.E., 1983, ApJ 266, 160

Lou, Y.-Q., Rosner, R., 1994, ApJ 424, 429

Mason, H.E., Young, P.R., Pike, C.D., Harrison, R.A., Fludra, A., Bromage, B.J.I., Del Zanna, G., 1997, Solar Physics 170, 143

McKenzie, D.E., Mullan, D.J., 1997, Solar Physics 176, 127

Mészárosová, H., Jiricka, K., Karlicky, M., 1999, A&A 348, 1005

Moore, R.L., Musielak, Z.E., Suess, S.T., An, C.-H., 1991, ApJ 378, 347

Moore, R.L., Hammer, R., Musielak, Z.E., Suess, S.T., An, C.-H., 1992, ApJ 397, L55

Musielak, Z.E., Fontenla, J.M., Moore, R.L., 1992, Phys. Fluids B 4, 13

Nakariakov, V.M., Roberts, B., Murawski, K., 1997, Solar Physics 175, 93

Nakariakov, V.M., Roberts, B., Murawski, K., 1998, A&A 332, 795

Nakariakov, V.M., Ofman, L., DeLuca, E.E., Roberts, B., Davila, J.M., 1999, Science 285, 862

Nakariakov, V.M., Ofman, L., Arber, T.D., 2000, A&A 353, 741

Narain, U., Ulmschneider, P., 1990, Space Sci. Rev. 54, 377

Narain, U., Ulmschneider, P., 1996, Space Sci. Rev. 75, 453

Narain, U., Sharma, R.K., 1998, Solar Physics 181, 287

Nocera, L., Leroy, B., Priest, E.R., 1984, A&A 133, 387

Ofman, L., Davila, J.M., 1995, Journal of Geophysical Research 100, 23 413

Ofman, L., Romoli, M., Poletto, G., Noci, C., Kohl, J.L., 1997, ApJ 491, L111

Ofman, L., Nakariakov, V.M., DeForest, C.E., 1999, ApJ 514, 441

Parker, E.N., 1991a, ApJ 372, 719

Parker, E.N., 1991b, ApJ 376, 355

Parnell, C.E., Priest, E.R., Golub, L., 1994, Solar Physics 151, 57

Parnell, C.E., 2000, Phil. Trans. R. Soc. Lond. 358, 669

Petkaki, P., Malara, F., Veltri P., 1998, ApJ 500, 483

Phillips, K.J.H., 1992, *A Guide to the Sun*, Cambridge University Press, Cambridge

Poedts, S., Goossens, M., Kerner, W., 1990, ApJ 360, 279

Poedts, S., Boynton, G.C., 1996, A&A 306, 610

Poedts, S., Goedbloed, J.P., 1997, A&A 321, 935

Poedts, S., Tóth, G., Beliën, A.J.C., Goedbloed, J.P., 1997, Solar Physics 172, 45

Porter, J.G., Toomre, J., Gebbie, K.B., 1984, ApJ 283, 879

Porter, J.G., Falconer, D.A., Moore, R.L., 1998, ESA-SP 421

Porter, L.J., Klimchuk, J.A., Sturrock, P.A., 1994a, ApJ 435, 482

Porter, L.J., Klimchuk, J.A., Sturrock, P.A., 1994b, ApJ 435, 502

Priest, E.R., 1982, *Solar Magnetohydrodynamics*, D.Reidel, Dordrecht

Priest, E.R. et al, 1998, Nature 393, 545

Priest, E.R. and Forbes, T.G., 2000, *Magnetic Reconnection; MHD Theory and Applications*, Cambridge University Press, Cambridge

Rae, I.C., Roberts, B., 1982, ApJ 256, 761

Reale, F., 1999, Solar Physics 190, 139

Robbrecht, E., Berghmans, D., Poedts, S., 1999, ESA-SP 446

Roberts, B., 1981a, Solar Physics 69, 27

Roberts, B., 1981b, Solar Physics 69, 39

Roberts, B., Edwin, P.M., Benz, A.O., 1984, ApJ 279, 857

Roberts, B., 1985, Phys. Fluids 28, 3280

Roberts, B., 1991, in *Advances in Solar System Magnetohydrodynamics*, Eds. Priest, E.R. and Hood, A.W., Cambridge University Press, Cambridge

Roberts, B., 2000, Solar Physics 193, 139

Ruderman, M.S., Berghmans, D., Goossens, M., Poedts, S., 1997a, A&A 320, 305

Ruderman, M.S., Goossens, M., Ballester, J.L., Oliver, R., 1997b, A&A 328, 361

Ruderman, M.S., Nakariakov, V.M., Roberts, B., 1998, A&A 338, 1118

Ruderman, M.S., 1999, ApJ 521, 851

Ruderman, M.S., Goldstein, M.L., Roberts, D.A., Deane, A., Ofman, L., 1999, Journal of Geophysical Research 104, 17 057

Ruzmaikin A., Berger, M.A., 1998, A&A 337, L9

Sakurai, T., Kitayama, O., Ma, J., 1995, Geophys. Astrophys. Fluid Dynamics 79, 277

Schrijver, C.J. et al., 1999, Solar Physics 187, 261

Schrijver, C.J., Brown, D.S., 2000, ApJ 537, L69

Sheeley, N.R. et al. 1997, ApJ 484, 472

Shimizu, T., 1995, Publ. Astron. Soc. Japan 47, 251

Shimizu, T., Tsuneta, S., 1997, ApJ 486, 1045

Similon, P.L., Zargham, S., 1992, ApJ 388, 644

Singh, J., Cowsik, R., Raveendran, A.V., Bagare, S.P., Saxena, A.K., Sundararaman, K., Krishan, V., Naidu, N., Samson, J.P.A., Gabriel, F., 1997, Solar Physics 170, 235

Smith, J.M., 1997, *PhD thesis*, University of St Andrews, Scotland

Strong, K., 1994, Proc. of Kofu Symposium, NRO Report 360, 53

Tayler, R.J., 1997, *The Sun as a Star*, Cambridge University Press, Cambridge

Tirry, W.J., Berghmans, D., Goossens, M., 1997, A&A 322, 329

Tirry, W.J., Berghmans, D., 1997, A&A 325, 329

Torkelsson, U., Boynton, G.C., 1998, Mon. Not. R. Astron. Soc. 295, 55

Torrence, C., Compo, G.P., 1997, Bull. Amer. Meteor. Soc. 79, 61

Tsubaki, T., 1977, Solar Physics 51, 121

Tsubaki, T., 1988, in *Solar and Stellar Coronal Structures and Dynamics*, Ed. Altrock, R.C., NSO, Sunspot NM

Ulrich, R.K., 1996, ApJ 465, 436

Vaiana, G.S., Rosner, R., 1978, Ann. Rev. Astron. Astrophys. 16, 393

Vigouroux, A., Delache, Ph., 1993, A&A 278, 607

Walsh, R.W., Bell, G.E., Hood, A.W., 1996, Solar Physics 169, 33

Walsh, R.W., 1999, ESA-SP 446, 687

Walsh, R.W., Georgoulis, M.K., 1999, A&A, in revision

White, O.R., Athay, R.G., 1979a, ApJS, 39, 317

White, O.R., Athay, R.G., 1979b, ApJS, 39, 347

Withbroe, G.L., Noyes, R.W., 1977, Ann. Rev. Astron. Astrophys. 15, 363

Withbroe, G.L., Habbal, S.R., Ronan, R., 1985, Solar Physics 95, 297

Wikstøl, Ø., Judge, P.G., Hansteen, V.H., 1997, ApJ 483, 972

Woo, R., 1996, Nature 379, 321

Woo, R., Habbal, S.R., 1999, ApJ 510, L69

Wright, A.N., Garman, A.R., 1998, Journal of Geophysical Research 103, 2377

Young, P.R., Klimchuk, J.A., Mason, H.E., 1999, A&A 350, 286

Zirker, J.B., 1993, Solar Physics 148, 43